Upheaval buckling of offshore pipelines buried in loose and liquefiable soils

Elizabeth S. Williams

New College

University of Oxford

A thesis submitted for the degree of

Doctor of Philosophy

Hilary Term, 2014

Abstract

Upheaval buckling of offshore pipelines buried in

loose and liquefiable soils

Elizabeth S. Williams
New College, Oxford
Hilary Term, 2014

Pipelines used for the transportation of oil and gas products offshore are often buried beneath the seabed for protection from mechanical damage and for thermal insulation. During high temperature and high pressure operations, these pipelines are susceptible to resurfacing behaviour known as *upheaval buckling*, a structural response that is strongly influenced by the resistance of the surrounding soil. Despite much previous research on pipe uplift, the influence of the initial soil state – particularly in loose and liquefiable soil conditions – on the uplift resistance and corresponding buckling behaviour of the pipe is not well understood.

This thesis presents research that examines the implications of these backfill conditions in the context of the global behaviour of the pipeline. The work consists of plane-strain monotonic uplift experiments focusing on density, rate, and stress level effects on the initial pipe-soil response. This is followed by numerical modelling of the global buckling behaviour using the experimental data as inputs. Finally, plane-strain cyclic experiments examine the possibility of progressive upward displacements over a number of cycles causing eventual upheaval buckling.

A key finding from the uplift tests is that very loose backfill conditions may result in a localised flow-around failure mechanism, associated with lower peak resistance and a softer force-displacement response than with the sliding block mechanism that is typically assumed. This leads to lower peak buckling loads/temperatures than those predicted by current design guidelines. High quality data from both the monotonic and cyclic experiments was used to assess and suggest improvements to design guidance for these conditions.

Acknowledgements

There are a number of people I would like to thank for their support and encouragement throughout this project. First of all, I would like to express my gratitude to my supervisors, Prof. Byron Byrne and Prof. Tony Blakeborough, for their invaluable input during the research and writing-up process. In particular, I thank Byron for his many suggestions, technical guidance, and enthusiastic support over the course of this project; and I thank Tony for the benefit of his substantial expertise and generous advice on the computational aspects of the work. I would also like to thank my examiners, Prof. Dave White and Prof. Chris Martin, for their thorough review of the thesis and their suggestions for its improvement.

My thanks go out to my colleagues in the Civil Engineering Group, who have helped me greatly along the way. I am very grateful to the laboratory technicians, Bob Sawala and Clive Baker, and the group secretary, Alison May, for their assistance and encouragement during my time in the department. Additionally, I am indebted to my fellow students in Room 11 – I could not have hoped for a better work environment in which to spend the last few years.

This work would not have been possible without the generous financial support of several organisations. I gratefully acknowledge the funding from the Clarendon Fund, New College, and the Vice Chancellors' Fund, which allowed me this opportunity to study at Oxford.

Finally, heartfelt thanks go to my friends (near and far) and family – especially to my parents – for their continuing love and support.

Contents

Notation

A	Cross-sectional area of pipe
A_d, A_k	Slope constants for cyclic displacements and stiffness
C_ϕ	Flow-around prediction factor accounting for problem geometry
d_{UB}	Predicted upper-bound displacement for irrecoverable infilling
D	Pipe diameter
D_{50}	Grain size (50% passing)
d	Pipe displacement (upward)
$\tilde{d}$	Normalised pipe displacement
d_f	Mobilisation displacement (displacement to peak uplift force)
d_0	Upward displacement to F_{max} in 0th cycle
E	Young's modulus
e_{max}, e_{min}	Maximum and minimum void ratio
$e(\lambda)$	Equivalent eccentricity function for initial pipeline imperfection
F_{ult}	Peak uplift force
F_a, F_v	Peak axial and vertical spring force used in buckling model
F_{max}, F_{min}	Upper and lower force targets for cyclic loading
f	Uplift factor
f_r	Post-peak uplift factor
H	Initial embedment depth to pipe centre
H_c	Initial embedment depth to pipe crown
H^*	Equivalent embedment depth with overburden
H/D	Embedment ratio
H/D^*	Equivalent embedment ratio with overburden

H/D_{trans}	Transition embedment ratio
I	Second moment of area
I_R	Relative dilatancy index
K_o	At-rest lateral earth pressure coefficient
K_p	Passive lateral earth pressure coefficient
K_b, K_c	Cyclic stiffness factors related to load magnitude and load type
k	Soil stiffness
$\tilde{k}$	Normalised soil stiffness
k_a, k_v, k_d	Axial, vertical (uplift), and downward soil spring stiffness in buckling model
k_{up}, k_{down}	Upward and downward cyclic soil stiffness
L	Pipe length
L_o	Initial imperfection length
N_{ult}	Soil breakout factor (peak uplift force normalised by $\gamma'HDL$)
N_{FAM}	Normalised force for flow-around mechanism
N	Cycle number
P	Effective axial force in pipe
P_{crit}	Critical buckling load
P_o	Longitudinal thermal force
P_{loc}	Axial force for buckle localisation
p_r	Reference pressure for stress level normalisation (constant value of 100 kPa)
q	Uniform vertical restraining force on pipeline
RD	Relative density
R_{FAM}	Predicted resistance for flow-around failure mechanism
R_{max}	DNV peak uplift resistance
SG	Specific gravity
T	Pipe temperature

T_b, T_c	Cyclic displacement factors relating to load magnitude and load type
t	Pipe wall thickness
u_e	Excess pore water pressure (averaged from several readings around the pipe)
v	Pipe uplift rate
v_{om}	Initial imperfection height
v_o	Initial pipeline shape
W_{ref}	Reference weight of soil cover for cyclic loading
y	Deflected shape of pipeline
α, β	Shape parameters for DNV tri-linear characteristic uplift curve
α_f, d_{fr}	Post-peak shape parameters for DNV tri-linear characteristic uplift curve
α_{FAM}	Flow-around force coefficient
α_T	Coefficient of thermal expansion
γ'	Effective unit weight of soil
ζ_b	Cyclic load magnitude parameter (defined in Figure 5-4)
ζ_c	Cyclic load type parameter (defined in Figure 5-4)
κ	Pipe-soil axial stiffness coefficient
λ	Wavelength of buckled pipeline
$\tilde{\sigma}_v$	Normalised effective stress level (stress ratio)
ϕ'	Effective friction angle
ϕ'_{peak}	Peak friction angle
ϕ'_{cs}	Critical state friction angle
ψ	Dilation angle

List of Abbreviations

FAM	Flow-around model
ISM	Inclined slip surface model
LC	Load control
LVDT	Linear variable displacement transducer
OB	Overburden
PPT	Pore pressure transducer
PWP	Pore water pressure
UHB	Upheaval buckling
aVSM	Adapted vertical slip model
VSM	Vertical slip model

1   Introduction

Offshore oil and gas production requires an extensive network of subsea pipelines to allow efficient transportation of the product between newly developed oil fields and existing production facilities. Often these pipelines are buried to some depth of soil cover for protection and stability during operation at high temperatures and high pressures. Under such conditions, pipelines may be susceptible to upheaval buckling, a structural response caused by compressive stresses due to thermal loading, which may lead to resurfacing of the pipe if insufficient vertical restraint is provided by the soil cover. Multiple thermal cycles may also lead to gradual upward displacement of the pipe over time and a corresponding reduction in the soil cover, increasing the likelihood of upheaval buckling failure on a subsequent cycle.

In order to assess pipeline stability against this mechanism, the uplift resistance of the soil must be determined; the value is then typically used as an input for finite element modelling to determine a safe embedment depth, following procedures recommended in design guidelines (such as in DNV-RP-F110, 2007). Much previous experimental research has examined plane-strain pipe uplift, with the aim of predicting the limiting soil resistance and the mobilisation displacement of the pipe (i.e. the vertical displacement required to mobilise the peak resistance). Shortcomings still exist, however, in the understanding of how the initial state of the soil affects the pipe's resistance to monotonic and cyclic loading, particularly in the loose and liquefiable soil conditions that often occur as a result of current installation methods (e.g. jet trenching). Furthermore, the relationship between soil parameters, the corresponding force-displacement response and the actual buckling behaviour of the pipe is seldom examined together in the literature.

This thesis presents research that addresses these shortcomings and provides further insight into upheaval buckling behaviour in loose and liquefiable soils, through both physical experiments and numerical modelling. The work consists of plane-strain monotonic uplift

experiments focusing on density and rate effects on the initial pipe-soil response, followed by numerical modelling of the global buckling behaviour using the experimental data as inputs. Finally, plane-strain cyclic experiments are used to examine the implications of possible upheaval creep (or cyclic ratcheting) for upheaval buckling design. Results are compared with current design guidance throughout, in order to assess their treatment of these conditions. A series of recommendations are made at the end of the thesis.

1.1. Background

Subsea pipeline networks represent critical infrastructure for the offshore extraction and transportation of oil and gas products. As explorations extend further offshore and into deeper waters to meet increasing energy demands, pipelines spanning hundreds of kilometres are often required for these developments. Typical components of an offshore pipeline network are shown in Figure 1-1 (Randolph and Gourvenec, 2011).
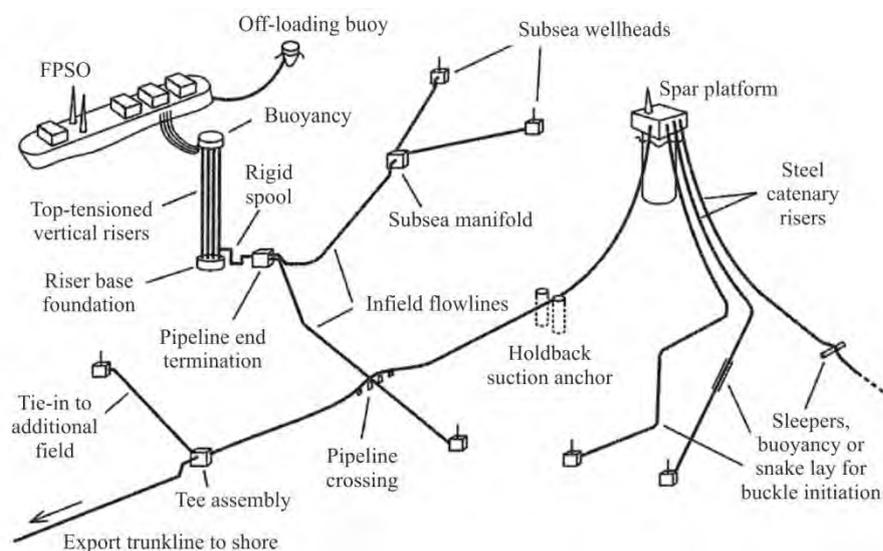

Figure 1-1 Schematic of a typical offshore pipeline network, after Randolph and Gourvenec (2011)

Small-diameter pipelines (of 0.1 to 0.5 m), also known as flowlines or tiebacks/tie-ins, are typically used to connect subsea wellheads to manifolds and existing centralised production platforms (as seen in Figure 1-1). During installation these pipelines are placed either directly

on the seabed, in open trenches that may be backfilled naturally or mechanically, or buried to a specified depth of cover. Although pipeline burial is associated with high installation costs, it is often required for several reasons: to avoid mechanical damage due to extensive trawling in some areas, to enable crude oil to be transported efficiently at high temperatures, and to increase overall stability compared to other installation types (Schupp, 2009).

For efficient installation of small-diameter flexible pipelines, long sections of pipe can be coiled on reel barges for transportation. On site the pipeline is then unwound, straightened, and laid continuously along the seabed (Dean, 2010). Current burial methods for pipelines of diameters less than 40 cm are either jet trenching or ploughing (Schupp, 2009). Jet trenching involves using high-pressure nozzles to liquefy the soil along the length of a pre-laid pipe; the pipe is then allowed to sink into the liquefied trench as the jetted material settles over it, likely in a very loose state. This concept is illustrated in Figure 1-2. Plough installation is achieved by using a plough to open a trench and lay the pipe, followed by a second device to backfill the trench. The latter method is typically more expensive than jet-trenching (Cowie and Finch, 2001). Additionally, jet-trenching is thought to be a superior technique for deep-water installations as it reduces the required tow force in dilatant soils, allowing increased trenching speed (Finch and Machin, 2001).

Both procedures may result in very loose backfill conditions, though wave and current action (as well as micro-seismic events or operational vibration of the pipe) may eventually densify the material (Clukey et al., 1989). During a five-month field study, Clukey et al. (1989) observed that continual natural densification of sandy backfill soil occurred over a mechanically trenched and buried pipeline. The authors found that in two to four weeks, the backfill had densified from a relative density of 57% to around 70% – a level judged to provide sufficient liquefaction resistance to withstand a 10-year storm event for that location. Aside from this work, however, few studies have further examined the time-dependent densification process in backfill that is placed by methods such as jet trenching.
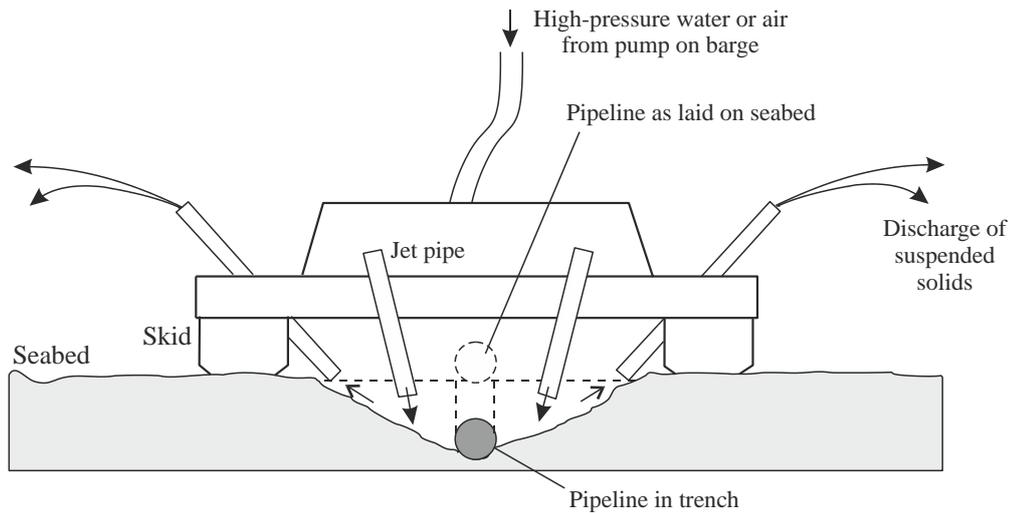
Figure 1-2 Jet-trenching schematic, after Dean (2010)

The main types of instability that must be addressed in the design of buried subsea pipelines are flotation and upheaval buckling. Flotation tends to occur as a result of cyclic loading of the seabed soil (through seismic events, wave or storm action, or dynamic movement of the pipe), which may lead to the development of positive excess pore pressures and even liquefaction. Upward movement occurs when the buoyancy/upward forces exceed the downward stabilising forces on the pipe. Recent work in this area has focused on the cyclic effects of external forces on seabed pore pressures (Dunn et al., 2006; Sumer et al., 2006b), and on predicting the resistance of partially and fully liquefied soil such that the required specific gravity of the pipe can be determined (Damgaard et al., 2006; Sumer et al., 2006a; Bonjean et al., 2008). The effect of pipe vibration in triggering liquefaction and possible flotation has also been examined experimentally (Schupp, 2009). Design against this mechanism requires careful consideration of the relationship between the weight of the pipe and its contents at various stages of operation, and the external influences that may alter the seabed soil properties.

The second form of instability, which is the focus of this thesis, is upheaval buckling. Upheaval buckling is a global soil-structure interaction problem, in which the resistance of the backfill soil over long stretches of pipe may influence its structural response to applied

thermal loads. At the same time, movement of the pipe may affect the resistance that the soil provides (for example, if there are rate effects). In order to correctly design against this behaviour, it is necessary to examine all aspects of this interaction. A brief overview of the problem is provided in the following sections.

1.1.1. Upheaval buckling overview

Upheaval buckling (UHB) is a load-induced structural effect comparable to Euler buckling of axially loaded columns. UHB been studied extensively in the past 30 years in relation to marine pipelines. Pipelines operating at high pressures and temperatures greater than the ambient conditions at the seabed level will tend to expand longitudinally. For buried conditions this expansion may be restrained by the frictional resistance of the soil, and/or by structural end restraints (PLETs), leading to an increased compressive force in the pipe. As the lateral and downward resistances are often greater than the vertical resistance of the soil cover, the pipeline may tend to buckle upwards to relieve these forces. This may be triggered at free spans or locations of high curvature caused by uneven seabed profiles (Croll, 1997). As shown in Figure 1-3, the main factors controlling the upheaval buckling of buried pipelines are the magnitude of the compressive axial force, the pipeline geometry, and the soil resistance.
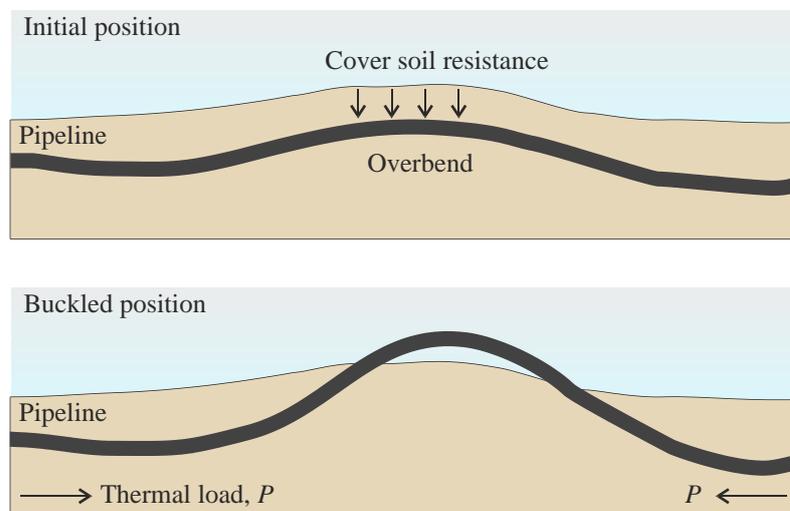

Figure 1-3 Upheaval buckling schematic, after: Palmer and King (2004), Thusyanthan et al. (2011)

Several observed resurfacing failures of pipelines in the North Sea in the late 1980's – including one reported by (Nielsen et al., 1990a) – led to increased interest in the problem around this time. One outcome of this interest was the initiation of a comprehensive joint industry project in 1987 by Shell International Petroleum Maatschappij (SIPM), aimed at addressing some of the major issues associated with UHB design (Guijt, 1990; Palmer et al., 1990). The findings of this work, published in a special 1990 Offshore Technology Conference session, helped define a framework for design guidance as well as for further research. The work on this problem can generally be categorised into two different streams: one looking at the buckling behaviour from a structural point of view, and the other examining the (vertical) soil resistance provided by the backfill cover.

Several methods exist to assess pipeline stability against UHB, by relating the driving compressive force (thermal and pressure loads) to the effective axial force in the pipe causing buckling. These include:

- analytical models that use classical buckling theory to determine critical loads for a variety of pipe geometries, but which often use simplified representations of the soil response (Hobbs, 1984; Taylor and Gan, 1986; Croll, 1997);

- a semi-empirical method which specifies two dimensionless parameters to calculate the required total resisting force for a given configuration (Palmer et al., 1990); and,

- finite element analysis, which can incorporate more realistic inputs for both pipeline geometry and backfill resistance.

A secondary concern related to this problem is a progressive response of the pipeline known as cyclic ratcheting or upheaval creep (Nielsen et al., 1990b). The theory behind this mechanism is that upward displacement of the pipe (for example at the location of an imperfection) will occur during thermal loading, even if unstable buckling does not occur. If the secant soil stiffness below the pipe exceeds the secant uplift stiffness, then cumulative upward displacements may occur. Beneath the pipe a gap may form. This might remain open

or fill with soil. If the gap fills with soil then permanent upward deflections are likely. This alone may not be unstable; however, over a number of cycles, a consequent loss of cover may lead to eventual UHB failure. Though one incidence of failure has been attributed in the literature to assumed upheaval creep (Nielsen et al., 1990a), little else is known about the propensity of this mechanism to occur.

1.1.2.   Vertical soil resistance

The vertical resistance provided by the soil cover is a key parameter in assessing pipeline stability against upheaval buckling (and cyclic ratcheting). Much research has been carried out in this area, usually involving monotonic uplift experiments aimed at assessing models for the peak resistance provided by the soil. Drained soil conditions are typically assumed in these models. The force-displacement response – in particular, the displacement required to mobilise peak resistance – has also been examined by several researchers. Recent work, however, has shown that in very loose backfill soil, existing prediction methods may over-predict the resistance achieved in these conditions (Schupp, 2009).

The shearing resistance of cohesionless soil strongly depends on its initial state. As mentioned above, current installation methods such as jet trenching may result in initially very loose backfill material. During an unstable buckling event, it possible that fast rates of uplift could induce partially drained soil conditions or even caused localised liquefaction. It is therefore important to consider how installation conditions (relative density as well as stress level) will influence the soil resistance. To provide context for the soil behaviour examined in this work, relevant theory is briefly highlighted below.

1.1.2.1.   Shearing of granular materials

The critical state theory governing the shear behaviour of granular materials is as follows: shearing of loose soil may cause the particle structure to contract, while in dense soil the structure tends to dilate. In both cases, the volumetric change will continue until a critical void

ratio – which is independent of the initial state – is reached. At this point (the critical state), plastic deformation can continue at a constant stress and volume. Whether the initial void ratio is above or below the critical void ratio for a given stress level determines the volumetric shear response of the soil: a higher void ratio results in contraction and a lower void ratio results in dilation. Additionally, the further the initial condition is from the critical state, the more rapidly the volume change occurs. As the effective stress level increases, the critical void ratio decreases; consequently, for sand with a given initial void ratio, dilation will decrease as the stress level increases (Houlsby, 1991).

The effect of this volumetric behaviour on drained soil strength is well known. Stress-strain curves for dense sands show a peak response followed by strain softening to the critical state value, whereas the response of loose soils is to increase monotonically to this value. The peak strength of cohesionless soil can be expressed, based on the Mohr-Coulomb failure criterion, as a function of the mobilised friction angle. This value is determined based on an assumed relationship between the critical state friction angle and the angle of dilation (known as a flow rule (Houlsby, 1991)), where the friction angle is an intrinsic property of the soil, and the dilation angle is a state property. One such relationship, which is referred to in a later section, is provided by Bolton (1986). Based on a database of experimental results, the paper proposes an empirical relationship between ϕ and ψ that incorporates relative density, mean effective stress, and the grain crushing strength of the soil. Although this relationship is widely used for a variety of soil mechanics applications – including pipe uplift – it provides little information regarding very loose, contractive conditions (RD <20%) at the very low stress levels which are of interest in the UHB problem.

1.1.2.2.   Static liquefaction

Liquefaction is a process whereby soil transforms to a fluid-like state, losing much, if not all, of its strength. This typically occurs in saturated or partially saturated granular soils as a consequence of increasing pore water pressure, which causes the normal effective stress to

reduce to zero (de Groot et al., 2006). The pore pressure response is highly related to the volumetric behaviour of the soil; thus, it makes sense to refer to the critical state framework for this problem (Jefferies and Been, 2006). In very loose saturated sands, for example, contractive behaviour during rapid shearing is prevented by the near-incompressibility of the pore fluid. Instead the pore pressures within the sand increase, which in turn decrease the effective stresses and consequently, the strength of the soil. It is the rapid build-up of positive excess pore pressures − influenced by both the drainage conditions and the rate of loading − that may lead to soil liquefaction. Two types of liquefaction are possible: static liquefaction, which occurs during monotonic shear; and cyclic liquefaction (or cyclic mobility).

Static liquefaction is of interest for the upheaval buckling problem, due to the potential for partially drained or undrained conditions arising from fast rates of uplift. A critical time constant for excess pore pressure dissipation during pipe uplift can be related to the coefficient of vertical consolidation of the soil, based on Terzaghi's one-dimensional consolidation equation (Byrne et al., 2013). This consolidation coefficient is a function of the soil permeability and stiffness, which are in turn influenced by the initial vertical effective stress level (Haigh et al., 2012). The force-displacement response during static liquefaction is characterised by an initial increase in strength to some peak value, followed by a brittle loss of strength as shown in Figure 1-4 (Been and Jefferies, 2004). Based on the volumetric behaviour described above, it is clear that soils with an initial void ratio greater than the critical value (which contract during shear) are susceptible to liquefaction, while soil that is denser than the critical state will not usually liquefy in this manner. Again, the influence of stress level on the critical state void ratio is important: at higher stress levels denser samples may experience flow liquefaction, though some residual shear strength will remain.
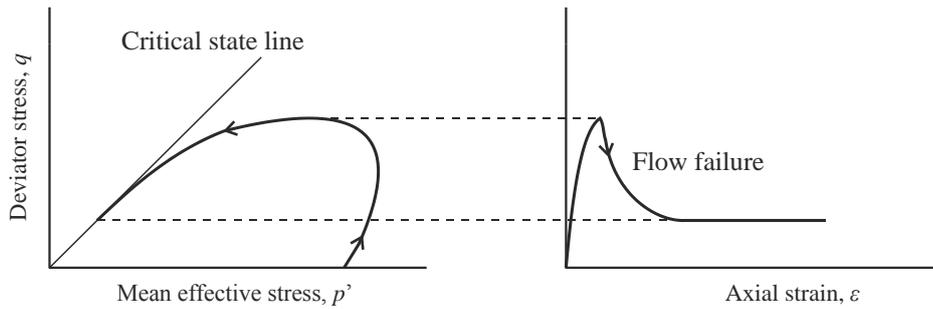
Figure 1-4 Undrained triaxial shear behaviour of loose soil, after Been and Jefferies (2004)

1.1.2.3.   Cyclic shear behaviour

Of primary concern for the cyclic loading response of sand is the possibility of cyclic liquefaction (or cyclic mobility). This may result from the gradual build-up of excess pore pressures as cyclic stress changes in the soil cause repeated densification of the particles (Jefferies and Been, 2006). This can arise in soil of loose to medium densities, though in denser samples the tendency of the particles to pack together more closely under cyclic stress changes may be offset by dilation of the particle structure during shearing. As a result, cyclic liquefaction manifests in a gradual softening of the soil instead of catastrophic strength loss (Youd and Idriss, 2001). In contrast to static liquefaction, maximum excess pore pressure generation during cyclic loading may occur in locations that experience the greatest shear stress, rather than in areas with the loosest soil; subsequent drainage and pore pressure migration may then lead to strength and stiffness reductions in other locations, causing delayed failure (Jefferies and Been, 2006).

Cyclic liquefaction as described above may be caused by wave loading, seismic events, or high frequency vibrations of the pipe. During thermal cycles, however, the vertical displacement of the pipe may be sufficiently slow that full drainage of the pore water will occur, and the soil uplift response is drained. In this case, the cyclic and permanent strains in the vertical plane are still of interest (for example, as related to cyclic ratcheting). This

response may be influenced by the amplitude and mean of the applied cyclic stresses (i.e. the range of the mobilised uplift resistance) (Randolph and Gourvenec, 2011).

1.2. Problem summary

Research on buried pipeline behaviour is strongly motivated by economic considerations. Increasing pipeline installation depths or applying post-installation mitigating measures (such as rock dump) are both associated with high costs, which become significant if applied over hundreds of kilometres of pipeline. The design must therefore be optimised to ensure sufficient safety factors against UHB, while avoiding over-conservative cover requirements; this can only be achieved through a better understanding of the major influences behind pipeline unburial behaviour. Combined with the anticipated future importance of subsea pipeline networks, there is great incentive for further research aimed at improving confidence in their design.

The stability of buried pipelines against upheaval buckling is highly dependent on the resistance of the backfill soil. Despite much research on the topic over the past several decades, shortcomings remain in the understanding of this soil-structure interaction problem. Given that current installation methods such as jet-trenching may result in initially very loose and liquefiable soil conditions, it is important to examine how the shear behaviour of the soil may affect the induced failure mechanisms and corresponding uplift resistance, in both drained and partially drained conditions.

Although many methods exist to assess the stability of buried pipelines against upheaval buckling, very little research has been published on how variation in the backfill resistance may affect the structural response of the pipe – especially for the conditions described above. As the relevant geotechnical parameters for this problem often require estimation based on limited field testing, it is necessary to determine what soil parameters may be most influential in design. This can then inform decisions on the most practical and economical methods to improve pipeline stability.

Finally, it has been suggested that the behaviour of the pipeline over a number of cycles may act to increase UHB susceptibility, by reducing the depth of cover and increasing the size of existing pipe imperfections (i.e. out-of-straightness in vertical and horizontal planes) in localised areas. Consequently, the critical buckling load assumed for the initial design may reduce over time, leading to resurfacing of pipeline sections after many cycles. Aside from two tests in the literature which confirm that the mechanism is possible (Finch, 1999; Wang, 2012), no systematic work has been carried out to determine the conditions under which this mechanism could occur. It is clear that the response will depend on the backfill conditions and the nature of loading; further experimental work is therefore required to explore this response.

1.3. Research aims

This thesis describes research aimed at addressing the shortcomings described above, through both physical modelling and numerical analysis. The work can be categorised into three major topics, with the primary objectives of each outlined as follows:

1) **Vertical uplift resistance**: Plane-strain uplift testing is carried out with the aim of further improving the understanding of failure mechanisms corresponding to peak monotonic resistance in loose and liquefiable backfill conditions.

2) **Upheaval buckling modelling:** Finite element analysis is carried out based on the current recommended approach for design against UHB. The work is intended to develop a clear picture of the structural aspects of the thermal buckling process, and to examine the influence of soil resistance generally, as well as for the specific conditions tested in (1).

3) **Vertical cyclic loading:** A plane-strain cyclic testing programme is conducted in order to assess the likelihood of cyclic ratcheting under various loading conditions, while examining the influence of backfill conditions as in the previous two sections.

In contrast to previous work in this area, this research aims to develop a complete picture of the upheaval buckling problem from a soil-structure interaction perspective, where the

implications of the backfill conditions described above are examined in the context of the global behaviour of the pipeline. The overall objective of the work is to assess the validity of the recommendations in the current guidance in relation to these topics, and to suggest improvements where required.

1.4.   Thesis outline

In **Chapter 2** (*Literature Review*), a summary of existing research relating to the three main topics in this thesis is provided. This includes a discussion of the main findings of previous experimental work for plane-strain pipe uplift, as well as a description of studies relating to global buckling (analytical, computational, and experimental). Further background to the cyclic ratcheting problem is also presented. **Chapter 3** (*Plane-strain pipe uplift*) describes an extensive experimental programme carried out using a plane-strain testing rig capable of simulating jet-trenching installation conditions. The tests examine rate, density, and stress level effects in both saturated and dry conditions. Results are compared to existing prediction models and current design guidelines. In **Chapter 4** (*FE buckling study*) a computational model, assembled using the finite element software Abaqus, is used to examine the influence of soil properties on the structural behaviour of the pipe. The work includes a preliminary study in which the behaviour of the model is verified, followed by a parametric study based on current design guidelines. Experimental force-displacement results from Chapter 3 are then used as model inputs for comparison. **Chapter 5** (*Cyclic loading*) presents a further experimental study examining the vertical cyclic behaviour of a model pipe segment in sand, using the same testing apparatus as in Chapter 3. This chapter focuses on establishing trends in the behaviour of the pipe over a number of cycles based on loading and backfill influences, and compares this response to an existing framework for cyclic loading in offshore applications. The implications of these results for upheaval buckling design are examined. Finally, concluding remarks and suggestions for future work are presented in **Chapter 6** (*Conclusions*).

2   Literature review

This chapter provides an overview of the main body of work relating to the upheaval buckling of buried pipelines in sand. In particular, the focus is on experimentation and modelling of vertical uplift resistance (both monotonic and cyclic), global buckling analyses, and how these areas are related. In keeping with the aims of this thesis, the literature review is presented, where possible, in the context of actual pipeline design. The topics in this chapter are presented in the order of work appearing in the thesis, that is: plane-strain uplift resistance, upheaval buckling modelling, and finally, cyclic ratcheting.

2.1.   Pipe uplift resistance

For pipeline stability against both upheaval buckling and upward ratcheting, the resistance of backfill soil to upward movement of the pipe is of primary importance. Although global buckling is a three-dimensional soil-structure interaction problem (influenced by soil and pipe properties along the pipe length), the vertical soil resistance is typically assessed for a representative two-dimensional cross section, and uniformly distributed across the pipe (segment) length. Formulations for the vertical soil restraint on buried conduits and plate anchors date back to works by Marston in the 1930's and Majer in the 1950's, while research focusing on the two-dimensional uplift response of buried pipelines began in earnest in the mid-1980's and early 1990's. Key work by Trautmann et al. (1985) and Dickin (1994) reviewed early theories for the uplift of foundations and applied them to buried pipes, using model scale uplift experiments to verify their applicability. For example, Trautmann et al. (1985) examined the effect of pipe embedment and soil relative density on the peak uplift resistance and force-displacement response of a model pipe section in sand ($D = 102$ mm, $L = 1.2$ m), comparing results to prediction methods for both pipes and plate anchors from previous authors (Meyerhof and Adams, 1968; Vesić, 1972; Rowe and Davis, 1982; Matyas

and Davis, 1983b). Dickin (1994) carried out further comparison of these models (plus those by Vermeer and Sutjiadi,1985; Murray and Geddes, 1987). This was done through centrifuge tests on a pipe of 25 mm diameter at accelerations ranging from 10 to 90 gravities (thus, simulating the behaviour of pipes of 0.25 to 2 m in diameter). Both papers found that the uplift resistance of a buried pipeline is broadly similar to that of strip anchor, although most models that were assessed tended to over-predict the available resistance in loose sand. One simple prediction model supported by this work, known as the vertical slip model, is still widely used in design today. In recent years, large amounts of data have been collected through full-scale tests, centrifuge modelling, and finite element analysis, and used to develop and/or verify the methods proposed by these early papers. While generally increasing in sophistication and complexity, new experimental data has not necessarily produced a clear and unambiguous picture that accounts for all of the main variables in design.

The research on this topic has focused on understanding the deformation mechanisms and force-displacement response during pipe uplift, leading to prediction models that attempt to match experimental data while accurately representing the assumed mechanics. What is generally agreed upon is that the mobilised resistance consists of a gravity contribution from the weight of the soil, plus a downward force provided by the soil's shearing resistance. The shear resistance comes from the frictional response of the soil and thus is highly related to its volumetric behaviour. Work that forms the basis for the understanding of pipe uplift has, until very recently, focused on the drained response of soil, though clearly the volumetric response in partially drained situations may have serious implications for the uplift resistance. The following sections outline previous work related to the force-displacement response, failure mechanisms, and key prediction models for dry/drained conditions. Recent experiments investigating uplift rate effects are also highlighted.

2.1.1.   Failure mechanisms

To develop a prediction model for peak uplift resistance, a realistic failure mechanism for the soil must be assumed, from which the forces comprising the uplift resistance can be approximated, either through limit equilibrium or plasticity solutions (see Figure 2-1). The early work by Trautmann et al. (1985), Schaminee et al. (1990), and Dickin (1994) concluded that that primary failure mechanism (corresponding to peak uplift force) consists of the upward heave of a sliding block of soil along shear planes/zones that, at shallow burial depths, extend to the ground surface. More sophisticated imaging techniques used in recent years have typically confirmed this assumption, and provide a better understanding of its range of applicability.

It has been observed that the orientation of these shear planes is related to the soil relative density and the depth of cover. In very loose sands at shallow embedment depths, the bounding failure planes/shear bands appear to be close to vertical (Schupp, 2009; Wang and Haigh, 2011). As the density is increased the failure planes then begin to extend outward at some angle to the vertical. The value of this angle was assumed, and later measured, to be approximately equal to the angle of dilation (White et al., 2001; Cheuk et al., 2008). Further work has confirmed that the sliding block mechanism governs at shallow embedment depths for sand at densities ranging from loose to dense. However, in very loose sand conditions at greater embedments, it has been observed that this mechanism does not develop at small strains (Schupp et al., 2006; Byrne et al., 2008; Schupp, 2009; Liu and Yan, 2011). Tests reported by Schupp (2009) show that localised compression followed by a flow-around mechanism may occur on initial displacement in these conditions. As the pipe moves closer to the surface, the sliding block again develops in a similar manner as described for shallower embedment depths. Thus, there seems to be a distinction between a shallow mechanism (sliding block), and a deep mechanism (flow-around), with the relative density also being a factor.

Figure 2-1 Pipeline geometry and simplified failure mechanisms (after White et al. (2008); Schupp (2009))

While an understanding of the mechanisms governing peak resistance is critical for stability calculations, more recent work has also examined the progression of soil deformation beyond the peak. The post-peak behaviour is particularly important in dilatant soils, where the residual strength when the soil approaches its critical state is often much reduced from that at peak. White et al. (2001) observed that this drop in resistance in fact exceeds what would be expected simply from strain softening, and suggests that at this point a transition to a new mechanism has occurred. Observations from this work confirm that in soils of varying initial densities, at some displacement beyond peak resistance the sliding block mechanism does appear to be gradually replaced by several mechanisms.

Image analysis techniques (PIV) carried out by several researchers (Cheuk et al., 2008; Wang, 2012) identified three definite stages that occur progressively after peak resistance is achieved: infilling, shear band formation and finally, flow-around. The onset of infilling was found to occur as a result of gap formation beneath the pipe as it displaces upward. Once the gap (an inverted triangular trench) is sufficiently large, small slope failures are triggered on either side of the pipe, reducing the gap. Further upward displacement causes the gap to re-open, until infilling occurs again. These regular 'miniature landslides' were found to correspond to high fluctuations in the uplift force on the pipe in this post-peak region (Chin et

17

al., 2006; Cheuk et al., 2008). Based on the problem geometry, Wang (2012) proposed the following upper bound for displacements, d_{UB}, beyond which irrecoverable infilling below the pipe would occur:

$$d_{UB} = \frac{1}{2} D (\sec \phi_{cs} - 1)$$

(2.1)

The above equation depends only on the pipe diameter and the critical state friction angle of the soil; it does not, however, take in to account earlier findings by Cheuk et al. (2008) which suggest that the onset of infilling is also influenced by grain size. In this work, Cheuk et al. (2008) examine four tests at $H/D = 3$, using PIV analysis to understand the effect of relative density and grain size on the uplift behaviour. Velocity profiles at peak resistance calculated by the authors showed significant downward soil movement on either side of the pipe in fine sand, but not in coarse sand − additional displacement was required beyond the peak before infilling was observed in the coarse sand. From the post-peak responses observed in these tests, it was found that in fine sand, 'thinner' but more regular landslides occurred, while in coarse sand wider shear zones were present near the pipe crown, although the rate of shear band formation was reduced. One further observation made by Cheuk et al. (2008), and subsequently by Wang (2012), was that the shear band width reduces as infilling around the pipe begins. Additionally, since the soil at the pipe sides is flowing downwards, the uplifted block of soil becomes narrower. Eventually, heave of the soil above the pipe could cease completely, leaving only the flow around the pipe.

The initiation of the flow-around mechanism in the post-peak response observed by several authors appears to be analogous to the mechanism observed initially by Schupp (2009) in very loose sand (below a certain depth). Since this mechanism seems to appear when the soil is either at critical state (post-peak) or when it is most likely contractive (very loose sand), the implication is that the initial failure mechanism may strongly depend on relative density (as well as stress level/embedment depth). Furthermore, based on the observations by Cheuk et

al. (2008), it is possible that if the above conditions are present, grain size may also have an influence on whether a flow-around or heave mechanism occurs initially.

2.1.1.1.   *Numerical work*

A small number of studies have been carried out using finite element analysis to examine the plane-strain uplift problem. Most of this work has confirmed the observed (or assumed) failure mechanisms from the experimental studies. For example, Vanden Berghe et al. (2005) were able to reproduce a local flow-around failure mechanism for very loose sands using an in-built hardening soil model in the FE software, Plaxis. The contractive behaviour of the soil was simulated in this study by applying a negative dilation angle to the model. Other work, such as by Bransby et al. (2001), Yimsiri et al. (2004), Jung (2011), and Jung et al. (2013), have examined uplift in loose to dense soil by implementing a Mohr-Coulomb elastic-perfectly plastic soil model in various software programmes (a further strain-softening sub-routine is applied by Jung et al., 2013). These studies aim to extend results beyond conditions obtained in a laboratory setting – for example, to very deep embedment conditions. Both Yimsiri et al. (2004) and Jung et al. (2013) suggest that a transition from a shallow failure mechanism to a deep failure mechanism occurs from *H/D* ratios of around 20-30 in medium-dense to dense sand.

2.1.2.   Prediction models

2.1.2.1.   *Vertical slip model*

One of the simplest models used to predict the uplift resistance of a pipe buried in sand is the vertical slip model (VSM). This model assumes that the failure planes of the soil extend vertically upwards from the pipe edges to the ground surface (see Figure 2-1 above). The uplift resistance is composed of the weight of the soil prism above the centre of the pipe – less the soil displaced by top half of the pipe – and the shear resistance of the slip surfaces caused by the lateral earth pressure, shown below:

19

$$F_{ult,VSM} = \left[1 - \frac{\pi D}{8H} + K\tan\phi'\frac{H}{D}\right]\gamma'HDL \tag{2.2}$$

where D is the pipe diameter, H is the depth of cover to pipe centre (note that this is different from the depth of cover defined in the industry, which is usually to the pipe crown), L is the length of the pipe, and ϕ' and γ' are the effective friction angle and unit weight, respectively. The factor, K, is related to the lateral earth pressure; the determination of its value for varying densities has been investigated by several researchers. Trautmann et al. (1985) suggest that K values of 0.5, 0.65, and 0.75 can be used for loose, medium, and dense sands, respectively. Dickin (1994), however, found that while a K value of 0.75 was adequate for dense sands, the at-rest coefficient $(K_0 = 1 - \sin\phi')$ provided a closer prediction for loose sands. Alternatively, $K\tan\phi'$ can be replaced by an empirical uplift factor f, based on soil and density classifications.

Figure 2-2 compares selected experimental data compiled by White et al. (2001) to predictions using various values of f. The experimental and predicted forces are presented as non-dimensional breakout factors, denoted as N_{ult}, obtained by normalising the force values by $\gamma'HDL$ (for the prediction models N_{ult} corresponds to the term in square brackets in equation 2.2). The figure demonstrates that changes in resistance due to relative density can be broadly captured by altering this factor. An adapted version of this semi-empirical model (denoted as the aVSM), which does not subtract the displaced soil (second term in the above equation), is what is used in the current design guidelines described later in this chapter.

Based on experimental results compiled by a number of authors, it appears that for very loose to loose sand at shallow embedment ratios the VSM provides an accurate prediction, if an appropriate method of determining the uplift factor is used. For example, in Figure 2-3 results from Schupp (2009) for different pipe diameters in very loose dry sand are shown to match very well with the VSM prediction, calculated using $K_o\tan\phi'$. Wang et al. (2010) conclude based on observed deformation mechanisms that the VSM gives a good estimate for H_c/D ratios between 0.5 and 3.5 (note: H_c goes to pipe crown in this case), while Byrne et al.

(2008) suggest it can be used for *H/D* ratios up to 5 for loose sand. In tests with very loose saturated sand at embedment ratios deeper than 2.5, however, Schupp (2009) finds that the VSM begins to over-predict soil resistance, indicating that the use of this method could prove to be unconservative for these conditions. This was suggested previously by Trautmann et al. (1985) for loose sands at embedment ratios greater than 4.
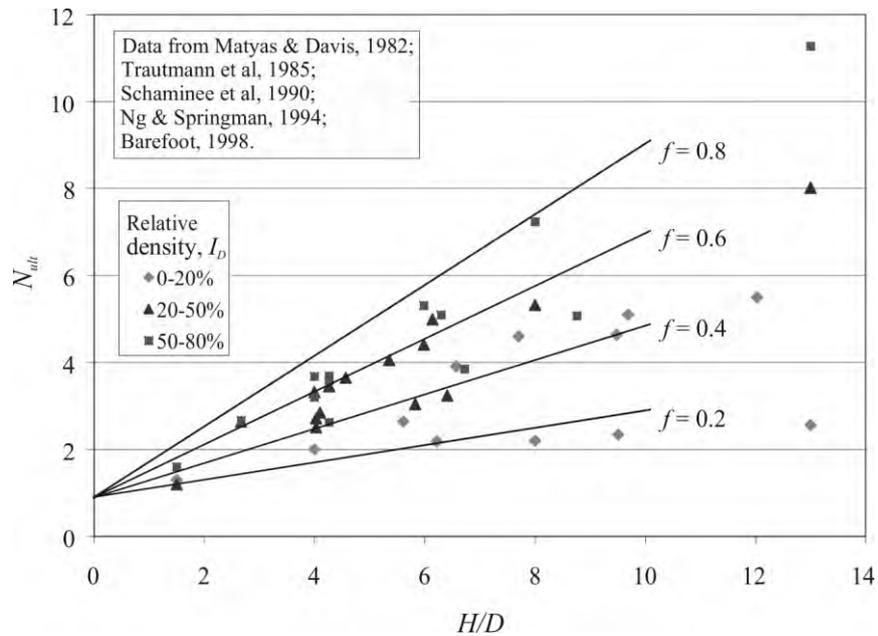

Figure 2-2 Normalised uplift resistance from sources in the literature compared to VSM predictions (using an uplift factor, f): adapted from White et. al (2001)
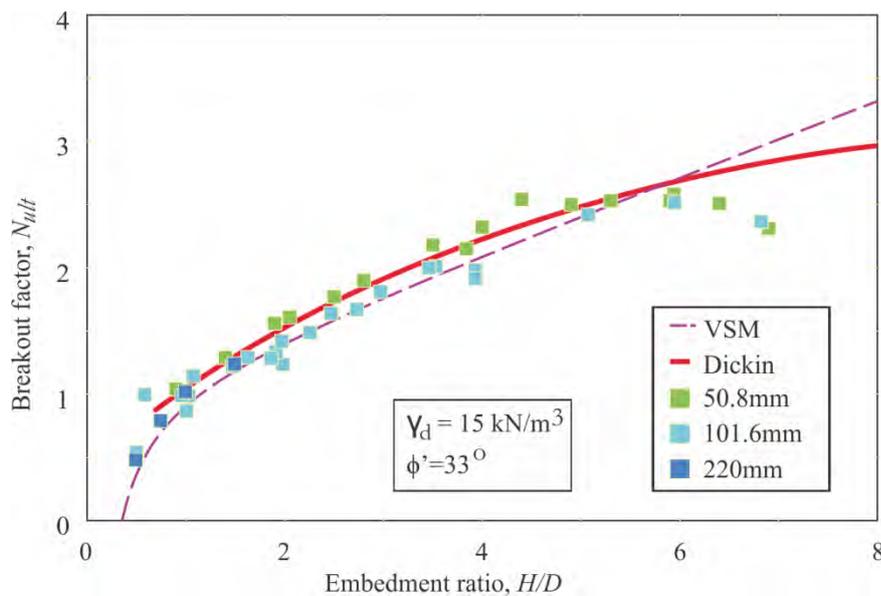
Figure 2-3 Normalised uplift resistance for very loose dry Leighton Buzzard 14/15 sand for different diameter pipes: adapted from Schupp (2009)

21

2.1.2.2. Inclined surface model

When the relative density of the soil increases, the shear planes may fan outwards. Several researchers have proposed theories that adapt the VSM by using these inclined shear planes. The formulation by White et al. (2001), based on the mechanism in Figure 2-1 (b), is presented here. This inclined slip surface model (referred to herein as the ISM) assumes that the normal stress acting on the shear planes (which is calculated based on at-rest conditions) remains constant, while the vertical stress level above the pipe increases as the uplift resistance is mobilised. Vertical equilibrium of the modified sliding block produces nearly the same equation as in the VSM, but with $K \tan \phi'$ replaced by f as follows:

$$F_{ult,ISM} = \left[1 - \frac{\pi D}{8H} + f\frac{H}{D}\right]\gamma'HDL \tag{2.3}$$

In this equation the friction factor is defined by White et al. (2001, 2008) as:

$$f_{ISM} = \tan\psi + (\tan\phi_{peak} - \tan\psi)\left[\frac{1 + K_0}{2} - \frac{(1 - K_0)(\cos 2\psi)}{2}\right] \tag{2.4}$$

The dilation and peak friction angles are determined following Bolton (1986) in which the following relationships are proposed:

$$\phi_{peak} - \phi_{cs} = 0.8\psi = mI_D \tag{2.5}$$

$$I_R = I_D(Q - \ln p') - 1 = I_D \ln\left(\frac{\sigma'_c}{p'}\right) - 1 \tag{2.6}$$

where σ'_c is the grain crushing strength, I_R is the relative dilatancy index, and p' is the mean effective stress at failure, approximated as $\gamma'H$. The parameter, m, is taken as 5 under plane-strain conditions, and K_o is as defined previously.

White et al. (2001) found that, for a given embedment depth, this model agrees well with experimental values of peak uplift resistance over densities ranging from loose to dense; however, less agreement is seen at low relative densities, as the model does not account for very loose samples that may exhibit contractive behaviour.

2.1.2.3. *Flow-around mechanism*

There are no established models or methods for calculating the peak force associated with a flow-around mechanism. It is therefore difficult to predict when flow behaviour could govern over the sliding block as the primary mechanism. Wang (2012) attempted to develop an analytical model for a deep flow-around mechanism, based on effective stress analysis of the assumed mechanism shown below (for a smooth pipe).
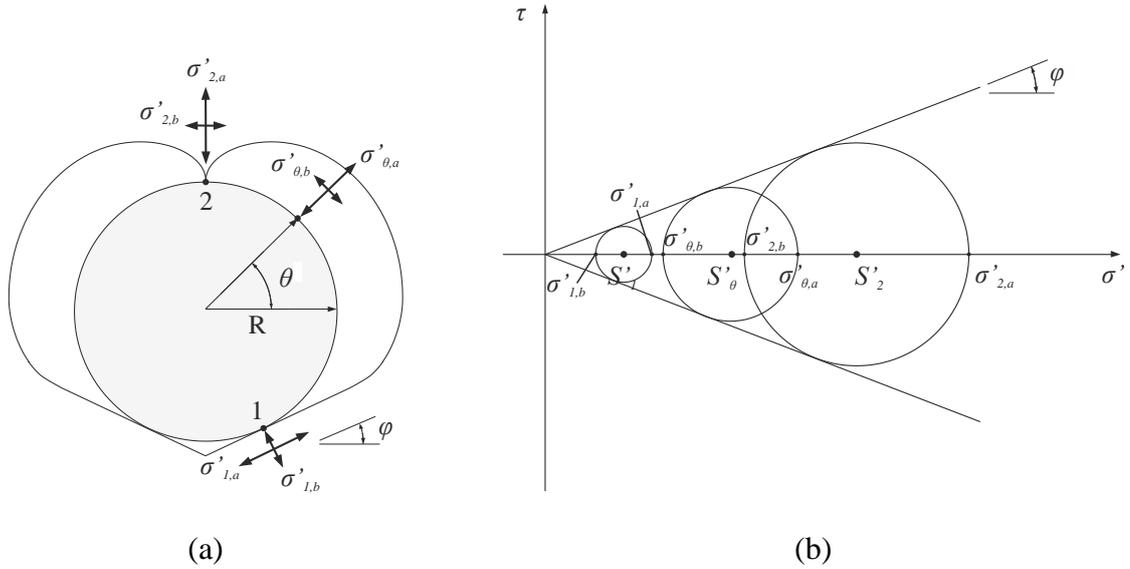

(a)   (b)

Figure 2-4 Theorised stress field for a flow mechanism around a smooth pipe, after Wang (2012): (a) principal stress states; (b) Mohr's Circle representation

The principal stress at the top of the pipe is assumed to be greater than the in situ vertical effective stress, by an arbitrary factor, α_{FAM}. Beginning with this assumption the author derives the following equation for a smooth pipe:

$$\frac{R_{FAM}}{\gamma' HDL} = \frac{\alpha_{FAM}}{1 + 4\tan^2\phi}\left\{2\tan\phi + \frac{\exp[(2\pi - 2\phi)\tan\phi]}{\exp[(3\pi - 2\phi)\tan\phi]}\right\} \tag{2.7}$$

For a rough pipe this is modified to become:

$$\frac{R_{FAM}}{\gamma' HDL} = \frac{\alpha_{FAM}}{1 + 4\tan^2\phi}\left\{2\tan\phi + \tan\theta + (1 - 2\tan\theta\tan\phi)\frac{\exp[(2\pi - 2\phi)\tan\phi]}{\exp[(3\pi - 2\phi)\tan\phi]}\right\} \tag{2.8}$$

where θ is the pipe-soil friction angle. By plotting curves for various values of θ and ϕ, it is shown that $\frac{R_{FAM}}{\alpha_{FAM}\gamma'HDL}$ is lower for soils with a higher value of ϕ (see Figure 2-5 (a)). It is then suggested that the multiplication factor, α_{FAM}, be taken as the passive earth pressure coefficient, $K_p = \frac{1+\sin\phi}{1-\sin\phi}$. With this factor now included in the calculation, new plots show that $\frac{R_{FAM}}{\gamma'HDL}$ increases with friction angle (Figure 2-5 (b)), as does the transition embedment depth.

This model could be a useful starting point for a prediction of the peak force associated with a flow mechanism. However, the above equations, and in particular the multiplication factor α_{FAM}, was compared to one test only, in which the sliding block mechanism was likely the governing mechanism. While plotting the quantity $\frac{R_{FAM}}{\alpha_{FAM}\gamma'HDL}$ against friction angle may demonstrate how the resistance can change depending on the problem geometry (controlled by ϕ), the parameter α_{FAM} is a direct multiplier and should therefore incorporate the effects of relative density, embedment ratio, and possibly even grain size. To identify α_{FAM} completely would be complex, requiring a large amount of experimental data investigating each of the factors identified above.
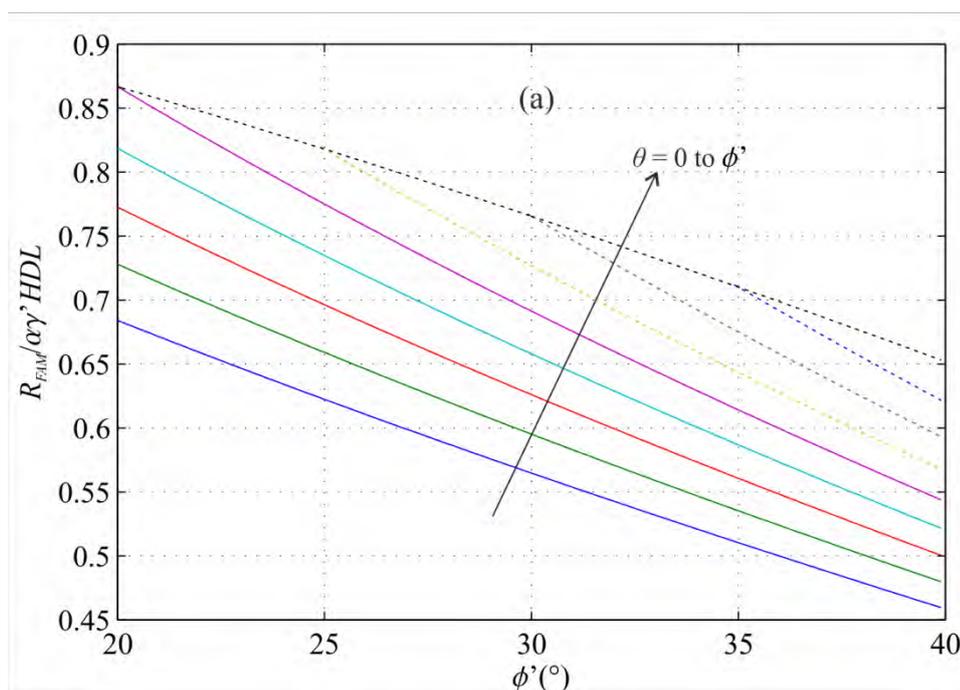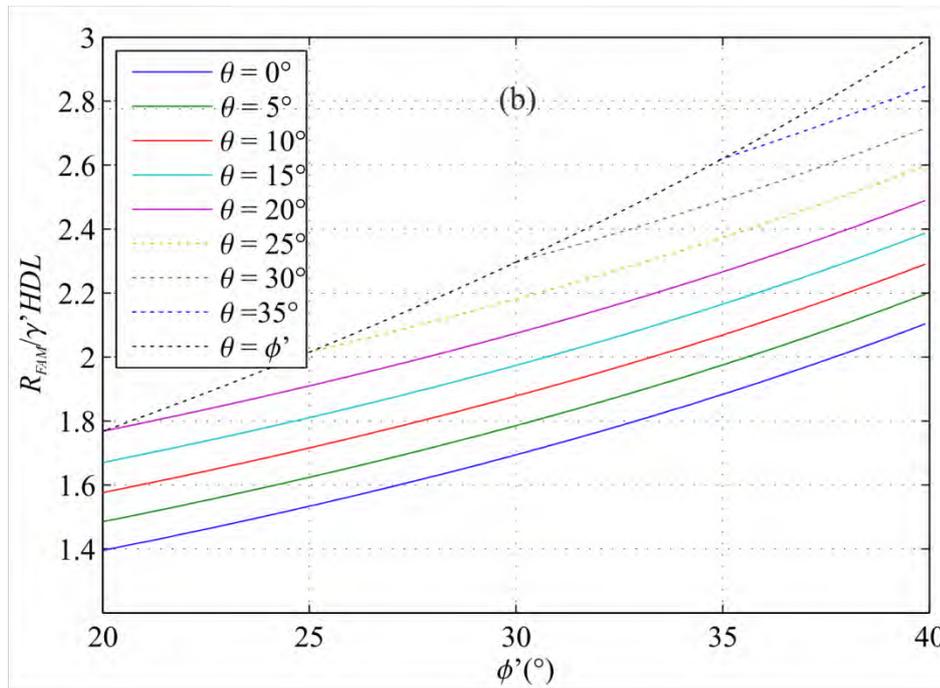
Figure 2-5 Limiting values of: (a) $R_{deep}/\alpha\gamma'HDL$ and (b) $R_{deep}/\gamma HDL$ based on ϕ and θ (after: Wang, 2012)

2.1.3.   Force-displacement response

An important characteristic of the uplift response for pipeline design is the displacement required to mobilise the peak resistance for a given embedment depth. Together with the peak force, this provides an indication of the pre-peak soil stiffness, which is expected to strongly influence the buckling behaviour of the pipe. Trautmann et al. (1985) first related this distance to the embedment depth, reporting mobilisation displacements in the range of 0.005 to 0.015H. Some more recent experimental work (at 1g) has generally been in line with this range (Matyas and Davis, 1983a; Bransby et al., 2002; Cheuk et al., 2008). In contrast, Thusyanthan et al. (2011) proposed an exponential relationship between displacement (normalised by D) and the embedment ratio, as follows:

$$\frac{d_f}{D} = 0.02 \exp\left(\frac{H}{2D}\right) \tag{2.9}$$

The above prediction curve is compared in Figure 2-6 with available mobilisation displacement data from 1g tests in the literature. Here it is shown that at higher embedment ratios, this curve predicts much larger mobilisation displacements than those reported in

several other studies (though recent data from Wang et al. (2011) exhibits a closer match). It should be noted that the data for the higher embedments used by Thusyanthan et al. (2011) to fit the exponential curve was very limited, and included only dry sand and centrifuge test data.

The limitations of centrifuge modelling for this problem have been highlighted by Palmer et al. (2003) and Cheuk (2005), who show that displacements from centrifuge tests, when scaled up to prototype value, are generally much larger than what is observed in full-scale tests. This effect was attributed to the influence of localised shear zones/bands where the mobilised shear stress depends on the relative displacement across the localisation (Palmer et al., 2003), which itself may be a function of the grain size used in the model (Stone et al., 2005). Therefore, unless appropriate grain size scaling is considered, centrifuge data should not be used when comparing mobilisation displacements. Instead, more full-scale tests at greater embedments are required to verify the above equation.
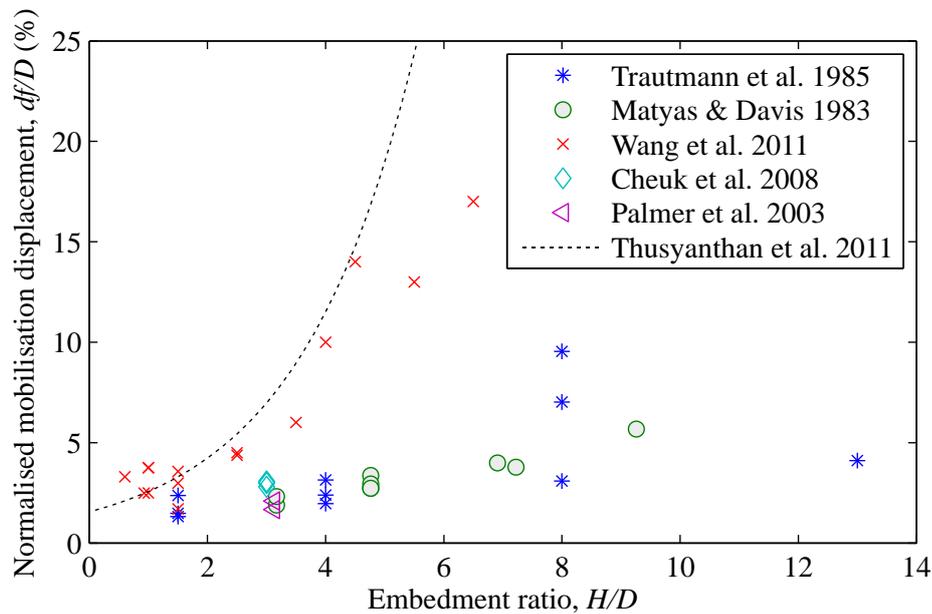

Figure 2-6 Mobilisation displacement data from the literature, normalised by pipe diameter

In addition to the influence of embedment ratio, the force-displacement response is also affected by relative density. In many of the above tests, the difference in the shape of the initial curve between dense and loose sand has been documented. In dense sand the pre-peak

response is typically much more stiff and exhibits a more distinct peak, as compared to loose sand. The relative density does not necessarily appear to affect the value of the mobilisation displacement, though this is not well documented in the literature and could be explored further.

2.1.4. Rate effects

Most of the research completed previously focuses on the drained behaviour of sand, attained through tests in either dry sand, or saturated sand with an uplift rate sufficiently slow to allow adequate drainage of the pore water. Plane-strain tests reported by Byrne et al. (2008, 2013), Bransby and Ireland (2009), Schupp (2009) investigate partially drained conditions generated by faster rate uplift tests, and the consequent effect on the mobilised soil resistance.

In very loose sand tests, described by Byrne et al. (2013), as the rate of uplift was increased, the uplift resistance was found to decrease significantly – almost to zero in some of the faster rate tests. Pore pressure transducers showed significant positive excess water pressures around the pipe circumference, which resulted in significantly reduced effective stresses acting on the pipe. In some instances the excess pore water pressure was found to increase to the value of the in situ vertical effective stress ($u_e = \gamma'H$), indicating full liquefaction. Conversely, in denser sand the peak uplift resistance was observed to be significantly larger than that predicted for fully drained conditions. This suggests that negative excess pore pressures were developed, resulting in an increase in the effective stress operating around the pipe.

A model to predict the partially drained uplift resistance in very loose sand is proposed by Byrne et al. (2013). This model is based on the VSM, but replaces the γ' term in the uplift equation with $\gamma'-u_e/H$. The excess water pressure is assigned an initial value equal to the vertical effective stress, and is assumed to decay based on Terzaghi's one-dimensional consolidation equation. Although the model does not account for additional development of excess pore water pressure as the pipe moves, it was found to match closely with experimental data for very loose sand. It should be noted, however, that the model uses a 2D

assumption for a 3D problem; in reality, the pipe would be expected to displace at different rates along its length.

2.1.5.   Mitigation measures – rock dump

In the event that the available soil cover does not meet the design requirements, mitigation measures may be necessary. Several possible approaches to prevent the development of buckling are described by Guijt (1990), such as increasing the soil cover or adding additional restraint, reducing the driving force, or changing the pipeline structural design. An effective method of increasing the vertical restraint on the pipeline (if increasing the depth of cover is not possible) is to apply a rock berm along the length of the pipeline, by a procedure known as rock dumping. This method can be extremely expensive, so instead of rock-dumping along the entire line, key sections are targeted. The targeted sections might either be at known locations of pipe overbend, or at regular intervals to allow controlled buckling – called intermittent rock dumping (Ellinas et al., 1990; Guijt, 1990).

Alternatives to rock dumping, which increase the downward resisting force on the pipe, include increasing the submerged weight of the pipe or improving the backfill soil resistance. Backfill improvement techniques such as compaction or ground improvement have been identified by Cowie and Finch (2001); however, since these techniques would require substantial development for use in offshore applications, the authors conclude that these are unlikely to replace rock-dumping as the main mitigating measure against UHB.

Centrifuge modelling carried out by Ng and Springman (1994) has examined the impact of the addition of a top layer of rocky backfill on uplift resistance in sand. The tests demonstrate that an additional 600 mm rockfill layer placed on 1.5 m of sand cover (values at prototype scale) will increase the uplift resistance, compared to the 1.5 m sand cover only. The authors conclude that the increased peak resistance is due to the additional overburden rather than a change in the mobilised friction angle (stating that the peak resistance is still governed by the strength of the sand). This conclusion was drawn by fitting the data in both cases to an uplift

28

resistance model and comparing the mobilised friction angles – the friction angles were found to be similar in both instances. Other uplift tests in uniform rock/gravel material presented by Boer et al. (1986) and Finch et al. (2000) show that when the frictional resistance of the rockfill is mobilised the resistance is increased from what would be seen in dense sand.

2.2. Upheaval buckling analysis

The global buckling behaviour of a pipeline is generally analysed as a two-dimensional problem, influenced by the axial and vertical constraints on the pipe. In reality there is also the out-of-plane behaviour to consider, but this is often ignored on the basis that the lateral resistance is high compared to that of the soil cover, and that imperfections in the vertical plane are likely to govern. This is probably true for deeply embedded pipes, but as the pipe location becomes closer to the seabed surface, lateral buckling is likely to become more important. Lateral buckling behaviour is not covered here, but recent work on this topic can be found in Sandford (2012). The structural behaviour of the pipe due to UHB can be described using analytical models, founded in beam column buckling theory. Semi-analytical models and finite element analysis stemming from this work are often used in design. This section reviews some of the basic models and the theory behind them, with particular focus on how soil resistance models have been incorporated.

2.2.1. Analytical models

Work has been done by many researchers to establish a theoretical basis for upheaval buckling analyses. Existing analytical models have been developed by relating the thermal buckling of pipelines to simple column buckling and the thermal buckling of railway lines (Hobbs, 1981,1984; Croll 1997). The starting point for most models is to consider a perfectly straight and stress free pipe with simple support conditions, under a compressive thermal load, P_o, calculated as:

$$P_0 = EA\alpha_T\Delta T \tag{2.10}$$

The effects of internal and external pressure can be added to the pipe wall force due to thermal loading in the above expression to determine the 'effective axial force', which is the equivalent driving force for a pipeline in air (DNV, 2007). The pipe is then assumed to experience a single buckle that can be described by the function $y(x)$, with the vertical movement typically resisted by the pipe self-weight, and/or a constant soil pressure, q. Assuming small slopes and curvatures, the following equilibrium expression based on classical beam column-theory can be used to determine the buckling load, P, of the pipe:

$$EIy'''' + Py'' + q = 0$$

(2.11)

This force can then be related to the driving thermal load based on the assumed boundary conditions, yielding a critical buckling temperature (an example derivation can be seen in Maltby and Calladine (1995b)). Analysis shows that the critical load maintained in the buckle, P, is reduced from the thermal load, P_o, due to the increased length of the buckled section compared to the pre-buckled shape.

Maltby and Calladine (1995b) note that the above theory does not account for the initiation of buckling, as it is assumed that buckling has already occurred. To avoid this issue, an imperfect (pre-buckled) shape can instead be imposed on the initial pipe geometry. Buckle initiation from this starting position can then be assessed using the new boundary conditions defined by the shape and type of the imperfection. The additional benefit of an initial imperfection model is that it can represent the typical pipe out-of-straightness (OOS) that occurs in the field, which can be taken to correspond to a critical location for upheaval buckling.

2.2.1.1. *Initial imperfection*

Much work in this area has focused on the derivation of imperfection models. Numerous studies have investigated the influence of size and shape of the initial imperfection on the peak axial force required for buckling, as well as on the deformed shape of the pipe (Hobbs, 1981, 1984; Taylor and Gan, 1986; Ju and Kyriakides, 1988; Ballet and Hobbs, 1992; Taylor

and Tran, 1993; Croll, 1997). The imperfection definition varies depending on the assumed support conditions of the resultant buckling mode. Commonly an 'empathetic model' is used, in which the initial imperfection shape is related to the idealised buckling mode. Most models consider the seabed to provide rigid support to the pipeline.

Three example imperfection types derived by Taylor and Tran (1996) include: a continuously supported empathetic model; a prop-type imperfection where an isolated point force (such as a rock) creates a vertical irregularity in the pipe, leaving voids on either side; and a prop model where the voids are subsequently infilled with sand. A schematic of the continuously supported imperfection shape is shown in Figure 2-7. The applied forces and subsequent buckled shape are also shown.
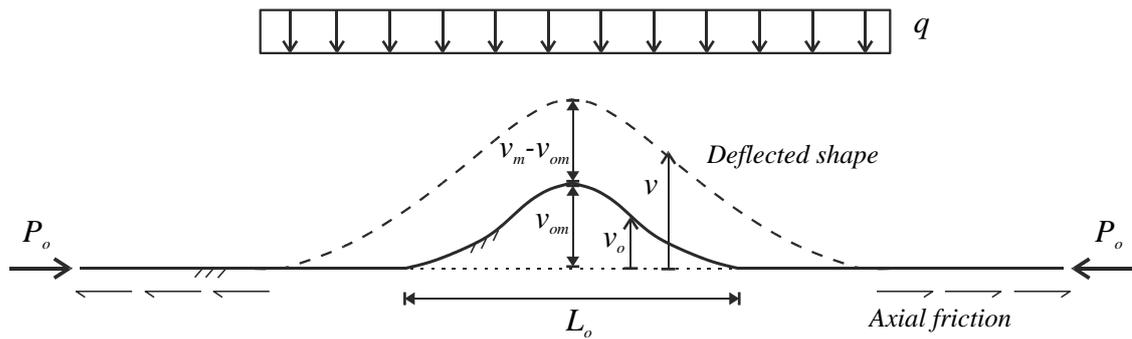

Figure 2-7 Schematic of typical analytical buckling model

The shape of the initial imperfection is given as:

$$v_o = \frac{v_{om}}{K_1}\left(1 + \frac{n_o^2 L_o^2}{8} - \frac{n_o^2 x^2}{2} - \frac{\cos n_o x}{\cos n_o L_o/2}\right)$$

(2.12)

for $L_o/2 \leq x \leq Lo/2$

where:
$$K_1 = 1 + \frac{n_o^2 L_o^2}{8} - \frac{1}{\cos n_o L_o/2} = 15.6985$$

(2.13)

$$n_o L_o = 8.9868$$

(2.14)

31

The peak amplitude and length of the initial imperfection are denoted as v_{om}, and L_o, respectively. A simpler version of this model, defined by Croll (1997), instead defines v_o using a cosine squared function, requiring only v_{om} and L_o to describe the shape.

Example derivations and comparisons regarding the behaviour of the above model, and other imperfection types can be found in Taylor and Tran (1996) or Wang, W. et al. (2011). For all types of imperfection, it was found that the initial amplitude strongly influences the buckling load in the pipe. The smaller the imperfection height, the greater the axial force required to cause buckling. Smaller imperfection heights were also associated with more unstable (snap-through) buckling behaviour, indicated by a sudden drop after the peak force was reached. As the imperfection height is increased, the response becomes more stable until no peak force is observed (see Figure 2-8).
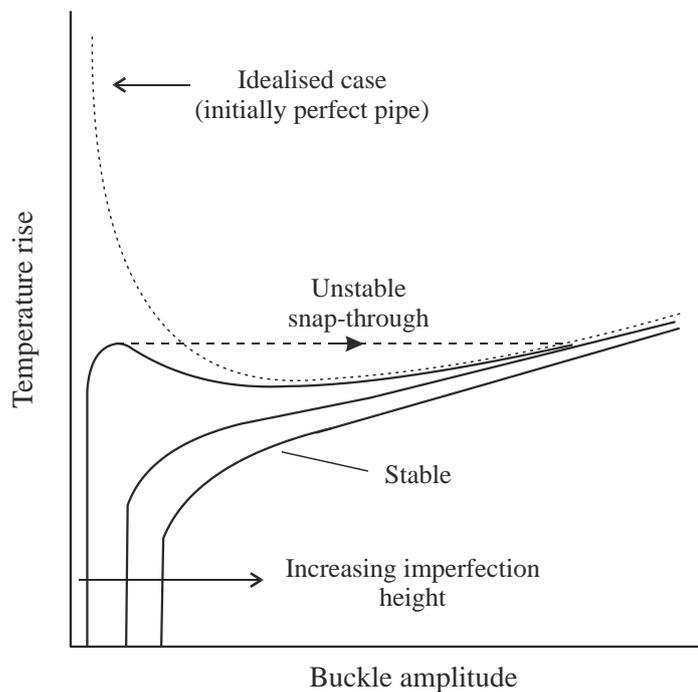

Figure 2-8 Thermal load vs. buckle amplitude – influence of imperfection height (after: Taylor and Gan, 1986)

2.2.1.2.   Axial friction

The axial friction mobilised by pipe slippage is included in some models, such as those described by Hobbs (1984), Taylor and Gan (1986), or Maltby and Calladine (1995). The

simplest application is to assume that the friction force per unit length is related to the vertical restraining force, q, by a friction coefficient, μ. The amount of force transferred to the buckled section then depends on the slipping length of the pipe, as well as the value of μ.

The influence of axial friction on the tendency of the pipe to buckle has been described simply by Bruton et al. (2008) (though in the context of lateral buckling). If the pipe ends are free to expand under thermal loading, the axial force builds up from zero at the ends to a maximum value near the pipe centre (based on the distance away from the ends and the value of the friction coefficient). For a given pipe length, if the friction coefficient is small, the pipe may experience significant end expansion, but the axial force may not build-up to the fully-constrained value (i.e. P_o). If the friction coefficient is increased in the model, the axial force at the centre may reach the value of P_o, and all sections at this force level will no longer move axially. Essentially this means that the higher the coefficient of friction, the smaller the displacement required for the buckling force to be reached in the pipe. If buckling does occur, lower friction coefficients will allow more axial feed-in to the buckle. The above considers only a fixed friction force per unit length, but it is clear that the axial force-displacement response will also be an influence for this problem.

2.2.1.3.   *Vertical soil resistance*

The theoretical models described above have been well developed in terms of the structural behaviour of the pipe, as influenced by the initial imperfection and the driving forces. In many models, however, the vertical restraint opposing the upward motion of the pipe is typically taken as the weight of the pipe (or the weight plus a soil surcharge), idealised as a uniformly distributed load applied once the pipe lifts from the rigid seabed. In reality, the resisting force mobilised is a function of the pipe displacement.

This issue is addressed by Maltby and Calladine (1995b) who incorporate simplified force-displacement characteristics of the pipe interaction with the soil (normal to the pipe) in order to better represent pipeline burial conditions. Using a periodic cosine imperfection, the effect

of both linear-elastic and elastic-perfectly plastic pipe-soil uplift behaviour is examined. The main conclusion of this work, which draws heavily on parallels to thermal track buckling analyses by Tvergaard and Needleman (1981), is that localisation of the buckling mode (defined as the growth of one buckled half-wave at the expense of others) occurs when the axial force reaches a maximum. This maximum was found to occur when the peak soil uplift resistance was reached. An expression for the minimum axial force at which localisation could occur was derived as:

$$P_{loc} = \sqrt{EIF_{ult}/v_{om}} \qquad (2.15)$$

This expression is actually independent of the displacement required to reach the peak soil load, and was found to be of similar form (but not value) to buckling load calculations using a prop-imperfection model (substituting the self-weight of the pipe and the height of the prop for F_{ult} and v_{om}, respectively).

A small number of other studies have examined influence of the soil resistance beneath the pipe, rather than assuming a rigid seabed (Yun and Kyriakides, 1985; Chiou and Chi, 1993). Chiou and Chi (1993) found that by modelling the foundation as an inelastic continuum the limit loads were smaller than for pipes founded on elastic soil. Additionally, a lower foundation stiffness was found to decrease these limiting loads.

2.2.2.   Semi-empirical methods and finite element analysis

For design purposes, semi-empirical equations and numerical modelling are used to estimate the operating conditions under which a pipeline will become unstable. For example, Palmer et al. (1990) derived a design curve in terms of dimensionless parameters which include a uniformly distributed restraining load (self-weight and/or soil overburden) and the length and height of the imperfection. The parameters originate from the elastic buckling theory discussed above, with an assumed sinusoidal deflected shape. From this the downward force required to maintain the shape profile is calculated and, based on the largest value occurring at the pipe crest, the following dimensionless load parameters are specified:

$$\phi_w = \frac{wEI}{v_{om}P_o{}^2} \tag{2.16}$$

$$\phi_L = L_o\sqrt{\frac{P_o}{EI}} \tag{2.17}$$

where ϕ_w is the maximum downward load parameter, ϕ_L is a dimensionless imperfection length, and v_{om} and L are the imperfection height and length, respectively. Palmer et al. (1990) propose a universal design curve to relate these two dimensionless parameters. The shape of this curve is determined directly from numerical analysis of the problem (described by Klever et al. (1990)). For a preliminary design calculation the required downward load, w, can then be compared to the available 'effective weight', q, which consists of the submerged weight of the pipe and the soil uplift resistance.

A finite element model for analysing the pipeline buckling response is described by Klever et al. (1990), and some useful results are presented. First, the effect of a non-linear soil response is compared with the 'effective weight' approach employed by Palmer et al. (1990). The results indicate that a non-linear soil response is quite different – and more critical – as the pipe experiences buckling at a lower temperature. Another comparison was made between elastic and plastic behaviour of the pipe material, which found that yielding of the pipe will cause buckling at lower temperatures.

The fact that unique (and various) imperfections can readily be incorporated into a finite element model, such as the one described above, make it a useful tool for detailed design. Recent finite element studies, which employ soil springs to represent the uplift resistance, have continued to investigate the influence of imperfection definitions on the critical buckling temperature (Gao et al., 2011; Thusyanthan et al., 2011). Thusyanthan et al. (2011) also compare numerical results for various imperfections and pipe diameters to Palmer's semi-empirical method, finding that a modification of the load parameter, ϕ_w, to include the mobilisation displacement of the soil provides better agreement between the methods.

2.2.3. Experimental studies

Compared to the analytical/theoretical work described above, relatively few experimental studies have explored longitudinal buckling of buried pipelines for a 3D perspective. The main works include centrifuge testing by Moradi and Craig (1998), small scale tests at $1g$ (Maltby and Calladine, 1995b; Maltby and Calladine, 1995a; Byrne et al., 2008; Schupp, 2009), and larger scale laboratory experiments by Schupp (2009). In a successful test reported by Moradi and Craig (1998), a 6 mm diameter pipe (1.8 m length) was buried in loose dry sand with 12 mm of soil cover and a 3 mm imperfection height, and subjected to a $21.1g$ acceleration. The pipe ends were fixed and a thermal load was applied by circulating hot water through the pipe (lateral movements were also restrained). Axial load (at the pipe ends) and vertical displacement measurements show that a snap-through buckling event was achieved in the test, characterised by a very small initial increase in vertical displacement with temperature, which was followed by a large jump in displacement at a constant temperature. The authors found that the test behaviour broadly matched snap-through predictions from theoretical models such as Ballet and Hobbs (1992).

A comprehensive buckling study was undertaken by Sandford (2006) and Schupp (2009), in which both a smaller scale pipe (D = 12.8 mm, L = 1.84m) and a large scale pipe (box section: W = 38.1 mm, H = 19.05 mm, L = 7.8 m) were tested in loose sand, in dry and saturated conditions. The main conclusion from the small scale tests was that the buckling load appears to depend on the depth of cover and the effective unit weight of the soil only; from this, it was inferred that the soil response prior to buckling was governed by drained soil conditions. From the larger scale tests – in which buckling was also successfully achieved – it was found that liquefaction could be observed during the post-buckling response. In some tests the pipe appeared to buckle along the entire length, while in others, a confined buckle occurred at one end only. The appearance of the latter, local mode is consistent with the theory that buckle localisation may occur when the peak soil resistance is reached.

2.2.4.　　　　Design guidance for upheaval buckling

The Det Norske Veritas Recommended Practice, DNV-RP-F110 (Det Norske Veritas, 2007; referred to herein as DNV) is commonly used in the offshore pipeline industry. This Recommended Practice defines global buckling as a load response rather than a failure mode, but one that may lead to an ultimate failure mode such as local buckling. However, as little guidance is given on post-buckled pipeline integrity, excess upward displacement is considered ULS failure for the purpose of buried pipeline design. The guidelines recommend that stability against this mechanism be assessed using finite element analysis. The preliminary design procedure involves using a 2D model to evaluate the temperature at which the pipe is deemed to have failed (i.e. when the displacement exceeds the mobilisation displacement of the soil, or the axial load cannot be increased further). Based on the modelling results, and appropriate safety factors, a minimum soil embedment for a given pipeline configuration can be determined.

The guidelines specify requirements for the modelling procedure, such as the use of non-linear pipe behaviour as well as large rotation theory. In the absence of survey-data on the as-laid configuration of the pipe (as would be the case for preliminary design), several imperfections of varying size and shape must be tested in the model. It is recommended that these be introduced from an initial straight and stress-free configuration. Finally, the resistance of the soil is typically represented using non-linear axial and vertical soil springs.
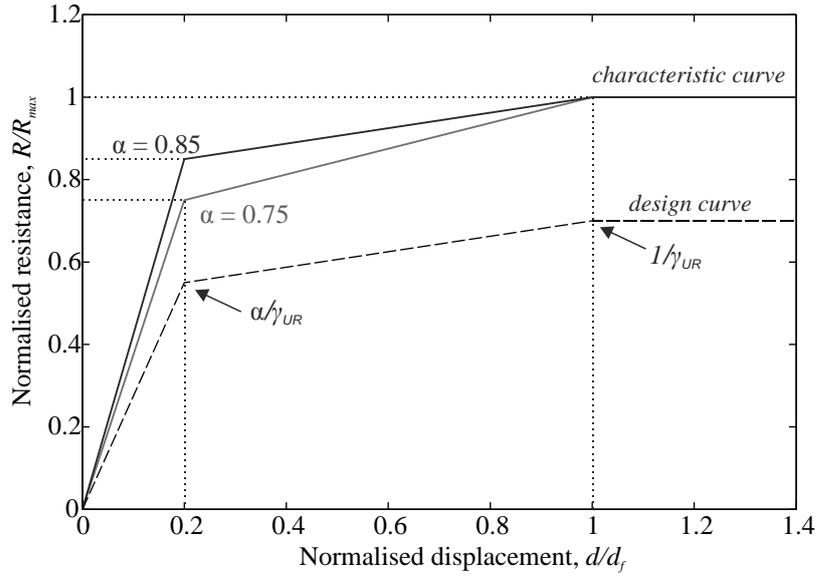
Figure 2-9 DNV uplift force-displacement curve (after DNV, 2007)

An important modelling input − and the primary focus of this thesis − is the resistance of the soil to pipe uplift. To approximate the force-displacement response in uplift, the DNV guidelines propose the tri-linear force-displacement curve shown in Figure 2-9. The peak uplift resistance, denoted as R_{max}, is usually determined from an adapted vertical slip model as follows:

$$R_{max} = F_{ult,aVSM} = \left[1 + f\frac{H}{D}\right]\gamma'HDL \tag{2.18}$$

The first term in the above equation represents the weight of a soil block above the pipe, while the second term accounts for the frictional component of the soil resistance. The uplift resistance factor, f, is selected based on three specified density categories: loose, medium/dense, or rock. A range for the mobilisation displacement related to the pipe embedment, H_c (measured to the top of the pipe), is also provided based on data by Trautmann et al. (1985). These values, along with the parameters that control the shape of the force-displacement curve are listed in Table 2-1. Additional factors affecting uplift resistance, such as rate effects and liquefaction susceptibility are not specifically addressed in these guidelines.

38

The guidelines also provide recommendations for the downward soil resistance, including a simplified chart for stiffness calculations. Limited information is given concerning the axial resistance of the soil.

Table 2-1 DNV suggested parameters for tri-linear uplift curve (Source: DNV, 2007)

Category	Parameter		Range
Loose sand $3.5 \leq \dfrac{H_c}{D} \leq 7.5$	f	$\in$	[0.1,0.3]
	d_f	$\in$	[0.5%, 0.8%]·H_c
	α	$\in$	[0.75, 0.85]
	β	$=$	0.2
Medium/Dense $2.0 \leq \dfrac{H_c}{D} \leq 8.0$	f	$\in$	[0.4,0.6]
	d_f	$\in$	[0.5%, 0.8%]· H_c
	α	$\in$	[0.65, 0.75]
	β	$=$	0.2
Post-peak resistance	f_r	$=$	$\alpha_f \cdot f$
at displacement	α_f	$\in$	[0.65, 0.75]
	d_{fr}	$=$	$3 \cdot d_f$

2.3. Cyclic ratcheting

Since the 1986 resurfacing of a buried pipeline in the North Sea was attributed to 'upheaval creep' by Nielsen et al. (1990a), there has been some interest in the theory of upward cyclic ratcheting; that is, the cumulative upward displacements of the pipe over multiple temporary shut-down cycles. This itself may not constitute failure but, due to progressive enlargement of an initial imperfection and a local loss of cover, upheaval buckling could occur at a lower temperature than that specified in the design (Nielsen et al., 1990b). Nielsen et al. (1990b) identified both the pipe-soil interaction and imperfection characteristics to be critical parameters for upheaval creep. The authors point to numerical work by Pedersen and Michelson (1988), which demonstrates that the imperfection shape and residual stress components strongly influence the amount of upward pipe displacement, noting that the uplift movement up to the peak temperature (prior to buckling) decreases with decreasing

imperfection amplitude. The cyclic aspect of the problem is of course highly dependent on the soil resistance. Pedersen and Jensen (1988) note that after a certain amount of upward displacement during heating, soil flow around and beneath the pipe may prevent it from moving back into its original position on a subsequent shut-down cycle. The process is therefore irreversible. An extreme example of this was demonstrated in the (centrifuge) buckling experiments described above (Moradi and Craig, 1998), in which it was shown that after snap-through buckling was induced and the temperature lowered, the pipe remained above its original position.

It is clear that to predict upheaval creep behaviour it is necessary to understand how both the downward and upward soil resistance evolves over a number of cycles. The vertical cyclic loading of pipelines buried in sand has been studied to a much lesser extent than monotonic pullout failure of the pipeline. In the literature, two independent plane-strain tests in sand have been reported which attempt to re-create conditions where cyclic ratcheting of a pipeline could occur. In the first test, reported by Finch (1999), a 220 mm diameter pipe was first displaced upwards to a pre-defined 'bedding gap' of 22 mm, after which 7 cycles were carried out from approximately the peak uplift force to a negative value of the same magnitude. The force-displacement results from this test show some incremental upward displacements, but it can be seen that both the upward and downward soil responses become stiffer with each cycle. Though upward ratcheting is demonstrated, the test may be somewhat unrealistic given that a pipe displacing at the peak soil resistance or beyond would be considered to have reached monotonic failure, and may experience snap-through buckling at this point. Nevertheless, if the pipe does tend to move upwards as shown, the incremental displacements are much less significant than the initial displacement of 22 mm.

More recent work by Wang (2012) explores in greater detail the force-displacement response of a 100 mm diameter pipe subjected to 60 loading cycles. The test was carried out in loose saturated sand at $RD = 30\%$, and an embedment ratio of $H/D = 3.5$. The aim of this

work was to determine, by varying the ratio of F_{max} (the peak force reached during cycling) to R_{peak} (the monotonic uplift resistance), whether diverging cumulative displacements could be observed. This was done in a single stepped test involving 6 consecutive groupings of 10 cycles, each starting from 0 N to a value of F_{max} that was varied in each grouping. The tested values of F_{max} ranged from 54% to 98% of R_{peak}. Figure 2-10 shows the resulting force-displacement response.
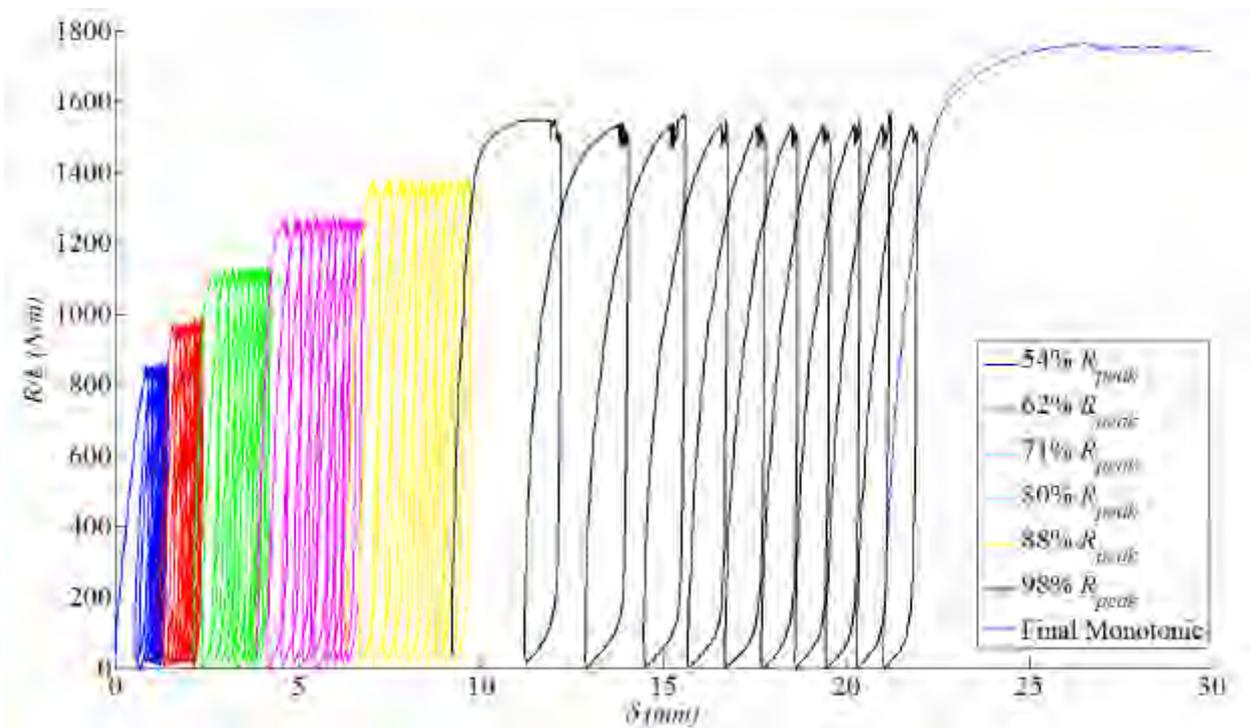

Figure 2-10 Cyclic test data from Wang (2012)

The analysis of the above test by Wang (2012) focuses on the incremental displacements at each cycle. The quantity examined in this instance is defined as d_{cycle}, and only considers the displacements in the upward half-cycle, i.e. from 0 N to F_{max}. In order to come up with an expression for d_{cycle} with respect to cycle number (N), the displacements in each grouping of 10 cycles were considered separately, and normalised by the 2nd displacement at the beginning of the grouping. The author states that the reason for this choice of normalisation (i.e. using the displacement at the end of the 2nd cycle rather than the 1st) is that it minimises

41

the influence of the both the monotonic mobilisation displacement and the compaction from previous cycles. The proposed equation is as follows:

$$\frac{d_{cycle,10N+i}}{d_{cycle,10N+2}} = f\left(\frac{F_{max}}{R_{peak}}, N\right) \tag{2.19}$$

where $N = 0,1,2,3,4,5$, and $i = 1,2,\ldots9,10$. Several functions were then fitted to the data, with the best fit obtained using an exponential function of the form:

$$\frac{d_{cycle,10N+i}}{d_{cycle,10N+2}} = C \cdot e^{-\frac{\ln C}{2}i} \tag{2.20}$$

It is then suggested that since this model fits well to the first grouping, $d_{cycle,10N+2}$ can replaced with d_o (the mobilisation displacement for the first cycle) for a more general case. The constant C is given as 1.12 (± 0.06), and was thought to be related to the relative density of the soil. Based on the above expression, a calculation for the cumulative displacement over a number of cycles, N, is proposed. However, the above relationships are based on only one test and are therefore not generalisable at this stage.

Some useful observations can be made from this test. From the force-displacement figure it is obvious that at all load levels the incremental displacements tend to decrease with cycle number. An exponential fit to the data implies that at large values of N these displacements tend to zero. It should be noted that the value d_{cycle} studied by Wang looks only at the upward portion of the displacements in each cycle, although the author acknowledges that some downward displacement (bearing on the soil beneath the pipe) is required to achieve a net force of 0 N on the pipe at the start of each cycle. This is a conservative approach, assuming that the net movement of the pipe is upwards (which is true for the test shown); however, the cyclic response of the soil beneath the pipe may also be an important consideration when predicting how the pipe behaves over a number of cycles.

2.3.1.   Design guidance

Because of the lack of experimental data on vertical cycling of pipelines, design guidance for cyclic ratcheting is typically limited to restricting the maximum allowed displacement during uplift. For example, Nielsen et al. (1990a,b) proposed that at maximum temperature and pressure this displacement should be less than 10-20 mm for natural backfill conditions. Based on the test described above, Wang (2012) suggests that these values could be unconservative in terms of the soil-pipe interaction response. It is clear, however, that more experimental work is needed to understand the influence of loading and installation conditions (such as RD, and H/D) on the cyclic behaviour of the pipe, before firm conclusions can be drawn.

3   Plane-strain pipe uplift

A key parameter in assessing pipeline stability against upheaval buckling is the vertical resistance provided by the soil to upward movement of the pipe. Previous research on this topic has focused on understanding the deformation mechanisms and the force-displacement response during pipe uplift, generally assuming drained conditions. This has led to uplift prediction models that form the basis of recommendations for pipeline designers, such as in the DNV-RP-F110: Global Buckling of Submarine Pipelines (DNV, 2007).

Although numerous studies on uplift resistance have been carried out over the last three decades, there are several issues that are unresolved, and therefore not properly accounted for in the industry guidelines; namely, the impact of the backfill relative density, particularly in very loose sand, on the induced failure mechanisms and the corresponding uplift resistance. Since the uplift response appears to be strongly related to the volumetric behaviour of the soil, both backfill relative density and vertical effective stress could be influencing factors. Furthermore, partially drained conditions stemming from faster uplift rates or pipe vibration may also be relevant when installation methods such as jet trenching result in very loose, liquefiable backfill soils. It is therefore important to have a better understanding of density, rate, and stress level effects, such that appropriate provisions for these conditions can be included in design guidelines.

This chapter reports a comprehensive investigation into these effects, through two-dimensional pipe uplift testing. Key features of this work are outlined in Figure 3-1. The bulk of the testing was carried out in saturated conditions, examining the influence of backfill relative density and uplift rate on the initial pipe-soil response; findings from this section have been published in the *Géotechnique* article: "Pipe uplift in saturated sand: rate and density effects" (Williams et al., 2013). Further testing in dry sand was aimed at identifying trends across different sands and stress levels. Finally, the impact on the mobilised resistance due to

a surface overburden pressure – mimicking the mitigation technique of rock dumping – is briefly examined. The overall aims of the investigation are:

- to improve understanding of the mechanisms involved in mobilising the soil resistance for buried pipes installed into loose sand by jet trenching;

- to evaluate prediction models presented in the literature; and,

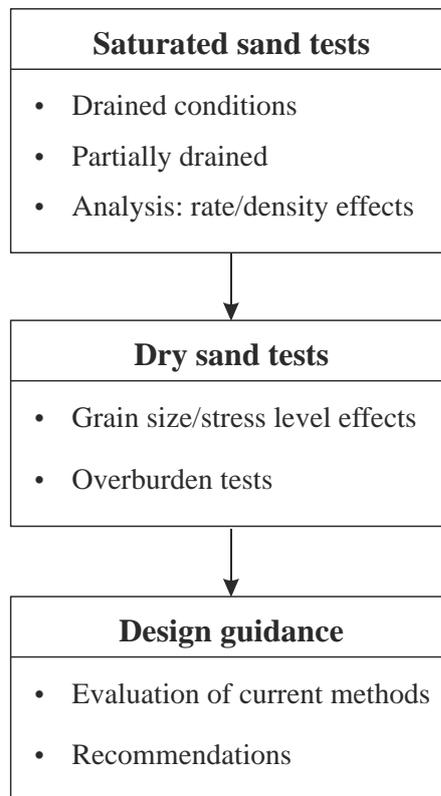- to assess the validity of the recommendations in the current design guidelines for these conditions.

<div align="center">

Saturated sand tests

- Drained conditions
- Partially drained
- Analysis: rate/density effects

↓

Dry sand tests

- Grain size/stress level effects
- Overburden tests

↓

Design guidance

- Evaluation of current methods
- Recommendations

</div>

Figure 3-1 Chapter 3 outline

3.1. Experimental method

3.1.1. Test equipment

The experimental rig used for plane-strain pipe uplift tests was developed by Schupp (2009), and is shown in Figure 3-2. The rig is a 1 m x 0.3 m x 1 m tank made of marine plywood, and reinforced by aluminium box sections. The front panel is made from Perspex to

allow viewing of the test as it progresses. The tank is equipped with a pumping mechanism for fluidising the soil sample by means of an upward hydraulic gradient. This was achieved in the saturated tests by cycling water through the tank using a pump, which draws from a reservoir mounted to the side of the tank and distributes water through the base of the tank via system of drainage channels. An even pressure distribution and therefore fluidisation of the sample is ensured by the use of a geotextile filter mounted across the base of the tank. A schematic of this process is shown in Figure 3-3.

The rig has a fully instrumented model pipe, which is moved vertically through the height of the tank by a stepper motor driven actuator (attached to the pipe ends by two aluminium pull rods). The 100 mm diameter pipe consists of a 200 mm central 'active' test section, and two 100 mm 'dummy' sections at either end, that sit flush with the tank side walls. The pipe ends are fixed to the middle section via an internal moment-compensated load cell, while the central test section moves independently. The three pipe sections (shown in Figure 3-4) are sealed with ultra-flexible silicone sealant, ensuring that the central test section is isolated from frictional end effects.

The pipe internal load cell allows for measurement of the net external force exerted on the central section of the pipe by the surrounding soil (i.e. the resultant of the vertical components of the soil forces above and below the pipe). This measurement is referred to throughout the thesis as the net soil force (positive values downward). Additional secondary load cells are fitted at the top of the pull rods as a backup measurement, though these reading are influenced by the wall friction effects. Calibration of the load cells was carried out by placing known masses on the central pipe section and correlating the voltage output to the force on the pipe. The maximum error in the load cell calibration was found to be less than 1 N.
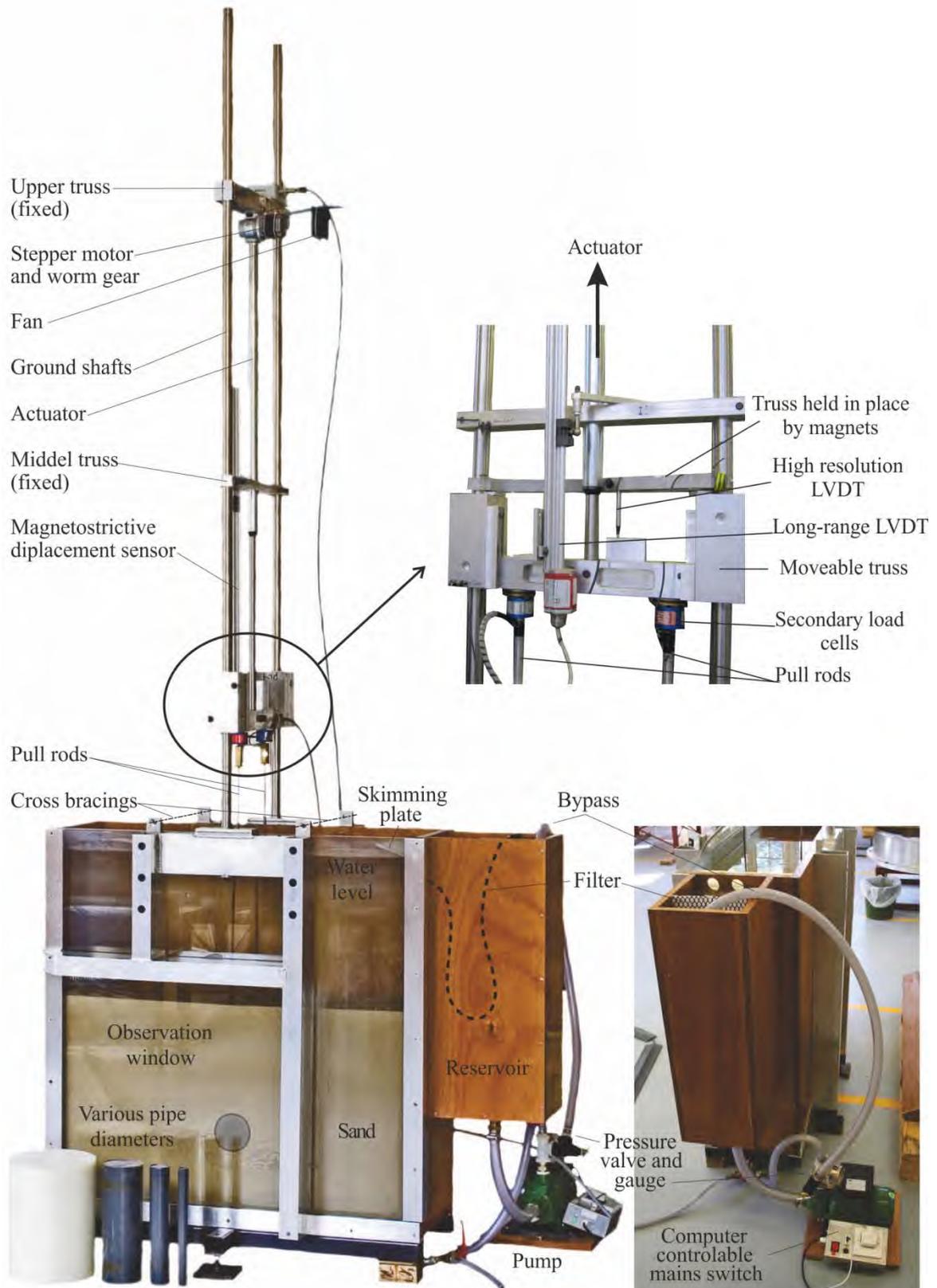
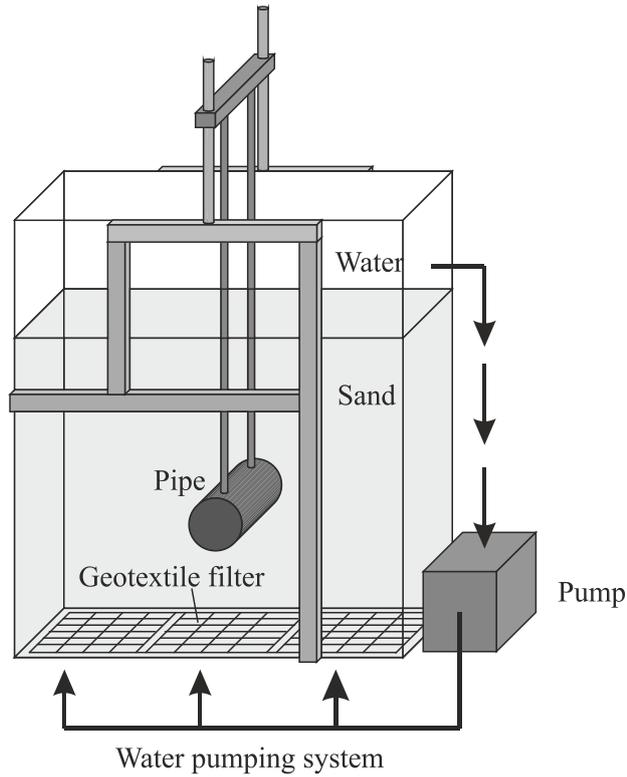*Figure 3-2 Plane-strain testing rig, after: Schupp (2009)*

Figure 3-3 Schematic of uplift rig and sample fluidisation, after Gould (2007)

Figure 3-4 Model pipe used in the testing rig (Source: Schupp, 2009). The internal load cell measures the resultant of the external soil forces acting on the central test section.

The pipe is equipped with five pore water pressure transducers (PPTs), evenly placed around the half-circumference of the pipe, for use in the saturated tests. Measurements from a fixed pressure sensor at the top of the tank were used to obtain a reference water level; based on these readings, the excess pore pressures around the pipe could be determined. An example calculation of the excess pore pressure at a transducer on the pipe, Δu_{ppt1}, is given in equation 3.1.

$$\Delta u_{ppt1} = u_{ppt1} - u_{ref} - \Delta u_0 - \Delta x \cdot \gamma_w \qquad (3.1)$$

where u_{ppt1} is the current pressure measurement at the transducer on top of the pipe, u_{ref} is the current water level measurement, Δu_0 is the initial pressure difference between the two instruments, and Δx is the vertical displacement of the pipe from the beginning of the test.

Vertical displacement of the pipe is measured with two displacement sensors. High-quality measurements of the initial displacement response of the pipe are made using a short-range, high-resolution displacement transducer (LVDT). This LVDT is attached to a truss that is initially held in place by magnets, a short distance away from the moveable truss (see Figure 3-2). After the first several mm of upward displacement of the pipe (and moveable truss), the magnets are disengaged and the LVDT truss travels freely with the other moving components. The full range of pipe displacement is recorded throughout each test using a longer range, lower-resolution displacement sensor. All displacement measurements are corrected for the stiffness of the rig under loading. This was calibrated prior to testing by measuring deflections at the pipe centre and at the location of the high-resolution LVDT due to applied loading on the pipe. This stiffness correction is thought to be more accurate than what was used by Schupp (2009), allowing for a more reliable estimate of the initial stiffness of the pipe-soil interaction than has previously been achieved in the literature.

For the experiments described in this chapter, a computer program was created in LabVIEW (LabVIEW, 2009) to control the rig components as well as log the data during each test. Commands are sent from the computer to the actuator via an RS232 connection, while components such as the pump and magnet for the short-range LVDT are engaged through simple circuits controlled by the program. The output voltage signals for all instruments were calibrated against measured or known quantities. Important considerations in the program were the data logging rate, which was varied depending on the uplift rate, and signal averaging (within the logging program) to reduce the level of noise in the data. For a

typical slow-rate test (see for example Figure 3-6), the data was sampled at 1000 Hz and time-averaged by a factor of 100, giving a compressed output signal at a frequency of 10 Hz.

3.1.2.   Procedure

3.1.2.1.   *Saturated sand tests*

All tests in this chapter followed a procedure that is predominantly automated, allowing changes to input variables such as embedment ratio and uplift rate. The uplift procedure is based on that described by Schupp (2009), though a new and more streamlined control program was developed. The tests were conducted in saturated Redhill 110 sand, with the assumption that full drainage could occur during uplift if a sufficiently slow uplift rate was selected. Prior to commencing the tests, the tank was filled with water and sand was added to achieve the target height within the tank. The height of the sand (approximately 500 mm) and the remaining free space in the tank was estimated based on calculations by Schupp (2009). The calculations determined the required height of the fully liquefied suspension relative to the height of the settled sediment, such that the specific gravity of the suspension mimicked the specific gravity achieved during jet trenching ($SG \sim 1.2$). Schupp (2009) reported that a specific gravity of 1.4 could be achieved given the dimensions of the testing tank, and found that any difference between the obtained and target specific gravities had a negligible effect of the final density of the sediment. After the initial placement of the sand in the tank, the same sample was used repeatedly for all of the saturated tests.

Prior to each test, the internal load cell is zeroed with the pipe in water, and initial measurements of the height of the sand and the initial position of the pipe are taken. With data logging continuously, the first step of the process is to turn on the pump to fluidise the soil. The soil is allowed to liquefy until the suspension height reaches the top of the tank, after which this height is maintained by cycling the pump on and off. The pipe is then lowered to the test depth, using the position output from the stepper motor to control the pipe

displacement. Near the final position, a magnet is engaged to lock the short-range LVDT at a specified distance above the pipe for the start of uplift. Once the installation position is reached, the pump is turned off and the liquefied soil begins to settle, with the sediment front rising from the bottom of the tank. A detailed explanation of the installation process, with accompanying figures, can be referred to in Schupp (2009).

When the approaching sediment reaches the bottom of the pipe (indicated by a rapid drop in excess pore pressure at the lowest PPT), a load control routine is engaged to simulate the self-weight of the pipe. This involves inducing very small downward pipe displacements to maintain a pre-defined net soil force on the pipe, based on the internal load cell readings. For the saturated tests this value was set at -10 N, which is a representative scaled value for the buoyant weight of a pipe in the field. It should be noted that the net force reading represents the difference between the upward reaction force of the soil beneath the pipe, and the downward overburden force of the soil settling over the pipe. Without measurements of the contact forces on the pipe, however, their respective magnitudes are unknown.

The load control routine is used until the sand has settled fully over the pipe. This was estimated to be when the excess pore pressures measured around the pipe cease falling and remain constant at the hydrostatic condition, a process that takes approximately ten to fifteen minutes. The soil typically settles over the pipe in its loosest state, e_{max} (i.e. zero relative density).

The next stage of the procedure, if required, is densification of the soil in the tank, which is achieved by vibrating the tank with impacts from a rubber mallet. This process was thought to represent the possibility that the backfill material can be densified by either pipe vibration or wave and current effects. The resulting relative density was determined by assuming that the soil settlement occurs uniformly throughout the tank, which is not unreasonable for the settlement of very loose sands. By taking measurements of the initial and final volume of the sample, the new relative density of the backfill can be calculated:

$$V_s = V_{T,0} \left(\frac{1}{1 + e_{max}} \right) \tag{3.2}$$

$$e_{new} = \frac{V_{T,new} - V_s}{V_{T,new}} \tag{3.3}$$

$$RD_{new} = \frac{e_{max} - e_{new}}{e_{max} - e_{min}} \tag{3.4}$$

$$\gamma'_{new} = \frac{1 + e_{max}}{1 + e_{new}} \gamma'_0 \tag{3.5}$$

where V_s is the volume of solids, V_T is the total volume, e is the void ratio, and RD is the relative density.

When the desired relative density of the backfill is achieved, the uplift test is carried out by pulling the pipe upwards at a constant rate. Based on the installation procedure and its assumptions, outlined above, it is thought that the net soil force on the pipe would initially reflect a reducing contact force beneath the pipe, and a constant or increasing overburden force above the pipe. After some displacement, however, the contact force beneath the pipe will reduce to zero and the measured force is then entirely due to the soil response above the pipe (consisting of the weight of soil above the pipe and a shear force component, as theorised by the uplift models in the literature).

3.1.2.1. *Dry sand tests*

The main difference between the dry and saturated testing procedures is in the installation process; otherwise, the test equipment and general methodology are unchanged. For each dry test, the sand is removed from the tank until there is sufficient space for the pipe to be buried at the required depth. Measurements of the initial soil profile are taken, and the pipe is lowered to a height of approximately 100 mm above the soil surface. The backfill is then placed beneath and over top of the pipe in layers, using a small scoop and a very low soil drop height. Once the target embedment is achieved, the relative density can be calculated from measurements of the weight and volume of soil added. A denser sample can be achieved if

required by increasing the soil drop height during soil placement. A load control routine to maintain a constant force on the pipe is also used during this installation procedure.

3.1.2.2. *Validation of experimental setup and test results*

During the development of the experimental apparatus, several studies were conducted by Schupp (2009) to verify the obtained results with work completed by previous researchers, as well as with calculated theoretical values. Schupp (2009) examined the following topics/issues:

- Surface roughness effects on uplift response: several materials were tested (PVC, nylon, and anodised aluminium) and it was determined that the uplift force results from the rig are comparable, regardless of the pipe surface.

- Scalability of the diameter of pipe selected with respect to grain size: tests were conducted in dry sand (Leighton Buzzard 14-25) with pipe diameters ranging from 25.4 mm to 220 mm. The measured breakout factors were consistent for diameters greater than 50.8 mm, and it was concluded that a 100 mm pipe has an adequate diameter to grain size ratio to negate any grain size effects for Leighton Buzzard 14-25.

- Self-weight of the pipe: to mimic in situ conditions, the load control routine was varied to simulate a number of different pipe densities. For pipes with a specific gravity (*SG*) ranging from 1 to 2, it was found that changing the pre-load value did not significantly influence the force-displacement response. A pipe *SG* of 1.65 was selected for subsequent tests, corresponding to a pre-load on the pipe of -10 N (i.e. 10 N in the upward direction).

3.1.3. Soil properties

Three sands with a range of grain sizes were used in the experimental work described in this thesis. All saturated tests were carried out using Redhill 110, a fine, poorly graded silica sand. This sand was selected as it resembles a typical North Sea sand, and the grain size distribution falls within the range classified as liquefiable (Damgaard et al., 2006). Redhill 110 was also tested in dry conditions, along with two coarser (dry) sands, Leighton Buzzard (LB) 14-25 and LB DA30. The grading curves for each of the three sands are shown in Figure 3-5.
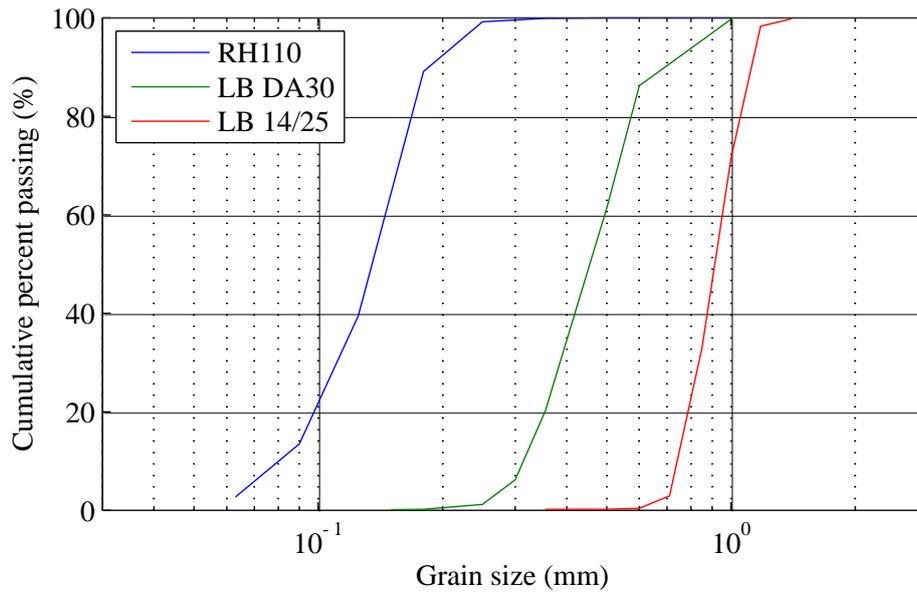
Figure 3-5 Grading curve for tested sands (data from Schupp, 2009 and Sandford, 2012)

Relevant soil parameters are listed in Table 3-1. Unless otherwise indicated, the values for Redhill 110 and LB 14-25 are obtained from Schupp (2009), while the properties for LB DA30 are given by Sandford (2012). Additional tests were required to verify the minimum void ratio value for Redhill 110, as the value of 0.64 found by Schupp (2009) differs from the value of 0.53 reported by Kelly et al. (2006). This variation would have a significant impact on relative density calculations. Several compaction tests based on ASTM D4253 were carried out, resulting in an average e_{min} of 0.639; thus, 0.64 is used.

Table 3-1 Soil properties

Property	Redhill 110	LB DA30	LB 24-25
Specific gravity, G_s	2.63	2.65	2.62
Critical friction angle, ϕ'_{cs} (°)	36[*]	34.3[†]	33
Max. void ratio, e_{max}	1.04	0.77	0.76
Min. void ratio, e_{min}	0.64	0.63	0.49
Min. dry/effective unit weight, $\gamma'_{min,}$(kN/m³)	12.65, *7.82 (sat.)*	14.7	14.6
Grain size (50% passing), D_{50} (mm)	0.135	0.456	0.94
Angularity	Sub-angular (SA)	Rounded (R)	SA to SR
Sphericity	Medium	Medium	Medium

[*] Source: Villalobos et al. (2005); [†] Value assumed by Sandford (2012)

3.2. Saturated tests

A comprehensive experimental investigation into density and rate effects in saturated sand conditions, across a range of embedment ratios up to *H/D* of 4.5, was completed. This involved two series of tests exploring drained and partially drained behaviour. Much of the work in this section (including data, figures and text) has been published in *Géotechnique* (Williams et al., 2013).

3.2.1. Drained response in saturated sand

The first test programme investigated the influence of backfill relative density, at various embedment depths, on the peak uplift resistance and the force-displacement response under drained conditions. The rate of pipe uplift was set at 0.002 mm/s, a speed judged to be sufficiently slow to ensure adequate drainage of the excess pore pressures during the test. This was confirmed by measurements of the pore pressures on the pipe circumference during uplift showing the hydrostatic condition. A summary of the tests conducted is provided in Table 3-2.

Table 3-2 Summary of drained tests

Set	Embedment ratio, H/D	Relative density, RD (%)	Uplift rate, v (mm/s)	Number of tests
Drained 1	0.5 to 4.5	0 to 20	0.002	62
Drained 2	1.5 to 4.5	21 to 60	0.002	13
Total drained tests				75

A representative uplift test in very loose sand is shown in Figure 3-6. In the figure, the test progresses from left to right, starting at an initial embedment of *H/D* = 3 and ending at the ground surface (*H/D* = 0), after 300 mm of upward displacement. Herein, the value of *H* is measured from the ground surface to the pipe centre, unless otherwise specified. The net soil force on the pipe (initially at -10 N), increases rapidly in the first several mm of displacement reaching a maximum value representing the peak uplift resistance. The force then decreases to a value close to zero as the pipe approaches the soil surface.
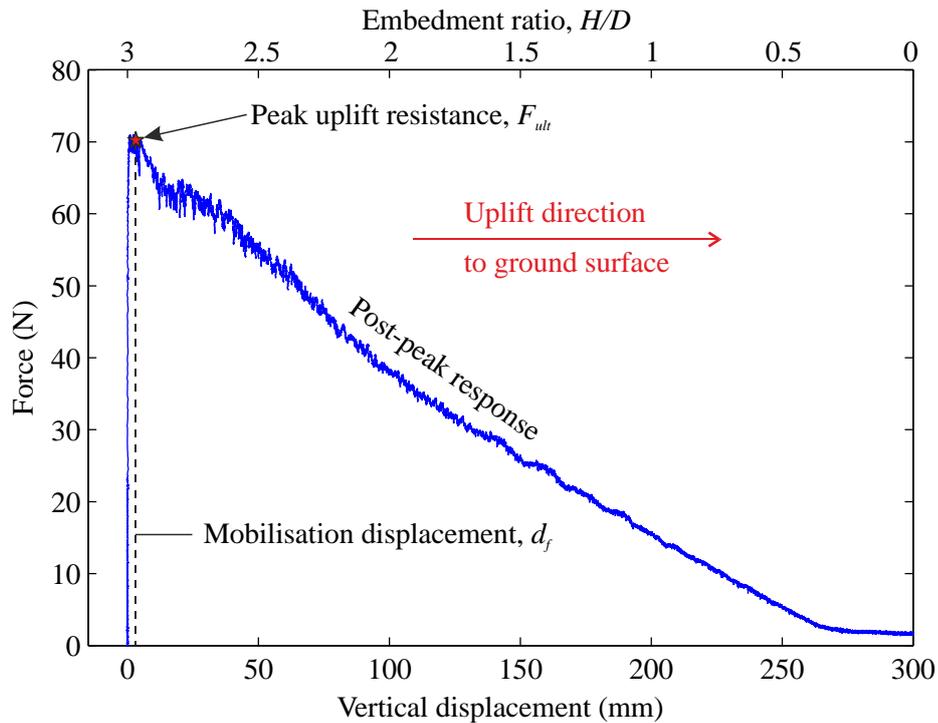
Figure 3-6 Example uplift test in very loose sand (RD = 0%) at H/D = 3

The key features of the response from a design perspective are the peak resistance, the mobilisation displacement (i.e. the vertical displacement corresponding to the peak force), and the shape and stiffness of the initial response prior to peak. In this section, representative force-displacement curves from across the test programme are presented first, followed by analysis relating to these three key areas. Where relevant, the experimental results are compared to three prediction models introduced in section 2.1.2: the vertical slip model (VSM), the adapted vertical slip model (aVSM), and the inclined surface model (ISM).

3.2.1.1.   Force-displacement response

Example force-displacement curves across the range of embedment depths tested are presented in Figure 3-7 and Figure 3-8, along with VSM and aVSM predictions. Figure 3-7 plots the first 8 mm of upward displacement for varying initial densities at embedment ratios of 1.5 and 3.5. It can be seen from the figure that the mobilised resistance tends to increase with both embedment ratio and relative density. As the relative density increases from 0%, an increasingly distinct peak response occurs, followed by rapid strain softening. Regardless of

the initial density and embedment depth, the tests show that, after the initial displacement, the soil resistance converges to a consistent load response (which appears to match the VSM prediction). The displacement required for this convergence is dependent on the embedment depth, where a greater uplift distance is required for convergence at deeper embedments. This is because the friction proportion of the overall resistance increases with depth (see equation 2.2), meaning that the influence of relative density on the overall uplift resistance will also increase with depth.

In Figure 3-8, a number of tests are plotted against embedment ratio (*H/D* decreases from left to right, as the pipe moves towards the surface). The measured and predicted forces are normalised by the soil effective unit weight and pipe diameter, as this preserves the shape of the force-displacement curve through the uplift test. For very loose sand at 0% relative density (blue curves) it can be seen that the VSM closely matches the force-displacement response of the pipe at low embedment ratios, while at greater depths it over-predicts the response. Tests at an embedment ratio of 4 demonstrate how an increase in relative density to 20% is required for the force to reach the VSM curves. The response at *RD* = 30% is higher than the predicted values, but appears to approach these curves after approximately 100 mm of displacement.
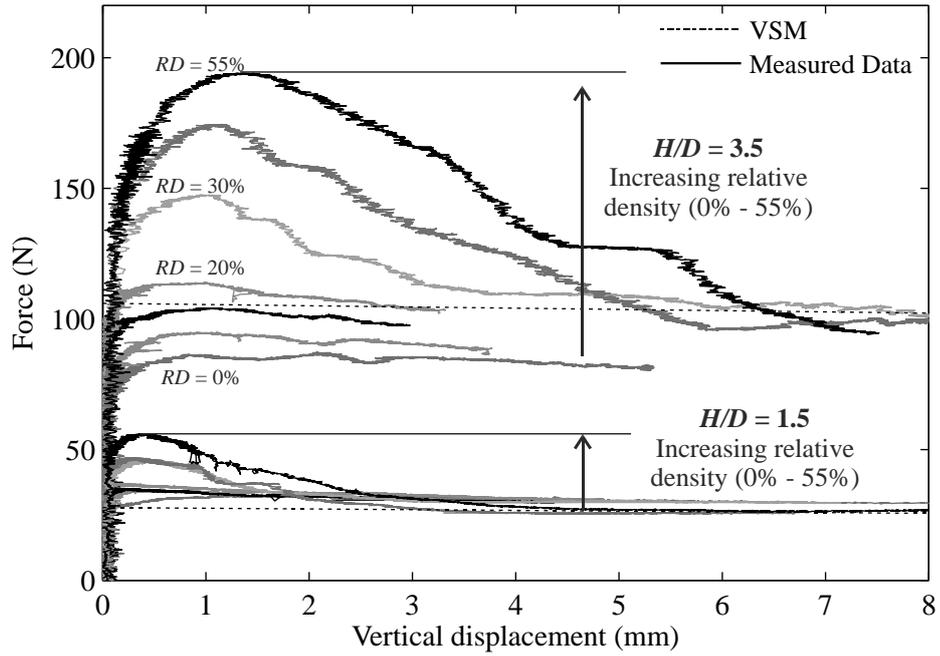
Figure 3-7 Initial force-displacement response at selected embedment ratios, using coarse displacement measurement system
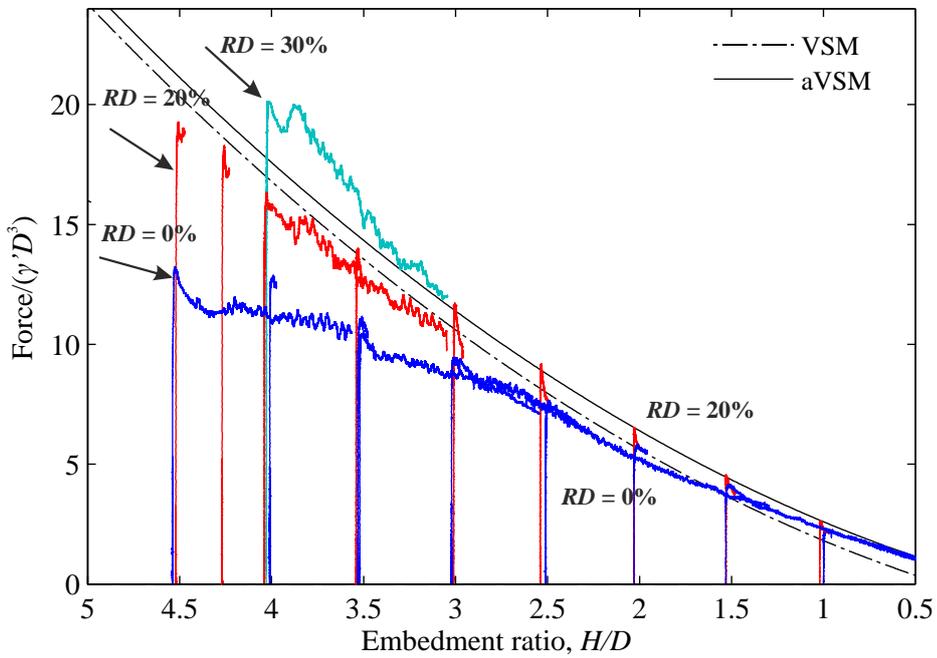
Figure 3-8 Representative curves of normalised force plotted against embedment ratio

The peak uplift force obtained in each test is presented in the following figures in the form of a soil breakout factor, N_{ult}, which normalises the force with respect to the effective unit weight of the soil, the embedment depth, and the pipe dimensions as follows:

$$N_{ult} = \frac{F_{ult}}{\gamma' H D L}$$

(3.6)

Essentially, the peak force is normalised by the weight of a block of soil above the pipe, where H is the embedment depth measured to pipe centre, D is the pipe diameter, and L is the segment length.

Figure 3-9 and Figure 3-10 plot peak breakout factors for backfill at various initial relative densities across a range of embedment ratios. Along with the VSM and the aVSM prediction curves, the DNV recommended ranges are included for comparison (Figure 3-10). These predictions are normalised in a similar manner as follows:

$$N_{ult,VSM} = \frac{\left[1 - \frac{\pi D}{8H} + K_o \tan \phi' \frac{H}{D}\right] \gamma' H D L}{\gamma' H D L}$$

$$= 1 - \frac{\pi D}{8H} + K_o \tan \phi' \frac{H}{D}$$

(3.7)

$$N_{ult,aVSM} = 1 + K_o \tan \phi' \frac{H}{D}$$

(3.8)

$$N_{ult,DNV} = 1 + f \frac{H}{D}$$

(3.9)

where $f \in [0.1, 0.3]$ for loose sand and $[0.4, 0.6]$ for medium/dense sand. Again, H is measured from the ground surface to the centre of the pipe.

(a)

(b)
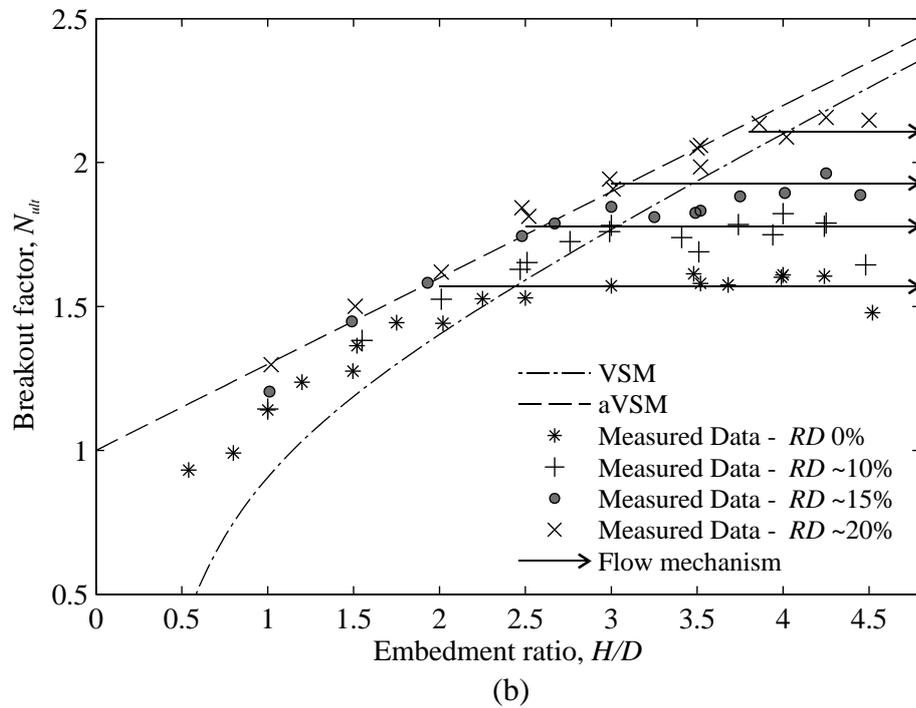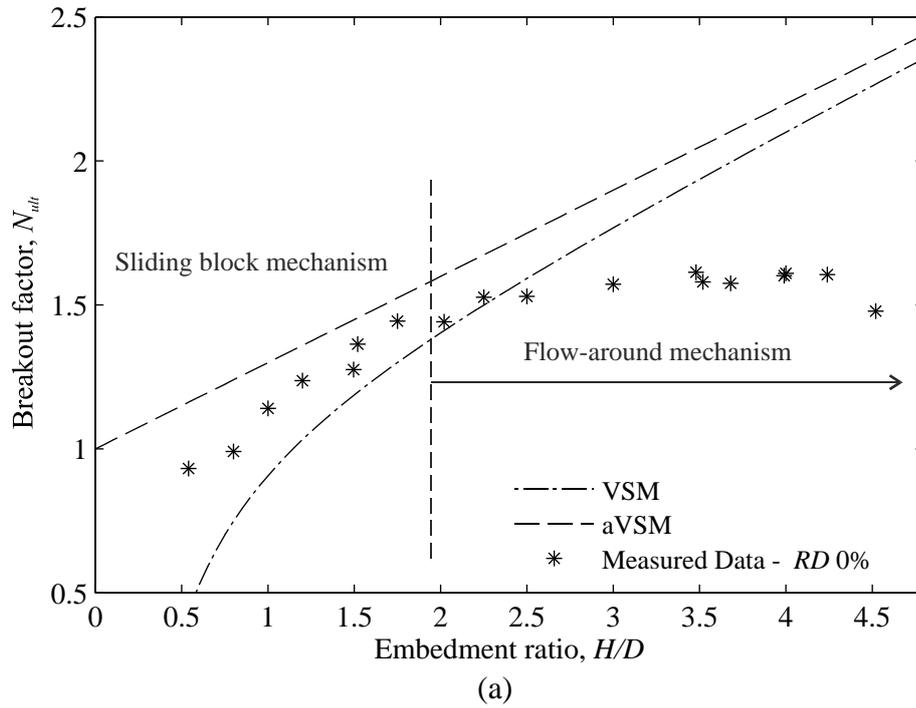
Figure 3-9 Summary of breakout factors compared with vertical slip models: (a) very loose sand, relative density 0%; (b) loose sand, relative density 0-20%.
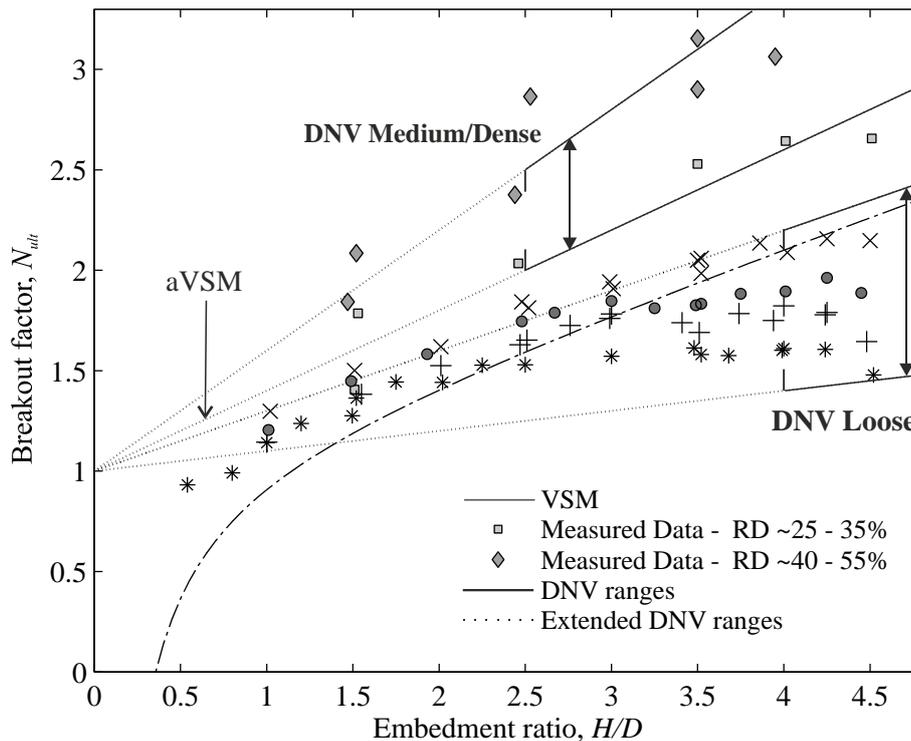
Figure 3-10 Summary of breakout factors compared with vertical slip models: loose to dense sand, relative density 0-55%

From Figure 3-9 (a) it can be seen that the VSM is an excellent predictor of the uplift resistance for soil at its loosest state, up to an embedment ratio of approximately 2. Beyond this depth the breakout factors level off and remain constant, indicating a possible transition to a different failure mechanism. As the relative density increases, the applicability of both the vertical slip models extends to greater depths, after which similar plateaus in the normalised resistance are observed (see Figure 3-9 (b)). The results indicate that, as the relative density increases, the transition from sliding block mechanism to another mechanism (probably a flow-around mechanism) occurs at greater values of *H/D*. Figure 3-10 includes breakout factors for tests in medium-dense soil conditions. The DNV predictions are also plotted in the figure, demonstrating that the ranges suggested in the guidelines broadly capture the data obtained in these experiments.

Figure 3-11 compares the peak breakout factors to prediction curves based on the inclined surface model (ISM) proposed by White et al. (2001), which is aimed at capturing density

61

effects. At an embedment ratio of 1.5, the breakout factors are very consistent with this model, across the entire range of densities. However, similar to the vertical slip models, as the embedment depth increases, the ISM increasingly over-predicts the peak force response. The results demonstrate that for very loose soil conditions, an increase in embedment depth, beyond a critical value, does not necessarily result in any significant improvement in the breakout factor.
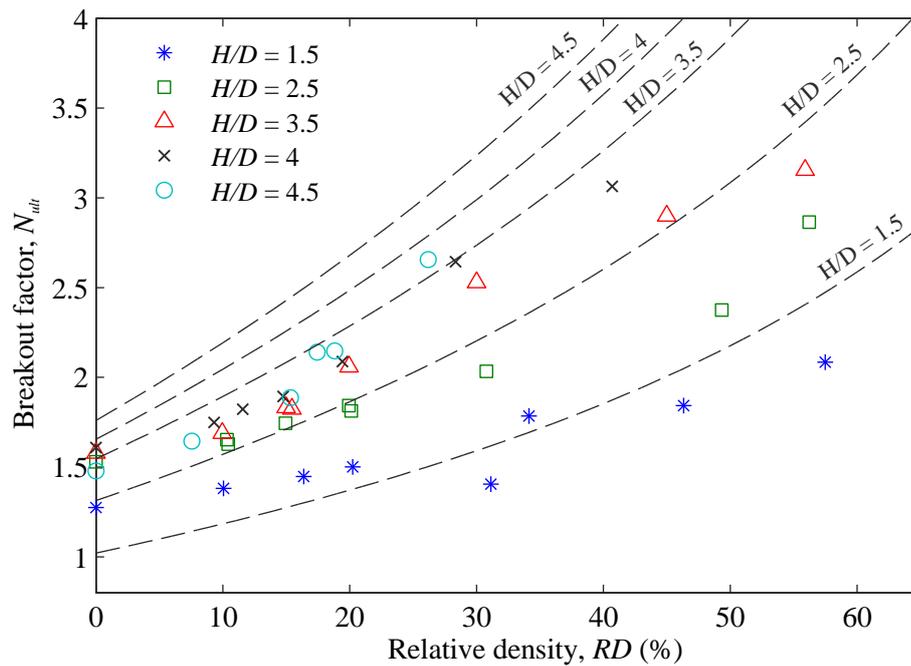

Figure 3-11 Breakout factors vs. RD, compared with the inclined slip surface model by White et al. (2001)

3.2.1.3. *Mobilisation displacement*

The measured mobilisation displacements, defined as the pipe displacement corresponding to peak resistance, are normalised by both H (Figure 3-12 (a)) and D (Figure 3-12 (b)). Both are presented for comparison with data in the literature; however, due to the potential for localised failure mechanisms, it is felt that pipe diameter (a local length scale) is possibly the more appropriate normalisation. The plotted displacements, d_f/H or d_f/D, appear to be dependent on both relative density and embedment ratio, though the overall variation is small, with values ranging from 0.1%H to 1.7%H. This is consistent with values found by several

researchers (Matyas and Davis, 1983a; Trautmann et al., 1985; Bransby et al., 2002; Cheuk et al., 2008), which range from 0.1%H to 1.5%H. The mobilisation displacements tend to be highest in loose tests at low embedment ratios; at deeper burial depths relative density has a lesser influence.
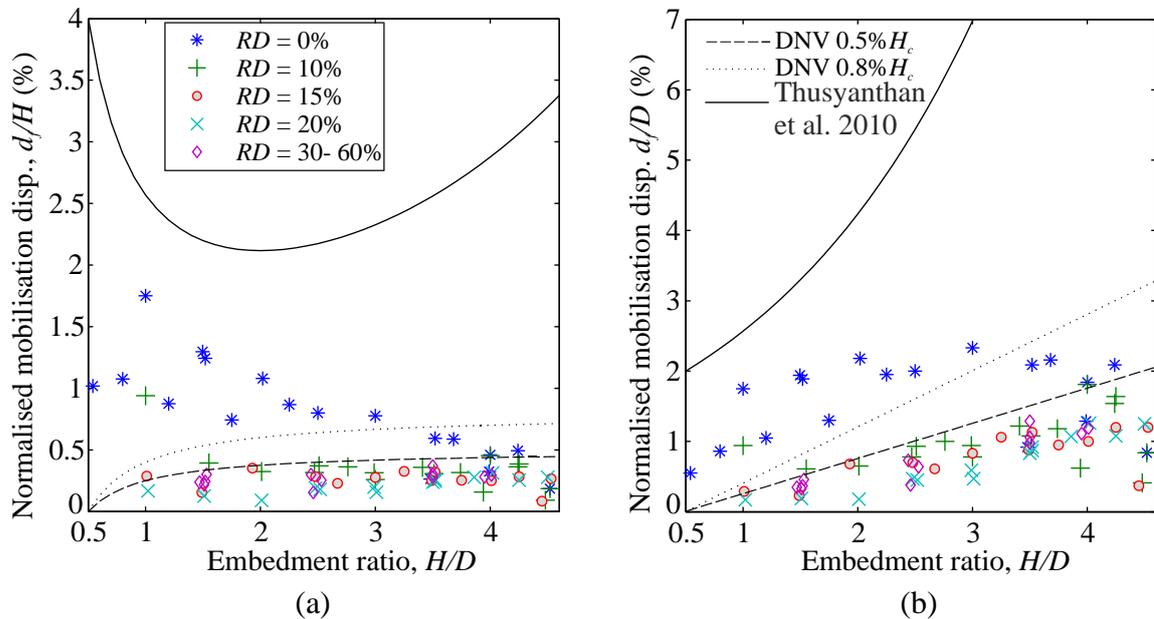

Figure 3-12 Mobilisation displacement for various relative densities, normalised by: (a) H; (b) D.

The DNV guidelines suggest mobilisation displacements for modelling purposes in the range of 0.5%H_c to 0.8%H_c, where H_c is measured to the pipe crown. This was challenged in a recent study by Thusyanthan et al. (2010), where it is suggested that this parameter could be related to H/D through an exponential relationship, as given in equation 2.9 previously. Both models are compared with the experimental data in Figure 3-12, where it is shown that while the DNV limits are appropriate for larger embedment ratios, they under-predict mobilisation displacements for loose sand at shallow embedment ratios. The model proposed by Thusyanthan et al. (2010) predicts higher mobilisation displacements than observed in these experiments, particularly at greater values of H/D.

3.2.1.4. Initial stiffness

The stiffness of the initial response can be examined using displacement measurements obtained from the high resolution LVDT, presented in Figure 3-13. By comparing this figure to the force-displacement curves in Figure 3-7, it can be seen that there is a significant reduction in noise with the high-resolution displacement measurements, compared to the longer range measurements. Figure 3-13 part (a) shows the influence of embedment ratio on tests at *RD* = 0%, while (b) plots tests at *H/D* = 3.5 with varying relative densities. The location marking 50% of the peak resistance is shown on each curve for comparison, as the shape of the curve was judged to be linear up to this level of force. In addition, the estimated locations of visible changes in slope in the curve are plotted in (a). The purpose of locating these point is to investigate how best the initial stiffness can be approximated across different densities and embedments; choosing the best position for the slope change may help in defining the tri-linear force-displacement relationship.

It can be seen in Figure 3-13 (a) that the initial response seems to scale with *H* in both the *x* and *y* directions, but otherwise the shape of the curves is similar. The displacement values corresponding to the changes in slope increase almost linearly, with the two locations indicated corresponding to approximately 0.022 and 0.04%*H*. In part (b) the force values increase with relative density but the displacements at which the slope changes appear to be consistent. The two values of 0.022 and 0.04% *H* are marked for this embedment, and provide a good representation of the observed shape. This suggests that initial displacements are strongly related to the embedment, *H*, but are less affected by relative density.
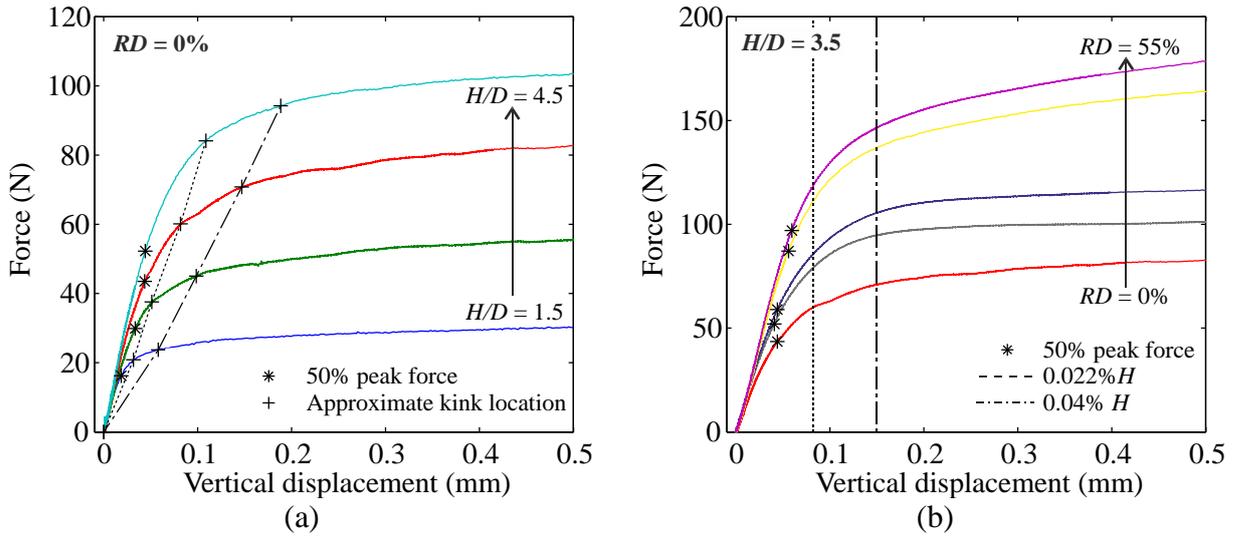
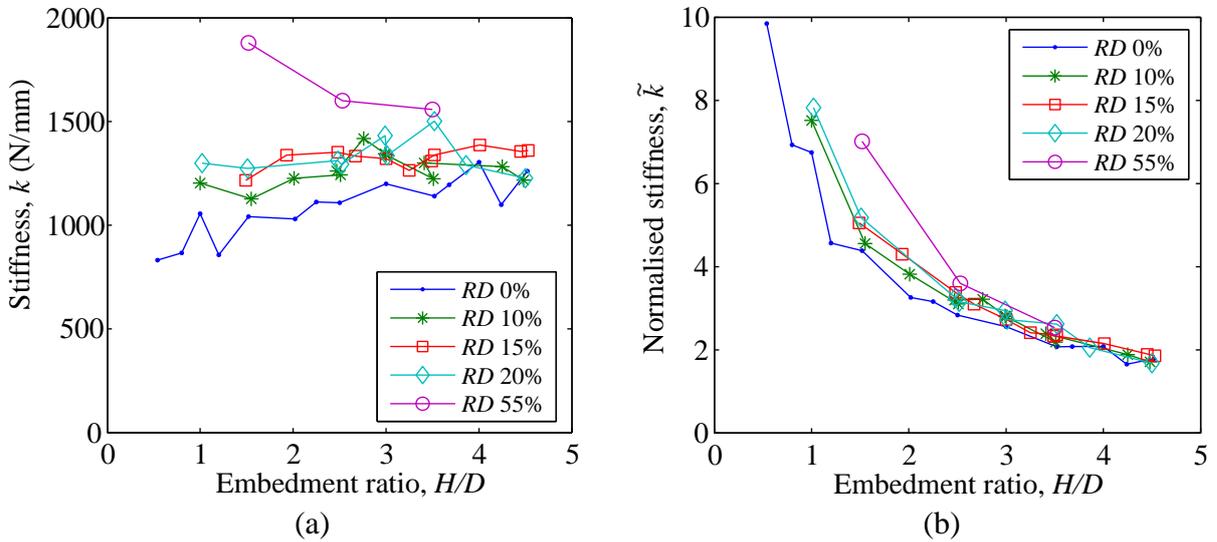*Figure 3-13 Small-displacement response: (a) RD = 0%, varying H/D; (b) H/D = 3.5, varying RD*

Figure 3-14 Initial stiffness to 50% peak vs. H/D: (a) without normalisation; (b) normalised by γ'HL

Figure 3-14 plots the initial stiffness values (best linear fit) to 50% of the peak force against *H/D*, for tests of varying relative densities. In Figure 3-14 (a) the relative density is shown to have a greater effect on the stiffness at low embedments. In loose conditions there is little change in this stiffness value as *H/D* increases, whereas in dense conditions the initial stiffness decreases with embedment. In Figure 3-14 (b) the same stiffness values are normalised using dimensionless parameters for force and displacement as follows:

$$\tilde{k} = \frac{F/(\gamma'HDL)}{d/D} = \frac{k}{\gamma'HL} \tag{3.10}$$

65

The normalised data now shows a distinct decreasing trend in all the tests with respect to *H/D*. While at low embedments there is still a difference due to density, at higher *H/D* ratios the stiffness values tend to converge for all densities.

In order to better define a tri-linear uplift response, it may be useful to identify trends in the peak force for a prescribed displacement (for example at a slope change location), rather than calculating the stiffness for a prescribed force level, as above. This is explored in section 3.3, where further data from dry sand tests is introduced, allowing additional comparison.

3.2.2. Partially drained response

The second series of saturated tests, summarised in Table 3-3, explored the effect of varying rates of uplift on the soil response at different relative densities, in order to examine the influence of the initial soil state under partially drained conditions.

Table 3-3 Summary of partially drained tests

Set	Embedment ratio, H/D	Relative density, RD (%)	Uplift rate, v (mm/s)	Number of tests
PD 1	3.5	0	0.01 to 5	8
PD 2	3.5	0 to 35	0.1	2
PD 3	1.5 to 4.5	0 to 55	1, 5	44
Total partially drained tests				54

3.2.2.1. Rate effects

Figure 3-15 presents the force-displacement curves and corresponding pore pressure response for tests conducted at an embedment ratio of 3.5, with a soil relative density of 0% (note that the pore pressures shown are an average of the readings from the 5 PPTs). It was observed that faster rates of uplift resulted in higher excess pore pressures around the pipe. At its loosest state the soil is contractive, so that positive excess pore pressures develop, leading to a decrease in resistance on shearing. It can be seen in Figure 3-15 (b) that the excess pore pressure rises rapidly on initial displacement of the pipe, followed by reduction as drainage occurs. It appears that no additional pressures develop at the larger displacements, as the soil

is shearing at constant volume. The observations from these tests are consistent with the conclusion by Schupp (2009) that the time required for dissipation of excess pore pressures in the loose sand is independent of the rate of uplift. Therefore, as the rate of uplift increases, the pipe displaces further in the time taken for the pressure to equalise (meaning that larger displacements occur before the resistance increases back to its drained residual value). At 5 mm/s, the uplift rate is rapid enough for the initial excess pore pressure to approach the vertical effective stress of the soil, reducing the resistance temporarily to zero. The rate is also such that the excess pressure does not have sufficient time to dissipate over the course of the test and consequently, the drained resistance is never achieved.

Tests with uplift rates greater than 0.1 mm/s are compared in Figure 3-15 with the model proposed by Schupp (2009) and Byrne et al. (2013). The plots demonstrate that the model can successfully capture the pore pressure response in fast rate tests, when the soil is at its loosest state, and for embedment depths for which the VSM is appropriate.

The small-strain response for the same tests is shown in Figure 3-16. All tests exhibit a similar initial pre-peak force over the first 0.1 mm, even as the positive excess pore pressures gradually increase. However, once the self-weight of the soil block is mobilised, the excess pore pressures increase rapidly and the uplift resistance drops to zero in the faster rate tests ($v \geq 0.1$ mm/s). After further displacement – and depending on the rate of uplift – the excess pore pressure dissipates and the force returns to the fully drained value. An important observation from Figure 3-16 is that the transition from negligible excess pore pressures to full liquefaction appears to occur very suddenly, over a narrow range of uplift velocities (between approximately 0.02 and 0.06 mm/s). This is in contrast to the observation by Bransby and Ireland (2009) that the uplift resistance and normalised test velocity (vD/c_v) in dilatant soil can be related using a backbone curve, with the transition between drained and undrained conditions occurring over a larger range of velocity (log cycles). The findings suggest that for the highly contractile and collapsible conditions tested here, any pore water

response will cause full liquefaction and a complete (but temporary) loss of resistance. The ultimate resistance that is subsequently regained depends on the rate of uplift compared to the rate of pore pressure dissipation. Note that in the test at $v = 0.1$ mm/s, the resistance recovers almost to its fully drained value.

3.2.2.2. *Density effects*

To explore the effect of relative density on the uplift resistance, a series of tests with an uplift rate of 1 mm/s was carried out. This was chosen as a representative rate at which a partially drained response occurred. The force-displacement results are shown for a range of relative densities in Figure 3-17 and Figure 3-18. In these tests, a gradual transition from a contractive to dilative soil response was identified, as evidenced by the excess pore pressure response. For backfill soil with a relative density ranging from 0% to 15%, positive excess pore pressures develop, though the magnitude and effect of these decrease as the density is increased. This is also evident in the recorded force curves. At 21% relative density, the pipe experiences positive excess pore pressures indicating contraction, but this is immediately followed by negative excess pore pressures indicating dilation. In this instance, the force reaches a higher resistance than the drained peak value at the same density. Finally, at a relative density of 35%, there is an immediate large negative pore pressure – indicating a dilating soil response – and a single peak resistance much larger than the drained value for this density.

The small strain response can again be examined in Figure 3-18. Here it is shown that the initial pre-peak resistance increases with relative density, and occurs at increasing displacements. This directly corresponds to the slower rate and magnitude of positive excess pore pressure development with increasing density. Not surprisingly the test at 35%, which experiences only negative excess pore pressures, exhibits no pre-peak in the resistance and instead increases monotonically.
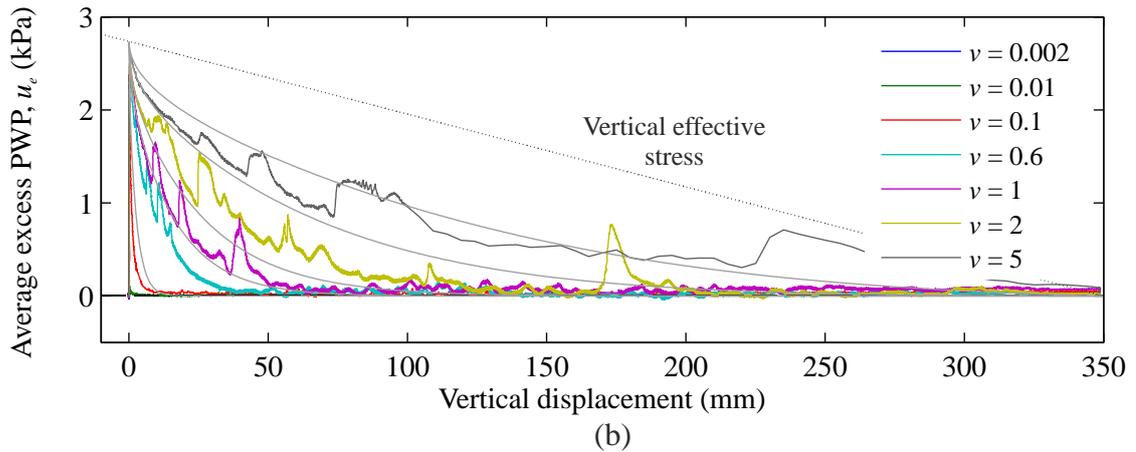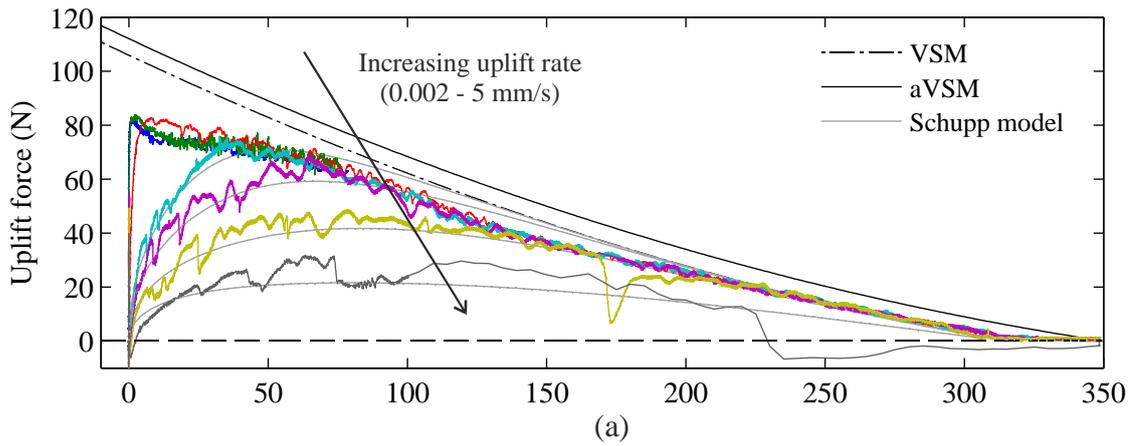
68

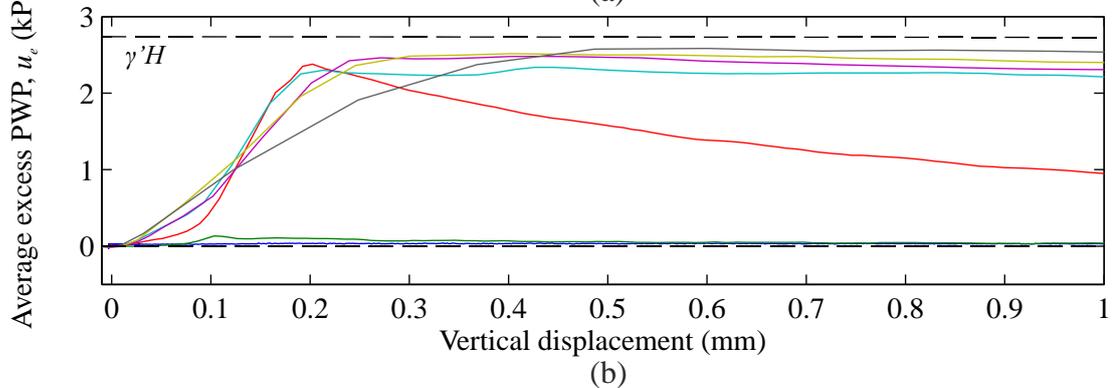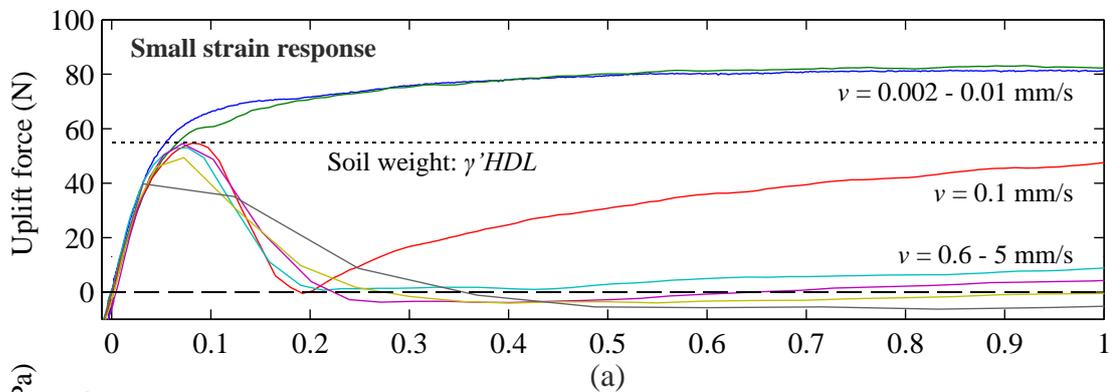*Figure 3-15 Rate effects at RD = 0%: (a) force response; (b) pore pressure response*

Figure 3-16 Small strain response - rate effects at RD = 0%: (a) force response; (b) pore pressure response
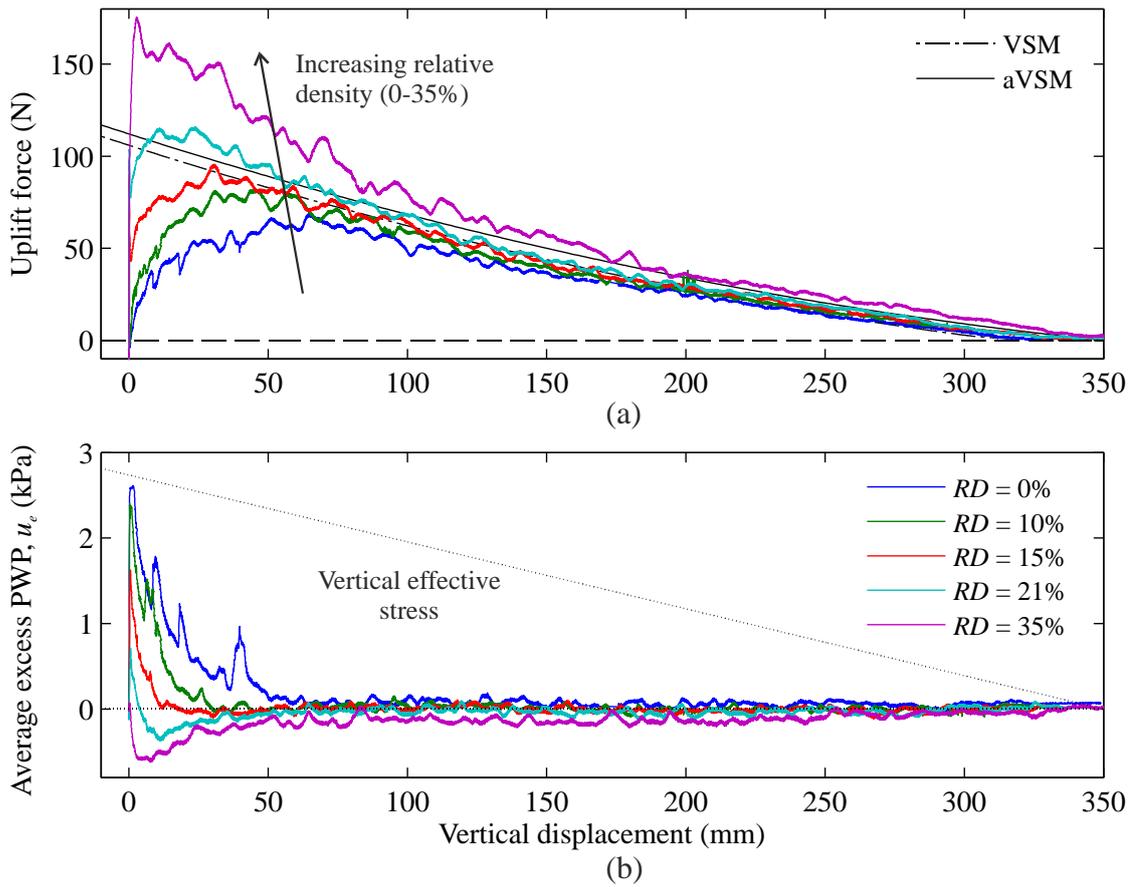
Figure 3-17 Density effects on fast-rate tests: (a) force response; (b) pore pressure response
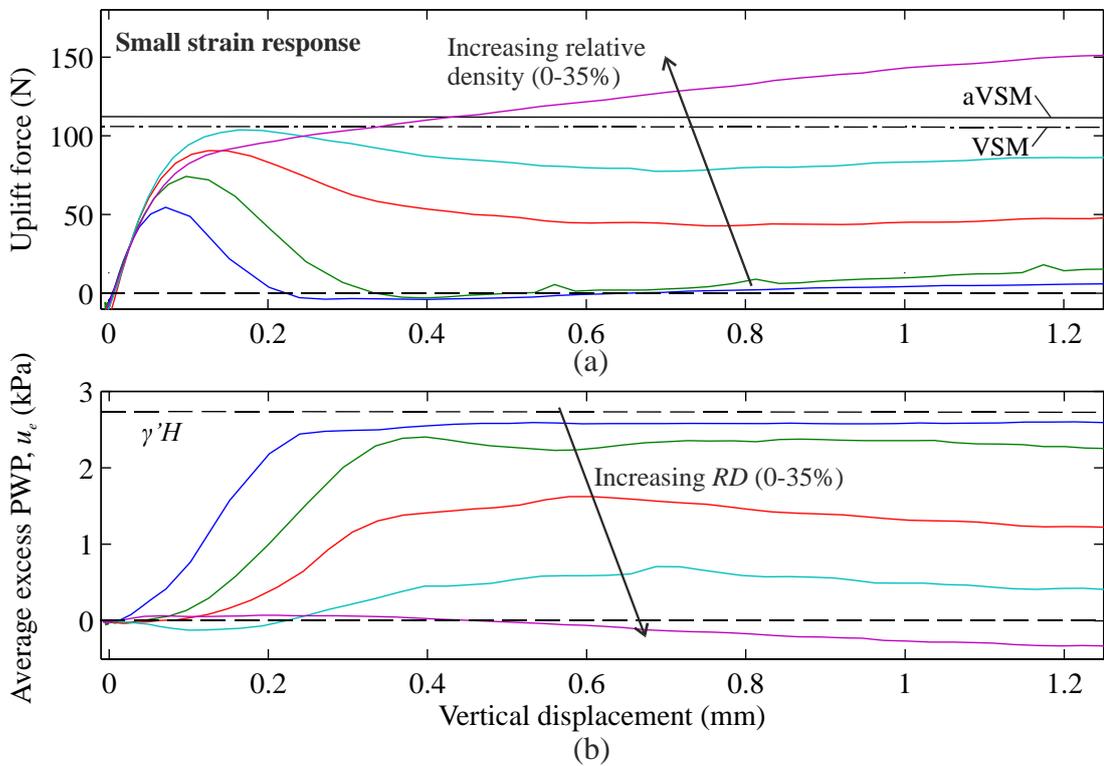

Figure 3-18 Small strain response - density effects on fast-rate tests: (a) force response; (b) pore pressure response

3.2.3. Comparison between drained and partially drained: transition densities

Figure 3-19 shows a comparison between drained and partially drained tests at an uplift rate of 1 mm/s for relative densities of 0% and 30%, respectively. For both relative densities, the influence of the measured excess pore pressures on the uplift resistance is examined, based on the fast-rate uplift model by Schupp (2009) and Byrne et al. (2013). The model assumes that in partially drained contractive tests, the vertical effective stress at the pipe centre is reduced by the positive excess pore pressures measured around the pipe, directly reducing the uplift resistance. The non-dimensional breakout factor, N_{ult}, is considered to remain constant (for a given relative density and embedment); therefore:

$$\frac{F}{\sigma_v'DL} = \frac{F_{drained}}{\gamma'HDL} = \frac{F_{PD}}{(\gamma'H - u_e)DL} = N_{ult} \tag{3.11}$$

Rearranging the above equation yields the expression:

$$F_{PD} = N_{ult}(\gamma'H - u_e)DL = N_{ult}\left(1 - \frac{u_e}{\gamma'H}\right)\gamma'HDL = F_{drained}\left(1 - \frac{u_e}{\gamma'H}\right) \tag{3.12}$$

where the partially drained resistance can be predicted from the drained resistance and the measured or expected excess pore water pressure around the pipe in a fast test. For both relative densities, predictions for the partially drained resistance and equivalent pore water force (second term in equation 3.12) are plotted in Figure 3-19, for comparison with the measured data.

At a relative density of 0%, it can be seen that the difference between the drained and partially drained response appears to be almost entirely due to the average excess pore water pressure around the pipe (since the measured partially drained resistance is well matched by the prediction). This suggests that contraction of soil occurring predominantly around the pipe is the main cause of the decreasing uplift resistance. At a relative density of 30%, the peak resistance in the partially drained test is matched by the prediction; however, on further displacement of the pipe, the measured force is greater than what is predicted based on the measured excess pore pressures. This indicates that the model assumptions are no longer

valid. It appears that in addition to dilation immediately around the pipe, soil must be attempting to dilate elsewhere in the soil mass (particularly on the shear planes), to increase the overall soil resistance. It is expected that this additional dilation effect would increase as the relative density and/or embedment ratio further increased.
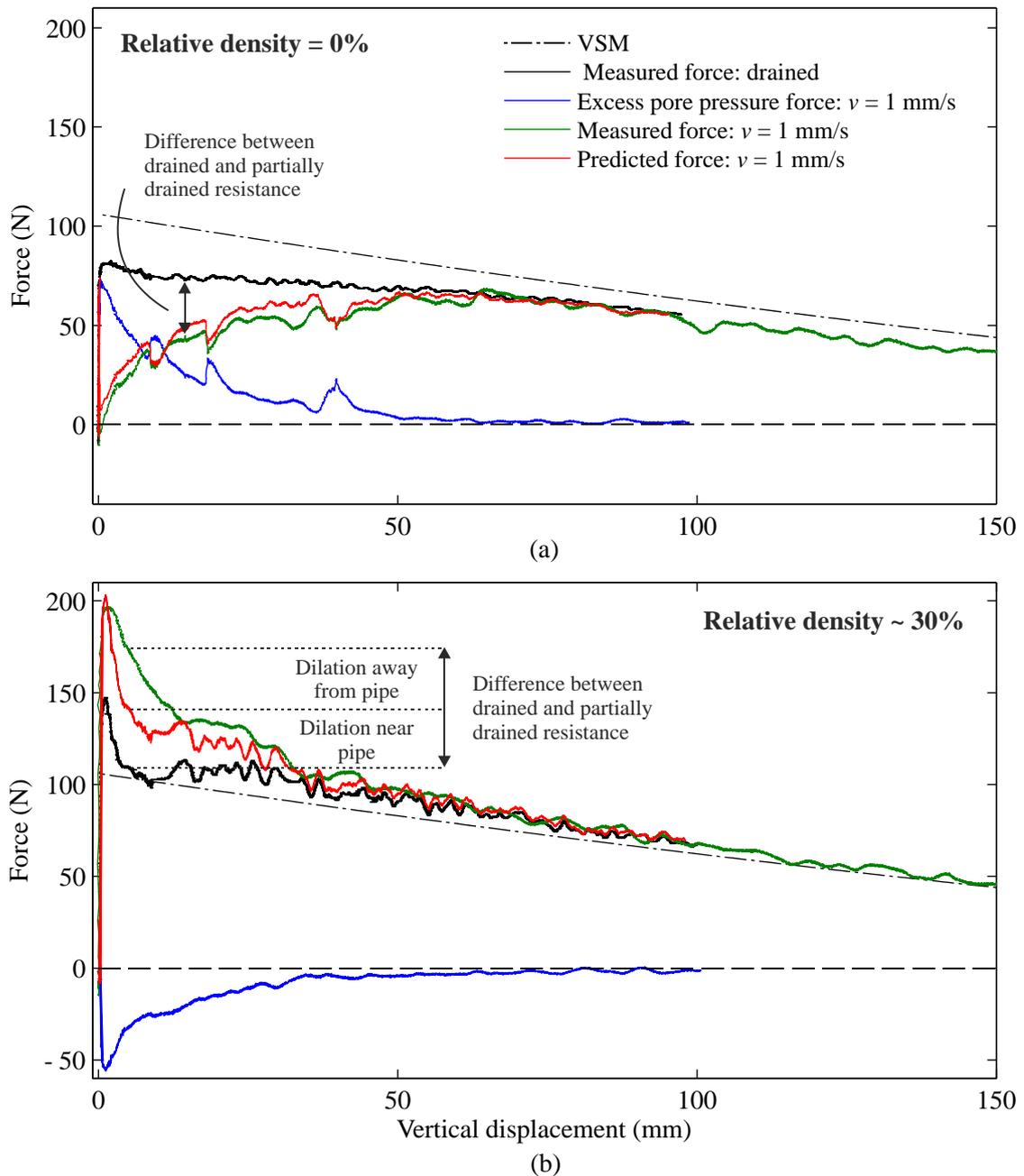

Figure 3-19 Comparison of drained and partially drained response for a fast-rate test: (a) relative density 0%; (b) relative density ~30%

Trends for peak uplift resistance due to variations in uplift rate and relative density for a given embedment ratio ($H/D = 3.5$) are summarised in Figure 3-20. For the faster rate

contractive tests, the peak values are measured after the initial drop in resistance (as shown in Figure 3-16). It should therefore be noted in Figure 3-20 (b) that for $RD = 0\%$, initial drops in resistance due to positive pore pressure development may occur at slower velocities than indicated in the plot. The relationship between peak resistance and uplift speed for $RD = 30\%$ appears to match well with the trend observed by Bransby and Ireland (2009). From both plots, estimates can be made regarding the transition density between net contractive and dilative behaviour, based on differences observed between the drained and partially drained responses during uplift. Note that the drained resistance is identified by the curve corresponding to tests at a rate of 0.002 mm/s. At this depth the transition range appears to occur at a relative density between approximately 17 to 21%, above and below which, net dilation and contraction occur respectively. It should also be noted that in drained tests at an embedment ratio of 3.5, $RD = 20\%$ is sufficient for the data to match the aVSM – a value consistent with the transition range identified above.

Figure 3-21 shows a plot of the 'transition densities' determined using fast rate tests for several embedment ratios (as described above), along with the required relative densities to reach the VSM and aVSM in drained tests. It can be seen that at embedment ratios greater than 2, the transition density between contraction and dilation falls within the range of relative densities required for the peak resistance to reach the vertical slip model predictions. Furthermore, values of H/D at which the breakout factors level off in the saturated tests are plotted in the figure and appear to be consistent with this trend.
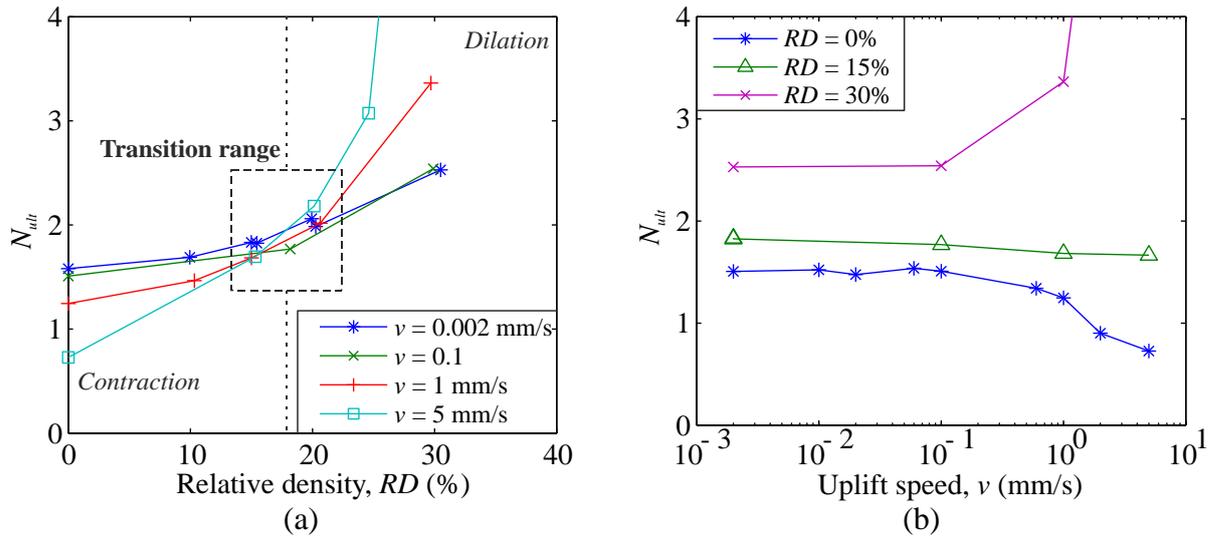
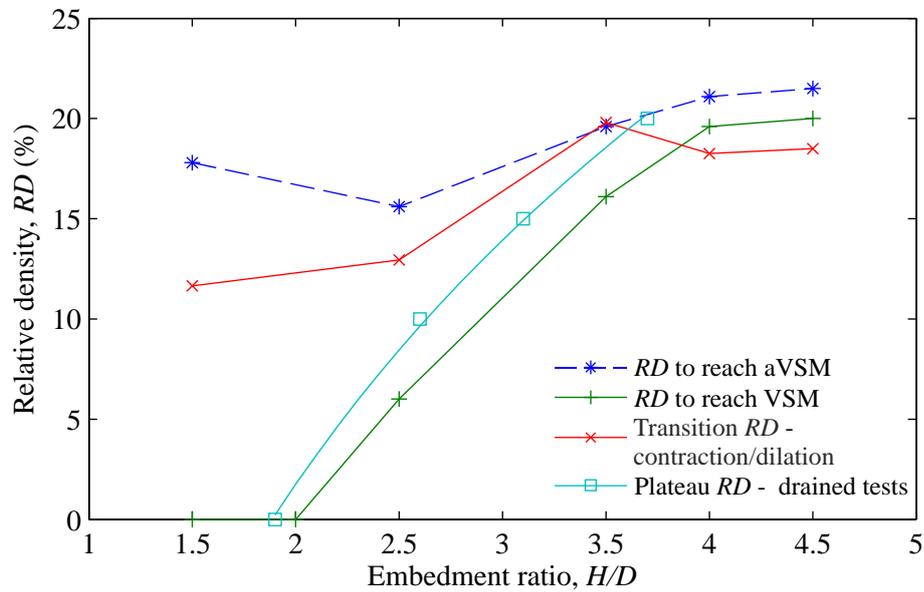*Figure 3-20 Summary of breakout factors with respect to: (a) relative density; (b) uplift speed (H/D = 3.5)*

Figure 3-21 Comparison of transition densities

3.2.4.   Summary: rate and density effects

The test results demonstrate that the volumetric behaviour of the backfill soil, which is dependent on its initial state, strongly influences both its drained and partially drained uplift resistance. In the drained tests, a plateau in the peak breakout factors observed in very loose soil indicates a possible transition from a sliding block failure mechanism (which is well captured by the vertical slip model) to another mechanism, possibly a flow-around failure mechanism, where shear planes do not extend to the surface. The mobilised mechanism

appears to be dependent on both relative density and embedment ratio – for example, looser backfills experiences a transition at shallower embedment ratios – which suggests that this behaviour may be determined by a combination of the soil properties (namely the critical state friction angle and state parameter) and the burial depth.

Tests conducted at fast rates, inducing partially drained conditions, allowed for relative quantification of dilation (and contraction) through measurement of the pore pressure response around the pipe and its contribution to the overall uplift force. Soil that contracts during shear sees the development of positive excess pore pressures and a subsequent reduction in peak force, while dilation results in the opposite effect. The existence of a localised flow-around mechanism is supported by evidence that at very low relative densities, contraction appears to occur primarily around the pipe, while at higher densities dilation away from the pipe contributes to the resistance increase. Accordingly, the density (for a given embedment ratio) at which the transition from net contraction to dilation occurs was determined based on total resistance, rather than pore pressure measurements. This relationship between the volumetric transition density and embedment depth was found to be consistent with the assumed transition density between failure mechanisms occurring in the drained tests (as shown in Figure 3-21).

3.3. Dry sand tests

From the work described so far in this chapter, it is clear that a flow-around mechanism may govern at peak resistance for saturated fine sand under certain conditions. The apparent influence of the volumetric behaviour of the soil on this mechanism suggests that state parameter of the backfill may be important. Though in general, the UHB problem occurs in low effective stress conditions, it is important to consider the influence of stress level and scaling on the problem. At full scale, small diameter pipelines may be twice the diameter of the pipe section used in these experiments; therefore, for a given H/D ratio the depth of cover and consequent vertical effective stress would be twice that in the experiments described so

far. Given the laboratory constraints, the best way examine this effect is to carry out the same tests as above, but using dry sand (since the dry unit weight is approximately twice the buoyant unit weight). An additional benefit of testing in dry sand is that, since the installation procedure does not require fluidisation of the sample, different coarser grained sands can also be used for comparison.

To address the above issues, a test programme was carried out investigating the uplift response of three different sands in dry conditions. The tested sands include Redhill 110 (RH110), for comparison with the saturated tests, as well as two coarser Leighton Buzzard sands, LB DA30 and LB14-25. The aim of this work is to supplement the findings from the saturated sand tests by enabling generalised trends to be established across different sands and stress levels.

3.3.1.   Test programme

In each test the sand was placed in layers by hand using a scoop and a very low drop height. The focus of these tests was on loose or very loose soil conditions, but for a few tests using LB DA30, the drop height during sand placement was increased to achieve a higher density backfill. Average values for the relative density and dry unit weight used in each test category were calculated using measurements of the weight and volume of soil placed. A summary of the tests is provided in Table 3-4.

Table 3-4 Dry sand tests

Set	Sand	Density category	RD (%)	γ_{ave} (kN/m^3)	H/D	Number of tests
	LB DA30	Very loose	< 10	14.8	1-7	9
Dry 1	LB DA30	Loose	15-20	14.9	2-7	4
	LB DA30	Medium-dense	40-55	15.2-15.4	3-6	4
Dry 2	LB 14-25	Very loose	< 5	14.7	3-7	8
Dry 3	RH110	Loose	20-25	13.3	1-6.5	8
Total dry tests						33

3.3.2. Dry sand test results

Similar to the framework established with the saturated test results, dry sand results are presented first as raw force-displacement curves, and then assessed in terms of peak breakout resistance, mobilisation displacements, and initial stiffness. Example figures for LB DA30 are provided for each category, followed by summary figures comparing the data from all three sets of dry tests to the saturated results.

3.3.2.1. Force-displacement response

The force-displacement curves for very loose LB DA30 are shown in Figure 3-22. In (a), the data is plotted against embedment ratio and compared to the adapted VSM prediction. The raw data shows high fluctuation in the force reading at deep embedments, the magnitude of which reduces as the pipe approaches the surface. This is similar to observations by Cheuk et al. (2008) for the post-peak response of denser tests, where these fluctuations were linked to miniature slope failures around the pipe associated with infilling. Also plotted in the figure are 'smoothed' force-displacement curves, obtained through further time-averaging of the data (in addition to the sample compression during data logging). These provide a better representation of the average peak force, showing that it diverges away from the aVSM prediction at deeper embedments. In Figure 3-22 (b), the first 30 mm of displacement in each test are compared. The figure shows that, in a given test, as the magnitude of the force fluctuation increases, the average force actually levels off. Thus, the initial response is approximately tri-linear, which is in line with the DNV recommendations. The first 'slope change' in the curve appears at very small initial displacements for all tests, but the force at which this occurs (as a percentage of the peak force) increases as *H/D* decreases.

When the force-displacement curves in Figure 3-22 (a) for LB DA30 are compared with dry RH110 results, shown in Figure 3-23, it appears that there is even greater divergence from the predicted values in the latter tests. At embedment ratios greater than 3, the tests show very large displacements at an approximately constant force, before the residual force begins to

decrease with depth and approach the aVSM prediction. Additionally, in deeper tests the displacement prior to peak appears to be quite large.
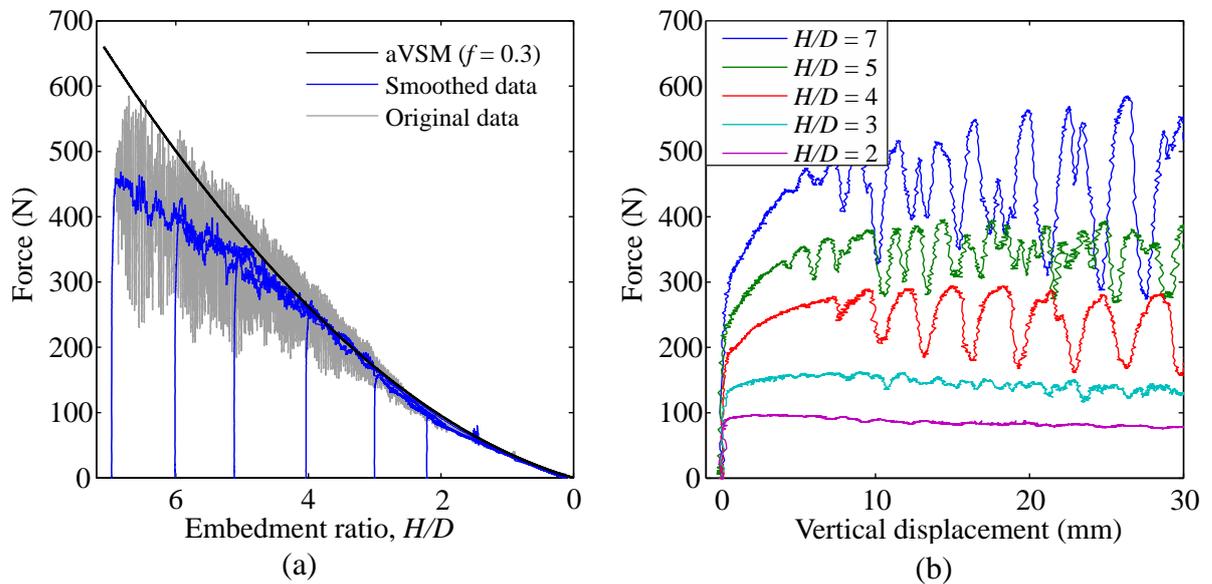

Figure 3-22 Force-displacement curves for very loose LB DA30: (a) staggered; (b) first 30 mm of displacement
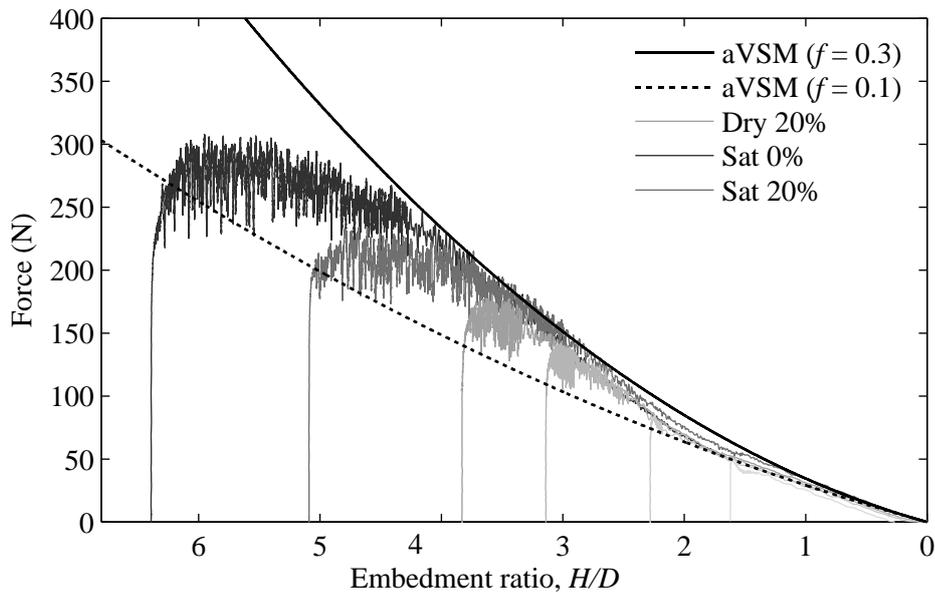

Figure 3-23 Force-displacement curves for loose dry RH110

3.3.2.2. Peak forces

In Figure 3-24, breakout factors are plotted against embedment ratio for LB DA30 tests in various density categories. Due to the highly fluctuating force readings at greater embedments, it was necessary use the smoothed data to obtain a representative peak force

value; the 'ultimate' value corresponding to the highest value of the fluctuating force would likely be unconservative. Both the smoothed peak (square markers) and the ultimate peak are shown in Figure 3-24. From this it is evident that as the embedment depth increases, the difference between the two values also increases (since the magnitude of fluctuation increases). The figure also shows that at *H/D* = 4.5, the breakout factors for very loose sand begin to level off. Similar to the saturated tests, this suggests that the mechanism may be transitioning from a sliding block at low embedments to a flow mechanism at higher embedments. The effect of increasing the relative density also increases with *H/D*.

Breakout factors for all loose dry tests (using smoothed force data when required) are presented in Figure 3-25, along with saturated tests at *RD* = 0% and 20%. All sets of tests show evidence of a transition to a possible flow-mechanism at higher embedments. While the responses for LB DA30 and LB 14-25 appear to be similar, interestingly, the breakout factors in the dry loose RH tests level off sooner (lower *H/D*) and at much lower values. This response is very close to the saturated sand tests at *RD* = 0%, rather than the tests at a similar density of 20% − an issue which is discussed in section 3.3.3.
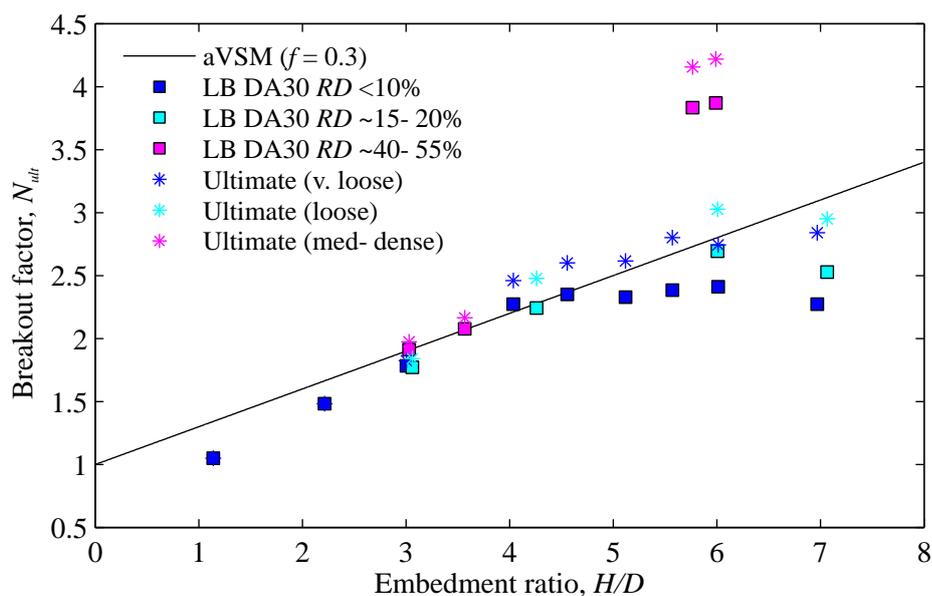

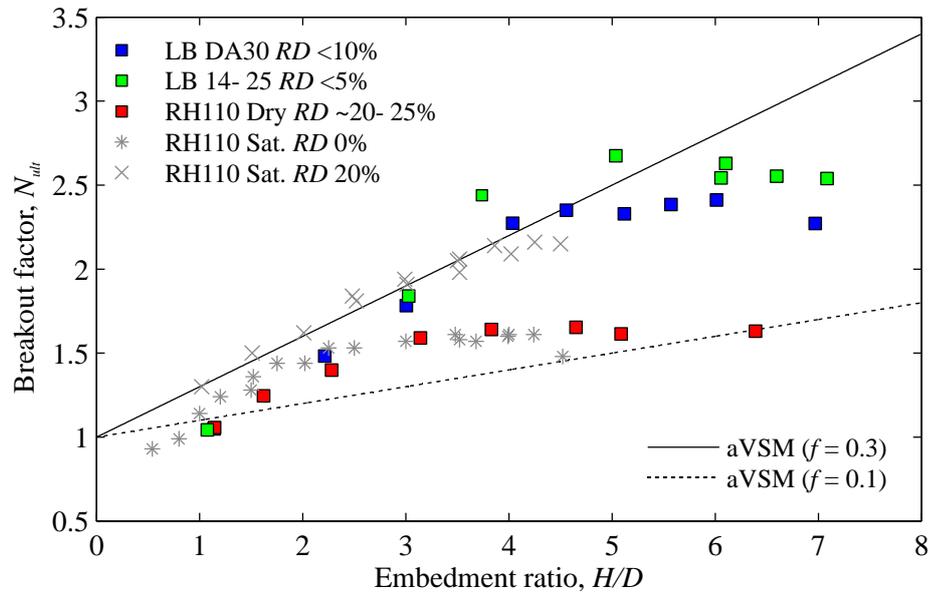*Figure 3-24 Breakout factors vs. embedment depth for dry LB DA30*

79

Figure 3-25 Breakout factors vs. embedment depth for dry and saturated tests

In the saturated tests presented previously, it was found that the depth at which the primary mechanism may begin to transition to a flow-around mechanism (H/D_{trans}) is influenced by the relative density of the backfill. The value of H/D_{trans} was seen to increase with increasing relative density. The above figures show that the type of sand also affects the transition depth (for the moment stress level effects will be ignored, as the dry unit weight for the three sands is similar). All three sands have different critical state friction angles, and if this were a factor, the experimental results show H/D_{trans} increasing with decreasing critical state friction angle. This contradicts the conclusions with respect to relative density, since an increase in density will increase the mobilised friction angle. Thus, the critical state friction angle (alone) is not considered a controlling factor in the transition between mechanisms. The difference in relative density between the three dry sands can also be ignored for the moment, since the lowest density tests (LB 14-25) have the highest H/D_{trans}.

The remaining influencing factor to be considered is the grain size. For this factor, PIV studies by Cheuk et al. (2008) may provide some explanation. In their paper, the authors find that post-peak infilling behaviour (in which the soil flows around the pipe to fill the void beneath) could be dependent on particle size. It was suggested that for tests in fine sand the

flow-around mechanism might occur at a smaller displacement compared to tests in coarse sand, due to the smaller width of the shear zones appearing in the finer sand. It was also observed that the post-peak mechanism for coarse sand was combined heave (of the soil block) and flow, while in fine loose sand there was little or no heave observed. If this post-peak infilling behaviour is considered to govern at peak resistance for the deep and loose conditions tested here, it might provide a satisfying explanation for the differences between the tested sands. Because a smaller displacement is required for infilling to begin, a flow mechanism may occur in fine sand for a given embedment ratio, while the sliding block mechanism still governs in coarse sand at the same depth. Though the critical state friction angle and the pipe diameter still likely affect the geometry of the problem (Wang et al., 2012), the ratio D/D_{50} may also be important.

To illustrate a possible grain size correlation, the transition H/D values obtained in the dry sand tests are plotted against the non-dimensional grain size parameter, D/D_{50}, in Figure 3-26 (note that grain size is decreasing from left to right). Although there are only three points, the figure suggests that H/D_{trans} decreases almost linearly with increasing D/D_{50} (or decreasing grain size). Saturated RH results are also included to show qualitatively the influence of density (though any stress level effects are ignored in the figure).
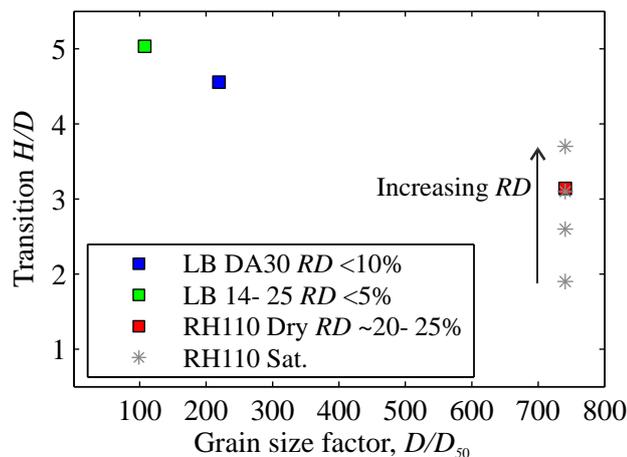

Figure 3-26 Transition H/D vs. grain size

A further consideration is that the width of the soil block above the pipe may reduce as infilling begins (Cheuk et al., 2008; Wang, 2012). If this mechanism is also assumed when comparing the peak resistance at different embedments in loose sand, it may be a change in the weight carried by the pipe, rather than in the mobilised friction, that contributes to the levelling-off of the breakout factors. This idea is explored in Figure 3-27, where the predicted frictional resistance (from the aVSM) is subtracted from the peak force to obtain an 'apparent' weight, which is then normalised by the calculated weight of a block of soil the width of the pipe ($\gamma'HDL$). The figure indicates that at low embedments, the apparent weight is reasonably close to the value of the expected weight (i.e. equal to a value of one) for all tests. At the point where the total force begins to level off, the normalised weight reduces almost linearly to zero. In fact, in the deepest test for dry RH110 this value falls below zero, implying that the friction also reduces at this point (possibly a complete flow mechanism). This interpretation is of course speculative, since normalising the 'apparent friction' in the same way (assuming a constant soil block) would also exhibit a similar peak. In all likelihood, the levelling-off of the peak force during transition to a flow mechanism is due to changes in both the weight and friction components.
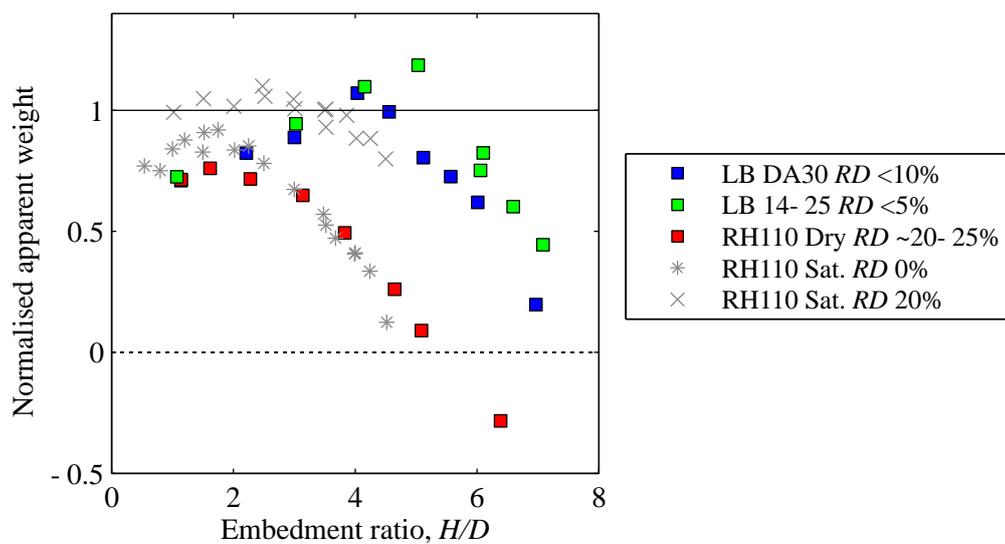

Figure 3-27 Apparent weight normalised by calculated weight (assuming fully mobilised peak friction), calculated as: $\frac{F-F_f}{W} = \frac{F-fH^2\gamma'L}{\gamma'HDL}$

3.3.2.3. *Mobilisation displacement*

If the force-displacement response is approximated as tri-linear, the required parameters are the peak force and mobilisation displacement, as well as the stiffness of the initial response (or the force and displacement values at the slope change). The mobilisation displacements recorded for LB DA30 are plotted in Figure 3-28 for both the smoothed (square markers) and raw data. The figure shows that that if a smoothed force response is assumed, the mobilisation displacement is smaller than if the highest point in the force fluctuation is used (unsmoothed). From the limited higher density data, there is no obvious influence of relative density, and nearly all the data points lie above the DNV recommendation of 0.8%H_c.
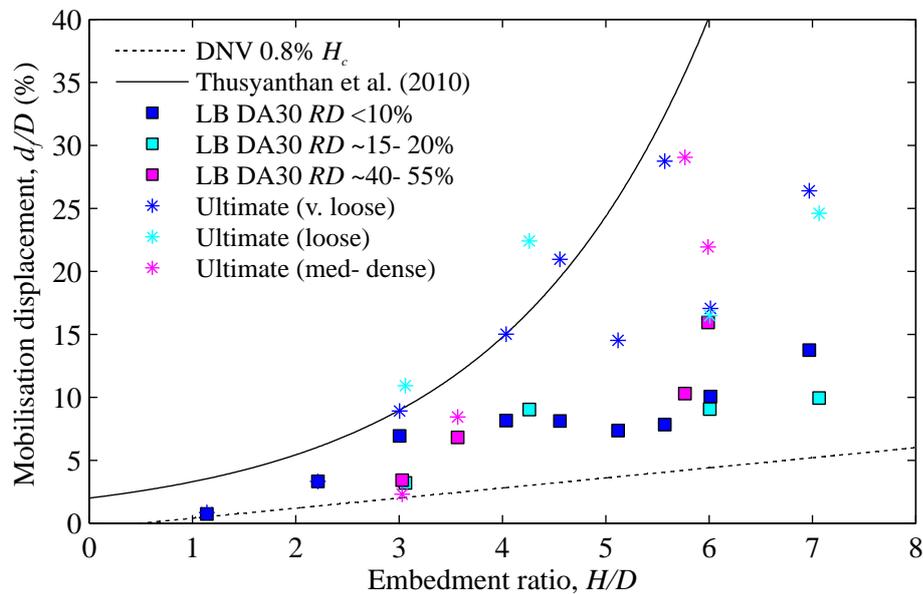

Figure 3-28 Mobilisation displacements for LBDA30

The normalised mobilisation displacements for all data are plotted against *H/D* in Figure 3-29 (a). In this figure the mobilisation displacements for dry RH110 are shown to increase greatly with embedment depth, such that the exponential prediction of Thusyanthan et al. (2010) − which was inappropriate for the saturated tests − now matches this data well. The saturated sand displacements do not appear to be consistent with the dry data when plotted against embedment. To address this inconsistency, the mobilisation data is plotted in Figure 3-29 (b) against a normalised effective stress level, referred to herein as the stress ratio. This is calculated, based on a normalisation used for displacements by Leblanc et al. (2010), as:

$$\tilde{\sigma}_v = \sqrt{\frac{p'}{p_r}} = \sqrt{\frac{\gamma' H}{p_r}} \qquad (3.13)$$

The above expression is based on the assumption that the shear modulus of the soil scales approximately with the square root of the stress level (Wroth and Houlsby, 1985; Cassidy et al., 2002) The parameter, p_r, is therefore simply a reference pressure, taken here to equal atmospheric pressure (~100 kPa).

The use of the above stress ratio in Figure 3-29 (b) shifts the saturated data so that the dimensionless displacements are now broadly consistent with those measured in dry conditions, within the range tested. At higher stress ratios, a large difference in the displacement values is observed between the dry RH110 and the two dry LB sands. While the values for RH110 appear to increase exponentially, d_f in the coarser sands increases at first, then appears to level off. This is again consistent with the inference that pipes in the finer RH sand predominantly experience a flow mechanism, while in the LB sand they experience a combination of heave and flow. In fact, the RH data (and possibly the exponential curve of Thusyanthan et al.) could tentatively be called the upper bound for displacements, representing flow-around only (with no heave), whereas the DNV recommendation is somewhat representative for a pure sliding block failure.
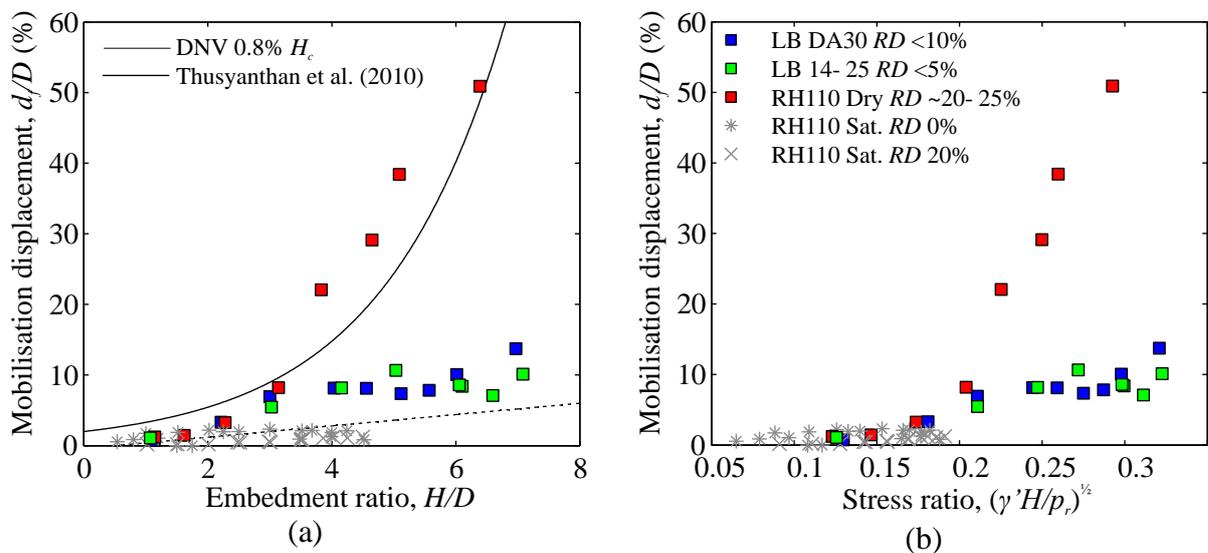

Figure 3-29 Mobilisation displacements for dry and saturated sand plotted against (a) embedment ratio; (b) stress ratio

3.3.2.4. Initial stiffness

As in the saturated tests, the stiffness was first examined at a fixed value of the force equal to 50% peak (equivalent to $\alpha = 0.5$ in the DNV guidelines), as this was below the observed slope change in most tests. Normalised values of the best-fit slope of the curves to this point are shown in Figure 3-30 (a). The plot demonstrates that the normalised stiffness is broadly consistent for all sands, in both dry and saturated test conditions, when plotted against stress ratio. The values all tend to decrease with increasing stress ratio (embedment). Figure 3-30 (b) plots the normalised displacements corresponding to 50% peak force. This shows a linear trend up to a stress ratio of 0.25, or around $H/D = 5$ in the dry sand. Beyond this stress level, however, the displacements increase rapidly, possibly because in these tests 50% of the peak force actually occurs after the slope change. It can be noted that in the linear region, the displacement appears to be related only to stress ratio.
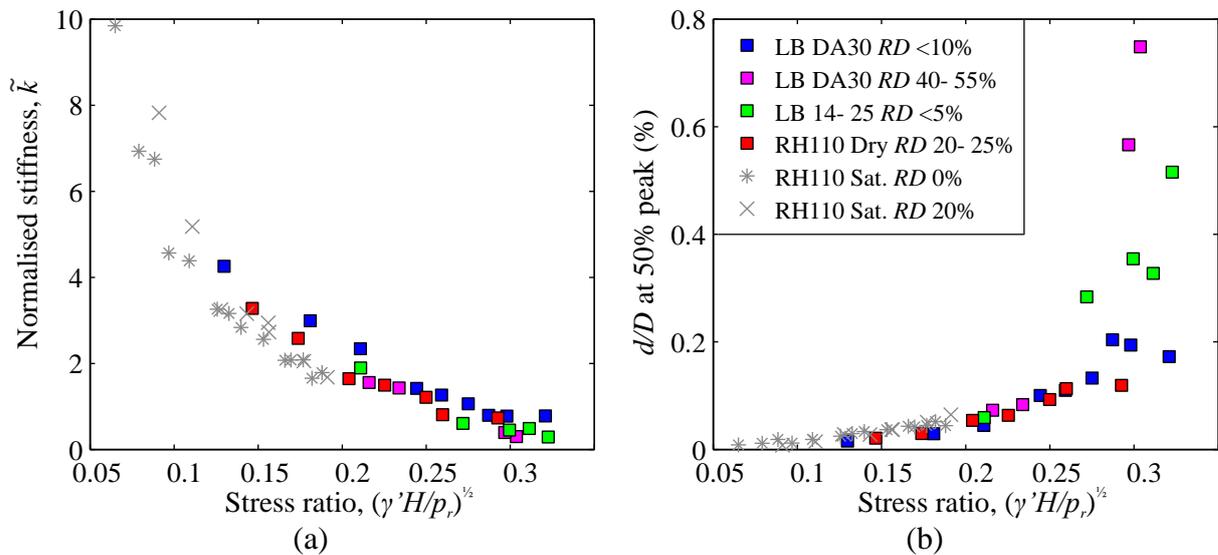
Figure 3-30 Initial response to 50% peak force – dry and saturated sand: (a) normalised stiffness (best fit) vs. stress ratio; (b) displacement at 50% peak force vs. stress ratio

Alternatively, in Figure 3-31 the force (as a percentage of the peak) is plotted, for a fixed displacement value, against the stress level. In the dry sand tests the slope change was found to occur at approximately 0.1%H – this is larger than the range (0.022 – 0.04%H) found in the saturated tests. If the displacements are instead related to stress ratio, the average slope

change displacement in the dry tests is $1.5\tilde{\sigma}_v$, while the range in the saturated tests becomes 0.4 to $4\tilde{\sigma}_v$. Since the change in slope is much more defined in the dry tests, it makes sense to assume a value close to $1.5\tilde{\sigma}_v$ for all tests. Accordingly, the values selected for comparison in Figure 3-31 are $0.5\tilde{\sigma}_v$ in (a), and $1.5\tilde{\sigma}_v$ in (b).

The figures show that there is a linear relationship between the force at prescribed displacement values and the stress ratio. At low stress levels, almost 100% of the peak force is mobilised, whereas at the highest *H/D*, in the dry tests, this reduces by around 50%. This trend is consistent with the shape of the force-displacement curves presented in section 3.3.2.1, and appears to be independent of grain size. In both figures, the data is contained within a vertical band the size of approximately 15-20% of the peak force. Increasing the prescribed displacement value from (a) to (b) causes an upward shift in the data, though the trend remains, for the most part, unchanged. One difference between the two figures is that in part (b), the very loose saturated RH sand levels off and then increases with stress level. Along with the fact that the denser tests are almost at 100% peak, this suggests that the lower value of $0.5\tilde{\sigma}_v$ may be a more appropriate approximation for the saturated tests.

In general, it appears that defining the location of the initial slope change in the curve at a prescribed displacement (related to the stress level) provides a good representation of the force-displacement response. It is useful to note that a prediction of the mobilisation displacement is therefore not needed to define the location of the slope change, although the force is still calculated as a percentage of the peak force. Thus, it is necessary to predict the governing failure mechanism and corresponding peak resistance, in order to define the initial stiffness correctly. In contrast to the DNV guidelines, the figures demonstrate that if prescribed displacement value is used (which depends on the stress ratio), it is not appropriate to assume a constant value for the force at that point. If the initial portion of the curve is assumed to mobilise the soil weight (predominantly), the observed trend is intuitive: as the

embedment increases, the shear resistance is expected to make up a greater portion of the total resistance with respect to the soil weight.
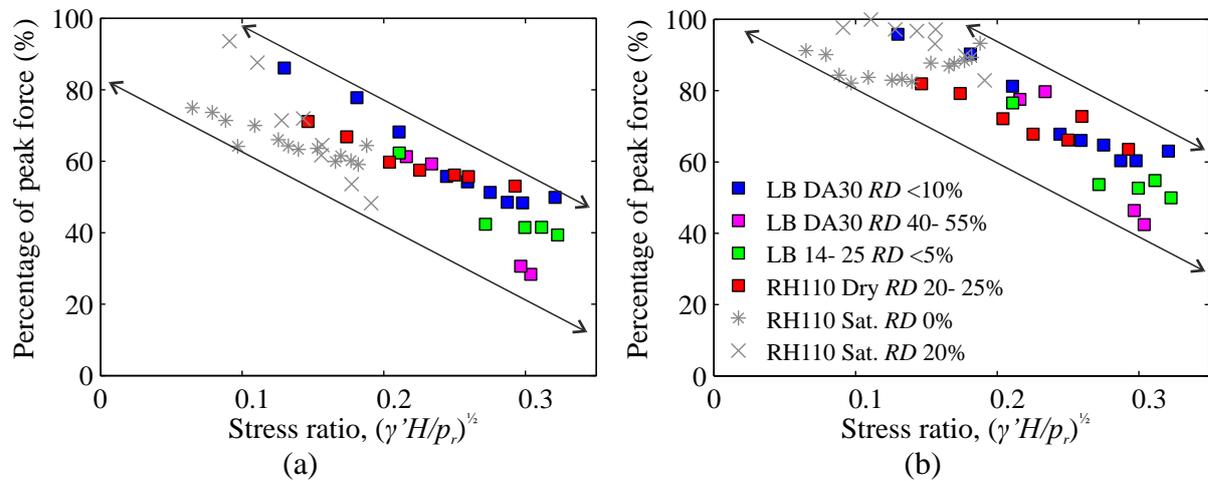

Figure 3-31 Initial stiffness: force at prescribed displacement value of: (a) $0.5 \cdot (\gamma'H/p_a)^{1/2}$; (b) $1.5 \cdot (\gamma'H/p_a)^{1/2}$

3.3.3. Comparison between dry and saturated tests

In the above analysis, some conclusions were drawn related to grain size effects at similar effective stress levels. One issue that remains is the observed difference between the dry and saturated RH110 tests, specifically in terms of the peak forces. While the above figures show that the displacements are generally consistent if plotted against stress level, it is not immediately clear why peak forces in the dry tests at $RD \sim 20\%$ are closer to saturated tests at 0%, rather than those at the same density. This discrepancy is examined further by comparing the dry and saturated force-displacement responses in Figure 3-32. In part (a), normalised forces are plotted (staggered by embedment) for the loose dry tests and saturated tests at 0% (blue curve) and 20% (red curve). Note that, as in Figure 3-8, the force readings are normalised by the soil effective unit weight and pipe diameter, to preserve the shape of the force-displacement curve through the uplift test. When presented in this manner it becomes clear that despite the initial difference, the residual force for 20% is the same in dry and saturated conditions, and lower for saturated sand at 0%, which is the expected trend. Figure 3-32 (b) shows that for example tests at $H/D = 4$, the saturated sand at 20% exhibits a higher

initial peak when compared to the dry test, but the force then converges to the same average value after approximately 5 mm of displacement. This difference could be attributed to two possibilities. First, the increased stress level in the dry sand may cause a more contractive response than in saturated conditions, reducing the chance of an initial distinct peak. Secondly, the vibro-densification used in the saturated tests may enable slightly more linking of the sand grains than in the dry case, meaning that the shear planes may briefly extend to the surface in these saturated tests, before a possible flow mechanism occurs.
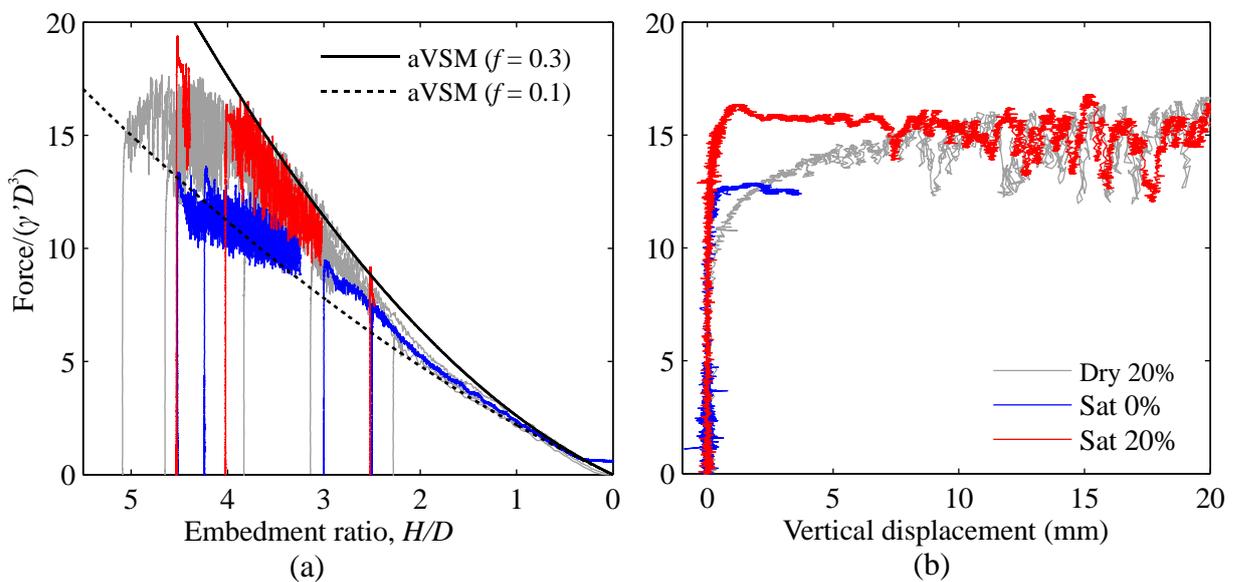
Figure 3-32 Force-displacement response – comparison between dry and saturated RH110: (a) staggered; (b) first 15 mm of displacement (H/D = 4)

3.4. Overburden tests

A small number of tests were carried out to investigate the influence of a surface overburden pressure on the mobilised uplift resistance in dry sand. The tests are intended to provide a guide as to how the uplift resistance can be modified through mitigating measures such as rock dump applied to the soil surface above the pipe. Additionally, the tests examine whether the increase in vertical effective stress provided by the surface overburden will cause more contractive behaviour of the soil and, as theorised above, promote a flow-around failure mechanism.

3.4.1. Test programme

The overburden tests were prepared using the same procedure as the previous dry sand tests. Dry Redhill 110 was placed in a loose condition ($RD \sim 25\%$) above the pipe to a target embedment depth. The depth of soil cover is referred to in this section as the actual embedment ratio, and is denoted by H/D, as before. To apply the overburden pressure (OB), weights were positioned evenly across a rigid wooden board, which was placed in direct contact with the soil surface in an attempt to ensure an even distribution of the pressure. A schematic of the test setup is provided in Figure 3-33. The total mass placed on the board was calculated by first determining a target equivalent embedment depth, $H/D*$ (i.e. the depth in a regular dry sand test that the OB test will attempt to replicate). The total required mass to increase the equivalent embedment from H/D to $H/D*$ for a pipe of a given diameter is then:

$$M_{OB} = \frac{(H^* - H)\gamma' A_{board}}{g}$$

(3.14)

where H^* is the equivalent depth to the pipe centre, M_{OB} is the total mass required in kg, and A_{board} is the area of the wooden board in m^2. For an average unit weight of 13.4 kN/m^3 and $A_{board} = 0.24$ mm^2, the mass required to achieve an effective increase in embedment of $H/D = 1$ was calculated as 32.6 kg.

In each test, once the overburden load was placed on the soil surface, the pipe was raised at a constant rate. However, since the overburden pressure was transferred to the soil via a rigid board, it was only possible to raise the pipe a small distance before heave of the board began to occur. At this point, the force on the pipe started to increase rather than decrease with reducing depth of cover. As this is no longer representative of the field conditions, the test was stopped. The overburden load was then removed, before upward displacement of the pipe was resumed.
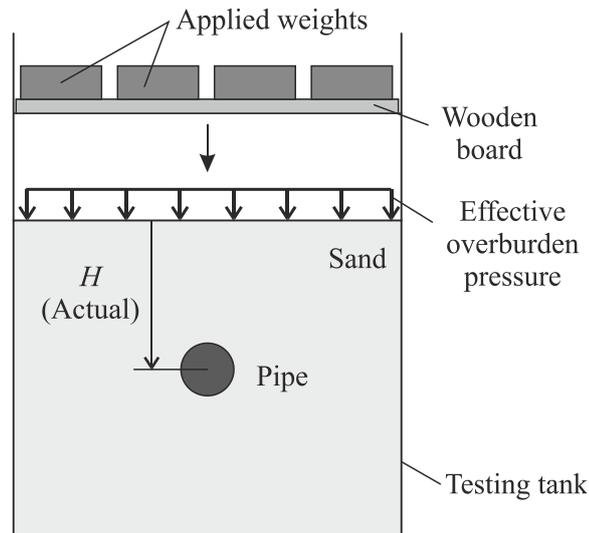
Figure 3-33 Schematic of overburden test setup

Details of the four tests conducted are listed in Table 3-5. Two tests each were run at actual embedments of 3 and 4.5. Three of the tests have equivalent embedments that can be compared to the Redhill 110 data from the previous section, while one has an equivalent embedment slightly deeper than what was possible using the current testing equipment.

Table 3-5 Overburden tests in dry RH110

ID	Sand	RD (%)	γ_{ave} (kN/m^3)	H/D Actual	H/D^* Equivalent
OB-1	RH110	~25	13.4	3	4.5
OB-2	RH110	~25	13.4	3	6
OB-3	RH110	~25	13.4	4.4	6.4
OB-4	RH110	~25	13.4	4.5	8
Total overburden tests = 4					

3.4.2.   Results

In Figure 3-34, force-displacement curves for each of the four OB tests are plotted starting from their actual embedment, *H/D*, and compared to normal loose dry RH 110 tests. The curves for each test consist of approximately 100 mm of displacement, followed by a vertical drop indicating the removal of the overburden, and then the remainder of the pullout. The figure shows that in all cases, the additional pressure results in an increase in uplift resistance.

Importantly, when extra load is removed, the response reverts to what is expected for a test with no OB at that embedment. This is even true for the deeper tests at $H/D \sim 4.5$; when the load is removed around $H/D = 3$, the fluctuation of the force is similar to the no OB response. Also included in the figure are three horizontal lines marking the peak (smoothed) forces for each equivalent embedment. This demonstrates that the peak force for a normal test at a given H/D can be consistently achieved by using an OB to reach the same equivalent H/D^*.
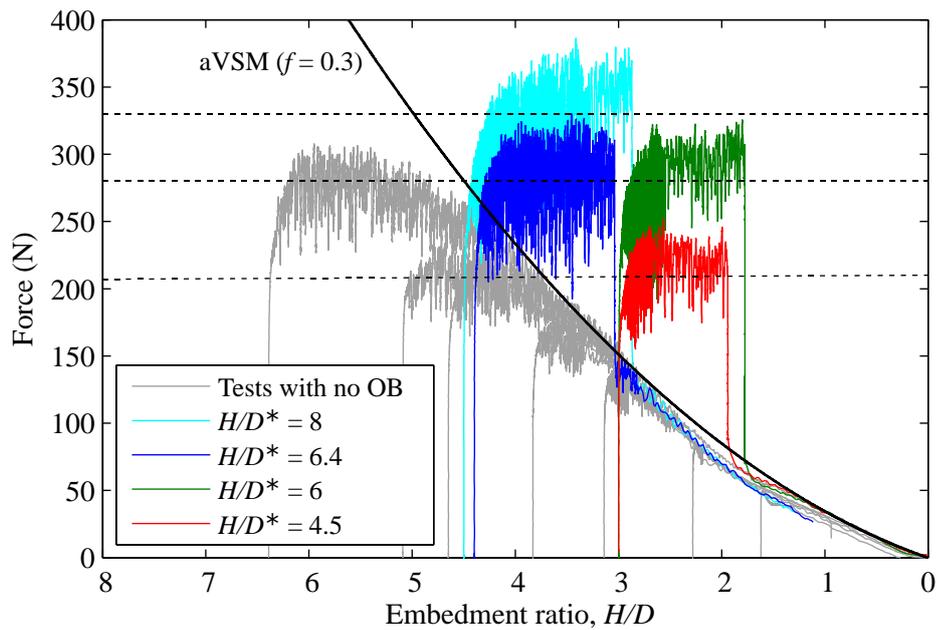

Figure 3-34 Force-disp. curves for OB tests shown at actual embedment vs. normal dry tests in RH110
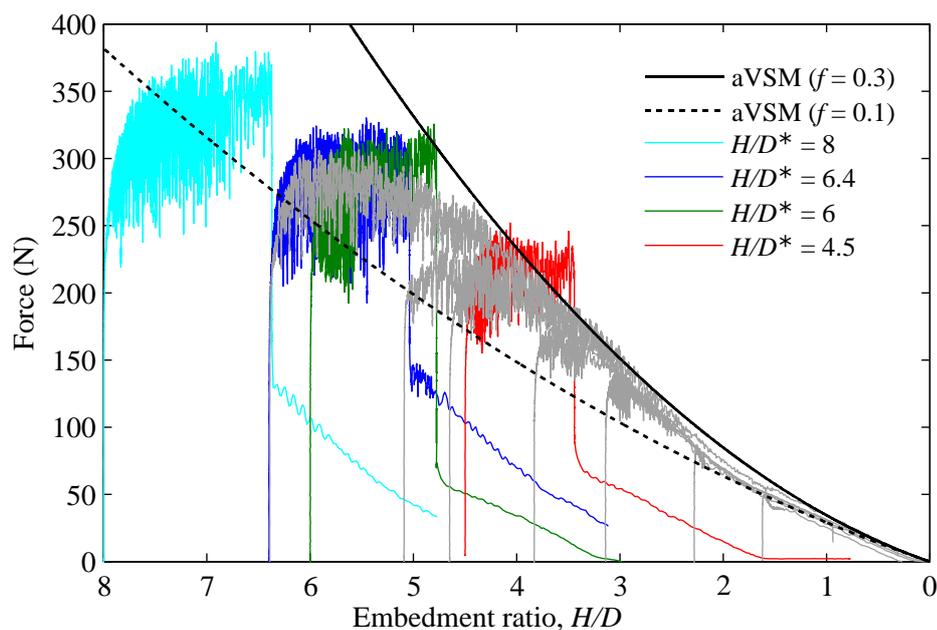

Figure 3-35 Force-disp. curves for OB tests shown at equivalent embedment vs. normal dry tests in RH110

The force replication is better illustrated in Figure 3-35, where the OB test are plotted starting from their equivalent embedment, *H/D**, instead. For the three tests in the range of the previous dry sand data, the responses match very well. It can also be seen how the forces in the OB test level off instead of decreasing after some displacement, which indicates that heave of the wooden board is beginning to occur. Finally, the 'deepest' test with an equivalent *H/D** = 8, shows that the trend of the peak forces diverging from the aVSM prediction continues with increasing depth/stress level. The mobilisation displacement also appears to become extremely large in this instance.

A closer look at the initial force-displacement curves for tests at an equivalent embedment of approximately 6 is provided in Figure 3-36. Curves at the actual depths of ~4.5 and 3 are also plotted for reference. This figure confirms that the force-displacement response in the overburden tests – with different actual embedments – is virtually identical to the equivalent normal test. Characteristics such as the initial stiffness, mobilisation displacement, and peak force all correspond to the response at the equivalent embedment depth. This means that not only is the weight term additive, but the friction mobilised is also consistent (this makes sense since the friction is dependent on stress level, which is replicated). By comparing the overburden test at *H/D** = 6 (green curve) to the reference curve at *H/D* = 3.1 (which is the actual burial depth for the OB test), it can be see than the shape of the curve does change slightly with the overburden, showing a higher mobilisation displacement and a larger force fluctuation. If these are considered indicators for the flow-around mechanism, the result suggests that the increase in stress level does tend to make the soil behaviour more contractive.

Finally, the peak forces in the OB tests were estimated and normalised by the soil weight plus overburden. These are plotted in Figure 3-37 at the location of their equivalent embedment. The breakout factors match well with the existing loose Redhill data. In the

'deepest' OB test, the breakout factor seems to fall below the plateau value of approximately 1.6, a trend that was also seen in some of the other sands.
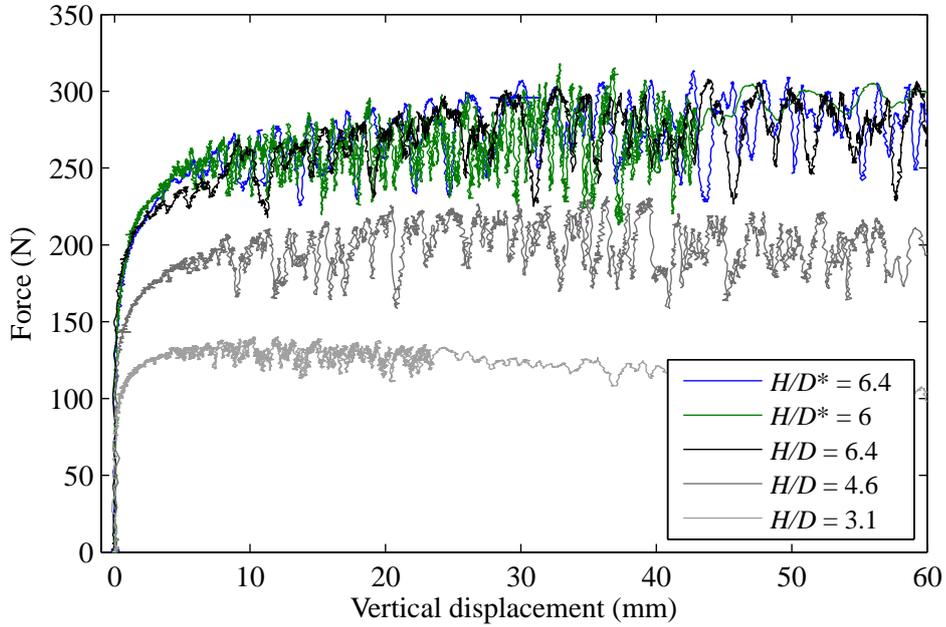

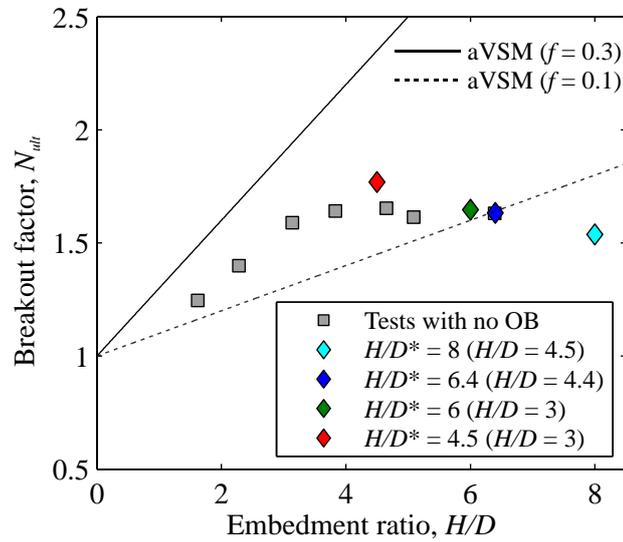Figure 3-36 Force-displacement curves for loose dry RH110

Figure 3-37 Estimated breakout factors for OB tests

3.5. Discussion

Continuing the discussion of rate and density effects from section 3.2.4, this section incorporates the new information provided by the dry sand tests related to grain size and stress level effects. The results from the entire chapter are then used to assess the validity of current prediction models, as well as the DNV guidance for the conditions investigated. Implications for UHB design are also discussed.

3.5.1. Grain size and stress level effects

Tests using three sands of different grain sizes in dry loose/very loose conditions were all found to exhibit a transition from sliding block to another possible mechanism (likely a flow-around mechanism), based on the indicators established in the saturated sand tests. In addition to a plateau in the breakout factors, force fluctuations at greater embedment depths appeared to mark the presence of a flow mechanism, as this has previously been correlated to miniature slope failures (infilling) around the pipe though PIV analysis by Cheuk et al. (2008). Significant differences between the three sands were observed in both the embedment depth and the peak forces at which this transition occurred. In fine sand, the onset of possible flow behaviour occurred at smaller embedments and lower peak forces than in the coarser sands. This difference could be attributed in part to the grain size to pipe diameter ratio, based again on PIV work by Cheuk et al. (2008). The reduction in force can also be explained by their observation that in coarse sand the mechanism tends to be a combination of flow and heave, whereas in fine sand, much less heave is observed.

The vertical effective stress level was also found to influence both the peak force and the force-displacement response. This effect was observed when comparing tests for the same sand (Redhill 110) in both dry and saturated (drained) conditions. The dry tests appeared to experience a flow-around mechanism at a lower force than the saturated tests at the same density. When compared directly, the residual force responses in both tests were similar, but the initial behaviour appeared to be more contractive in the dry sand (at around twice the

effective stress). This was also confirmed through a small number of overburden tests, which demonstrated that through the application of a surface load, the exact behaviour of the soil at a deeper embedment could be replicated – including the onset of a flow-type mechanism.

Clearly, the peak resistance achieved is governed by the failure mechanism, which in turn is influenced by relative density, stress level, and grain size. The mobilisation displacement and initial stiffness are also governed by the mechanism and thus, strongly depend on these factors. As the mechanism transitions from heave to flow, the force response becomes progressively softer, resulting in very high failure displacements. Therefore, the best way to plot displacements for different sands and initial conditions is against stress level, rather than *H/D*. At low stress levels the values of d_f are very consistent, while at higher stress levels the differences due to relative density and grain size become more prominent. Mobilisation displacements for very loose fine sand appear to be the most critical (as they correspond to a reduced initial stiffness). The dry RH 110 tests could possibly be considered close to the upper bound for displacements (and corresponding lower bound for peak forces) since it is likely that the most localised behaviour was occurring in this sand, at the greater depths.

3.5.2. Evaluation of prediction models

3.5.2.1. *Peak force – sliding block mechanism*

As shown in the previous sections, the adapted vertical slip model was found to be an excellent predictor of the peak resistance for loose sand (in drained conditions) when the sliding block failure mechanism is mobilised. This mechanism appears to occur for all relative densities up to an embedment ratio of approximately 2, after which an increasing density is required to reach the aVSM for increasing embedment depths. The prediction model proposed by White et al. (2001) has applicability for a greater range of densities, as it accounts for dilation along its failure planes. However, as with the aVSM, this model over-predicts the resistance at greater embedment ratios once a possible flow-around mechanism is mobilised.

3.5.2.2. Flow-around predictions

Using data from both the saturated and dry sand tests, the validity of the flow-around model developed by Wang et al. (2012) can be assessed. The predicted normalised force for this mechanism (assuming a rough pipe) has been given previously as:

$$N_{FAM} = \frac{R_{FAM}}{\gamma' HDL} = \frac{\alpha_{FAM}}{1 + 4\tan^2 \phi'} \left\{ 2\tan\phi' + \tan\theta + (1 - 2\tan\theta\tan\phi') \frac{\exp[(2\pi - 2\phi')\tan\phi']}{\exp[(3\pi - 2\phi')\tan\phi']} \right\}$$

where ϕ' is taken as the critical state friction angle. The above equation can be further simplified to become:

$$N_{FAM} = \alpha_{FAM} C_{\phi} \tag{3.15}$$

where C_{ϕ} relates to the friction angle only. For an arbitrary pipe-soil friction angle ($\theta = 15°$), the values of C_{ϕ} were calculated as 0.57 for RH110; 0.6 for LB DA30; and 0.61 for LB 14-25. This indicates that the difference in critical state friction angles between these sands does not have a significant influence on this term.

The transition embedment ratio, H/D_{trans}, can be calculated by comparing the above equation to the normalised resistance of the adapted vertical slip model, as follows:

$$N_{ult} = N_{FAM}$$

$$1 + f \frac{H}{D_{trans}} = \alpha_{FAM} C_{\phi}$$

$$\frac{H}{D_{trans}} = \frac{\alpha_{FAM} C_{\phi} - 1}{f} \tag{3.16}$$

Based on the observed plateau in breakout factors, experimental values were determined for N_{FAM} for the sands at various relative densities. From this, the corresponding value of α_{FAM} could be determined. Figure 3-38 plots this flow-around coefficient against relative density index for each sand, which is calculated from Bolton (1986) to account for stress level effects. The assumed stress level used in this calculation was determined using H/D_{trans} for each value. It should be noted that the calculation for I_R is taken beyond its range of applicability (<0) to

incorporate the contractive tests. This implies a mobilised friction angle that is less than the critical state angle, which clearly has little physical meaning. However, the negative values of I_R are included in the following analysis in order to differentiate between contractive tests at different densities. It is recognised that further work is required to better account for these low density and low stress level conditions.

The calculated values are listed in Table 3-6. As expected based on the experimental work presented previously, the back-calculated flow-around coefficient is greater for the LB sands than for RH110 in all tests; however, the trend across different relative densities appears to be similar.

Also included in Figure 3-38 are calculated values of K_p for each test, since Wang (2012) suggests that this value could be used for α_{FAM}. In order to account for density effects, the peak friction angle is used for this term, and is calculated based on Bolton (1986). Again, Bolton's method is used beyond the range of applicability to include negative values of I_R, for the sake of differentiating low density tests. The figure shows that K_p over-predicts the coefficient for RH110, but under-predicts the results for LB DA30. Also due to the difference in critical state friction angles, the use of K_p actually reverses the trend seen in experiments between the two sands (i.e. it predicts LB DA30 will experience flow-around at a lower force than RH110). One explanation for this is that the LB sand could be experiencing a combined heave and flow mechanism, rather than a completely localised flow-around; therefore, the force it mobilises is higher than predicted. Despite this discrepancy, the value of K_p captures the trend with respect to density quite well. This suggests that α_{FAM} could be related to K_p, but requires additional modifiers to account for other influences. Additionally, the issue related to the choice of effective friction angle for contractive soil conditions must be addressed.
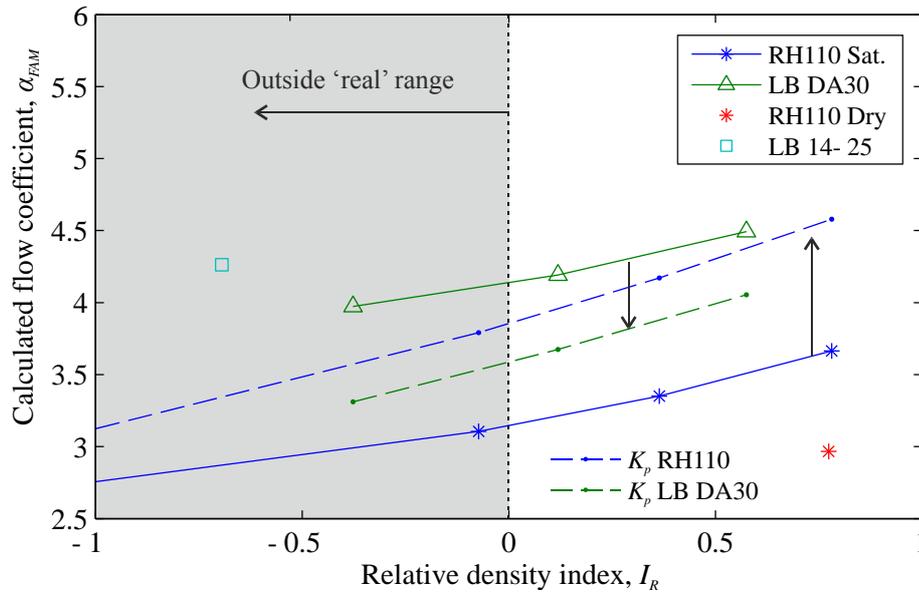
Figure 3-38 Flow-around coefficient, α, calculated for different sands vs. relative density index

The above figure again highlights the difference between the dry and saturated Redhill 110, showing a much lower value of α_{FAM} for the dry tests than the saturated. Since the saturated tests experience a greater peak resistance, before converging to the force response of the dry tests, it may be more accurate to take this residual force as N_{FAM}. In Figure 3-39, the normalised force-displacement response for RH110 is used to calculate new values of N_{FAM}, which represents a more conservative estimate. In (a), the dry and saturated responses for *RD* = 20% is plotted along with the peak force prediction (where $\alpha_{FAM} = 3.67$) and the new, more representative flow-around force (obtained using $\alpha_{FAM} = 3$). This lower value is consistent with the peak in the dry tests, and seems to be an adequate representation of the post-peak flow response. Figure 3-39 (b) shows the modified prediction for the saturated tests from 0 to 15% *RD*. It can be seen from both figures that, particularly for the dry tests, the slope of the curve is not exactly matched at higher embedments. This suggests that at greater embedments the force may drop even further from this predicted value. Some indication of this was also found previously in the peak breakout factors, which appear to begin decreasing at the upper range of *H/D* ratios tested in this work.
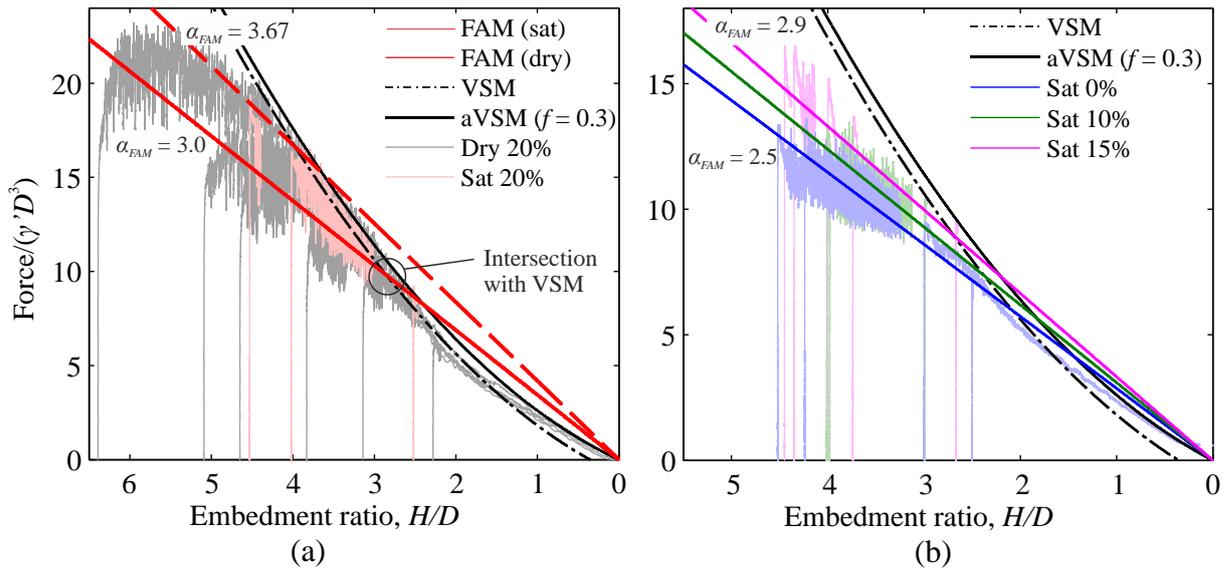
Figure 3-39 Flow-around model fitted to force-displacement curves for RH110: (a) RD = 20% (dry and sat.); (b) RD = 0 to 15% (saturated).

Table 3-6 Relevant parameters for flow-around model

Sand	RD (%)	IR	N_{FAM} (measured)	α_{FAM} (measured)	$K_p{}^\dagger$	α_{FAM-LB} (curve fit)	H/D_{trans} (aVSM)	H/D_{trans} (VSM)
RH110 (S)	0	*-1.00*	1.58	2.76	*3.12*	2.5	1.4	2.1
RH110 (S)	10	*-0.07*	1.78	3.11	*3.79*	2.7	1.8	2.4
RH110 (S)	15	0.36	1.92	3.35	4.17	2.9	2.2	2.7
RH110 (S)	20	0.78	2.1	3.67	4.58	3.0	2.4	2.9
RH110	20	0.77	1.7	2.97	4.57	3.0	2.4	
LB DA30	7.7	*-0.38*	2.37	3.97	*3.31*	-	-	-
LB DA30	14	0.12	2.5	4.19	3.67	-	-	-
LB DA30	20	0.58	2.68	4.49	4.05	-	-	-
LB 14-25	4	*-0.69*	2.62	4.26	*2.94*	-	-	-

One further observation from this model is related to the intersection of the flow-around prediction and the sliding block predictions (VSM and aVSM), which locates the transition embedment, H/D_{trans}. While the aVSM predicts the peak resistance well, the vertical slip model better captures the residual force response; therefore, the intersection of the FAM and the VSM may be the better prediction for the transition embedment. Both calculations are listed in Table 3-6.

3.5.2.3. *Partially drained conditions*

For partially drained conditions, the only available prediction model is that proposed by Schupp (2009) and Byrne et al. (2013), which adds a term to the VSM to account for the pore pressure response. This is only applicable to soil at its loosest state, likely because in this state the excess pore pressure development appears to occur primarily around the pipe. At higher relative densities, the phenomenon becomes more complex as dilation effects further away from the pipe contribute to the overall uplift resistance.

3.5.2.4. *Force-displacement response*

A tri-linear curve, as proposed in the DNV guidelines, seems to provide a good representation of the actual shape of the force-displacement curve – if an accurate prediction for the peak force and mobilisation displacement is made. With this in mind, the remaining requirement is to locate the first slope change in the curve, which is the purpose of the parameters α and β. This work has shown that the displacement parameter β can be related to the stress ratio, $\tilde{\sigma}_v$, rather than the mobilisation displacement. A representative range for this slope change displacement was found to be 0.5 to $1.5\tilde{\sigma}_v$. The force can then be calculated as a percentage of the peak with the parameter, α. Unlike in the DNV recommendations, it should not be constant; instead, α varies linearly with stress ratio from almost 100% at very low stresses to 40% at $\tilde{\sigma}_v = 0.3$ for the conditions tested. This relationship was found to be consistent for different sands and densities, likely because the influence of these parameters is already accounted for in the peak force value.

Mobilisation displacements were compared across all tests against a stress ratio normalisation, though the value of d_f/D was primarily dependent on the failure mechanism. The current DNV upper bound prediction of $d_f = 0.8\%H_c$ appears to be adequate if the sliding block mechanism is mobilised, while the prediction by Thusyanthan et al. (2010) captures the high peak displacements associated with a flow-around mechanism. At low stress ratios the

value of d_f/D predicted by these two methods is similar, and this was reflected in the experimental results.

3.5.3.   Implications for design

The DNV guidelines currently specify two broad ranges to predict the peak uplift resistance for loose and medium/dense sand in drained conditions, using empirical frictional factors (shown in Figure 3-10). For the saturated sand tests, the upper bound of the loose sand region is equivalent to the calculated aVSM, and virtually all of the data for 0 to 20% RD is contained within this band when it is extended to lower embedment ratios. The data for relative densities of 25% to 55% also fit very well within the medium/dense region. Thus, as a broad estimate the DNV provides good guidance for the range of breakout factors for saturated sand at low stress levels. However, the assumption behind these ranges is still that a sliding block mechanism governs; no provisions currently exist to predict the onset of a possible flow-around mechanism, which may eventually cause the peak force to fall below the current lower bound.

The dry sand tests demonstrated a critical scenario for fine sand, in which a flow-mechanism may occur at lower embedments than in coarse sand. This leads to much lower peak forces and higher mobilisation displacements than what is accounted for in the guidelines. Initial stiffness values are also affected. The results highlight the importance of having a model to predict this flow behaviour that accounts for relative density, stress level, problem geometry, and grain size effects. The model proposed by Wang (2012), with the coefficients calculated above for fine sand, can provide an approximate lower bound prediction of the possible flow-around resistance (within the range of embedments tested). Early indications suggest that inclusion of the passive earth pressure coefficient can capture relative density effects on this mechanism; however, more testing would be required to determine a robust method for predicting α_{FAM}.

For partially drained conditions, limited design guidance is available. Current design practice appears to treat the drained case as conservative, assuming that if fast rates of uplift were to occur, the soil would be sufficiently dense to dilate and cause an increase in resistance. However, the findings in this chapter confirm observations by Schupp (2009) and Byrne et al. (2013) that in very loose sand, fast rate tests may cause liquefaction, and drastically reduce the uplift resistance. Given that it is an extremely complex task to quantify the pore pressure effects across varying densities, and estimate the rate of uplift that might occur during buckling, it makes little sense to attempt to predict this partially drained response. Instead, it follows that the design should stipulate a minimum backfill relative density for a given embedment ratio (and stress level), which will ensure that dilation occurs upon shearing of the soil. Practically, this could be as simple as establishing, through field measurements, the time required for sufficient natural densification of the backfill to occur. As a result, the flow-around failure mechanism at peak resistance will probably be avoided, and the conservative drained resistance (and force-displacement response) can then be predicted using the aVSM and the DNV guidelines.

3.6. Design recommendations

This chapter has examined key areas for determining the monotonic uplift resistance of cohesionless soil for upheaval buckling design. In the following section the results of this work are summarised as recommendations relating to the main procedural steps. The focus of this method is on predicting the drained uplift resistance under given embedment conditions, rather than on the iterative process of determining a design embedment depth (such as the methodology presented by Wang (2012)). However, this procedure could be modified in order to calculate a design embedment, starting from a required peak resistance.

The previous sections have made extensive comparisons to the DNV guidance for this problem, concluding that the general framework for prediction uplift resistance is sound, but that modifications are required in the treatment of loose and very loose soil conditions. As

noted above, further experimental work is required to develop a robust prediction model for the flow-around mechanism and as such, the procedure given here requires validation before use in design. Furthermore, though predictions are made for the resistance mobilised by a flow-around mechanism, a conservative design would ensure that the relative density of the backfill is such that this mechanism would typically be avoided.

1) Design parameters

Starting with a given pipe configuration, the following parameters are required to determine the uplift resistance used for calculating a critical buckling temperature:

- Embedment depth, H

- Pipe diameter, D

- Soil parameters: critical state friction angle, ϕ'_{cs}; effective unit weight, γ', and pipe diameter to grain size ratio D/D_{50}

- Soil state: Actual or expected relative density/void ratio of the backfill soil given the installation method. Note that the time-dependent densification response of the soil may be important. If possible, compare the void ratio to the critical void ratio, to determine whether the expected soil behaviour is contractive or dilative at the given effective stress levels.

2) Peak uplift resistance and failure mechanism

If the backfill soil is classified as very loose or loose, the dominant failure mechanism should be determined. This can be predicted based on Figure 3-40, which plots breakout factors against embedment ratio for different proposed mechanisms. The figure includes two adapted vertical slip model (aVSM) prediction curves (using $f = 0.1$ and $f = 0.3$), along with a horizontal line calculated using the flow-around model. The expected breakout factor for a given embedment ratio can be found on the upper bound line; however, the aVSM prediction using $f = 0.1$ is included as a realistic lower bound.
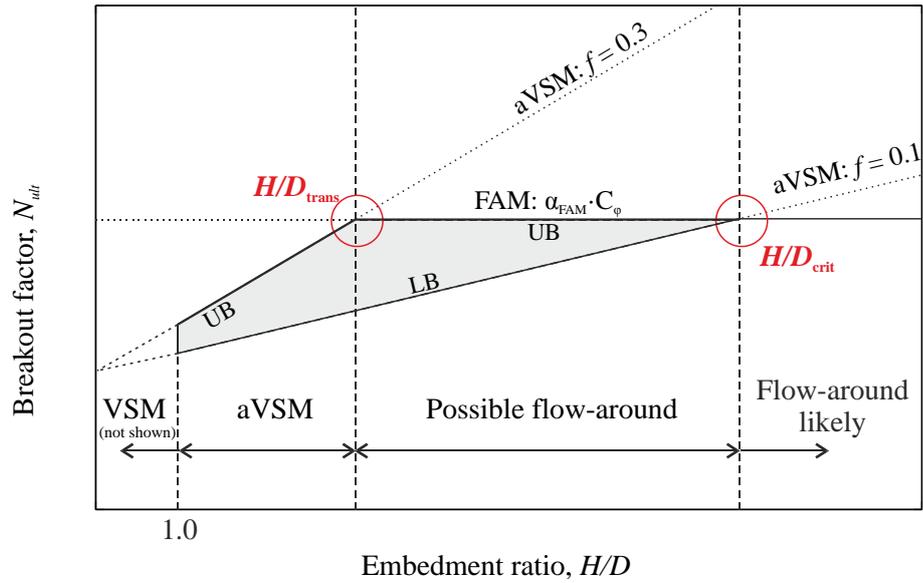
Figure 3-40 Design chart for failure mechanism and peak resistance

The equations used for Figure 3-40 are:

Adapted VSM (DNV guidelines):
$$N_{ult,aVSM} = 1 + f\frac{H}{D}$$
(D.1)

$$f = 0.1, 0.3$$

Flow-around mechanism:
$$N_{FAM} = \alpha_{FAM}C_\phi$$
(D.2)

$$C_\phi = \frac{\left\{2\tan\phi' + \tan\theta + (1 - 2\tan\theta\tan\phi')\dfrac{\exp[(2\pi - 2\phi')\tan\phi']}{\exp[(3\pi - 2\phi')\tan\phi']}\right\}}{1 + 4\tan^2\phi'}$$

where ϕ' is the critical state friction angle, θ is the pipe-soil interface friction angle, and α_{FAM} can be determined from Table 3-7.

Table 3-7 Recommended values for α_{FAM}

Soil properties/state	*RD*: Very Loose to Loose
Fine	α_{FAM} = 2.5 to 3
Coarse	α_{FAM} = 4 to 4.5

104

Vertical slip model (VSM): $\qquad N_{ult,VSM} = 1 - \dfrac{\pi D}{8H} + K_o \tan \phi' \dfrac{H}{D}$ (D.3)

From the above equations, H/D_{trans} and H/D_{crit}, can be calculated as:

$$\frac{H}{D}_{trans} = \frac{\alpha_{FAM} C_\phi - 1}{0.3}$$ (D.4a)

$$\frac{H}{D}_{crit} = \frac{\alpha_{FAM} C_\phi - 1}{0.1}$$ (D.4b)

Using this information, the following three scenarios are possible:

A) If $H/D < H/D_{trans}$, the sliding block is assumed to govern. For $H/D < 1$, the vertical slip model should be used to determine the peak resistance (equation D.3). For $1 < H/D < H/D_{trans}$, N_{ult} can be calculated using the adapted vertical slip model (equation D.1, with $f = 0.3$).

B) If $H/D_{trans} < H/D < H/D_{crit}$, a transition to a flow-around mechanism is possible. Therefore, the peak breakout factor should be determined using equation D.2.

C) If $H/D > H/D_{crit}$, a deep flow-around mechanism is likely, with the resistance falling below the DNV lower bound ($f = 0.1$). Based on the experimental results, the peak resistance may be even less than the FAM prediction. Design in this region should carried out with caution; additional model tests should be considered to confirm the available resistance.

From step 1, if the soil relative density is classified as medium-dense and above, the DNV guidance can be followed, using equation D.1. The suggested range for the parameter f is 0.3 to 0.6 – note that the lower bound is less than what is proposed by the DNV guidelines and by Wang (2012). If a very deep embedment is required in these soil conditions, further testing may be necessary to check for a transition to a deep flow-around mechanism.

3) Mobilisation displacement

In order to estimate the mobilisation displacement, it is necessary to calculate the stress ratio:

$$\tilde{\sigma}_v = \sqrt{\frac{\gamma' H}{p_r}} \tag{D.5}$$

where the reference pressure, p_r, is equal to 100 kPa. Using the calculated stress ratio, mobilisation displacements can be estimated from Figure 3-41, depending on the mechanism determined in step 2. Note that the curves are based on the experimental data shown, and are intended to represent approximate upper bound values. For stress ratios up to 0.2, the mobilisation displacements for all mechanisms are located below the line defined by:

$$\frac{d_f}{D} < 0.2 \cdot \tilde{\sigma}_v \tag{D.5}$$

Above this stress ratio, approximate ranges for the mobilisation displacements depend on the mechanism, as shown in the figure.
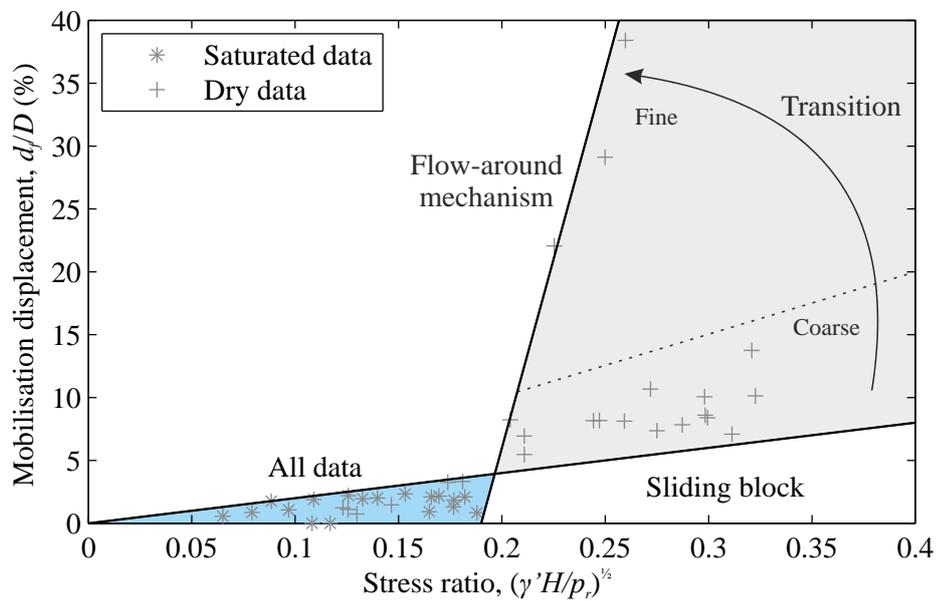

Figure 3-41 Mobilisation displacement design chart

4) Characteristic uplift curve

Finally, the shape of the characteristic force-displacement curve can be estimated using a tri-linear approximation, shown in Figure 3-42, using R_{max} and d_f as calculated in the previous steps. The range of the slope change displacement, d_1, is approximately 0.5 to $1.5 \cdot \tilde{\sigma}_v$. From Figure 3-31 (a), α depends on the stress ratio. The upper and lower bounds for the range of values can be calculated as:

$$\alpha_{LB} = 0.82 - 2 \cdot \tilde{\sigma}_v \qquad \text{for } 0.05 \leq \tilde{\sigma}_v \leq 0.35 \qquad \text{(D.6a)}$$

$$\alpha_{UB} = 1 \qquad \text{for } 0.05 \leq \tilde{\sigma}_v \leq 0.1 \qquad \text{(D.6b)}$$

$$\alpha_{UB} = 1.15 - 2 \cdot \tilde{\sigma}_v \qquad 0.1 < \tilde{\sigma}_v \leq 0.35 \qquad \text{(D.6c)}$$
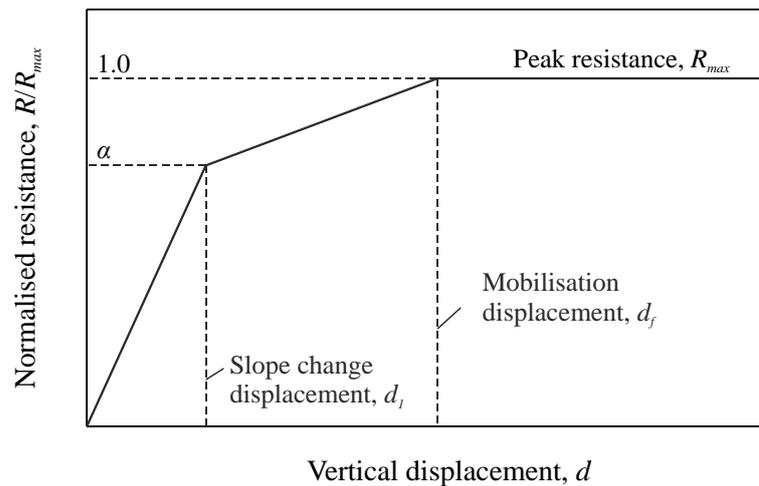
Figure 3-42 Modified characteristic uplift curve definition

3.7. Conclusions

The results from this study of pipe uplift resistance in dry and saturated conditions illustrate the importance of the backfill relative density, among other factors, in controlling the failure mechanism and corresponding peak resistance. Given these findings, it is recommended that a minimum relative density of the backfill is reached to avoid negative effects of contraction of very loose, fine soil. With further development, a prediction model for the flow-around failure

mechanism could be used, along with the established vertical slip models, to determine this minimum density for a given embedment depth and soil type.

The work in this chapter has helped to established general trends in the uplift force-displacement response across different sands and backfill conditions; as a result, improvements to the DNV design approach are suggested. However, as with many geotechnical problems, much of the behaviour can only be predicted in terms of a range of values, and the accuracy is subject to the limitations of in situ measurement techniques. It is therefore necessary to apply the information gained from plane-strain uplift of pipe sections to studies of the global buckling behaviour of pipelines, to better understand the sensitivity of the problem to the variables studied here.

4   FE buckling study

In order to design against upheaval buckling behaviour, it is important to understand the relationship between the structural behaviour of the pipe and the soil resistance. Though it is a well-studied topic, there is a lack of discussion in the literature of upheaval buckling as a soil-structure interaction problem. In particular, great attention is given to the plane-strain uplift resistance of the soil (for example, in recent studies by Cheuk et al., 2008 and Wang et al., 2012), yet there is little indication as to how these results impact the buckling behaviour of the pipe. At the same time, much work has been carried out to develop structural buckling models (Hobbs, 1984; Taylor and Tran, 1996; Croll, 1997), but few of these incorporate realistic vertical soil characteristics (with the exception of Maltby and Calladine, 1995b).

In this chapter the issue is examined through a computational study, using a 2D pipeline model developed in the finite element software, Abaqus (Abaqus, 2010). The chapter consists of three phases of work, outlined in Figure 4-1. The aim of this work is to first assess the structural aspects of the thermal buckling process in a preliminary study, examining:

- how axial soil resistance contributes to the effective force-build up and buckle feed-in;
- the effect of uplift resistance (specifically force-displacement and limiting soil force) on the axial force/temperature initiating buckling.

In the preliminary study, the model is validated against theoretical predictions, and the influence of various model components is systematically examined. Following this, a parametric study is used to evaluate the DNV modelling procedures, focusing on the variables listed in Figure 4-1. Finally, results obtained using experimental data from Chapter 3 as model inputs are compared with the guideline recommendations. The overall objective of this work is to combine two areas of research – plane-strain uplift resistance and a structural

understanding of buckling behaviour – and to assess the importance of characterising and predicting certain soil parameters.
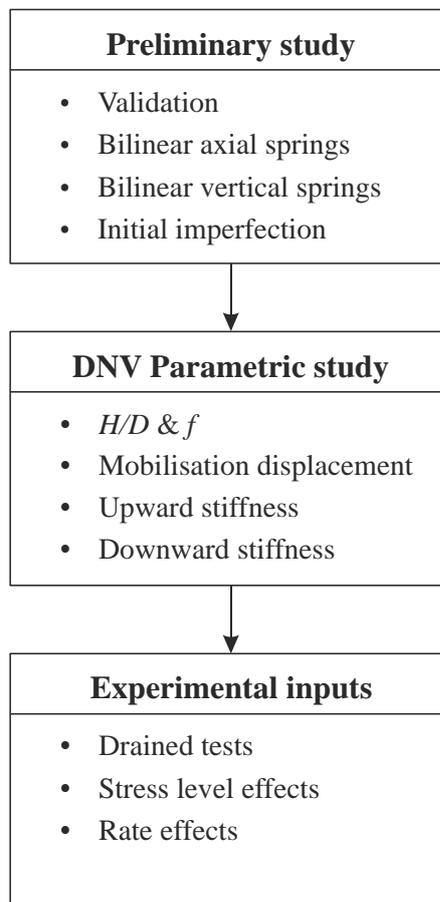
Preliminary study

- Validation
- Bilinear axial springs
- Bilinear vertical springs
- Initial imperfection

DNV Parametric study

- *H/D & f*
- Mobilisation displacement
- Upward stiffness
- Downward stiffness

Experimental inputs

- Drained tests
- Stress level effects
- Rate effects

Figure 4-1 Chapter 4 outline

4.1. Preliminary buckling study

For this study, a simple 2D pipeline model was assembled in Abaqus to investigate the influence of three controlling variables: axial soil resistance, vertical soil resistance, and the initial imperfection in the pipe. The model followed DNV recommendations as closely as possible, except where specific variables are examined.

4.1.1. Model description and parameters

The basic model (shown in Figure 4-2) consisted of a length of pipe split into smaller elements at nodes, with axial and vertical soil springs at each node and an initial stress-free out of straightness imposed on the node geometry. Euler-Bernoulli beam elements (type B23

in Abaqus) of length 1 m were used to represent the pipe (unless otherwise specified). The tests consisted of a uniform increase in temperature to 100°C, applied gradually to the pipe during a static analysis step. This temperature range was chosen as it is just above typical values found in the literature, which are around 80 to 85°C (Ellinas et al., 1990; Nielsen et al., 1990a). The expansion of the pipe due to thermal loading is resisted by the axial springs and/or end restraints, which cause axial compression in the pipe. In all analyses, the Abaqus option 'NLGEOM', which accounts for large-displacement effects (i.e. geometric nonlinearity), was activated. In each test several model outputs were examined, including: axial force in the pipe, vertical and horizontal pipe displacement, and spring forces. Of particular interest were these values at the pipe centre (i.e. the location of the initial imperfection). The results were used to provide information on how these values change:

- along the pipe for a given pipe temperature;
- with temperature for a given test; and,
- across a set of tests as a function of the variable under investigation.

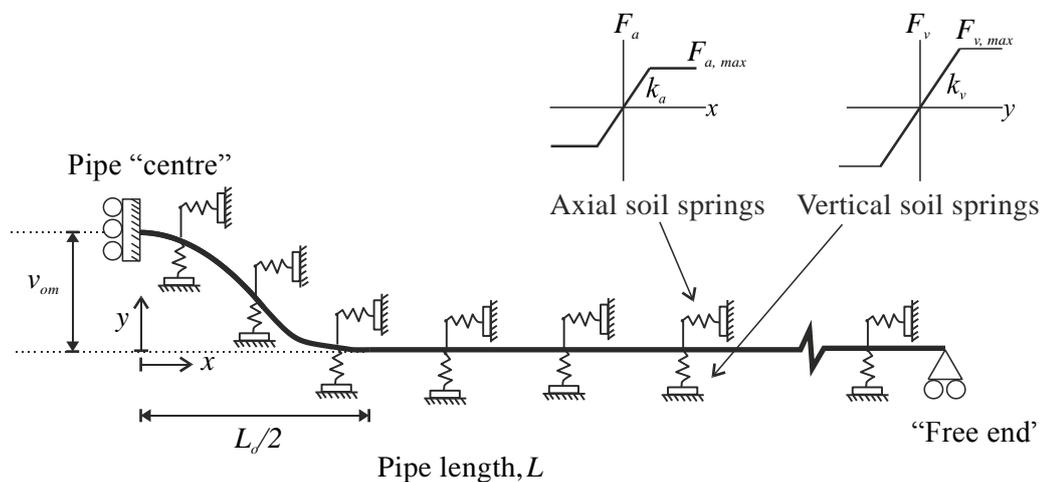*Figure 4-2 Abaqus model schematic*

The model pipe properties, listed in Table 4-1 below, were selected from various sources (Nielsen et al., 1990a; API, 2004) to represent a typical pipe in the field. For the preliminary study, internal pressure and pipe self-weight were ignored. If considered, typical values for these parameters would be around 10-20 MPa for the internal pressure (Klever et al., 1990;

Palmer et al., 1990), and 0.52 kN/m for the submerged weight of an empty pipe (based on a weight of 64.64 kg/m for the given pipe dimensions, obtained from API, 2004). This self-weight value would be greater if additional coating (for example, concrete) was specified, and could change after installation depending on the fluid passing through the pipe. The material behaviour was assumed to remain elastic throughout the simulations. Additionally, the pipe was defined as stress-free in its imperfect shape rather than having an imposed imperfection on an initially perfect geometry. The above assumptions represent simplifications from the DNV modelling recommendations and from realistic field conditions; however, these were not considered important for examining the variables of interest in this study.

Table 4-1 Pipe properties

Pipe properties			
Diameter	D	0.219	m
Wall thickness	t	0.0127	m
Modulus of elasticity	E	210	GPa
Shear modulus	G	81	GPa
Area	A	0.0823	m^2
Second moment of area	I	$4.40 \cdot 10^{-5}$	m^4
Flexural rigidity	EI	$9.23 \cdot 10^{6}$	Nm^2
Axial rigidity	EA	$1.73 \cdot 10^{9}$	N
Thermal expansion coefficient	α_T	$12.5 \cdot 10^{-6}$	K^{-1}

Representative ranges calculated for the soil springs and imperfection size/shape are listed in Table 4-2; these formed the basis for variation of the model parameters in this study. The properties of Redhill 110 (see Table 3-1) were used for the soil spring ranges, assuming the pipe embedment ratio (*H/D*) varies from approximately 1 to 5. For the axial soil springs a simple bilinear model was selected from ALA (2001) which takes the average effective stress around the pipe at a given *H/D* to determine the limiting friction force. The peak vertical force was calculated using the DNV guidelines for pipe uplift (downward stiffness is assumed here to be the same as the uplift stiffness). For both the axial and vertical springs, recommended values of mobilisation displacements were used to calculate the range of stiffness values.

For example, to calculate the lower bounds for the vertical springs, the values for loose sand ($f = 0.1$) at an embedment ratio of $H/D = 1$ were inserted into the adapted vertical slip model (equation 2.18). The corresponding minimum stiffness was approximated by dividing the force by a maximum mobilisation displacement ($0.8\%H$). Conversely, the maximum values were obtained using an $H/D = 5$, $f = 0.6$ for dense sand, and a mobilisation displacement of $0.5\%H$. The same procedure was used for the axial spring ranges, given a limiting axial force calculated as:

$$F_a = \pi \gamma' H D \left(\frac{1 + K_o}{2}\right) \tan(\phi' \delta) \tag{4.1}$$

where $K_o = 1 - \sin\phi'$; δ is the pipe roughness factor (0.7-0.8); and ϕ' is the effective friction angle. The range of mobilisation displacements given in ALA (2001) for the axial soil springs are 5 mm for loose sand and 3 mm for dense sand. This expression accounts for the average normal stress due to the soil overburden – if the weight of the pipe was included in these simulations, the axial friction force would be likely to increase (the magnitude of the overburden force ranges from 1 to 2 times the pipe self-weight value given above).

Finally, an initial imperfection was defined at the pipe centre, consisting of a single hump of length L_o and height v_{om}, as shown in Figure 4-2. For the preliminary tests, the pipe curvature was determined based on Taylor and Gan (1986) (equation 2.12), with a range of size parameters selected from real pipeline data (Thusyanthan et al., 2011).

Table 4-2 Suggested ranges for variables tested

Variable	Suggested range for model inputs			Source/Notes
Axial springs	Stiffness, k_a	80 – 650	kN/m/m	ALA (2001)
	Peak force, F_a	0.4 – 2	kN/m	H/D range: 1 - 5
Vertical springs	Stiffness (uplift), k_v	230 – 1370	kN/m/m	DNV (2007)
	Peak force, F_v	0.4 – 7.5	kN/m	H/D range: 1 - 5
Imperfection	Height, v_{om}	0.01 – 0.5	m	Thusyanthan et al. (2011)
	Length, L_o	10 – 60	m	

4.1.2. Outline of preliminary study

The details of the preliminary testing programme are listed in Table 4-3. The shaded cells in the table indicate the variable under examination in each test set (and sub-set).

Table 4-3 Preliminary testing programme

Set	L (m)	End conditions*	Imperfection ID[†]	L_o (m)	v_{om} (m)	Axial k_a (kN/m/m)	Axial F_a (kN/m)	Vertical k_v (kN/m/m)	Vertical F_v (kN/m)	# of tests
Initial	200	simply supported	I1	-	-	-	-	5-100	-	4
	16-350	simply supported (SS)	I1	-	-	-	-	20,50	-	5
	200	pin-pin	I1	-	-	-	-	50	-	1
	200	SS (applied disp.)	I1	-	-	-	-	50	-	1
Axial	400	LHS: 1,6; RHS: 2	I1	0.05	20	5-600	-	-	-	5
	400	LHS: 1,6; RHS: 2	I1	0.05	20	5-600	-	5	-	5
	400	LHS: 1,6; RHS: 2	I1	0.05	20	400	0.4-2	5	-	5
	600-1000	LHS: 1,6; RHS: 2	I1	0.05	20	400	1.6	5	-	3
	400	LHS: 1,6; RHS: 1,2	I1	0.05	20	400	1.6	5	-	1
Vert. 1	400	LHS: 1,6; RHS: 2	I1	0.05	20	400	1.6	25-100	-	4
	1000	LHS: 1,6; RHS: 2	I1, I2 I3	0.05	20	400	1.6	5	-	3
	1000	LHS: 1,6; RHS: 2	I3,I4	0.05	20	400	1.6	5,25	-	3
	1000	LHS: 1,6; RHS: 2	I3	0.05-0.35	10-50	400	1.6	25	-	8
Vert. 2	2200	LHS: 1,6; RHS: 2	I3	0.05	30	400	1.6	25-1200	-	5
	2200	LHS: 1,6; RHS: 2	I3	0.05	30	400	1.6	200	0.5	2, 1[R]
	2200	LHS: 1,6; RHS: 2	I3	0.05	30	400	1.6	200	0.5-5,16	5[R]
	2200	LHS: 1,6; RHS: 2	I3	0.05	30	400	1.6	200-1200	3	4[R]
Total preliminary tests										65

* For end conditions, numbers indicate fixities (1 = x-direction, 2 = y-direction, 6 = rotation); LHS = left-hand side of pipe (pipe 'centre'); RHS = right-hand side (pipe 'end').

[†]imperfection types: I1 = Taylor and Gan (1986), I2 = Croll (1997), I3 = Gaussian peak, I4 = equivalent cosine imperfection.

[R] Denotes Riks analysis (all other tests are static analyses).

In this study, the influence of each of the variables described above was systematically examined. The initial tests aimed to validate the response of the model to changes in pipe length and spring stiffness, with vertical soil springs only. The influence of the axial spring stiffness and a limiting axial force was tested in the second set, while the final two sets varied the definitions for the vertical soils springs and the initial imperfection (size/shape). For each test, it was necessary to assume a base case for the other variables. For example, when examining both the axial and vertical springs, a constant imperfection size and shape were used.

4.1.3.   Initial verification

The pipeline model was validated by comparing its basic buckling behaviour to theoretical predictions. The initial set-up was a simply supported straight pipe, with linear vertical springs along its length. Three different loading scenarios were used to determine the critical buckling load of the pipe: eigenvalue buckling with a unit axial load applied at the roller end, eigenvalue buckling with a unit temperature increase (both ends pinned), and static analysis applying a displacement at the roller end. All three analysis methods produced consistent results; for example, the buckling temperature achieved in method 2 could be related to the buckling force in method 1 using $P = EA\alpha\Delta T$.

The critical buckling load in each test was compared to theoretical predictions made using the Rayleigh Method. It is known that the theoretical buckled shape for this problem is a sine wave function, so:

$$y = \sin\frac{n\pi x}{L}$$

Therefore:
$$P = \frac{EI \int_0^L \left(\frac{d^2y}{dx^2}\right)^2 dx + k_v \int_0^L y^2 dx}{\int_0^L \left(\frac{dy}{dx}\right)^2 dx} = \frac{EI\pi^2 n^2}{L^2} + \frac{k_v L^2}{\pi^2 n^2} \tag{4.2}$$

where y is the assumed deflected shape of the pipe, EI and L represent the pipe stiffness and length, n is the buckling mode, and k_v is the vertical spring stiffness. Buckling force curves produced using the above equations are presented in Figure 4-3 and are in very good agreement with the Abaqus results.
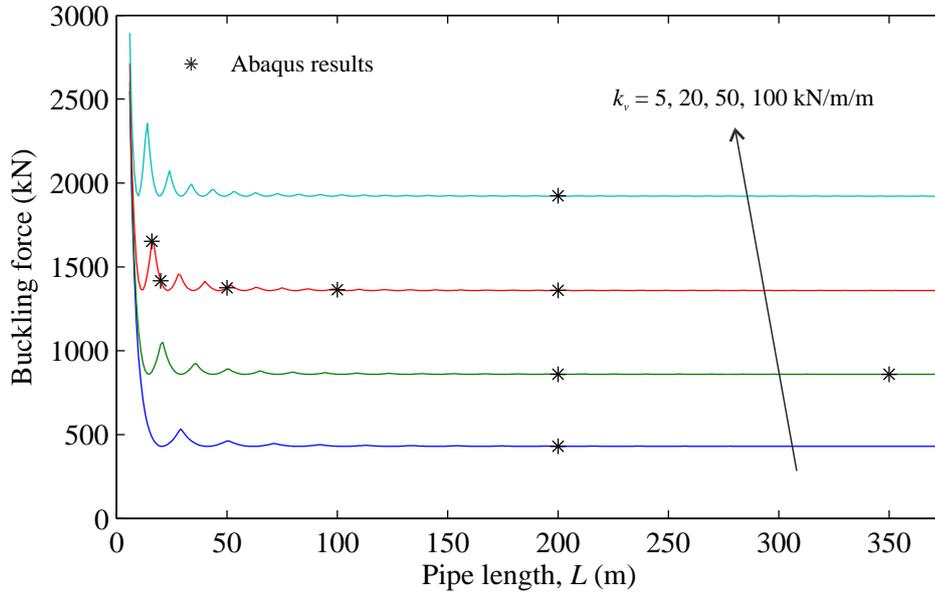

Figure 4-3 Buckling force predictions using Rayleigh method compared to Abaqus results

The results of this verification demonstrate that beyond a certain length (for a given vertical spring stiffness), the critical buckling force remains relatively constant with increasing pipe length. This agrees with analysis by Xia and Zhang (2009), which finds that when $n \geq 2$ and $k_v > EI(\pi/L)^4$, the critical load is independent of length and approaches the value:

$$P_{crit} = 2\sqrt{k_v EI} \tag{4.3}$$

For example, when $k_v = 100$ kN/m/m, P_{crit} is calculated as 1922 kN, which closely matches the results in the above figure. This equation can then be used to determine a limiting linear spring stiffness value for a given temperature rise, above which the pipe will not buckle:

$$k_{min} = \frac{P^2}{4EI} = \frac{E(A\alpha_T \Delta T)^2}{4I} \tag{4.4}$$

116

It can also be shown that the periodic wavelength of the buckled shape is given by:

$$\lambda = \frac{2\pi}{\sqrt[4]{k_v/EI}}$$

(4.5)

4.1.4. Axial soil springs

After initial verification of the buckling behaviour with linear vertical springs, several modifications were made to the model. The overall pipe length was increased and the support conditions were modified to allow for the introduction of axial springs. At one end of the pipe ($x=0$), rotations and axial displacements were fixed and vertical displacements were free, in order to represent the centre of a pipe twice as long (this end is now referred to as the pipe centre). At the other end (the 'free end'), only vertical displacements were fixed. Instead of imposing a virtual anchor point by fixing the horizontal displacements, the free end condition was used to investigate where an anchor point might develop in a long, freely displacing section of pipe. The length of the modelled section was set as $L = 400$ m, resulting in a total pipe length equivalent to 800 m ($2 \cdot L$). The initial imperfection was also introduced in the model at this stage (equation 2.12), with $y = v_{om}$ located at $x = 0$ (the pipe centre) and decreasing to zero at $x = L_o/2$. The imperfection parameters were set at $v_{om} = 0.05$ m and $L_o = 20$ m, representing approximate average values based on the range of imperfection data presented by Thusyanthan et al. (2011).

Two cases were examined for the axial springs in this section: varying the elastic spring stiffness in tests where the peak force is not reached (linear case), and varying the limiting soil force for a constant initial stiffness (bilinear case). In both instances, a stiffness value of 5 kN/m/m was used for the vertical springs (upward and downward directions), in order to provide a small amount of vertical restraint to control the buckling process. For the first set of tests, the axial spring stiffness was varied from 5 to 600 kN/m/m. The reaction force and relative vertical displacement at the pipe centre due to the increasing thermal load is shown in Figure 4-4 for each test. When the temperature change was applied, the pipe was found to

117

reach a buckling load in all cases except for k_a = 5 kN/m/m − in this test the buckling had only just begun at the pipe centre. This is due to the obvious fact that for stiffer axial soil springs, less axial displacement (expansion) is required to build up the force at the pipe centre; if the pipe length is not sufficient to build up the axial friction force, the entire pipe will displace without experiencing buckling.
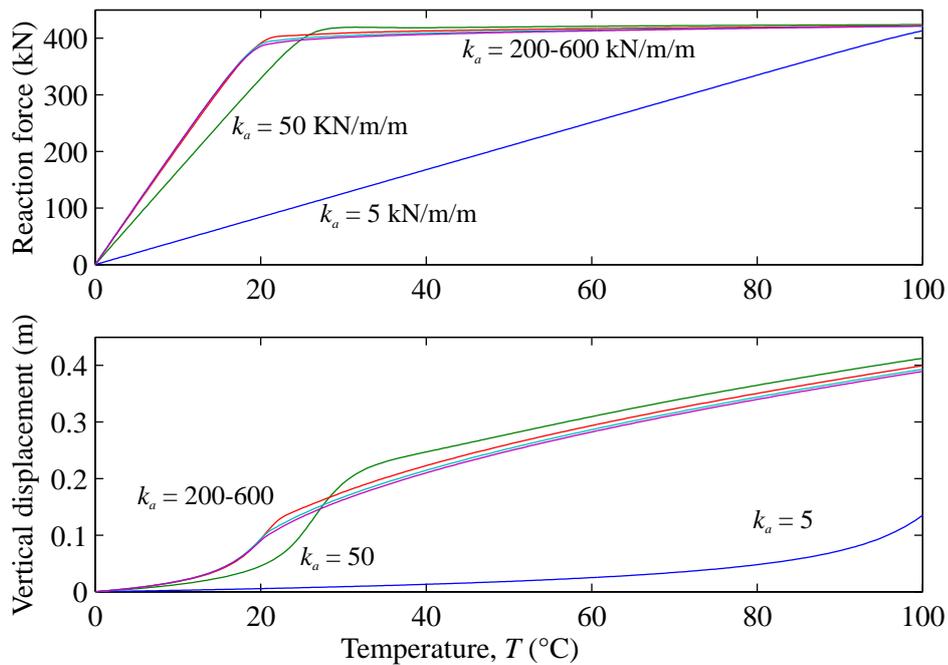

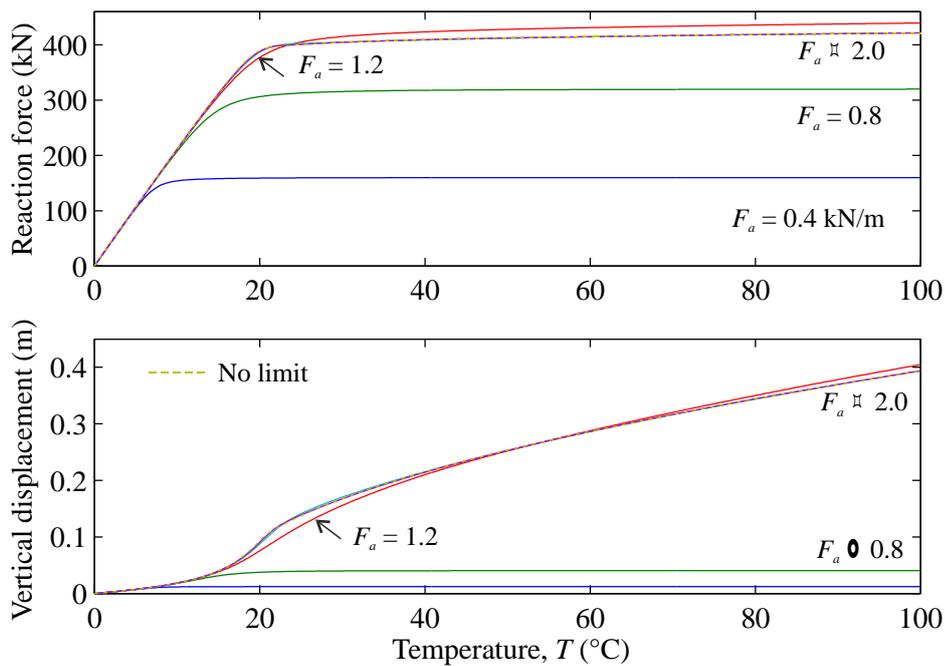*Figure 4-4 Response at pipe centre: varying axial stiffness (k_v= 5 kN/m/m)*

Figure 4-5 Response at pipe centre: varying limiting axial force (k_a = 400 kN/m/m)

For an intermediate spring stiffness value of 400 kN/m/m, a limiting value for the axial force (F_a) was then imposed. The response at pipe centre for varying values of F_a is presented in Figure 4-5. Here it is shown that, in contrast to the previous case, the stiffness of response (i.e. the initial slope of reaction force over temperature) is constant. For high values of F_a, the response at the centre is identical to (and limited by) the linear spring case; however, at lower values of F_a, the vertical displacement and the axial force stabilise before the critical load is reached. A description of the key buckling phases observed in both sets of tests is provided below, with reference to Figure 4-6, Figure 4-7, and Figure 4-8, which show examples of the effective axial force, axial and vertical displacements, and friction forces along the length of pipe. Note that the term 'effective axial force' is used in the following sections, although in the absence of internal and external pipe pressures, this force is equivalent to the actual pipe wall force due to the thermal loading. In the following figures, displacement values shown are relative to the initial shape (i.e. the axial and vertical displacements are zero at $T = 0$).

4.1.4.1. Pre-buckling

At the free end, where the effective axial force remains zero, the pipe begins to slip immediately as it starts to expand. As the temperature increases, displacement of the free end increases and the slip front begins to move towards the centre of the pipe. With displacement, the axial (friction) force in the springs increases, resulting in an effective axial force developing in the pipe. At a given temperature step, the force in the pipe increases from zero at the free end through a zone of shear lag, until the force levels off towards its maximum value at the pipe centre. The length of this shear lag zone (where the force is transferred from pipe to soil) depends on the stiffness of the pipe compared to the stiffness of the soil. For linear springs, this relationship can be derived by considering a pipe element of length dx under compression (positive), with an axial displacement u and an axial spring stiffness $k{\cdot}dx$. Taking horizontal force equilibrium gives:

$$P = P + \Delta P + ku \cdot dx$$

$$\frac{dP}{dx} = -ku \tag{4.6}$$

The force P can also be expressed using Hooke's law:

$$P = -EA\left(\frac{du}{dx} - \alpha_T \Delta T\right) \tag{4.7}$$

Substituting equation 4.7 into 4.6 gives:

$$\frac{d}{dx}\left[EA\left(\frac{du}{dx} - \alpha_T \Delta T\right)\right] = ku$$

$$EA\frac{d^2u}{dx^2} - ku = 0 \tag{4.8}$$

Setting $\kappa = \sqrt{k/EA}$, the equation is simplified to:

$$\frac{d^2u}{dx^2} - \kappa^2 u = 0 \tag{4.9}$$

Which has the general solution:

$$u = Ae^{\kappa x} + Be^{-\kappa x} \tag{4.10}$$

This problem can be solved for a semi-infinite pipe by considering a fully restrained pipe under compression, $P_o = EA\alpha_T\Delta T$, which is then loaded by pulling with force P_{pull} at the free end (note that $x = 0$ at the free end for the following equations). The boundary conditions for this applied loading are:

1) u is finite as $x \to \infty$

2) $EA\frac{du}{dx} = P_o$ at $x = 0$

which are used to obtain the solution:

$$u = -\frac{P_o}{\kappa EA}e^{-\kappa x} \tag{4.11}$$

Differentiating equation 4.11 and substituting back into equation 4.7 (Hooke's law) yields the following expression for the axial force along the pipe, prior to buckling:

$$P = P_o(1 - e^{-\kappa x}) \tag{4.12}$$

where $P_o = EA\alpha_T\Delta T < P_{crit}$. The shear lag length, λ_{SL}, is equal to $1/\kappa$. This implies that the stiffer the axial springs, the smaller the lag length.

If, however, a limiting axial soil force is achieved as the pipe displaces (starting from the free end), the pipe continues to slip but with a constant frictional force per unit length acting on it. The effective axial force increase is then linear from the free end towards the centre, until after a certain distance it levels off (see Figure 4-7). The force transfer length between pipe and soil now consists of the length of pipe which is slipping freely at the limiting friction (x_1), plus a shear lag length. Equation 4.12 can be modified to obtain:

$$P = F_a x \qquad\qquad \text{for } 0 \leq x \leq x_1 \qquad\qquad (4.13)$$

$$P = \frac{F_a}{\kappa}\left(1 - e^{-\kappa(x-x_1)}\right) + x_1 F_a \qquad\qquad \text{for } x \geq x_1 \qquad\qquad (4.14)$$

$$x_1 = \frac{P_0}{F_a} - \frac{1}{\kappa} \qquad\qquad (4.15)$$

It is clear from the above expressions, and from the figures, that with lower values of F_a greater lengths of pipe must displace at this limiting friction value for the total resisting force to reach the buckling force in the pipe. As in the linear spring case, if the length required to build up the buckling force (for a giving value of F_a) is greater than the length of the pipe, buckling will not occur. Predicted forces calculated using equations 4.14 and 4.15 are compared in Figure 4-8 to the effective axial force along the pipe when F_a = 1.6 kN/m. It can be seen that the force build-up away from the imperfection is well captured by these expressions; however, as the temperature increases and the imperfection amplitude grows, the axial force drops further away from this predicted value due to the shortening of the pipe length (as found in Maltby and Calladine (1995b)).

4.1.4.2.   Buckling

When the axial force in the pipe approaches the critical buckling load, global buckling of the pipe begins to occur, and is characterised by a sharp increase in the rate of vertical displacement with temperature. The buckle starts at the centre and propagates towards the free

end as the axial force becomes critical along the pipe (the location of peak axial force along the pipe moves towards the free end with the buckling front). It can be assumed that overall buckling has occurred when the rate of vertical displacement at the centre has reached a maximum, and the response has propagated and amplified along the pipe. As the pipe buckles, the average axial force in the pipe becomes limited by the critical buckling load, P_{crit}, and an anchor point develops. Beyond this point, axial displacement towards the free end continues, and between this point and the centre the axial displacement begins to decrease and then reverse as the pipe is fed back into the buckling sections (see Figure 4-7). In the limiting friction case, the anchor point occurs at a distance from the free end consisting of the slip length plus the lag length, but limited by the critical buckling force, estimated as follows:

$$x_{anchor} = x_1 + \frac{1}{\kappa} = \frac{T\alpha_T EA}{F_a} \leq \frac{2\sqrt{k_v EI}}{F_a} \tag{4.16}$$

If the buckled length is sufficiently long, the first several wavelengths (from the centre) are identical in both the linear spring and limiting force tests and can be estimated using equation 4.5 from the previous section.

4.1.4.3. Post-buckling

If the temperature continues to increase post-buckling, further expansion of the pipe feeds directly into the buckles. Between the anchor point and the centre, the amplitude of the buckles increases but at a decreasing rate. Both the apex and the inflection points of the buckle do not move horizontally, but positive and negative axial displacements occur on either side of these points (demonstrating localised feed-in). The effective axial force is approximately constant at P_{crit} across the buckled section, though it undulates (along with the x-displacement and frictional force) at half the wavelength of the buckle. Beyond the anchor point, axial displacement continues at a constant rate as there is no further increase in axial force beyond the limiting friction value.
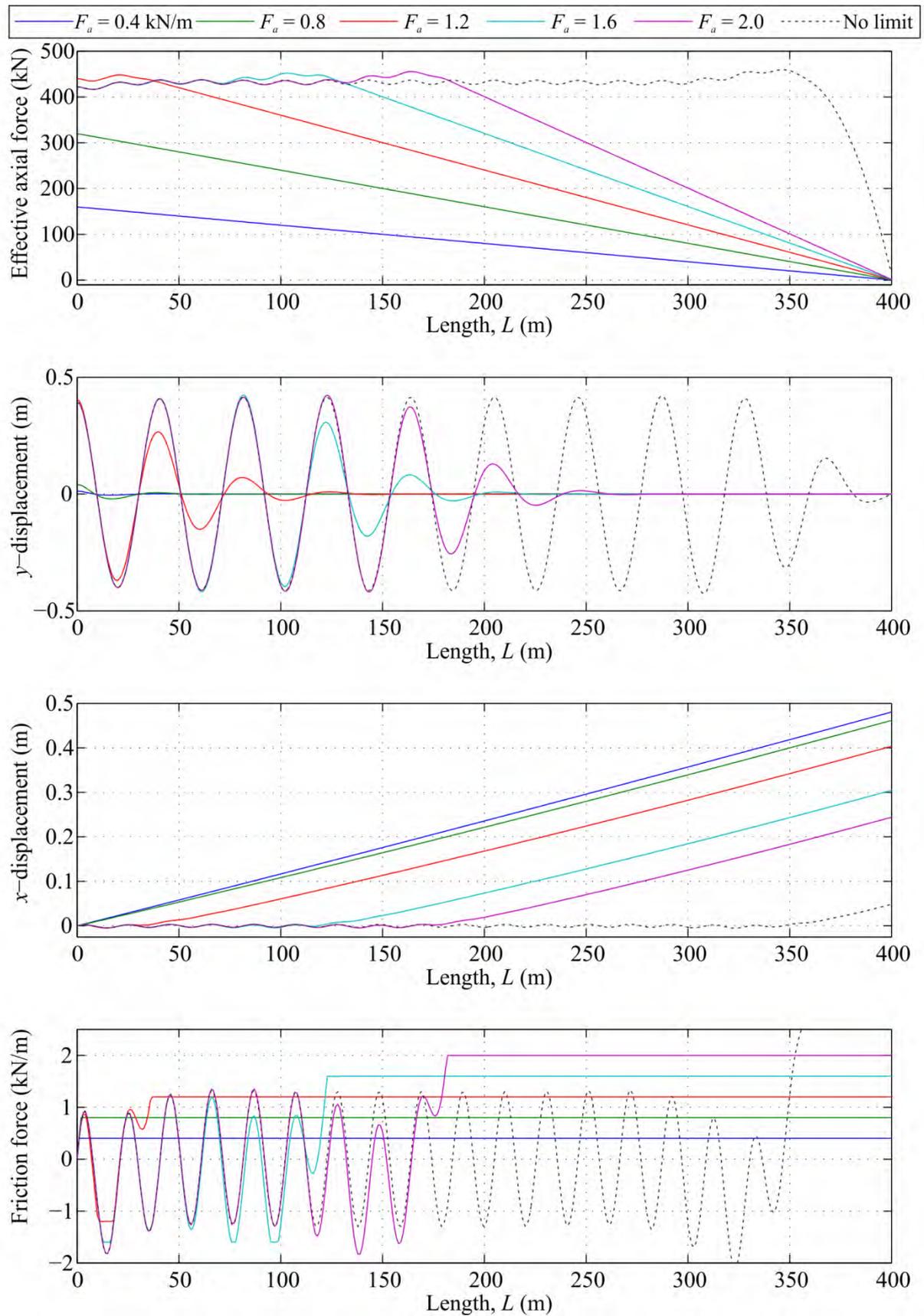
Figure 4-6 Axial force, displacement and friction force along the pipe length at T = 100°C for varying values of F_a (k_a = 400 kN/m/m, k_v = 5kN/m/m)
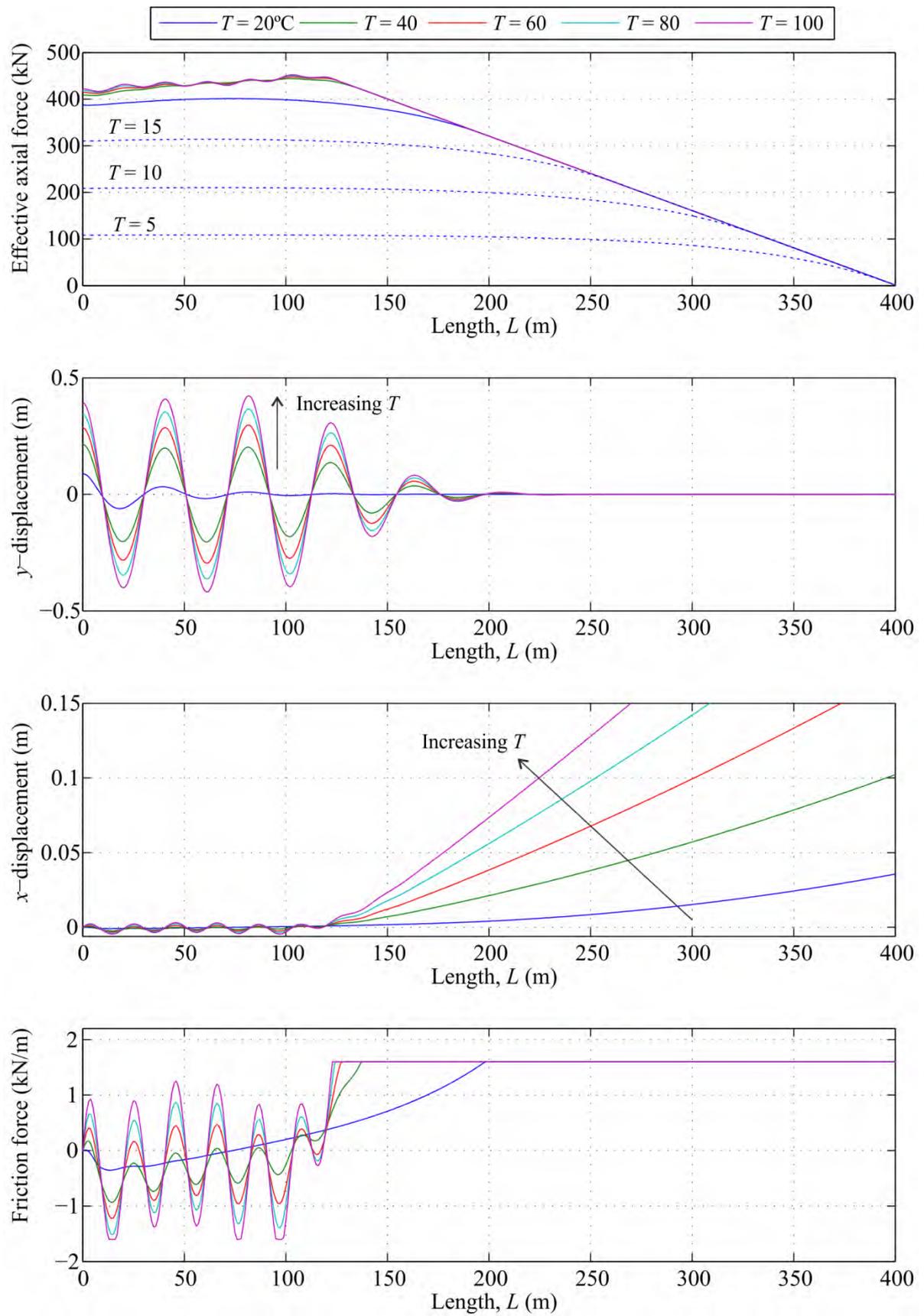
123

Figure 4-7 Axial force, displacement and friction force vs. length for varying temperature steps ($F_a = 1.6$ kN/m, $k_a = 400$ kN/m/m, $k_v = 5$kN/m/m)
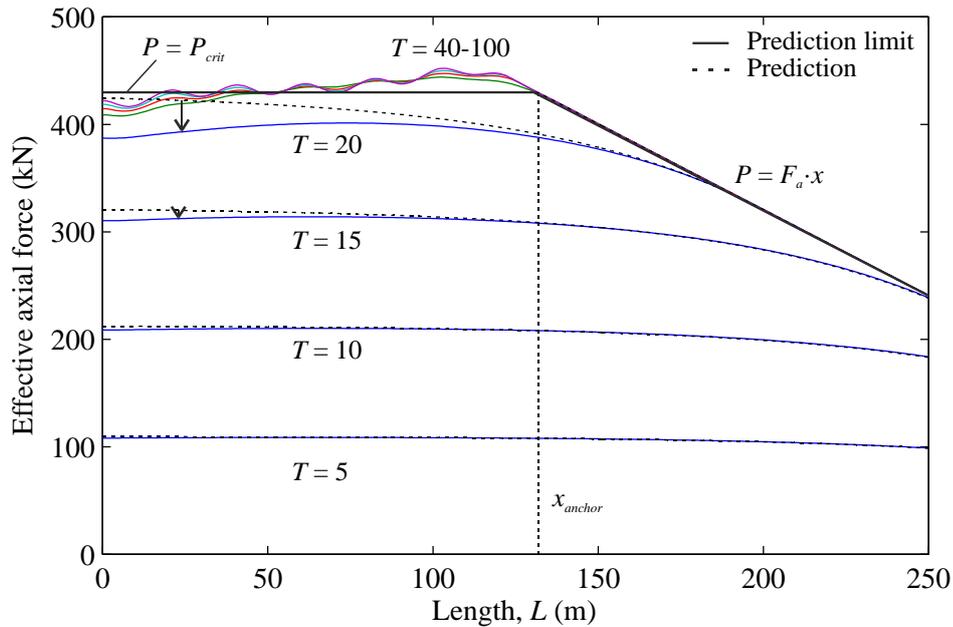
124

Figure 4-8 Effective axial force vs. length for varying temperature steps compared with predictions using equations 4.14 and 4.15(F_a = 1.6 kN/m, k_a = 400 kN/m/m, k_v = 5kN/m/m)

4.1.5. Linear vertical springs and initial imperfection

The main observation in the axial spring tests was the dependence of the buckling behaviour on the relationship between the pipe length (and axial stiffness, *EA*) and the frictional spring characteristics. If the modelled pipe length is sufficient for the axial force to reach the critical load for a given limiting force and stiffness combination, the pipe will buckle; further increases in length will only serve to increase the length of the buckled section. Regardless of the axial spring characteristics, the first few buckled wavelengths will be similar, provided that several full wavelengths exist from the centre before decaying away. Thus an intermediate axial spring combination of k_a = 400 kN/m/m and F_a = 1.6 kN/m was used for tests examining the vertical spring characteristics, described in the following.

Initially the same set-up as above was used, though the overall length of pipe was increased as required in each test in order to induce buckling along at least 200 m of pipe. This method was only effective, however, for a low range of k_v values, as beyond a threshold stiffness the pipe did not buckle. Using equation 4.4, this maximum stiffness was calculated as 126

kN/m/m for an applied temperature of 100°C. Figure 4-9 shows that an increase in the vertical spring stiffness results in a higher critical buckling load, requiring a greater temperature increase; however, the initial build-up of the axial force at the centre is consistent. The vertical displacement and maximum rate of displacement (with temperature) at the centre decrease with increasing vertical stiffness. Along the pipe, the buckle amplitude and wavelength also decrease.

Interestingly, at higher values of k_v the axial force has a greater reduction at the initial imperfection (pipe centre) compared to nearby un-deflected elements, and negative axial displacement (feed-in) towards the centre begins to occur. In fact, the negative axial displacement becomes such that the limiting friction force is reached, meaning further feed-in would occur at a constant rate. This corresponds to a slight increase in the vertical displacements at the pipe centre, indicating some localisation of the buckle at the imperfection. Typical force and displacement variations along the pipe length for a stiffness of $k_v = 75$ kN/m/m are shown in Figure 4-10. These results imply an additional influence of the axial friction values at greater vertical stiffnesses, above the effects already described in section 4.1.4. For example, if the axial resistance was reduced, there would be greater feed-in to the buckle and a higher maximum buckle amplitude.
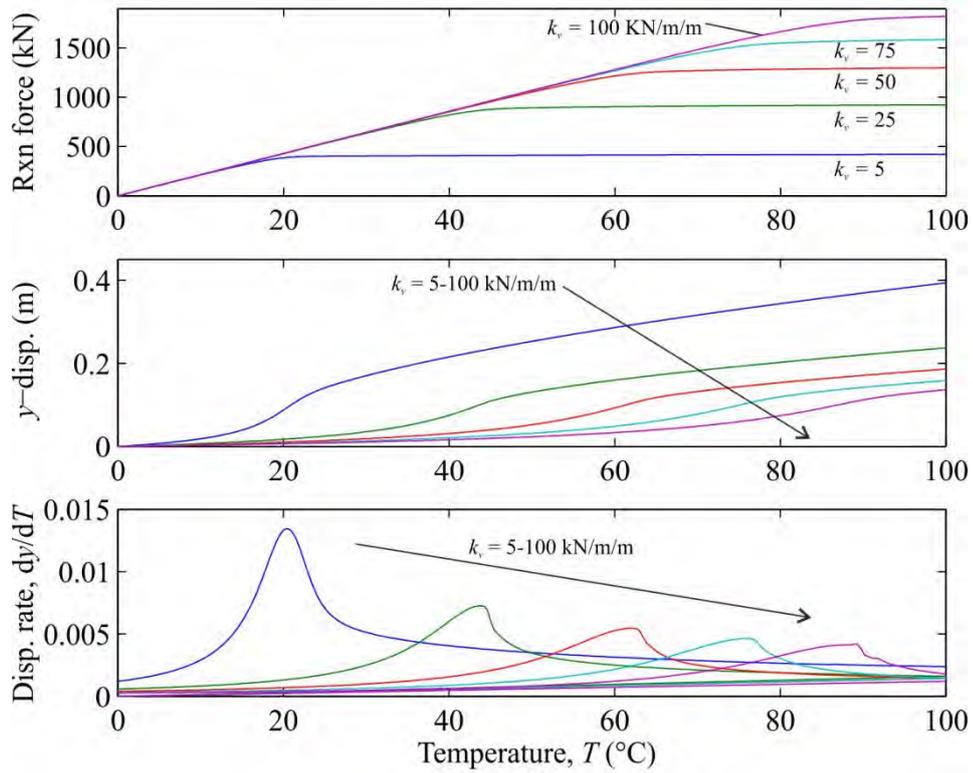
Figure 4-9 Response at pipe centre: varying k_v (F_a = 1.6 kN/m, k_a = 400 kN/m/m)
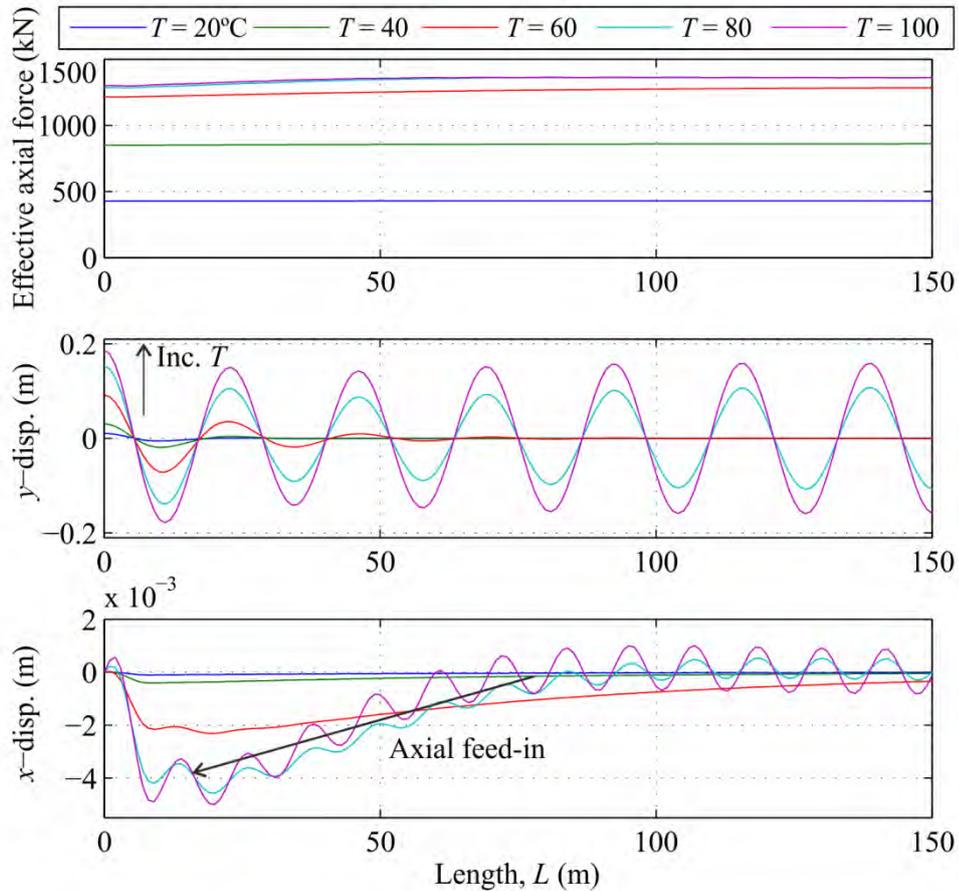

Figure 4-10   Axial force and displacement vs. L for several temp. steps (k_a = 400 kN/m/m, F_a = 1.6 kN/m, k_v = 75kN/m/m)

At this stage it is important to discuss the influence of the imperfection size and shape, as variation in the buckled wavelength could influence the relative effect of the imperfection. It should be noted here that the DNV guidance does not specify the shape of the imperfection to be used in the buckling analyses. Three imperfection types of equivalent amplitudes are examined here: the mode defined by Taylor and Gan (1986) and used in the tests thus far (I1); a simple cosine imperfection (I2), and a Gaussian peak imperfection (I3). The cosine imperfection, adopted in a buckling model by Croll (1997), assumes the continuously supported imperfect profile takes form of the dominant buckling mode:

$$v_{0,I2} = \frac{v_{om}}{2}\left(1 + \cos\frac{2\pi x}{L_o}\right) = v_{om}\left(\cos^2\frac{\pi x}{L_o}\right) \tag{4.17}$$

The third, Gaussian peak imperfection is given by:

$$v_{o,I3} = \frac{a}{\sqrt{2\pi\sigma}}\,exp\left(\frac{-x^2}{2\sigma^2}\right) \tag{4.18}$$

$$\text{where } a = \frac{v_{om}L_o}{2}$$

A standard deviation of $\sigma = 0.1948L_o$ was found to provide the best fit to a cosine function (Blakeborough, 2012). By computing the cosine Fourier transform of each imperfection profile, the equivalent eccentricity of each type could be calculated for a range of buckled wavelengths (see Figure 4-11). This eccentricity calculation allows for the relative influence of the imperfection size and shape on the buckling response to be compared for the three types. For the Gaussian peak this equivalent imperfection is calculated as follows:

$$e(\lambda) = \int_0^\infty v_o \cos\frac{2\pi x}{\lambda}\,dx = \int_0^{L_o/2} v_o \cos\frac{2\pi x}{\lambda}\,dx \tag{4.19}$$

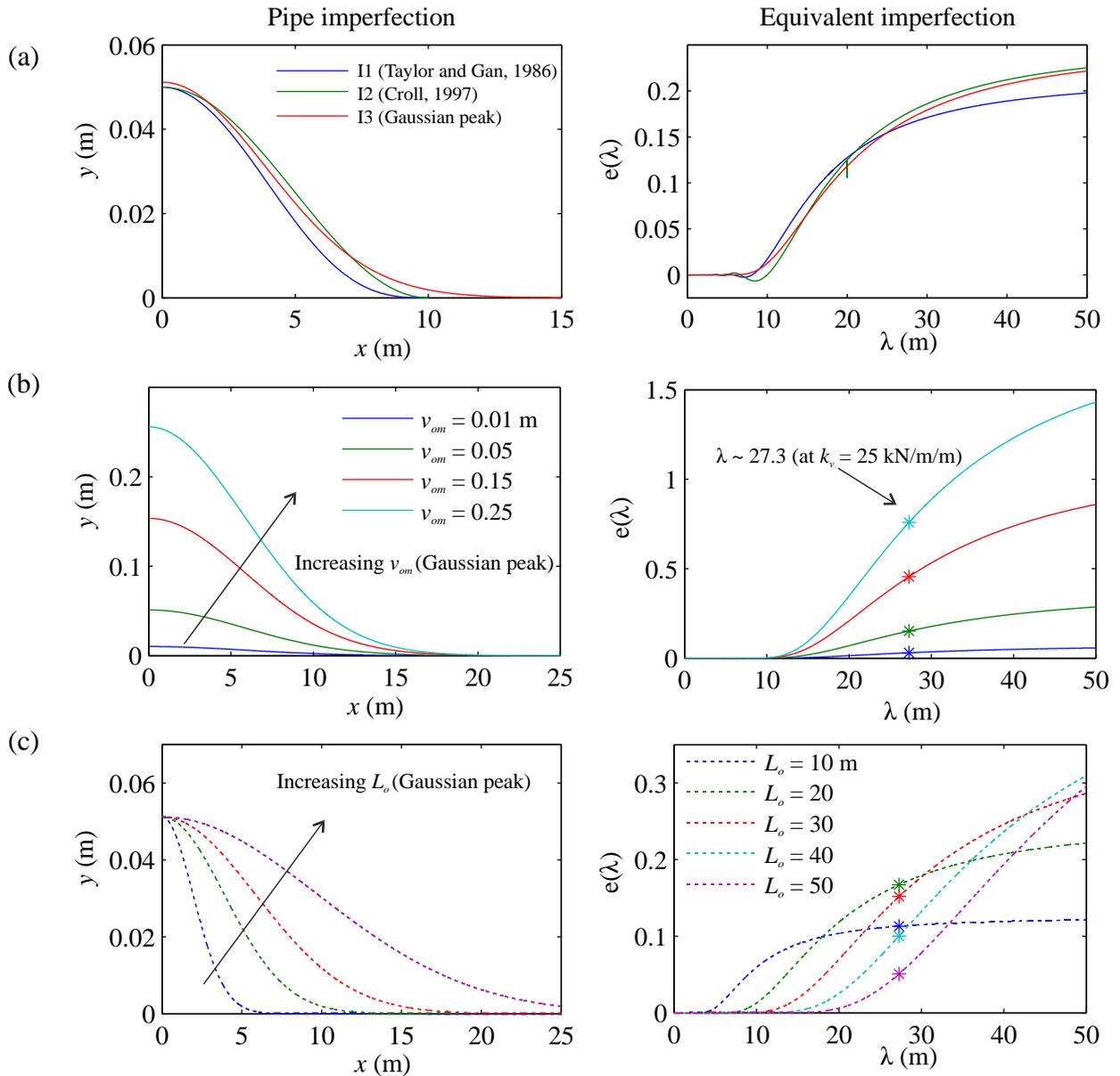$$e(\lambda)_{I3} = \frac{a}{2}\exp\left(\frac{-2\pi^2\sigma^2}{\lambda^2}\right) \tag{4.20}$$

Figure 4-11 Varying pipe imperfection: (a) type; (b) height ; (c) length and equivalent eccentricity as a function of buckled wavelength e(λ)

The actual and equivalent imperfection functions are shown for each of the three assumed profiles in Figure 4-11 (a). From the figure it can be seen that only the Gaussian equivalent imperfection curve increases monotonically with the buckled wavelength; the other two change sign at small wavelengths. In order to avoid unexpected behaviour of the pipe as the vertical spring stiffness is changed (which alters the buckled wavelength), smooth and monotonic behaviour of the eccentricity function across different wavelengths is necessary.

The Gaussian peak is the only shape that meets this requirement and thus, this imperfection type was chosen for the subsequent studies.

In several tests examining the variation of the imperfection height, v_{om}, and length, L_o (see Figure 4-11 (b) and (c)), similar behaviour to that observed in previous studies occurred (Taylor and Gan, 1986; Croll, 1997). Small imperfection heights have a higher buckling load and a more brittle response, while larger values of v_{om} have a smoother response at lower buckling loads, as well as greater axial feed-in with higher vertical displacements at the imperfection (i.e. a more localised response). Typical results for this parameter are given in Figure 4-12 and Figure 4-13. The wavelength of the imperfection, L_o, has a lesser influence; however, the relative eccentricity diagrams illustrate that the relative influence of L_o will change depending on the buckled wavelength (i.e. on the spring stiffness, k_v).
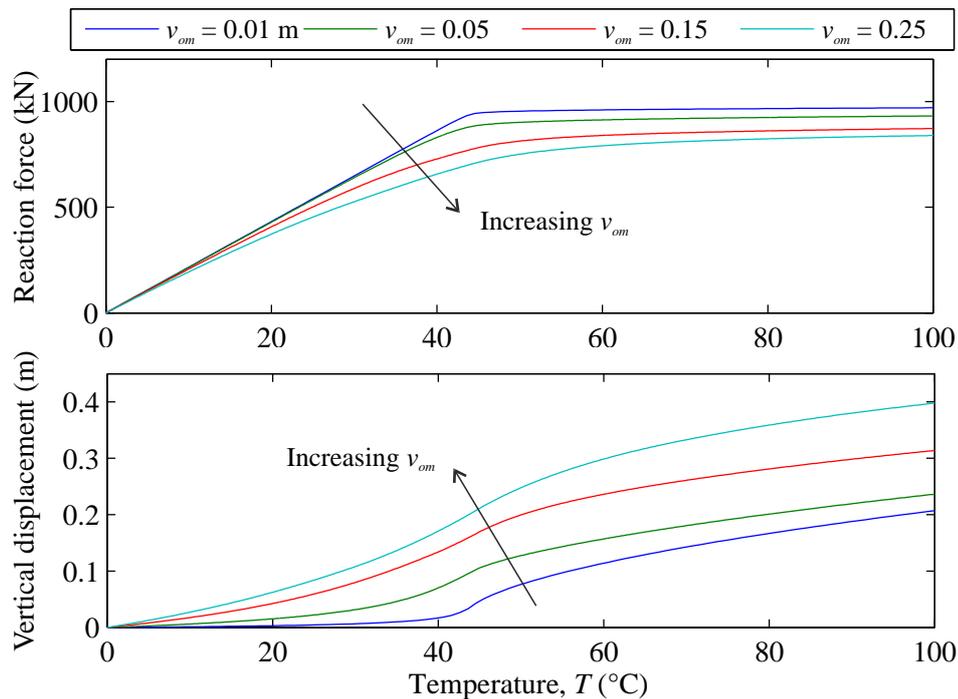

Figure 4-12 Response at pipe centre: varying v_{om} (L_o = 30 m, k_v =25 kN/m/m, F_a = 1.6 kN/m, k_a = 400 kN/m/m)
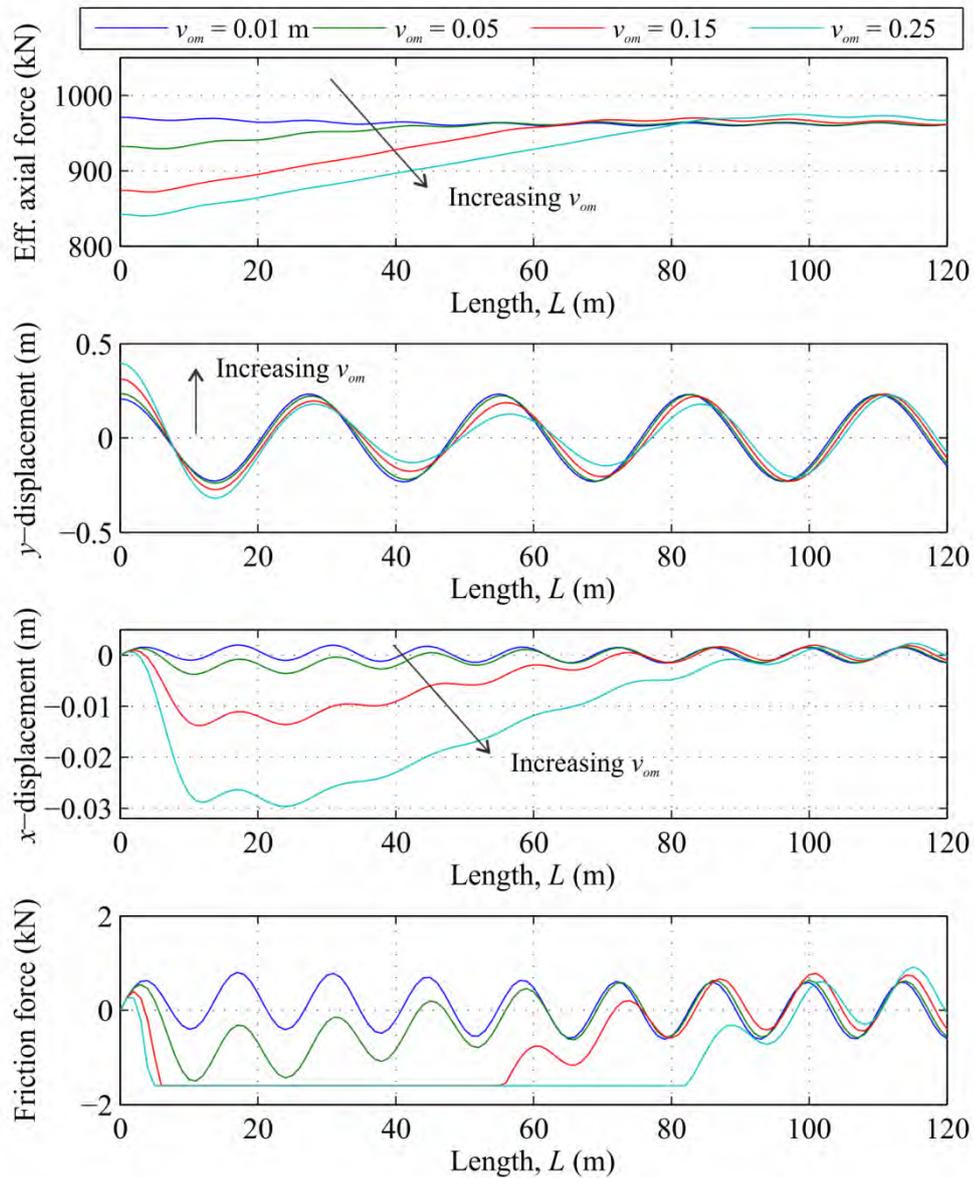
Figure 4-13   Axial force and displacement vs. length at T = 100°C : varying v_{om} (L_o = 30 m, k_v =25 kN/m/m, F_a = 1.6 kN/m, k_a = 400 kN/m/m)

4.1.5.2.   Local vs. global imperfection

While imperfection studies in the literature generally focus on localised imperfections of varying lengths and amplitudes, another possible cause of buckling could be numerous small undulations in the seabed surface over a long stretch of pipe. This might be particularly critical if the wavelength of these undulations is similar to the buckled shape of the pipe. Using the same approach as above, an equivalent cosine imperfection over the pipe length was identified (I4), with:

$$v_o = v_{eq} \cos \frac{2\pi x}{\lambda} \qquad (4.21)$$

$$e(\lambda)_{I4} = \int_0^\lambda v_{eq} \cos^2 \frac{2\pi x}{\lambda} \, dx \qquad (4.22)$$

$$e(\lambda)_{I4} = \frac{\lambda v_{eq}}{2}$$

Figure 4-14 presents two tests with k_v values of 5 and 25 kN/m/m, and the base imperfection of $v_{om} = 0.05$ m and $L_o = 20$ m. The Gaussian imperfection tests were run to determine the buckled wavelengths, which were 42 and 27 m, respectively. For these wavelengths, the equivalent cosine amplitude, v_{eq}, was calculated by equating the values of $e(\lambda)$ in equations 4.20 (Gaussian peak), and 4.22. The same two cases were run with this smaller amplitude cosine imperfection defined along the entire length of pipe. Plots from these tests illustrate that while the reaction forces at pipe centre are comparable, axial forces and displacements along the pipe differ significantly (Figure 4-14 and Figure 4-15).

Figure 4-15 plots the axial forces and vertical displacements along the pipe at various temperatures for $k_v = 25$ kN/m/m. Prior to buckling, the axial forces for both imperfection types are similar. For the cosine imperfection, as the temperature increases the axial force and vertical displacements increase uniformly along the pipe (up to the virtual anchor point) until the buckling load is reached; at this point the pipe begins to buckle uniformly. In the localised imperfection case, however, when the buckling force is reached at the centre, the displacement at this point increases rapidly. Away from the centre, the axial force must increase further in order for the buckle to propagate. Therefore, at a given temperature the displacement of the local imperfection is greater at the centre than at any location in the global case, but is less further along the pipe. This is due to the uniform but smaller amplitude displacement of the cosine imperfection along its length. The results of this comparison suggest that if large displacements are of primary concern, the localised imperfection case is

more critical than the equivalent multiple wavelength imperfection. For this reason, the localised (Gaussian peak) imperfection was used for all further tests.
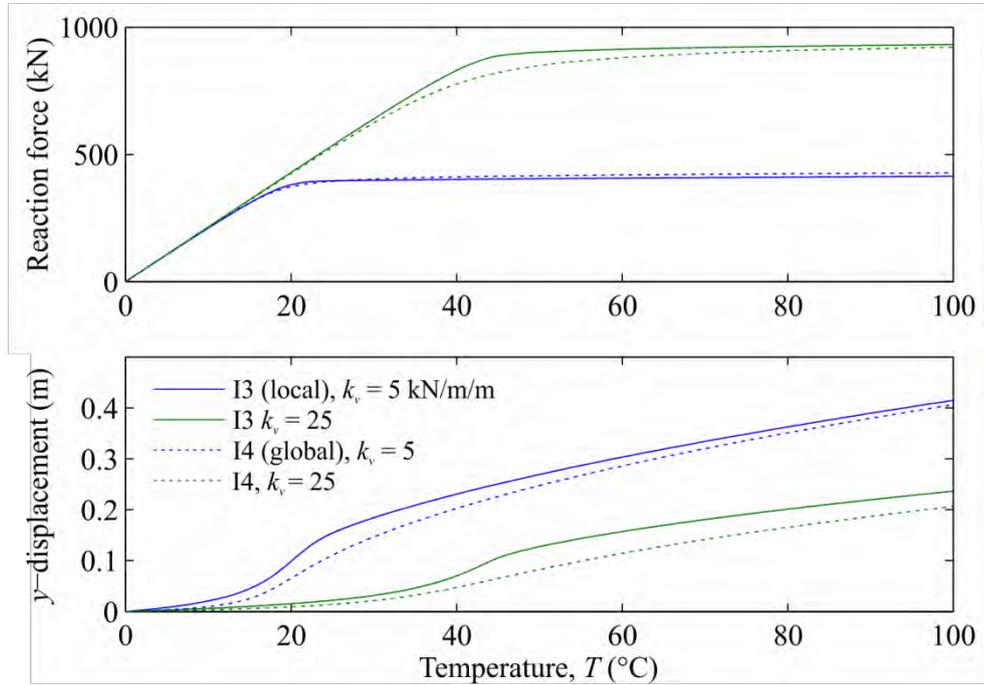

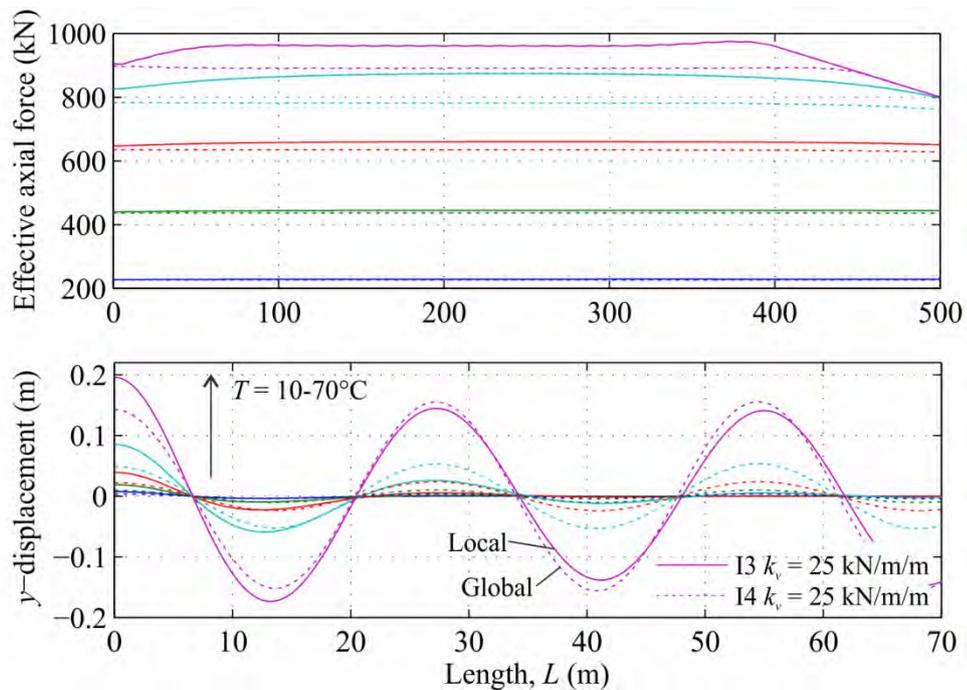*Figure 4-14 Response at pipe centre: local vs. global imperfection*

Figure 4-15 Response along the pipe length at various temperature steps: local vs. global imperfection

133

4.1.6. Limiting soil force

The final stage of the preliminary study was to introduce a limiting force to the linear vertical springs, to simulate the peak soil force at a given burial depth. This part of the study investigates the effect of various peak values, along with several vertical stiffnesses. The axial spring parameters were carried forward from the previous tests $(k_a = 400$ kN/m/m and $F_a = 1.6$ kN/m) and, as discussed in the preceding section, a Gaussian peak imperfection was used, with approximate values $v_{om} = 0.05$ m and $L_o = 30$ m.

To justify the selection of the peak force values in these tests, the vertical spring forces in linear tests (with no limit) are plotted against temperature for a range of k_v values (Figure 4-16). Within this temperature range, it can be seen that the spring force – and therefore, vertical displacement – is greatest at a low stiffness, $k_v = 100$ kN/m/m, where the pipe has only just buckled. At greater (and more realistic) stiffness values the spring force is much lower as the pipe displaces prior to buckling. It is then obvious that if a peak resistance is introduced that is higher than what is achieved in the spring, there will be no effect on the pipe response. Realistic values of peak soil resistance, however, could be as low as 0.5 kN/m – well within the range of spring forces shown below. The effect of a limiting spring force in this latter case is examined in the following section.
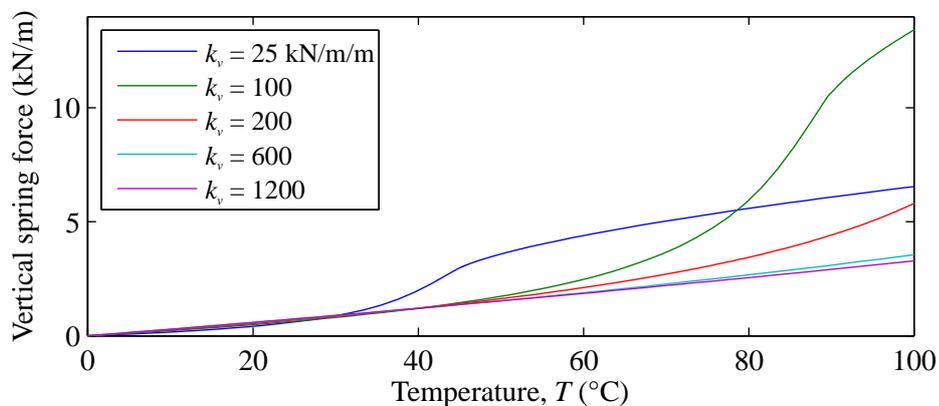

Figure 4-16 Vertical spring force at pipe centre – varying k_v, no vertical force limit ($F_a = 1.6$ kN/m, $k_a = 400$ kN/m/m)

For the previous aspects of the study, a static analysis step – where the temperature is uniformly applied – was sufficient; however, for typical tests with a limiting force, unstable localised buckling may occur (Maltby and Calladine, 1995b). This means that the amplitude of the buckle may experience rapid growth without further increase in temperature; in other words, it snaps unstably from one position to the next. A normal static numerical analysis typically cannot deal with this step, as shown in Figure 4-17. In a test with small increments (0.002), the analysis crashes immediately after the point of buckling, when the program detects a negative stiffness. For a coarser increment (0.02), on the other hand, the peak buckling load is bypassed. This issue can be avoided by using the modified Riks method (Abaqus, 2010), which allows the analysis of unstable problems by increasing (or decreasing) the applied load as a proportion of the original value. In Figure 4-17 it can be seen that when the peak load is reached, the analysis then reduces the temperature as the displacement continues to increase.

One disadvantage of this method is that time as a parameter is replaced by the imaginary 'arc length' value. In reality, this entire force-displacement path would not be followed; instead, when the peak force is reached the buckle would snap from one stable position to the other at the same temperature. A possible concern with this analysis is that the artificial decrease in temperature, occurring after the peak load, may cause the soil springs to unload (elastically) – a response which would not occur in the real (plastic) case. However, since the vertical displacement appears to increase monotonically beyond the peak (meaning that the vertical springs do not unload), this was not judged to be a significant issue. Therefore, for the purpose of this study – which is primarily concerned with the behaviour of the pipe up to the peak buckling load – it is thought that the Riks analysis method is adequate.

Despite the adoption of the Riks analysis method, the model experienced convergence issues in certain tests. This was addressed by:

(a) fine-tuning the analysis increments in each test;

(b) reducing the element length from 1 m; and,

(c) changing the element type from cubic Euler-Bernoulli to a linear Timoshenko beam element (Abaqus type B21).

To ensure that these changes did not alter the model behaviour, several of the previous simulations were re-run with the new element type, and the effect on the results was negligible.
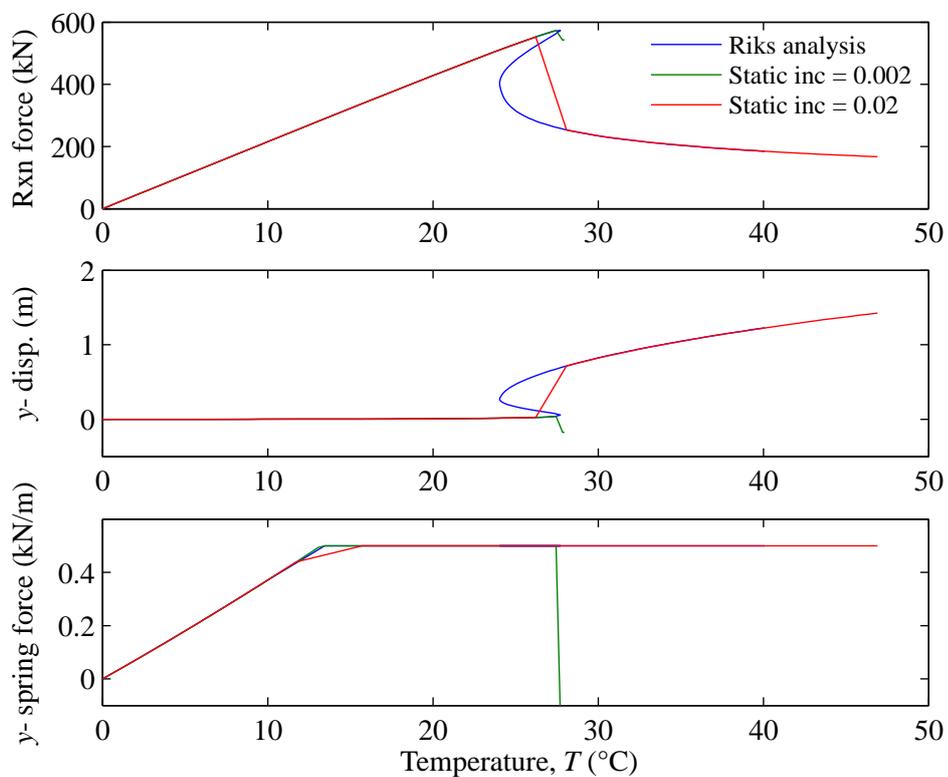
Figure 4-17 Response at the centre for different analysis methods and limiting soil force (F_a = 1.6 kN/m, k_a = 400 kN/m/m, k_v = 200 kN/m/m, F_v = 0.5 kN/m)

4.1.6.2. *Varying peak force and stiffness*

For a vertical stiffness of k_v =200 kN/m/m – an approximate lower bound for real soils – a variety of limiting spring forces were tested. Figure 4-18 shows the reaction force and vertical displacement at the centre vs. temperature for F_v ranging from 0.5 to 5 kN/m (limits which

136

caused the pipe to buckle within the 100°C temperature range). This figure confirms that an unstable snap-through process occurs when the peak soil force is reached, meaning that the axial force at the pipe centre drops quickly, and the displacement increases rapidly. This occurs at a lower buckling load than the critical value for linear springs.

The force and displacement response along the length of pipe for various temperature steps is shown in Figure 4-19, for $k_v = 200$ kN/m/m and $F_v = 3$ kN/m (the solid lines indicate increasing temperature up to peak, and the dashed lines indicate decreasing temperature post-peak). This figure confirms that the periodic failure mode obtained with linear vertical springs is replaced by a localised failure mode at the pipe centre. When the peak temperature is reached the vertical displacement, buckle wavelength, and axial feed-in to the buckle all increase, while the force at the buckle decreases as expected. This post-peak decrease in effective axial force only occurs at the centre (though over expanding length); further along the pipe the force is the same as at the equivalent pre-peak temperature.
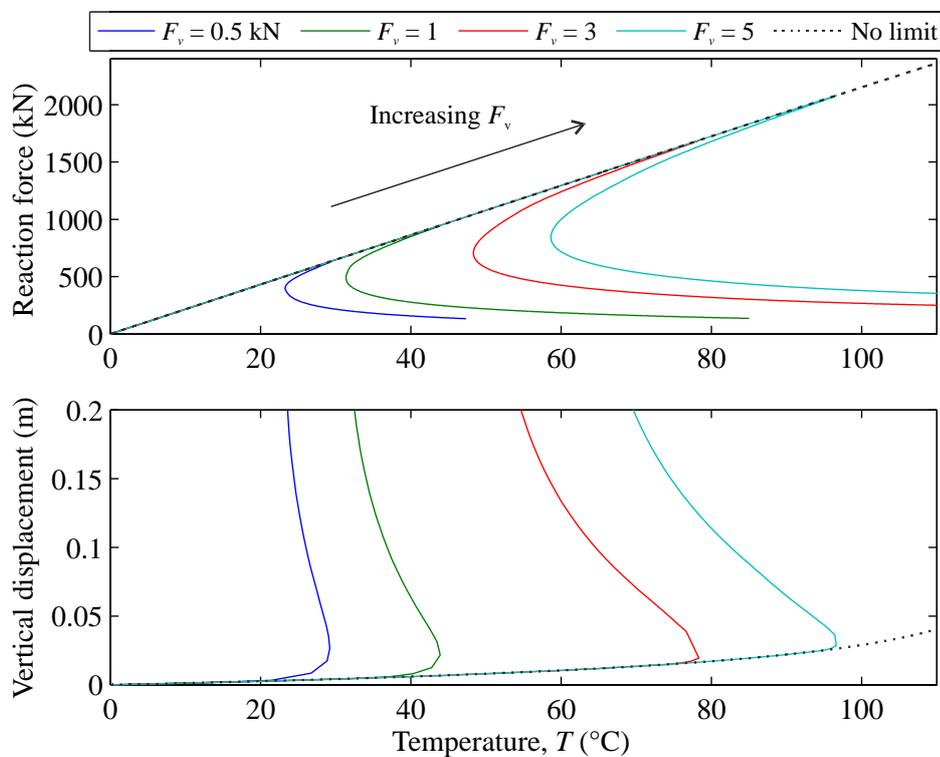
Figure 4-18 Response at the centre – varying vertical force limit ($k_v = 200$ kN/m/m, $F_a = 1.6$ kN/m, $k_a = 400$ kN/m/m)
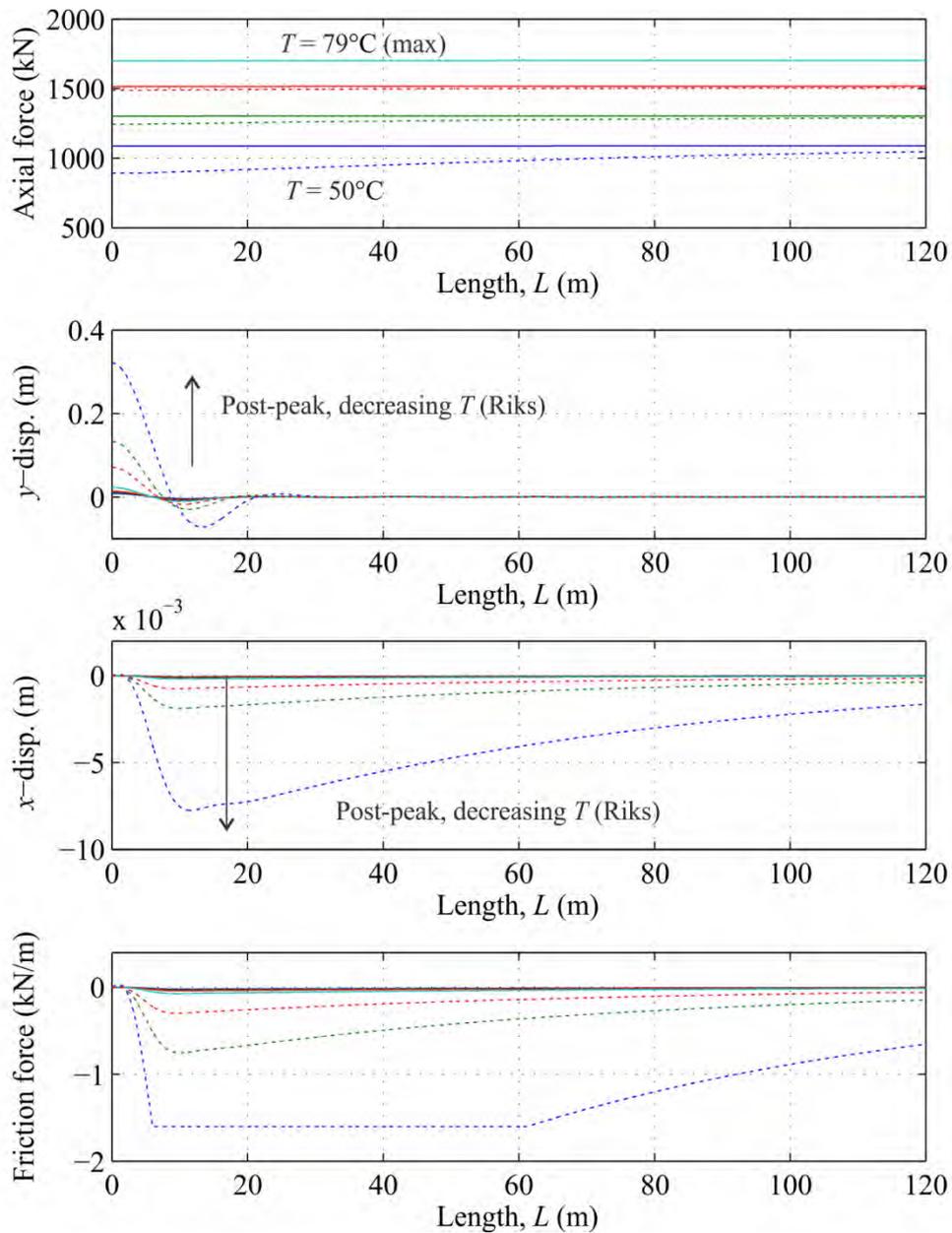
Figure 4-19   Axial force, displacement and friction force vs. length for varying temperature steps ($F_v = 3$ kN/m, $k_v = 200$ kN/m/m, $F_a = 1.6$ kN/m, $k_a = 400$ kN/m/m)

Figure 4-20 (a) plots the axial force in the pipe and the equivalent thermal load (calculated as P_o) against vertical displacement at the centre for the above tests. Additional tests with $F_v = 3$ kN and varying initial stiffnesses are shown in Figure 4-20 (b). The shapes of these curves compare well with the results presented in the literature, and are generally above the predicted minimum axial force required for localisation to occur (Maltby and Calladine, 1995b). While this predicted minimum (see equation 2.15) is independent of the mobilisation displacement of the soil (being related to the peak soil force and the height of the imperfection only), it is

clear from the figures that the initial stiffness of the soil affects the axial force at which localisation occurs (for a constant imperfection size). For the realistic soil characteristics tested, the buckling force is significantly above this minimum predicted value. It is also known from the literature that the size of the imperfection will influence the unstable buckling process, with several researchers demonstrating that an increase in the height of the imperfection will increase the stability of buckling (while lowering the required axial load), until a maximum force is not reached and localisation does not occur (Taylor and Gan, 1986; Maltby and Calladine, 1995b). This trend for increasing imperfection size is similar to that of decreasing vertical spring stiffness shown in Figure 4-20 (b).
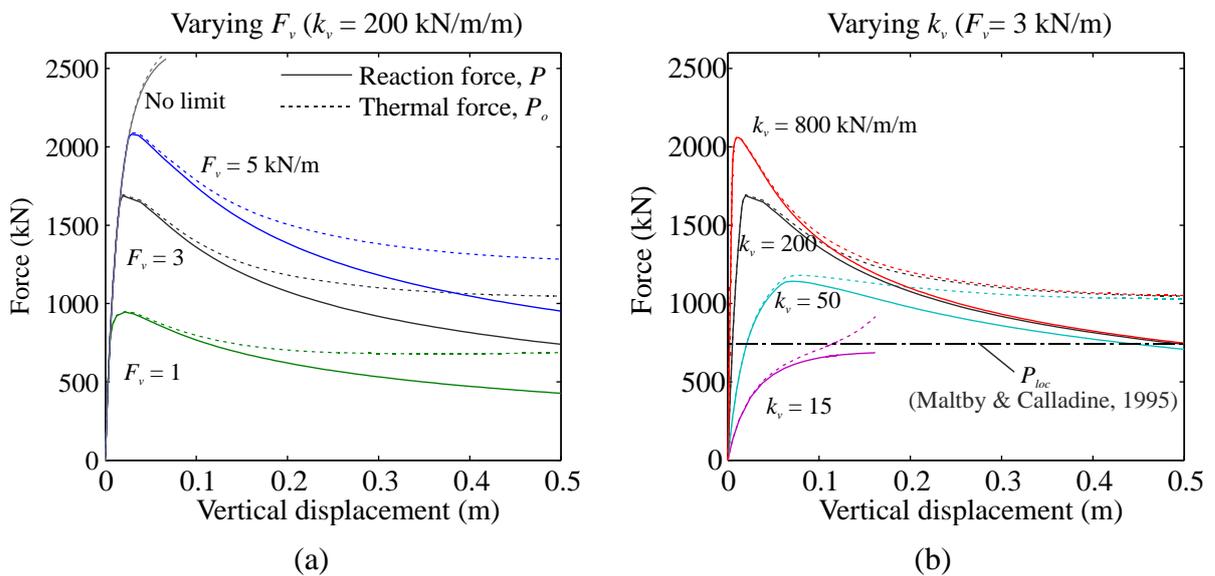
Figure 4-20 Reaction force and thermal load vs. vertical displacement for: (a) varying F_v; (b) varying k_v

4.1.7.   Summary

The preliminary FE analysis in this section investigated the influence of axial and vertical soil resistance (modelled using spring elements) on the buckling behaviour of a buried pipe. The axial soil resistance was shown to control the build-up of effective axial force in the pipe due to thermal expansion. Comparisons with force predictions along the pipe demonstrated that the axial force at the imperfection location falls increasingly below the predicted thermal load as the temperature increases prior to buckling. Despite the reduced force at the pipe

centre, when the thermal load approaches the critical buckling load, global buckling of the pipe occurs. This is characterised by a rapid increase in the vertical response of the pipe, propagating from the centre towards the free end. Increasing the stiffness of the vertical soil springs results in a higher critical buckling load and smaller amplitude buckles of shorter wavelength.

The effect of the size and shape of an initial pipeline imperfection was also examined. By calculating the equivalent eccentricity of different imperfection shapes, the relative influence of each type could be compared. Based on this analysis, a localised Gaussian peak imperfection type was found to ensure a consistent model response when the vertical spring stiffness is varied; thus, this imperfection type was selected for use in further studies in this chapter. As found by previous researchers, it was observed in the above tests that when the amplitude of the imperfection is increased, the buckling load is reduced, but a more stable response occurs.

The introduction of a limiting vertical soil force was found to alter the buckling behaviour (compared to the linear spring case), causing a localised snap-through response occurring at a lower axial forces. The results of these tests were consistent with observations on buckle localisation by Maltby and Calladine (1995b), but here the initial vertical stiffness of the soil prior to the limiting soil force being reached was shown to have a significant effect on the buckling load and the snap-through behaviour – much like the influence of the initial imperfection height.

4.2. Parametric study and comparison with experimental uplift results

The 2D finite element pipeline model – which was systematically assembled and tested above – can now be used as the basis of an investigation into the DNV recommendations for upheaval buckling analysis. The purpose of this work is to understand the influence of the parameters specified in the guidelines on pipeline buckling behaviour, such that the importance of predicting and defining the soil characteristics can be assessed. Specifically, the

focus is on how the uplift resistance and force-displacement response of the soil are accounted for in these guidelines. Following this, tests using experimental force-displacement data from Chapter 3 as model inputs are compared against the guidelines.

4.2.1. DNV parametric study

4.2.1.1. Model parameters

The model used in this study was for the most part the same as used in the previous section, except with respect to the primary component of interest, the vertical soil springs. Throughout this DNV study, the objective was to keep the model as true to the DNV guideline recommendations as possible; however, some simplifications were made for ease of computation, where deemed acceptable within the context of the study. As in the preliminary study, the internal pressure and the pipe self-weight were neglected. The self-weight in particular was not included due to the difficulty in ascertaining what its value may be during different stages of the buckling process. In fact, it is possible that under some circumstances, changes in the pipe and soil relative density will mean that the net external force on the pipe is upward (e.g. soil liquefaction could lead to pipeline flotation). Additional simplifications were made with respect to the pipeline installation. The guidelines recommend that the downward stiffness of the soil be represented as a non-linear function that changes for installation and operation. Furthermore, the pipe should typically be modelled as stress-free in its undeformed shape, meaning that the deformation due to the initial imperfection would cause some initial stress in the pipe. Both issues were not addressed in this model, as these installation effects were not considered to affect the sensitivity study and direct comparison of results in this chapter.

Since the primary focus of this study is the soil resistance to vertical movement of the pipe, the vertical soil springs are the only variable that was changed at any point; all others variables were kept as defined here (unless otherwise specified). The pipe material properties

are given in Table 4-1, and the soil properties used for any calculations are those of Redhill 110. All other model properties are listed in Table 4-4 below. The uplift resistance was defined as a tri-linear curve using the DNV guidelines, with a peak resistance, R_{max}, mobilisation displacement, d_f, and shape parameters α and β (for the definitions of these parameters see Figure 2-9). In each test the downward stiffness was set equal to the initial upward stiffness. It should be noted here that the post-peak vertical soil response is not defined as the guidelines suggest, for this part of the study. As the pipeline behaviour up to peak buckling load is of primary interest, the resistance of the soil beyond the peak was instead kept constant at the peak value. The effect of a reducing post-peak resistance is addressed in section 4.2.2.

Table 4-4 Model properties for DNV parametric study

Variable	Properties			Description
Pipe	Pipe length	L	2200 m	Element length: <1m for first 200m of pipe, 10 m for next 2000m
	Left-side support condition	LHS	Zero rotation and x-displacements	'pipe centre'
	Right-side support condition	RHS	Zero y-displacement	'free end'
Axial soil springs	Stiffness	k_a	400 kN/m/m	Preliminary study
	Peak force	F_a	1.6 kN/m	
Imperfection	Height	v_{om}	0.05 m	Gaussian peak equivalent shape
	Length	L_o	30 m	

The sensitivity study in the following sections examines the effect of each of the uplift variables on the overall buckling problem. In each section, the variable in question is tested across a specified range, the remaining variables being set to a 'base case' value. While d_f, α, and β were all examined individually, the limiting soil force was calculated in each case depending on the variables H/D and f. The focus in these tests was the behaviour at the pipe centre (or the crest of the buckle) up to the point of buckling. Peak temperatures, axial forces and displacements were also recorded and are discussed. The details of the parametric testing programme are listed in Table 4-5.

Table 4-5 DNV parametric testing programme

Set	Parameter						Number of tests
	H/D	f	d_f	α	β	k_d	
Peak force	1-6	0.3	$0.008H_c$	0.75	0.2	-	6
	3	0.1-0.6	$0.008H_c$	0.75	0.2	-	4
	1-6	0.1, 0.6	$0.008H_c$	0.75	0.2	-	6
Mob. disp.	3	0.3	$0.002H_c$-$0.05H_c$	0.75	0.2	-	5
	6	0.3	$0.005H_c - 0.02H_c$	0.75	0.2	-	4
Stiff 1	3	0.3	$0.008H_c$	0.2-1	0.2	-	4
	3	0.3	$0.008H_c$	0.75	0.1-0.5	-	3
Stiff 2	3	0.3	$0.008H_c$	0.75	0.2	DNV	5
Total parametric tests							36

4.2.1.2. *Embedment depth and friction factor*

The results from the preliminary study demonstrate that the most significant variables in these tests are the embedment ratio, *H/D*, and the uplift factor, *f*, as these control the calculated peak resistance. For the first set of tests, the pipe diameter was kept constant and the depth of cover was varied; this cover was assumed to be constant along the pipe for a given test, regardless of the elevation of the imperfection. This means that increasing *H/D*, in addition to causing an increased peak resistance, has the secondary effect of slightly increasing the mobilisation displacement. The initial stiffness, however, remains approximately constant, as can be seen from the force-displacement definitions for the vertical springs at the pipe centre, plotted in Figure 4-21 (in kN/m). Figure 4-21 also shows the axial reaction force at the centre for increasing vertical displacements (as the temperature is increased). The figure confirms that the peak axial force achieved is related to the limiting spring force, while the initial rate of axial force-build up with vertical displacement corresponds to the initial spring stiffness. The location of the peak axial force (and onset of snap-through buckling) with respect to the mobilisation displacement of the soil appears to

vary with embedment ratio: at greater embedments the peak occurs shortly after d_f is reached, but at shallower depths, the pipe displaces for increasing distances at the limiting soil force before the peak axial force occurs.

Figure 4-22 plots the reaction force and displacement response at the pipe centre against temperature (the driving variable). Note that in this figure, vertical (y) displacements are shown in the bottom two plots; the middle plot shows the entire range of displacements, while the bottom plot shows only the pre-peak and peak displacements (a magnified view of the middle plot). The results show a similar build-up of the reaction force with temperature in the pre-buckling region of each test. This is followed by a snap through buckle to a much greater displacement, in all tests except $H/D = 6$. At this depth the displacement at the pipe centre stabilises prior to the peak soil force being reached. Both figures demonstrate that increasing the embedment ratio results in in an increasing reaction force and temperature required to cause buckling. A similar trend was observed in the tests with varying values of f, though the range of peak values is smaller (note that equation 2.18 for R_{max} contains H^2 and f).
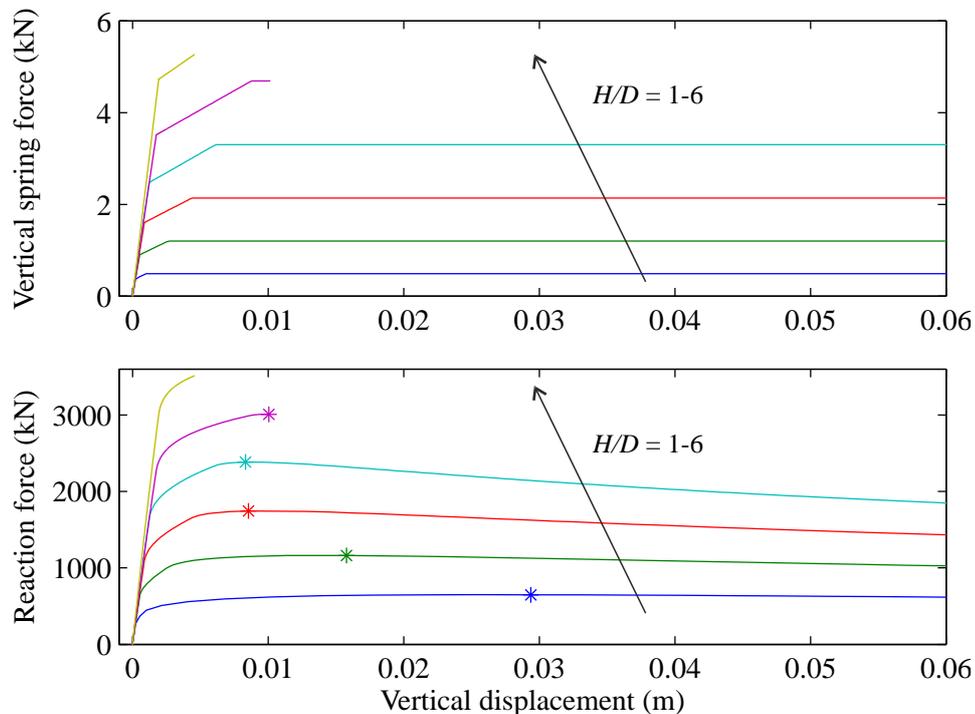

Figure 4-21 Vertical spring force and reaction vs. displacement, varying H/D (f = 0.3, d_f = 0.8%H_c, α = 0.75, β=0.2)
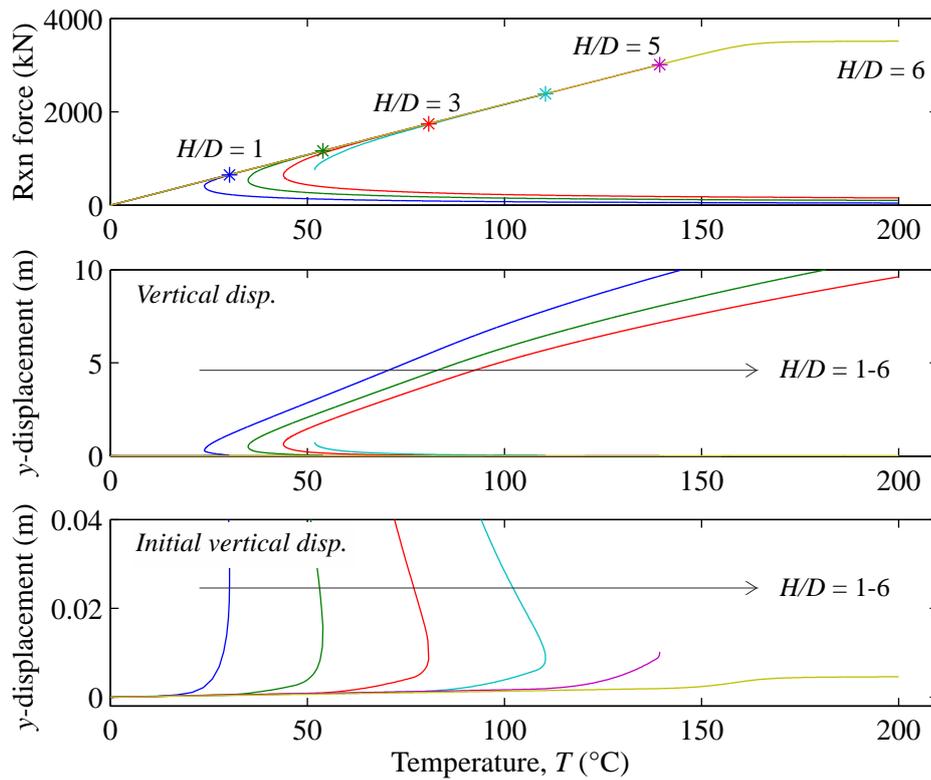
Figure 4-22 Response at the centre for varying H/D (f = 0.3, d_f = 0.8%H_c, α = 0.75, β=0.2)

4.2.1.3. *Mobilisation displacement*

In the preliminary study, the initial soil stiffness at a given limiting soil force for a bilinear soil spring was shown to influence the axial force (and temperature) required to cause buckling (see Figure 4-20 (b)). In the DNV approximation, adjusting the mobilisation displacement parameter has the effect of increasing or decreasing the stiffness of the first two portions of the tri-linear force-displacement curve. To study this variable, the value of the mobilisation displacement was varied from 0.2%H_c to 5%H_c (values exceeding the bounds of the DNV range). Note that the depth used to define this range, H_c, is measured to the pipe crown. This variable was also tested at two different embedment ratios: *H/D* = 3, where the pipe buckled in previous tests, and *H/D* = 6, where the pipe did not buckle in the first test.

Figure 4-23 plots the results for an embedment ratio of 3. The plots show that the mobilisation displacement (and corresponding spring stiffness) does affect the buckling force/temperature, as well as the rate of initial displacement. An increasing value of d_f results

in a lower force required for buckling, which occurs at a greater displacement. The results from tests at $H/D = 6$ are plotted in Figure 4-24. In this case, the difference in mobilisation displacement determines whether or not the pipe undergoes snap-through buckling. At mobilisation displacements within the DNV range (0.5% to 0.8%H_c), the pipe does not buckle, though the final stabilised displacement of the pipe increases with d_f. Once d_f reaches 2%H_c, however, the change in slope (occurring at a displacement, β, that depends on d_f) is sufficient to cause a run-away displacement at a relatively constant temperature.

4.2.1.1.   Initial stiffness

The effect of varying the initial shape parameters, α and β, was investigated at $H/D = 3$. The first set of tests varied α from 0.2 to 1, with both bounds resulting in a bilinear force-displacement curve (as shown in Figure 4-25 (a)). This varies the stiffness as well as the initial length of the first portion of the curve. The figure shows that the corresponding axial reaction force at the centre as the pipe moves vertically very closely mimics the shape of the vertical spring definition; however, despite having the same limiting soil force and mobilisation displacement, tests with lower values of α experience a lower peak buckling force and temperature. The initial rate of displacement varies significantly between the tests (Figure 4-25 (b)), though the displacements tend to converge after the peak force has been reached. In general, the peak buckling forces do not appear to be as greatly affected by this variable alone as when the mobilisation displacement was varied in the previous section. A second set of tests where β was varied, keeping α constant at 0.75 (all other parameters the same), was also carried out. From these it was found that varying β from 0.1 to 0.75 (which is equivalent to $\alpha = 0.2$ when $\beta = 0.2$) has a similar effect on the peak values as decreasing α only.
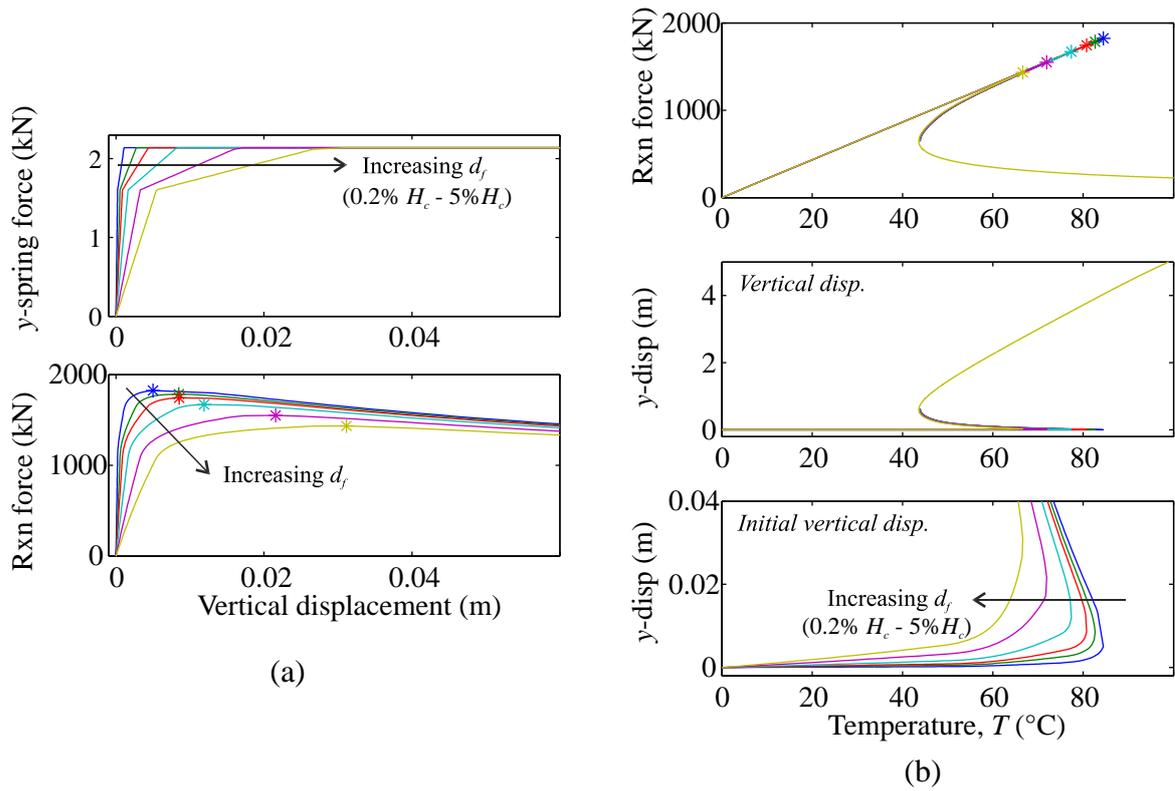
Figure 4-23 Response at the centre for varying d_f at H/D = 3, plotted against: (a) vertical displacement; (b) temperature
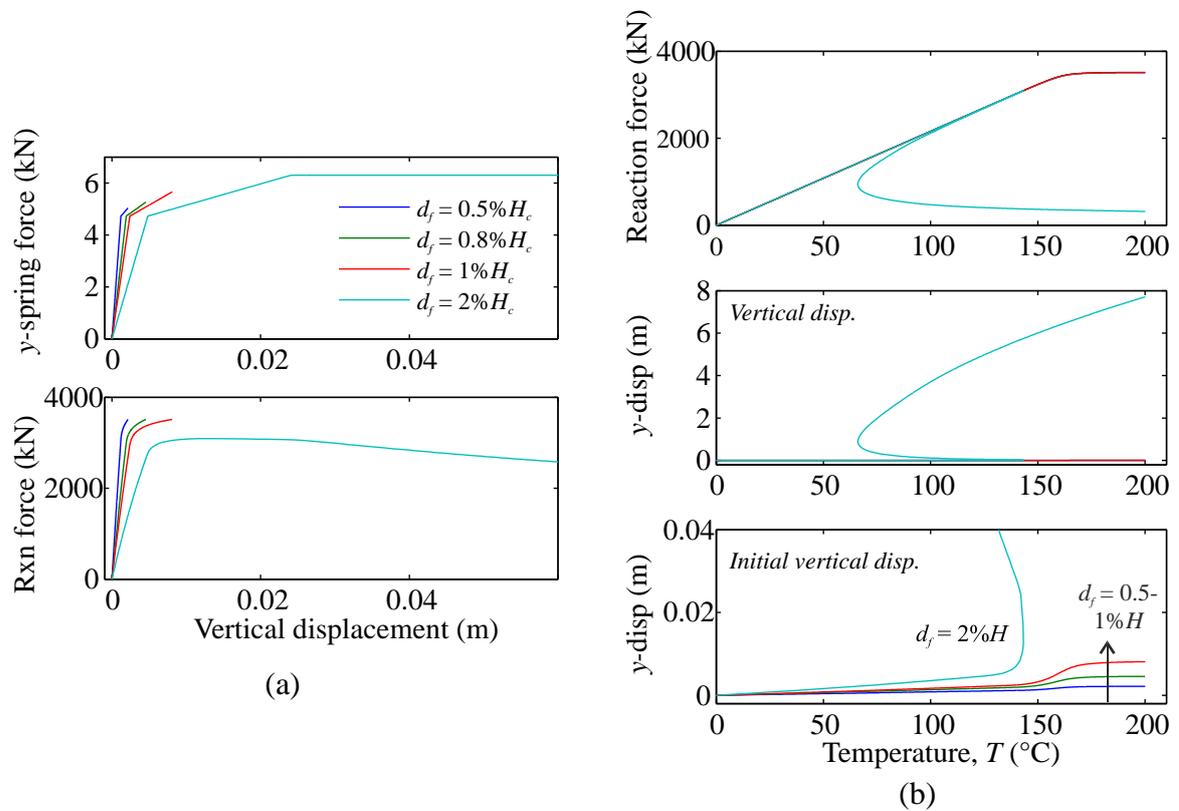

Figure 4-24 Response at the centre for varying d_f at H/D = 6, plotted against: (a) vertical displacement; (b) temperature
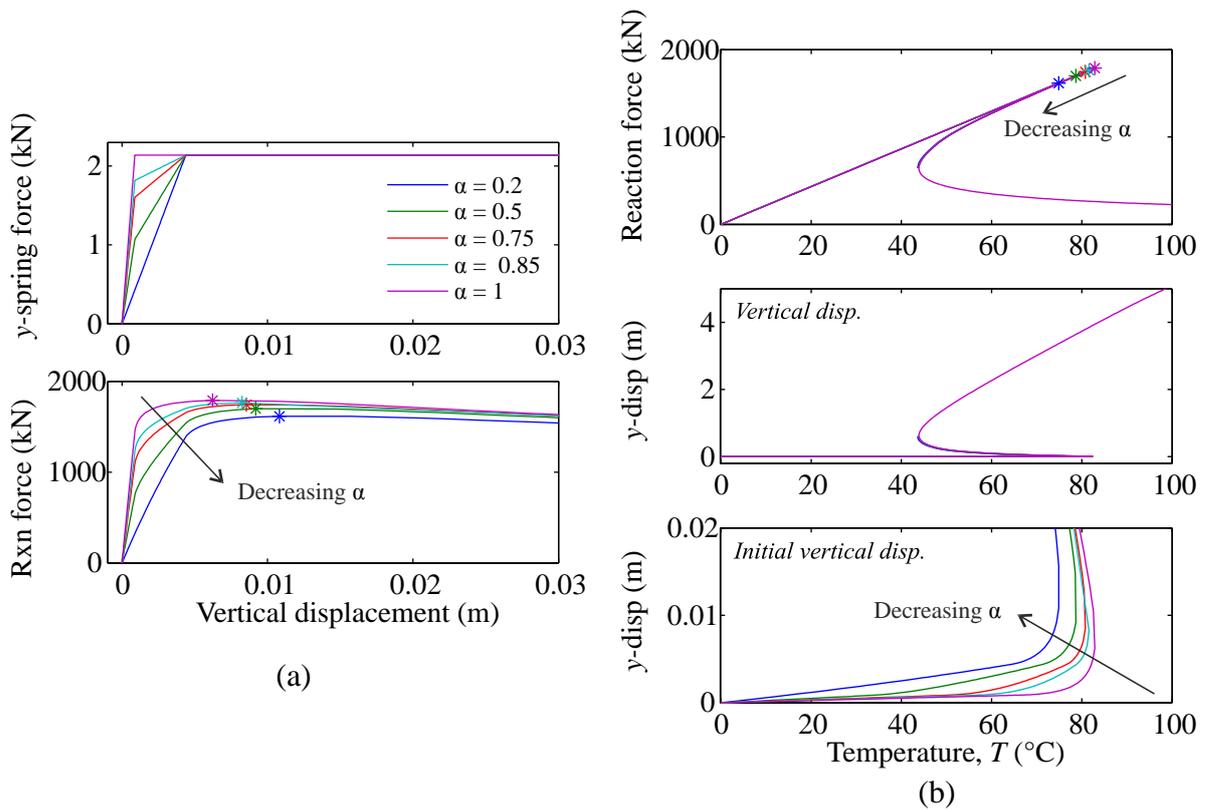
Figure 4-25 Response at the centre for varying α at H/D = 3, plotted against: (a) vertical displacement; (b) temperature

4.2.1.2.   *Downward stiffness*

In the tests described so far, the downward stiffness of the vertical soil springs was set equal to the stiffness of the first portion of the tri-linear uplift curve in each test. To test the influence of this parameter on the buckling behaviour, the downward stiffness was modified according to the simplified recommendations in the DNV guidelines, shown in Table 4-6. Although it is recommended that a full non-linear analysis of the downward soil response be carried out, for this study only linear behaviour is tested, since the pipe installation is not simulated. For calculating the downward secant stiffness, the guidelines distinguish between two conditions: 'intact', where backfill soil is present above the pipe while undisturbed soil is below; and 'homogeneous', where backfill material is both above and below the pipe.

Table 4-6 Typical vertical downward stiffness values (DNV, 2007)

Soil Type	k_d (kN/m/m) 'Intact conditions'	k_d (kN/m/m) 'Homogeneous conditions'
Loose sand	$D \cdot \left(750 + 670\dfrac{H_c}{D}\right)$	$D \cdot \left(960 + 1500\dfrac{H_c}{D}\right)$
Medium	$D \cdot \left(1700 + 1450\dfrac{H_c}{D}\right)$	$D \cdot \left(2850 + 3300\dfrac{H_c}{D}\right)$
Dense sand	$D \cdot \left(5300 + 4300\dfrac{H_c}{D}\right)$	$D \cdot \left(11800 + 9800\dfrac{H_c}{D}\right)$

The downward stiffness parameter, k_d, was varied in this section, testing values (in order of increasing stiffness) for: 'Loose-intact', 'Medium-intact', 'Dense-intact', and 'Dense-homogeneous'. For $H/D = 3$, these values range from 530-7950 kN/m/m. The base case stiffness for the previous tests is 1535 kN/m/m, which is closest to the 'Medium-intact' prediction (1162 kN/m/m). Reaction forces and vertical displacements at the pipe centre are shown against temperature in Figure 4-26, for the range of values tests. It can be seen that the downward stiffness has some influence on this response, with lower values of k_d resulting in a lower peak buckling force. This is consistent with analytical findings by Chiou and Chi (1993). The results imply that although the localised buckle tends to displace upwards at the centre due to the initial imperfection, the downward moving lobes on either side of the buckle (see Figure 4-19) also have an influence on the overall behaviour. Considering the large range of stiffness values tested, the difference between tests is not significant, though the result does suggest that a rigid seabed assumption is not conservative for this problem.
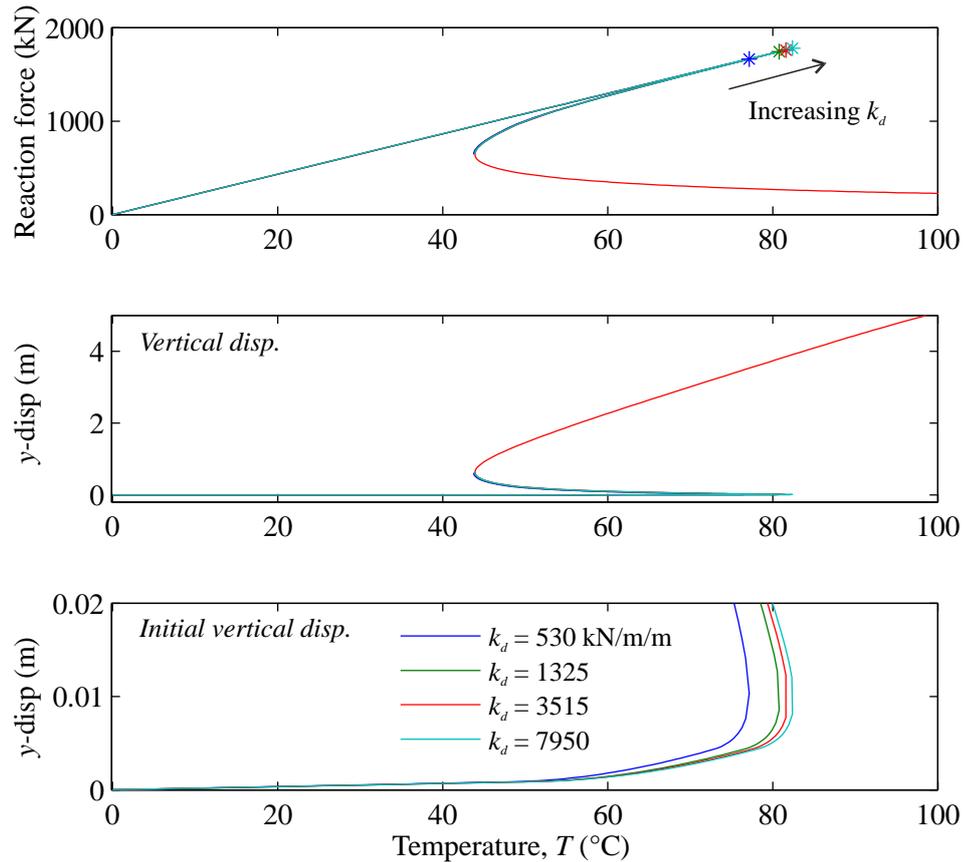
Figure 4-26 Response at the centre for varying k_d (H/D = 3, f = 0.3, d_f = 0.8%H_c, α = 0.75, β=0.2)

4.2.1.3. Summary

The peak buckling forces for the tests described in this section are plotted against embedment ratio in Figure 4-27. In this figure the influence of each variable is compared with the base case ($H/D = 3$, $f = 0.3$, $d_f = 0.8\%H_c$, $\alpha = 0.75$, and $\beta = 0.2$). Tests that appeared to stabilise rather than experiencing snap-through buckling are not plotted (as they did not have a distinct peak force); however, the approximate region where this begins to occur is highlighted. This suggests that once the limiting vertical soil resistance, in combination with the initial stiffness, are increased beyond a threshold region, the pipe configuration is stable.

As expected, *H/D* appears to have the largest effect on the buckling force, followed by the uplift factor, *f*. The influence of the uplift factor increases with embedment depth, which is also to be expected given how the peak soil force is calculated. Although the range of buckling forces for varying mobilisation displacements is much smaller, at high embedment

150

ratios, differences in the upward soil stiffness may determine whether the pipe experiences snap through buckling or self-stabilises (as seen in Figure 4-24). The effect of the shape parameters, along with the downward soil stiffness definition, is shown to be less important.
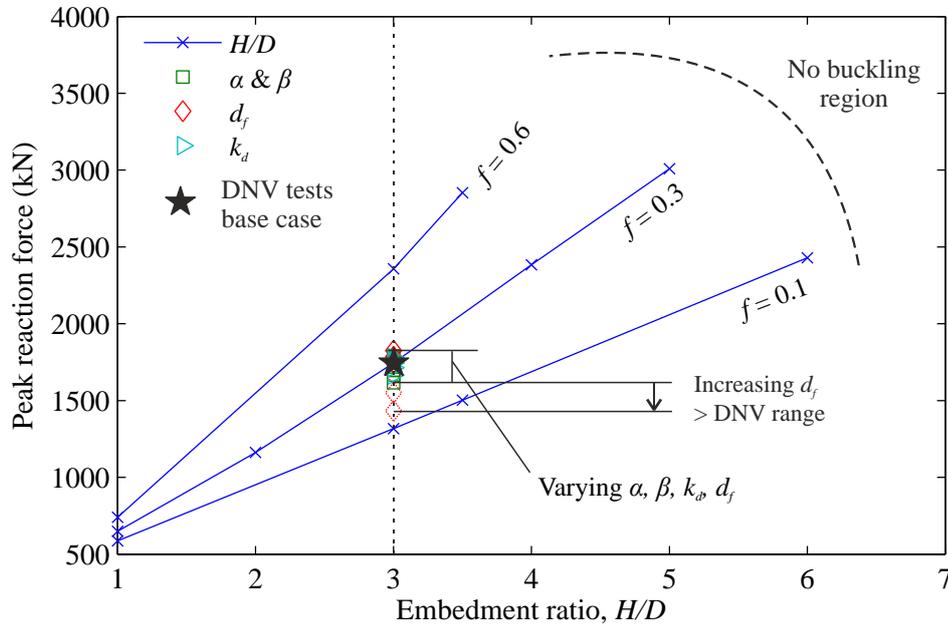
Figure 4-27 Summary of parametric study results - peak reaction force vs. H/D

In Figure 4-28 the displacement characteristics at the imperfection location are summarised for the parametric study. In (a) and (b) vertical displacements at the pipe centre corresponding to the peak buckling force are plotted against *H/D*; the displacement is normalised by pipe diameter in (a), and mobilisation displacement in (b). The first of these indicates that the upward stiffness has much more of an effect on the pipe displacements leading to buckling than it does on the critical force: the lower the stiffness, the greater displacement at which the pipe buckles. However, the point at which the limiting soil force is reached (d_f), does not necessarily trigger buckling immediately. For example, at shallower depths the pipe buckles at displacements many times the value of d_f (as seen in Figure 4-28 (b)). This is probably because in general, the buckling process is more stable under lower peak vertical restraint. Consequently, the change in slope of the spring force when d_f is reached is less likely to cause immediate catastrophic buckling.

151

In Figure 4-28 (c) the buckle crest length at peak force is shown for the same tests. This is defined as the combined length of pipe on either side of the centre that experiences positive displacements. It can be seen in the figure that this value is less than the initial 30 m width of the imperfection; this is likely to be due to the downward-displacing lobes that form on either side of the crest during buckling. The length of the upward-displacing crest scales with the height of the crest shown in (a), though the stiffness of the soil response has less of an influence. The downward stiffness also appears to have its greatest influence on this variable (higher values of k_d results in a longer buckle crest length).
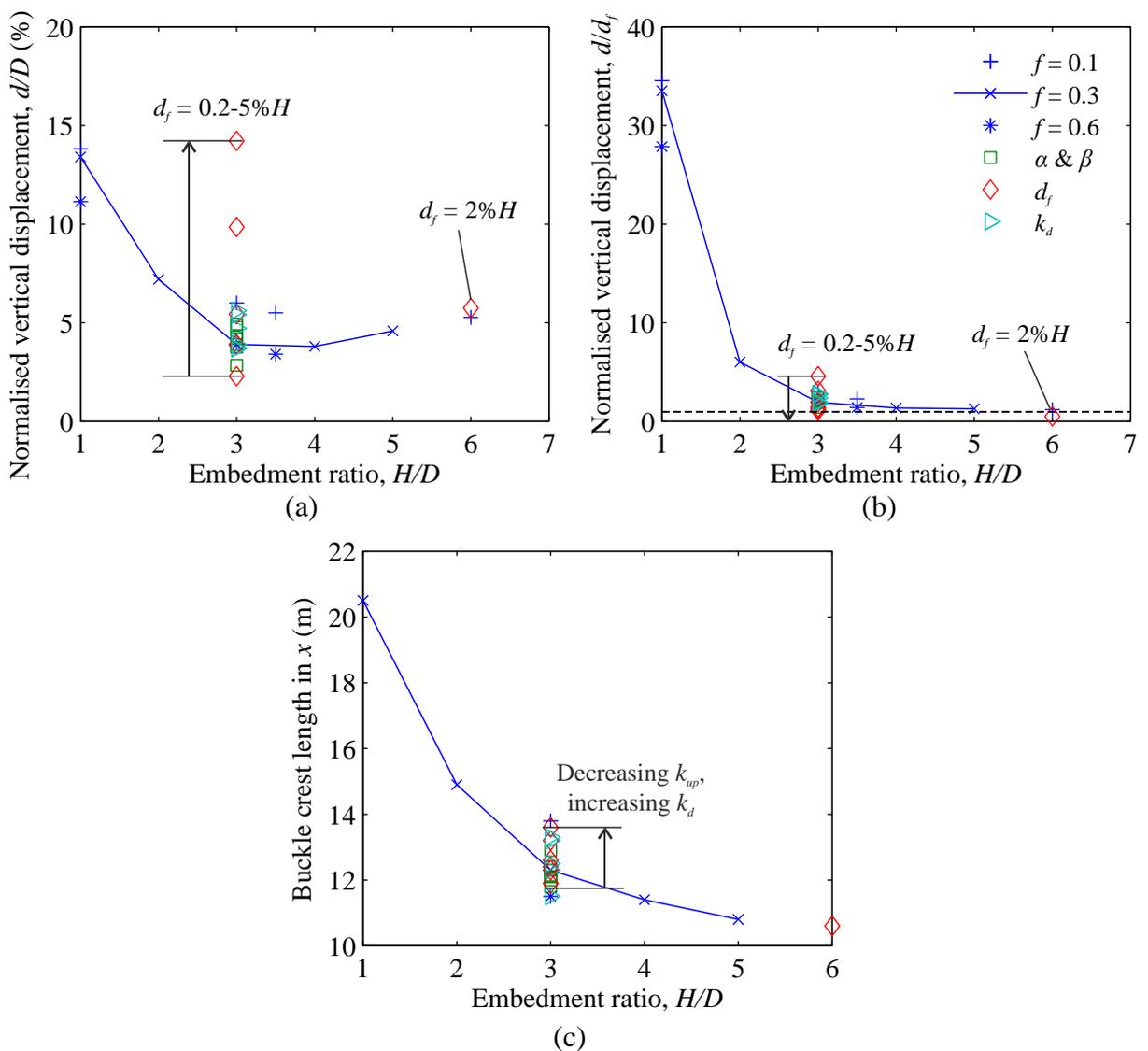

Figure 4-28   Summary of parametric study results – displacements at peak vs. H/D: (a) vertical displacement at the centre normalised by pipe diameter; (b) vertical displacement at the centre normalised by d_f; (c) buckle crest length.

4.2.2. Experimental results

In order to put the results of the DNV parametric study into context, the experimental force-displacement results from Chapter 3 were used to modify the model parameters. The uplift study in Chapter 3 demonstrated that the peak soil resistance and the initial stiffness have a clear dependence on the relative density of the soil, among other factors. Furthermore, the work highlighted the possibility of a flow-around mechanism replacing or combining with the sliding block mechanism at high embedments or low relative densities. By using experimental data to improve the model and making comparisons with the above parametric study, observations can be made regarding the influence of the soil parameters studied on the global buckling response.

4.2.2.1. *Drained experiments*

The force-displacement results for saturated Redhill 110 sand are considered in this section, as these uplift tests were designed to mimic true installation conditions in the field. Results from the previous chapter suggest that for this set of experimental results, the DNV tri-linear characteristic curve is an adequate framework for capturing the significant features of the soil response; however, the mobilisation displacements and shape parameters require modification to account for the influence of effective stress level and the governing failure mechanism. In the first set of tests here, the uplift parameters are used as defined in the guidelines, with only the ranges modified to fit typical force-displacement data. This enables comparisons with the DNV study in the previous section. Modifications to the definition of these parameters based on Chapter 3 results are then examined.

Two sets of saturated sand data were fitted with the DNV tri-linear parameters: tests at H/D = 3.5 with varying relative densities; and tests at varying H/D ratios with $RD = 0\%$. The experimental results typically show a much stiffer response than predicted by the DNV guidelines; whereas peak forces were generally captured by DNV range of uplift factors, the mobilisation displacements were typically smaller (~0.3%H_c). Two sets of curve fits were

estimated by selecting two values of β and varying α to obtain the best fit. The parameters defining the peak (d_f and f) were estimated from the data and kept constant in both sets. Note that the uplift factor was back-calculated from the experimental data using the actual unit weight for all tests; however, for consistency with the DNV parametric study, a constant unit weight (7.82 kN/m^3) was used to calculate the equivalent soil springs. This resulted in a slight under-prediction of the buckling force for the higher density tests in Figure 4-31. The softer estimate ($\beta = 0.2$) is shown in Figure 4-29 for varying relative densities at $H/D = 3.5$. As seen in the figure, an approximate post-peak response has been incorporated through one additional point, as suggested in the guidelines. The residual force was calculated in the same manner as the peak, but with the peak uplift factor reduced by α_f as follows:

$$f_r = \alpha_f \cdot f \tag{4.23}$$

The displacement at this point, d_{fr}, was then calculated as a multiple of the mobilisation displacement (the value given in the guidelines is 3). Finally, the last point in the force-displacement definition is a force value of zero at a displacement of H. All fitted parameters are listed in Table 4-7 along with the DNV recommended range for each parameter.
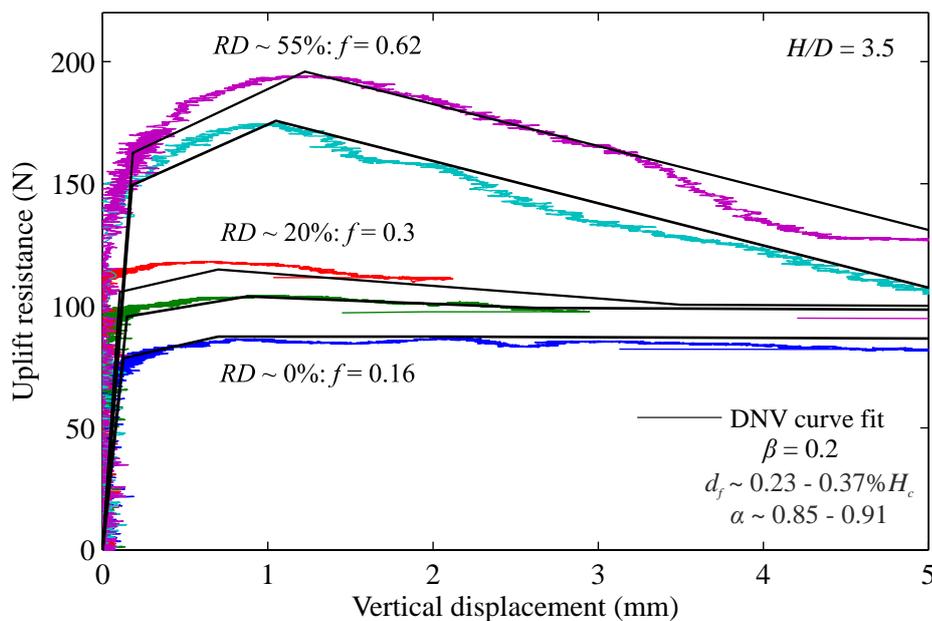

Figure 4-29 Experimental force-displacement and DNV fitted curves for varying relative densities at H/D = 3.5

Table 4-7 DNV tri-linear parameters fitted to saturated RH110 data

Set	H/D	RD (%)	Peak force and displacement		Stiffness Curve fit #1		Stiffness Curve fit #2		Post peak response	
			f [0.1,0.6]	d_f (%H_c) [0.5, 0.8]	α [0.65, 0.85]	β [0.2]	α [0.65, 0.85]	β [0.2]	d_{fr} ($\cdot d_f$) [3]	α_f [0.65, 0.75]
RD	3.5	0	0.16	0.29	0.72	0.1	0.85	0.2	3	1
	3.5	15	0.24	0.23	0.72	0.1	0.91	0.2	3	0.9
	3.5	20	0.30	0.23	0.70	0.1	0.90	0.2	5	0.75
	3.5	~45	0.55	0.35	0.70	0.1	0.85	0.2	5.2	0.34
	3.5	~55	0.62	0.37	0.70	0.1	0.85	0.2	5.6	0.28
H/D	1	0	0.13	2.0	0.88	0.1	0.9	0.2	3	0.75
	2	0	0.22	0.80	0.80	0.1	0.89	0.2	3	0.8
	3	0	0.19	0.36	0.78	0.1	0.87	0.2	10	0.85
	4	0	0.15	0.40	0.83	0.1	0.92	0.2	3	0.94
	4.5	0	0.11	0.21	0.76	0.1	0.8	0.2	3	0.94

The parameters in the above table were used to define soil springs for representative tests with the buckling model. A pipe diameter of 219 mm was used in the model for comparison with the ranges from the DNV study. This meant that values such as d_f were scaled with H_c according to the guidance. For the test at $H/D = 3.5$ and $RD = 0\%$, the two curve fits ($\beta = 0.1$ and 0.2) are compared with a multi-point fit to the force-displacement data (also scaled up proportional to the peak force and mobilisation displacement). Results for the response at the centre plotted against displacement are presented in Figure 4-30. Here it is shown that there is little difference in the response between the three tests in terms of the buckling force and the displacement at which it occurs, so either of the tri-linear approximations could be used to represent the force-displacement response to peak.

The curve fit with $\beta = 0.2$, which has the softest initial stiffness, experiences the lowest buckling load of the three cases; therefore, this curve fit is used for the remaining tests. A

summary of the buckling force results for the cases listed in Table 4-7 is presented in Figure 4-31. The figure shows that the peak buckling forces found using experimental inputs generally fall within the range of the DNV parameters, though slightly above the lower and upper bounds (likely due to the higher stiffness values). However, for loose soil, the buckling force moves from the $f = 0.3$ prediction line at low embedments towards the $f = 0.1$ prediction at higher embedments. This is due to the plateau observed in the experimental breakout factors at high embedments (see Figure 3-10 in the previous chapter). These results suggest that if the adapted VSM equation is used to predict the uplift resistance for modelling, a constant value of f cannot be used to represent a given density across varying embedment ratios. Furthermore, if the trend in the uplift resistance were to continue, it is possible that the peak buckling force could fall below the DNV lower bound.
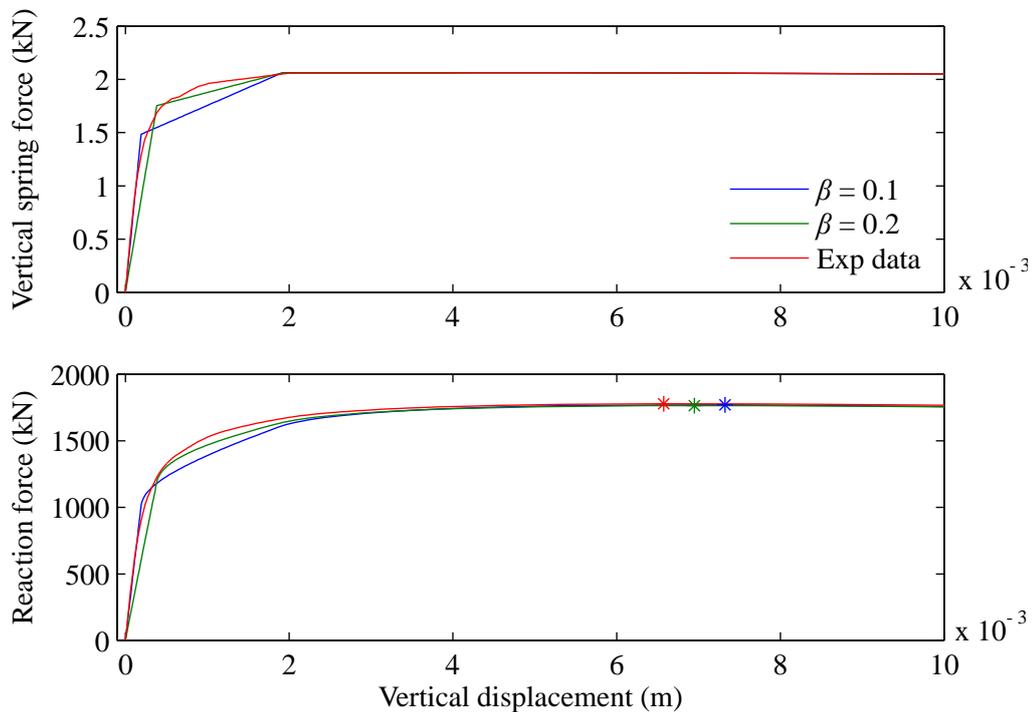

Figure 4-30 Response at the centre vs. vertical displacement for different curve fits – H/D = 3.5, RD = 0%: (a) vertical spring force; (b) reaction force
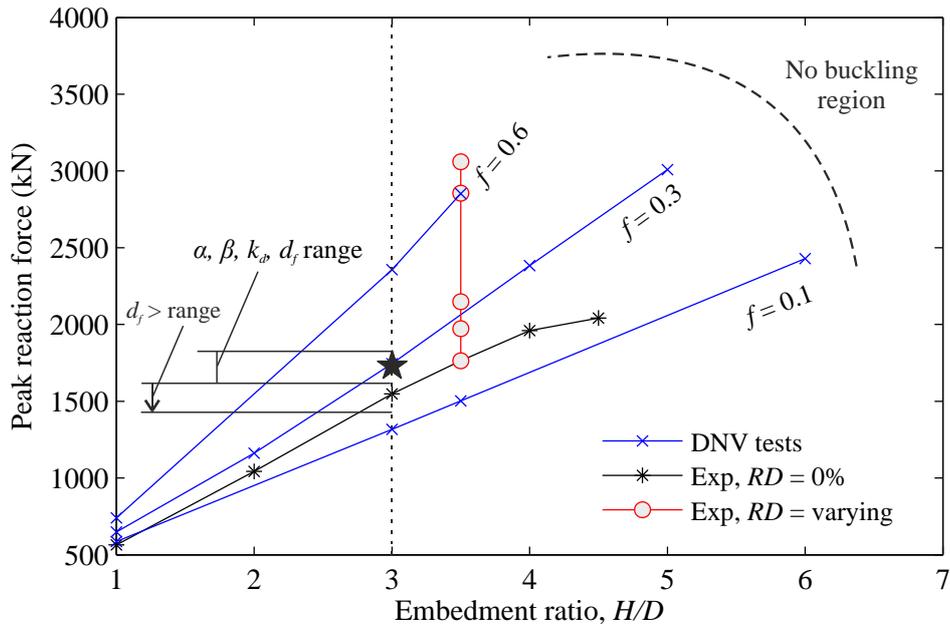
156

Figure 4-31 Peak reaction forces for experimental inputs (β=0.2) compared to DNV study results

The responses of two tests at $RD = 0\%$ are compared with the (approximate) corresponding cases from the DNV parametric study in Figure 4-32 ($H/D = 1$ and $H/D = 2$). While the response to peak is similar, the figure shows a significant difference between the tests in the post-peak region. This is due to the drop in soil resistance beyond peak that was defined in the experimental cases (in the DNV study the resistance was kept constant as the response up to the peak buckling force was of primary interest). It can be seen from the figure that if the post peak resistance is reduced to zero (simulating loss of cover as the pipe is uplifted), the snap-through buckling response becomes even more unstable. In Figure 4-32 (b), the displacement at which the soil resistance reaches zero (i.e. the buckle crest reaches the surface) is indicated. In both cases this occurs well before the Riks analysis returns to its 'real' force path. At the end point of the $H/D = 2$ test, it was found that pipe sections up to 100 m from the centre had experienced upward displacement, with 87 m reaching the 'surface' (though this is in an artificial region of the analysis – i.e. the temperature is decreasing). The implication here is that if the soil force is allowed to reach its peak resistance, catastrophic unstable buckling will occur. It is therefore of vital importance to define the peak resistance and pre-peak force-displacement response accurately in design calculations.

157
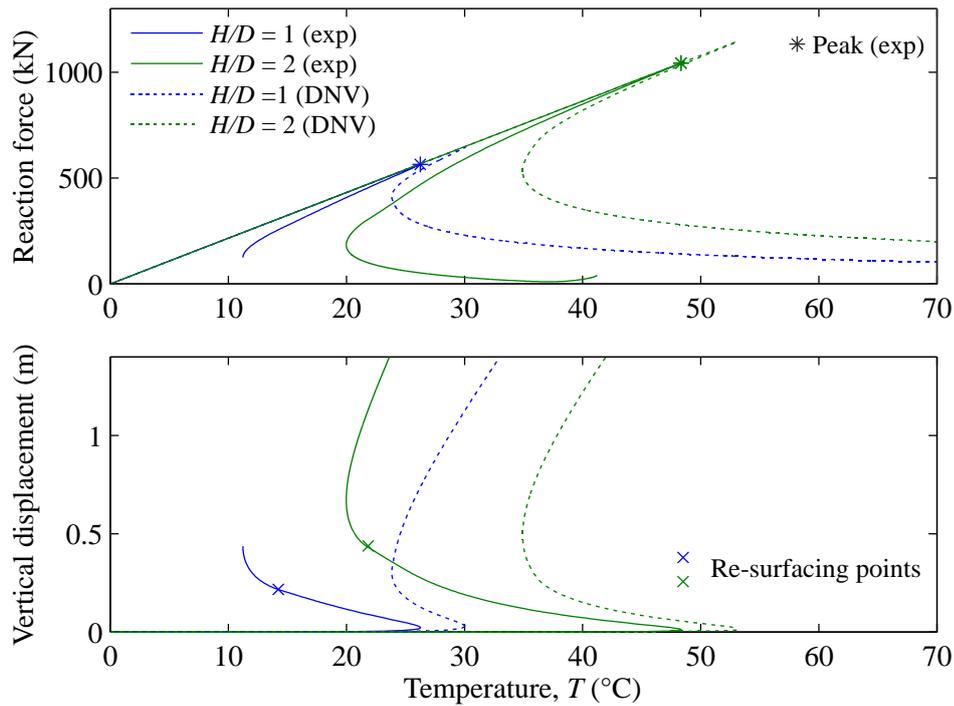
Figure 4-32 Response at the centre vs. temperature for varying H/D ratios – experimental inputs (β=0.2 curve fit)

4.2.2.2. Stress level effects

The above tests used experimental results from a model scale test programme in saturated sand to evaluate the DNV modelling recommendations and to examine the influence of embedment ratio and backfill relative density on the buckling response of the pipe. Based on the DNV guidance, the results from a model pipe of 100 mm diameter were scaled up to a pipe diameter of 219 mm – accounting only for changes in the embedment depth H that correspond to this. However, as discussed in Chapter 3, stress level effects may strongly influence the force-displacement response of the pipe. By increasing the pipe diameter by a factor of 2.2, the vertical effective stress level at a given H/D ratio will increase by the same amount. The stress ratio, defined as $(\gamma'H/p_r)^{0.5}$, would then increase the by the square root of this factor (~1.5). Though the stress level increase in the physical experiments was achieved by moving from saturated to dry sand conditions, a worst-case scenario would be to assume that similar effects could occur if the pipe diameter was increased. Of primary concern is the

increase in mobilisation displacements and the overall softening of the initial force-displacement response (in very loose sand) as the stress level is increased.

To examine the possible influence of the above on the buckling response of the pipe, several tests were carried out where the vertical spring response was modified according to uplift test results using dry Redhill 110. The most critical backfill conditions were considered (i.e. very loose fine sand at high embedment ratios). For the selected cases, the uplift response for the vertical springs was not fitted to actual test data as above; instead, the trends observed in the experiments were used to select values for the tri-linear characteristic curve. For embedment ratios of 3.5, 5, 6.5, and 8 (an overburden case), breakout factors were interpolated from Figure 3-37, and the corresponding uplift factors were calculated. Though the breakout factors used were obtained with relative density of 20% in the dry sand tests, the unit weight in these simulations was kept at 7.82 kN/m^3 ($RD =0\%$), for consistency with the previous results. Next the mobilisation displacements, d_f/D, were estimated from Figure 3-29 according to the calculated stress ratio. Finally, the displacement of the slope change in the tri-linear curve (d_k/D) was located at $1.5 \cdot \tilde{\sigma}_v$ as was suggested in the previous chapter. The corresponding force value (as a percentage of the peak force) was selected from Figure 3-31, again according to stress ratio. The above soil spring parameters for four tests are listed in Table 4-8. As in the previous sections, the downward stiffness was set equal to the initial upward stiffness.

Table 4-8 Tri-linear parameters estimated for Redhill 110 , scaled for stress level effects

H/D	Stress ratio $\widetilde{\sigma_v}$	Peak force[1] N_{ult}	f	Mob. Displacement[2] d_f/D (%)	d_f (m)	Stiffness[3] at $1.5 \cdot \tilde{\sigma}_v$ α	d_k/D (%)	d_k (m)
3.5	0.25	1.62	0.177	27.7	0.061	0.678	0.367	0.000804
5	0.29	1.62	0.124	50.9	0.111	0.585	0.439	0.000961
6.5	0.33	1.64	0.098	71.8	0.157	0.505	0.500	0.00101
8[*]	0.37	1.54[*]	0.068	90.5	0.198	0.434	0.555	0.00122

[1] Estimated from Figure 3-37; [2]Estimated from Figure 3-29; [3] Estimated from Figure 3-31;[*]Overburden test data.

The spring force (input) and reaction force for each of the above tests are plotted in Figure 4-33. The figure shows that despite the nearly constant breakout factor, the peak spring force continues to increase with embedment depth. Compared to the unscaled experimental data at *H/D* = 3.5 (see Figure 4-29), the softening of the force-displacement response in the springs is significant. In fact, the difference in stiffness is so great at the location of the slope change that buckling occurs well before the peak soil force is reached. Despite the differences in resistance provided by increasing the embedment depth, buckling occurs at close to the same force and vertical displacement in each test.

Finally, the peak forces for the modified experimental inputs are compared with the results from previous tests. At *H/D* = 3.5, the predicted buckling force is lower than the results found previously. This trend can also be observed at greater embedment depths than tested with the saturated sand and, as expected, the peak axial force falls well below the DNV predictions at these depths. The results confirm that the sliding block mechanism assumed in the guidelines may not adequate for all conditions. Predictions for the flow-around resistance, as well as the influence of stress level on displacements, must be included in the model to correctly predict the buckling force for a given set of installation conditions.
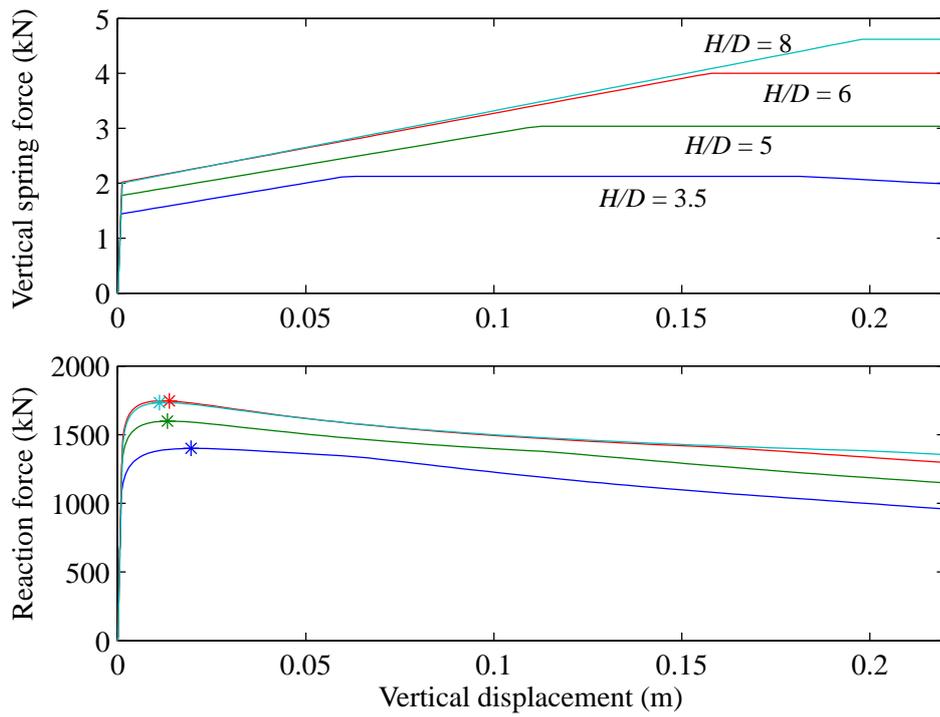
Figure 4-33 Response at the centre vs. displacement for varying H/D ratios – stress level effects
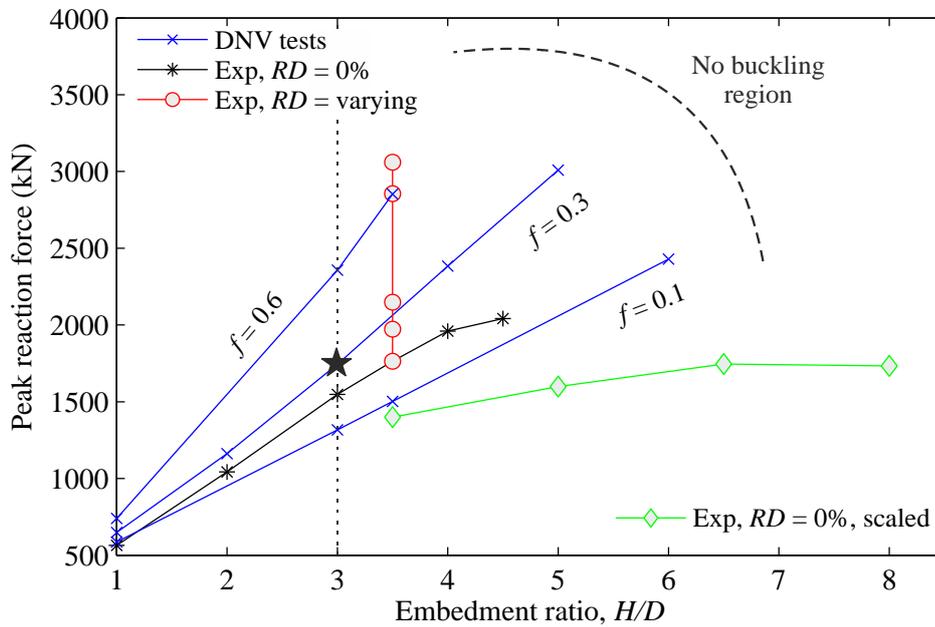

Figure 4-34 Peak reaction forces for scaled experimental inputs (stress level effects) compared to previous results

4.2.2.3.   Rate effects

Though rate-effects were an important aspect of the uplift experiments described in Chapter 3, it remains a difficult problem to incorporate them into the computational modelling of upheaval buckling. The physical experiments demonstrated a high sensitivity of the pore-water response to higher rates of pipe movement, manifesting in very rapid drops in uplift resistance. It is clear from both the preliminary and parametric buckling study that any significant reduction in the stiffness of the soil would directly reduce the resistance of the pipe to upheaval buckling, and possibly even cause immediate buckling. For modelling purposes, however, not only would this sudden change in stiffness be likely to cause convergence issues, but with Riks analysis 'time' is not a real parameter; thus, an evaluation of the speed of movement cannot be done with the model in its current form. Despite this, there was indication in the preliminary study of a sharp increase in the rate of displacement immediately prior to buckling, in the linear region of the soil stiffness. It follows that this sharp increase in 'rate' could cause a pore pressure response, resulting in partially drained soil resistance. Furthermore, external influences such as pipe vibration or seismic excitation could result in excess pore pressures developing in loose, liquefiable soil. Accordingly, a brief study of the 'uplift rate' variable was undertaken in this section.

In Figure 4-35 (a) the force-displacement results for fast-rates of uplift are shown alongside a drained test (v = 0.002 mm/s) for an embedment ratio of 3.5. The predicted curves shown for each test are calculated using the model by Schupp (2009) for different uplift speeds. For the purpose of the tests in this section, these curves were assumed to represent different levels of pore water drainage, occurring at the time of pipeline start-up. In other words, some pore-pressure or liquefaction response unrelated to the initial pipe movement is assumed to have caused this response. In each test, the vertical soil springs were defined using the Schupp (2009) predictions, and the pipe was heated as usual. The results are show in Figure 4-35 (b) and Figure 4-36.
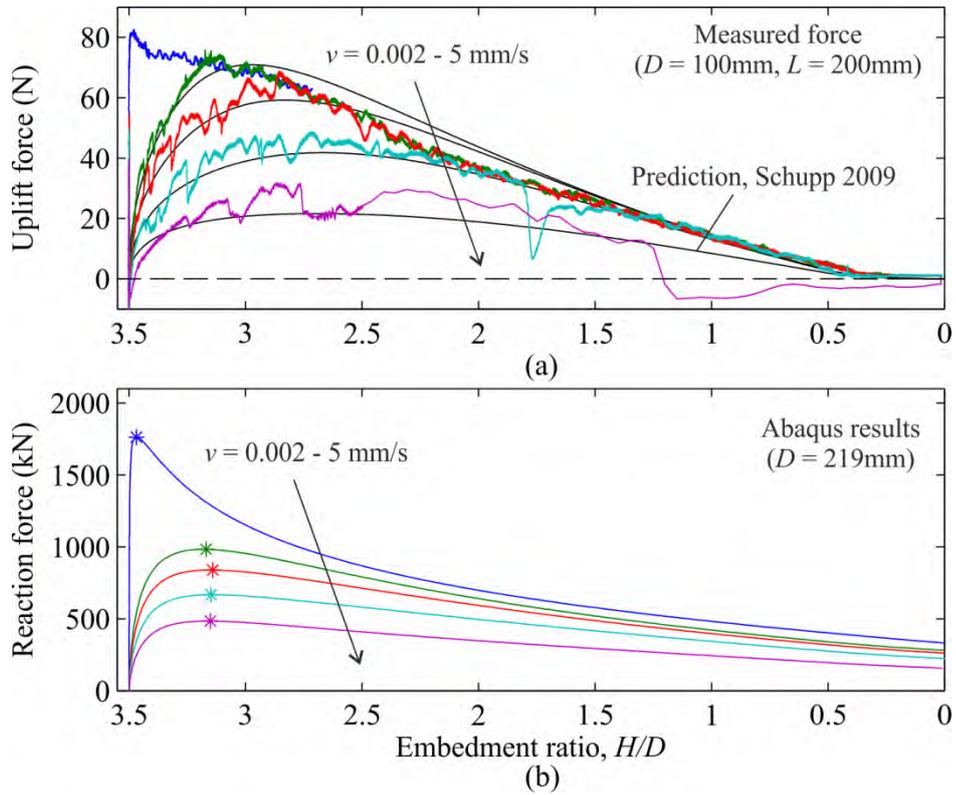
Figure 4-35 Rate effects: (a) Experimental force and predictions vs. embedment ratio for 100mm diameter pipe; (b) Axial force at the centre using scaled up force-displacement predictions
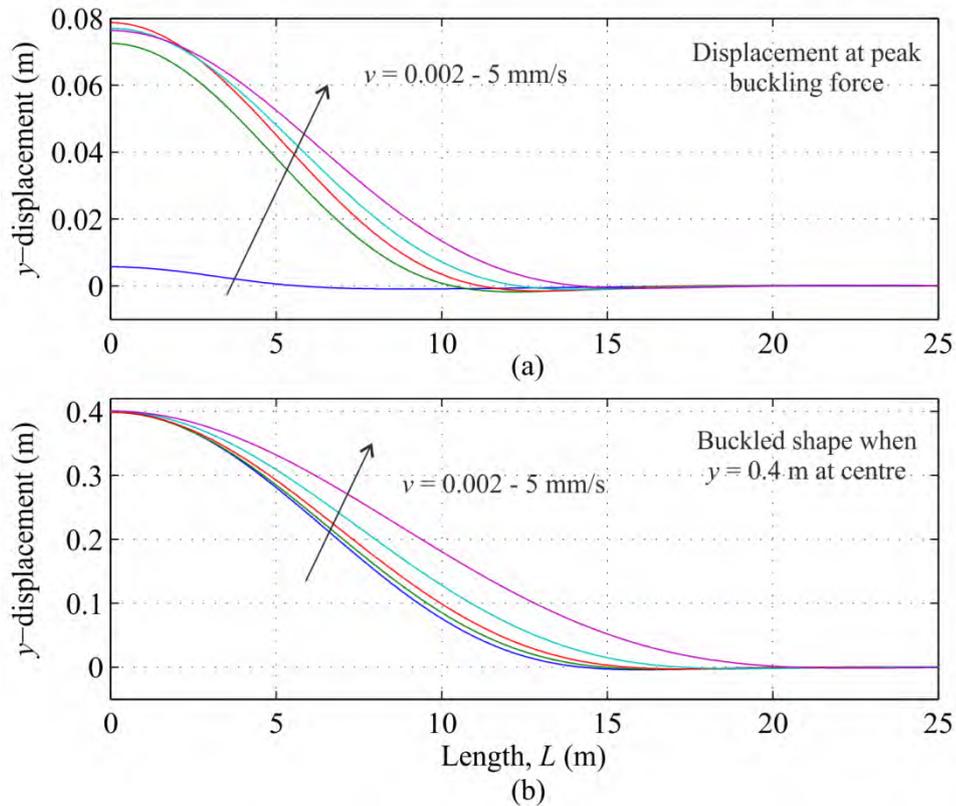

Figure 4-36 Rate effects: displacement along pipe at (a) peak buckling force and (b) central disp. of 0.4 m

The above plots show a sharp reduction in the peak axial force and temperature required to buckle the pipe compared to the drained case, as anticipated. The pipe also displaces further prior to buckling, though as a consequence the post-buckling snap-through response becomes increasingly less severe. On further displacement of the pipe, the axial force and displacements at the centre in the drained case approach those in the partially drained cases, as the soil resistance also converges. This could be compared to the buckling response when the imperfection height is increased.

The vertical displacement of the pipe at both the peak buckling force and at a central displacement of 0.4 m (post-buckling, but prior to re-surfacing) are shown in Figure 4-36. In (a), the overall displacement of the pipe in the drained case is shown to be far less than the displacement in the partially drained tests at peak axial force. At a common post-buckling displacement of 0.4 m at the centre (occurring at different temperatures in each test), part (b) shows the differences in the buckling displacements of the pipe. For lower soil resistance ('faster rate') tests, the overall upward displacement of the pipe is greater, over increasing distances from the pipe centre. In the fastest rate test there is positive vertical displacement over the first 20 m from the centre (40 m total), which is greater than the length of the initial imperfection. This could possibly indicate a tendency of the pipe to 'unzip' during buckling if the soil resistance is decreased to the levels of these tests. Although this is perhaps not a realistic representation of how pore water effects might occur in the field, it provides an indication of how detrimental the effects of a loss of resistance due to liquefaction could be in the context of upheaval buckling.

The experimental uplift curves used in this study were obtained for constant pipe uplift velocities, but applied to a model in which different structural elements displace at different rates (varying throughout the buckling process). Despite its simplifications, however, the structural model could still be used as an effective tool to assess the impact of rate effects. As shown in Figure 4-9, the rate of pipe displacement with temperature can be extracted for a

given element in the model; if the rate at which the temperature of the pipe increases is also known, the 'true' uplift velocity of this element can be determined. A possible design approach would involve running the model with a selected uplift resistance curve, to obtain the maximum pipe velocity, v_{pipe}, at the most critical location during buckling (the buckle crest). This value should be checked to ensure that it is less than the test velocity, v_{test}, of the experimental uplift curve used. Satisfying this requirement implies that the uplift resistance assumed in the model is conservative – i.e. the actual soil resistance would always be greater than the value used in the analysis. If, however, v_{pipe} is found to exceed v_{test}, the simulation should be repeated with a reduced resistance curve (i.e. a greater value of v_{test}), or the rate of temperature increase should be reduced, until the design requirement is met.

4.3. Conclusions

This chapter describes a computational study examining the soil-structure interaction aspects of upheaval buckling through simplified finite element modelling. Preliminary analysis investigating the influence of axial and vertical soil resistance, by using representative soil springs, allowed for the development a comprehensive picture of the pipe buckling behaviour and for comparisons with the literature where applicable. This was then used as the basis for assessing current design guidelines and understanding the implications of trends in soil uplift resistance for UHB design.

A parametric study based on the DNV (2007) guidelines for upheaval buckling analysis was carried out, focusing on the influence of uplift resistance parameters on the peak forces causing buckling. This work demonstrated that the embedment ratio, H/D, and the empirical uplift factor, f, were the most important parameters in controlling the buckling load, as they directly contribute to the limiting soil force calculation. Shape parameters (in particular, the mobilisation displacement) which represent the initial stiffness of the soil, were also shown to influence the buckling load, where a less stiff backfill soil allowed buckling at a lower axial force/temperature. Importantly, in tests at a high embedment ratio, the mobilisation

displacement was the difference between unstable snap-through buckling and stabilisation of the vertical displacements at a given temperature. When comparing the influence of each parameter on the peak buckling force with respect to embedment ratio, it was found that the effect of the other variables – most notably soil relative density – increased with increasing embedment ratio.

The comparison of the DNV guidelines with experimental results for drained conditions showed that in general, the guidelines can effectively cover the range of data obtained in physical tests, resulting in similar design temperatures being calculated. This is mainly due to the fact that the peak soil forces observed in the uplift tests are largely contained within the bounds from f = 0.1 to 0.6. Where the guidelines differ from the experimental results is in the mobilisation displacement and initial stiffness calculations – the stiffer experimental values resulted in higher buckling forces than predicted by the guidelines.

One major implication of these results for pipeline design is in the treatment of the backfill relative density. Although most of the saturated sand data was contained in the range between f = 0.1 to 0.6, the plateau effect on the peak soil resistance exhibited at greater embedment ratios may cause the equivalent soil friction factor to change with H/D for a given relative density. For example at a relative density of 0%, the equivalent friction factor is 0.22 at H/D = 2, reducing to 0.11 at H/D = 4.5. The difference between these factors at H/D = 4.5 might result in a reduction of approximately 500 kN in the peak buckling force, or approximately 20°C in temperature. Additionally, when stress level effects observed in the uplift experiments were incorporated in a worst-case scenario, it was found that at greater values of H/D the buckling force not only fell well below the DNV predictions, but actually reached a peak at an embedment ratio of 6.5. In these extreme cases, where the displacements were scaled up according to stress level, the reduction in initial stiffness caused buckling to occur even before the limiting soil force was reached.

These results highlight the importance of accurately predicting both the peak soil force as well as the initial stiffness response for use in buckling calculations. In light of the experimental uplift findings, it is clear that this requires the development of a prediction model to determine the peak soil force and displacement response if a flow-around failure mechanism is mobilised in the backfill. The DNV guidance, which assumes only a sliding block failure mechanism, was found to be unconservative for conditions where this is possible (i.e. very loose backfill and high embedment ratios).

Finally, preliminary results relating to 'rate effects' or more specifically, to a loss of stiffness caused by pore water effects and liquefaction, show that the pipe may experience a different response under these conditions compared to a drained scenario – in particular, a lower peak buckling temperature and greater displacements occurring further along the pipe. A simple design approach that employs the analysis methods described in this chapter, along with experimental uplift resistance curves, could be used to ensure that these possible rate effects are conservatively incorporated in upheaval buckling assessments.

5 Cyclic loading

Cyclic ratcheting – or upheaval creep – has been identified by several researchers as a possible cause for the observed resurfacing of buried subsea pipelines (Nielsen et al., 1990a; Nielsen et al., 1990b). The basis of the mechanism is that cumulative upward displacements of a pipeline, due to thermal loading over multiple cycles, may lead to the enlargement of existing imperfections and a gradual loss of soil cover. This in turn may increase the pipeline's susceptibility to an eventual upheaval buckling failure. Support has been given to this theory by observations from plane-strain uplift tests, which show that after some upward displacement soil tends to flow down around the sides of the pipe to fill the void that is created (Cheuk et al., 2008; Wang, 2012). This infilling is thought to prevent a complete return of the pipeline to its original position on a subsequent shut-down cycle.

The results from previous work suggest that in order to test the validity of this hypothesis, both the upward and downward response of the backfill soil to repeated loading must be understood. Despite interest in the problem, the vertical cyclic loading of pipelines buried in sand has been studied to a much lesser extent than monotonic pull-out failure. Researchers such as Finch (1999) and Wang (2012) have identified scenarios where upward ratcheting is possible; however, very little data is available that can be used to predict if, and under what conditions, this phenomenon could occur. To address this shortcoming, an experimental study on plane-strain cyclic loading was carried out, using both dry and saturated sand. The objective of this work is to assess the likelihood of upward cyclic ratcheting under a range of loading conditions, so that provisions for the design against this mechanism can be established accordingly. The influence of factors such as soil relative density, embedment depth, and stress level is also explored. Redhill 110 was used in the cyclic testing, to enable comparison with the monotonic tests described in Chapter 3. The main features of the test programme are shown in Figure 5-1.
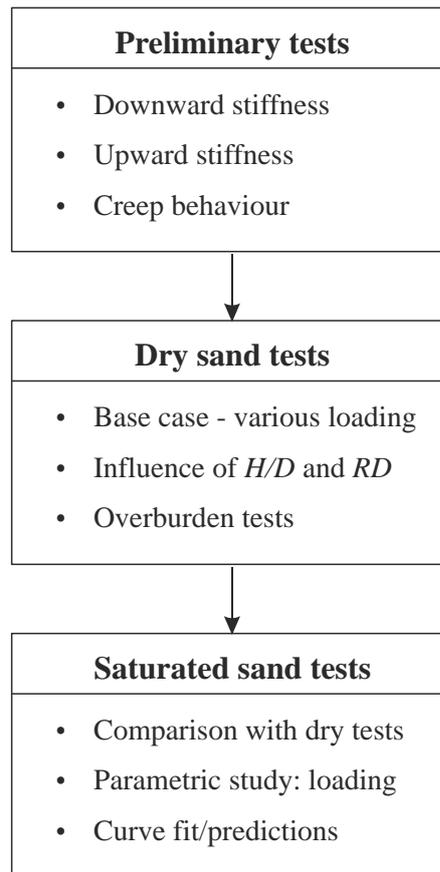
```
                    ┌─────────────────────────────┐
                    │      Preliminary tests      │
                    ├─────────────────────────────┤
                    │  • Downward stiffness       │
                    │  • Upward stiffness         │
                    │  • Creep behaviour          │
                    └──────────────┬──────────────┘
                                   │
                                   ▼
                    ┌─────────────────────────────┐
                    │       Dry sand tests        │
                    ├─────────────────────────────┤
                    │  • Base case - various loading │
                    │  • Influence of H/D and RD  │
                    │  • Overburden tests         │
                    └──────────────┬──────────────┘
                                   │
                                   ▼
                    ┌─────────────────────────────┐
                    │     Saturated sand tests    │
                    ├─────────────────────────────┤
                    │  • Comparison with dry tests │
                    │  • Parametric study: loading │
                    │  • Curve fit/predictions    │
                    └─────────────────────────────┘
```

Figure 5-1 Chapter 5 outline

Key considerations in any cyclic investigation are the method of control (i.e. load or displacement), the mean and amplitude of the cycles, and the frequency of the cycles. For this work load control was used, based on the measured net soil force on the pipe segment, to simulate the pipe displacement during heating/cooling. The amplitude and mean of the load cycles were varied, and a slow rate of loading was used in all tests to ensure a drained soil response. The test programme, outlined in the above figure, included the following phases:

- preliminary tests in dry sand to examine the initial cyclic response of the soil in bearing (below the pipe) and uplift (above the pipe), as well as creep behaviour;

- dry sand tests investigating the general behaviour of the pipe under cyclic loading and testing the influence of embedment depth and relative density;

- dry sand tests with an overburden pressure;

- and finally, saturated sand tests to confirm whether the behaviour is consistent in both dry and saturated conditions, and to establish trends with respect to load magnitude and direction.

Throughout the study, cumulative displacements and the evolution of the upward and downward soil stiffness (which may not necessarily be the same) are assessed, with the aim of understanding how a buried pipeline might be expected to behave over a number of shut-down cycles.

5.1. Experimental Method

5.1.1.   Framework

There is very little work in the literature on cyclic loading of buried pipelines to act as a guide for tests on this problem. It is therefore instructive to explore other similar problems to identify whether a framework exists within which the study can be planned. One area with much recent experimental work is the lateral cyclic loading of stiff piles, relating to large diameter monopile foundations for offshore wind turbines. Although the full-scale problem occurs at much greater stress levels than typically seen for shallowly buried pipelines, the laboratory tests available in the literature are of comparable scale to the pipeline problem. In some aspects the lateral problem is more simple; for example, the resistance is symmetric across the origin in the direction of movement, unlike the pipeline problem which compares shear resistance (and soil weight) in the upward direction to bearing capacity in the downward direction. However, in terms of normalised quantities such as accumulated displacements (or rotations) and stiffness, the response may be similar in how it evolves with the number of cycles.

Thus, a framework proposed by Leblanc et al. (2010) for the cyclic lateral loading of stiff piles is introduced here, and modified for pipeline problem. First, the type and magnitude of loading is defined through independent parameters, ζ_b and ζ_c, which are normalised measures

170

of the size of the cyclic load and its characteristics (one-way vs. two-way), respectively. Non-dimensional parameters (specific to the conditions of the pipeline problem) are then applied to obtain expressions for normalised displacements and stiffness. Table 5-1 below lists the relevant parameters and definitions for both problems.

Table 5-1 Framework for assessing cyclic displacements and stiffnesses (after: Leblanc et al. 2010)

Parameters	Piles		Buried pipelines	
Base	Moment	$\widetilde{M} = \dfrac{M}{L^3 D \, \gamma'}$	Vertical force	$\tilde{F} = \dfrac{F}{\gamma' H D L}$
	Rotation	$\tilde{\theta} = \theta \sqrt{\dfrac{p_a}{\gamma' L}}$	Displacement	$\tilde{d} = \dfrac{d}{D} \sqrt{\dfrac{p_r}{\gamma' H}}$
Loading	Loading size	$\zeta_b = \dfrac{M_{max}}{M_r}$	Loading size	$\zeta_b = \dfrac{F_{max} - W_{ref}}{F_{ult} - W_{ref}}$
	Loading type	$\zeta_c = \dfrac{M_{min}}{M_{max}}$	Loading type	$\zeta_c = \dfrac{F_{min} - W_{ref}}{F_{max} - W_{ref}}$
Measured	Accumulated rotation	$\dfrac{\Delta\theta(N)}{\theta_s} = \dfrac{\theta_N - \theta_0}{\theta_s}$	Accumulated displacement	$\dfrac{\Delta d(N)}{d_s} = \dfrac{d_N - d_0}{d_0}$
	Stiffness	$\tilde{k} = \dfrac{\widetilde{M}}{\tilde{\theta}}$	Stiffness	$\tilde{k} = \dfrac{\tilde{F}}{\tilde{d}}$
		$\tilde{k} = \dfrac{k}{L^{\frac{5}{2}} D \sqrt{p_a \gamma'}}$		$\tilde{k} = \dfrac{k}{L \sqrt{p_r \gamma' H}}$

As shown in the above table, moments and rotations in the pile problem are analogous to forces and displacements in the pipe problem, but with the normalisations for force and displacement adopted from those used in the monotonic tests (Chapter 3). Note that the value of p_r in the pipe displacement equation is taken as 100 kPa.

The definitions for loading size and type require modification for use in the pipeline problem, due to the difference between the upward and downward resistance mechanisms. For simplicity, the hypothesis proposed here assumes a sliding block failure mechanism (see Figure 2-1 (a)) governing for monotonic uplift (this is taken as the base case, although the influence of possible flow-around behaviour is examined later in the chapter). The assumed

reference point for cyclic loading, W_{ref}, is illustrated in Figure 5-2, with respect to a tri-linear monotonic uplift resistance definition (note that the figure plots the net external soil force acting on the pipe section). The value of W_{ref} is set equal to the weight of the soil block above the pipe ($\gamma'HDL$), and the upper portion of the curve represents the shear resistance mobilised during uplift. While representing a simplification of the actual (complex) response, this separation of force components could be a reasonable assumption for a sliding block mechanism, based on the test results shown in Chapter 3.
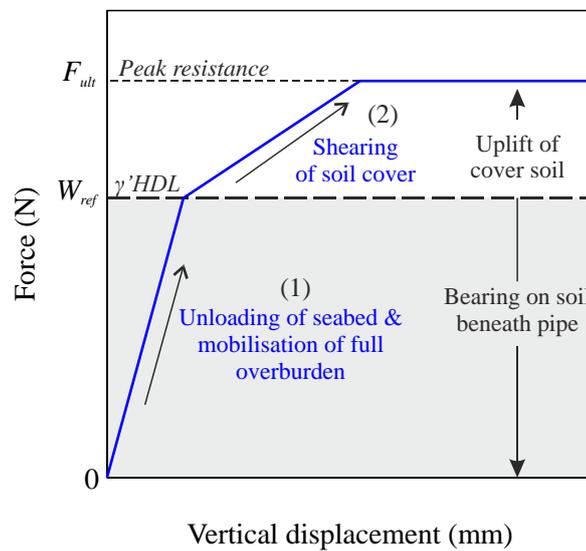

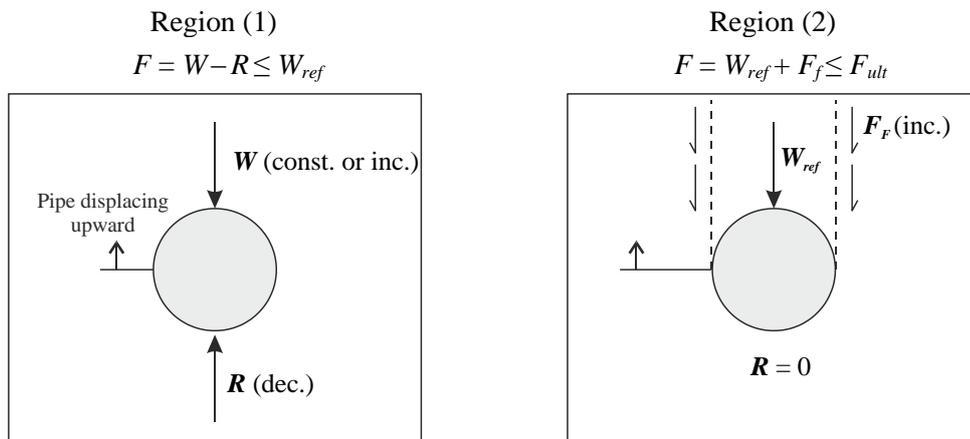*Figure 5-2 Reference point for cyclic loading based on monotonic uplift response*

Figure 5-3 Hypothesised pipe forces during the two phases of uplift (pipe self-weight neglected): Region (1) – $0<F<W_{ref}$; Region (2) – $W_{ref}<F<F_{ult}$

172

As indicated in Figure 5-3, in the force region below W_{ref}, the pipe is thought to be bearing on the soil beneath it, in order to have a net soil force which is less than the overburden force. If pipe uplift begins when the net soil force is zero, the initial response would primarily consist of a stiff unloading of the seabed, causing the net soil force to increase to W_{ref}. The actual overburden force carried by the pipe may also increase slightly from its (unknown) installation value, up to the value of the weight of the soil block. This is followed by shearing of the cover soil above the pipe between W_{ref} and F_{ult}. Although the initial seabed reaction is unknown, in this region it is assumed that no further contact forces exist on the bottom half of the pipe (i.e. $R = 0$). Of course, some mobilisation of the frictional resistance would occur as soon as the pipe begins to move upwards; however, it is thought that this would be relatively small compared to the soil weight, in the region below W_{ref}. Based on these assumptions, the definitions for load magnitude and type, given in Table 5-1, are calculated with respect to W_{ref}.

The cyclic load definitions (type and magnitude) are illustrated in Figure 5-4 (a). The orientation for the load parameters shown in the figure is based on an average cyclic load that is equal to or above W_{ref}. Of course, if the average cyclic load was below W_{ref} (i.e. in the seabed loading region), the definitions could be reversed, but different responses might be expected in each case. Both loading directions are examined in this study, although the primary focus is on the upward case (as defined in Figure 5-4 (a)), as tests carried out in this region may provide insight into the possibility of upward cyclic ratcheting.

The relevant definitions for calculating displacements and stiffnesses are shown in Figure 5-4 (b) and (c). In the figure it is shown that the static displacement (d_s) to F_{max} is equivalent to the initial displacement in the 0th cycle (d_0); therefore, the expression for accumulated displacement is modified from the pile equations accordingly. It should also be noted that the stiffness value is taken as the secant stiffness, i.e. the slope measured from values at the top and bottom of the cycle (F_{max} and F_{min}).
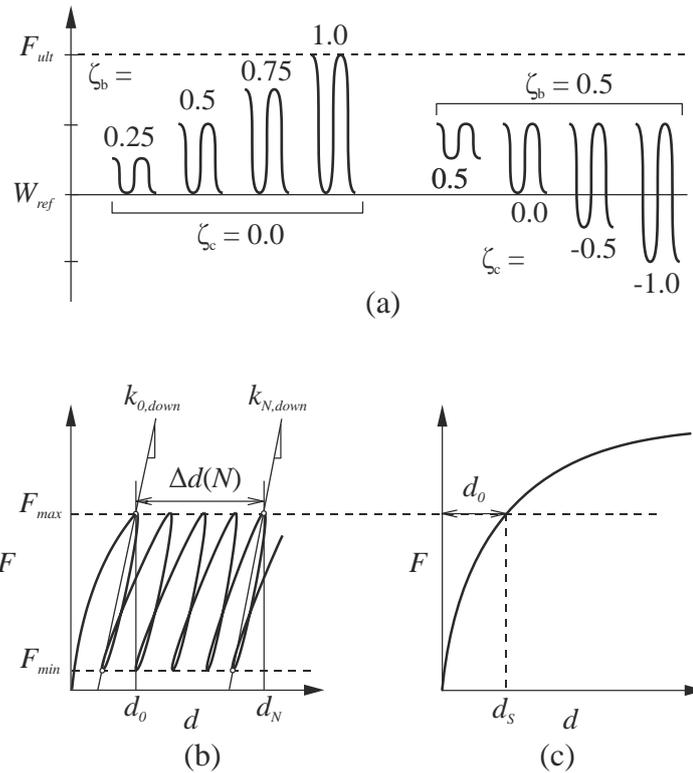
Figure 5-4 Cyclic load definitions and measured parameters, after Leblanc et al (2010): (a) load parameters; (b) stiffness and displacements for cyclic test; (c) displacement in a monotonic test.

Leblanc et al. (2010) found that the accumulated rotation of a pile over a large number of cycles exhibits a linear relationship to cycle number when plotted on a log-log scale. Using a least squares regression analysis they found that the rotations could be predicted by the following power function:

$$\frac{\Delta\theta(N)}{\theta_s} = T_b(\zeta_b, RD)T_c(\zeta_c) \cdot N^{0.31} \tag{5.1}$$

where the constant T_b is a function of the relative density of the sand and the load magnitude (T_b tends to increase linearly with ζ_b). The value of T_c (set at 1 when $\zeta_c = 0$), was found to be independent of relative density, and instead depends only on the value of ζ_c. Interestingly, the peak value of T_c occurred at $\zeta_c = -0.6$, which indicates that the greatest accumulated displacements occur during partial two-way loading. The increase in stiffness with cycle number was approximated as:

$$\tilde{k}_N = \tilde{k}_0 + A_k \ln N$$

$$\text{where } \tilde{k}_0 = K_b(\zeta_b)K_c(\zeta_c)$$

(5.2)

In this equation, the dimensionless constant A_k was found to be constant across the various tests, suggesting that it is independent of relative density and load characteristics. Both K_b and K_c appeared to be independent of the relative density, though the authors note that this may only be the case for low to medium densities.

The above framework provides a starting point for assessing the results obtained from the experimental programme in this chapter. Of particular interest is the assessment made by Leblanc et al. (2011) of the effect of variables such as relative density, cyclic load magnitude and loading type, as these are also of interest for the pipeline problem.

5.1.2.   Experimental setup

For the cyclic experiments, the same testing equipment as for the monotonic uplift tests was used. This means that the experiments focus on the plane-strain behaviour of a pipe segment under cyclic loading. The work assumes that the model pipe represents a segment of pipe (for example, at the apex of an imperfection), which is supported by the backfill below and bears the weight of the soil cover above.

For both the dry and saturated sand tests, the installation procedure was identical to the monotonic test procedures in Chapter 3. In the dry tests the pipe was lowered to a distance of 10 cm above the surface of the sand. The sand was then placed in loose uniform layers from a scoop held a short distance above the sand surface. First, the void beneath the pipe was filled in this manner and, when the soil level reached the pipe crown, a load-control (LC) routine was implemented (if required). Since the downward stiffness is of more importance in the cyclic tests than previously in the monotonic tests, the influence of the load control routine was examined in the preliminary tests. The relative density of the sample in the dry sand tests was around 20-30%; due to the variability in these measurements, a representative value of

175

25% was used for post-processing calculations (unless otherwise specified), corresponding to a unit weight of 13.4 kN/m^3. The saturated samples were again prepared by fluidisation of the backfill material, and a load control routine was initiated as the sand settled over the pipe. An initial relative density of 0% ($\gamma' = 7.82$ kN/m^3) for these tests could then be assumed. Details specific to each test are provided in tables at the beginning of the relevant section.

The cyclic loading was carried out using a load-control routine, which changes the direction of the pipe when the target loads (F_{max} and F_{min}) are reached, based on acquired data from the internal load cell in the pipe. After the specified number of cycles, the pipe was subjected to a final monotonic uplift. Although the actuator was set at a constant speed during cycling, the high-resolution displacement transducer was vital in capturing the actual displacements of the pipe. It was observed that within some transitional regions the rate of pipe movement was not constant (for example, when the soil response transitions from uplift to bearing, as well as when the pipe changes direction). When the force is plotted against the measured high-resolution displacement, however, the response is smooth.

5.2. Preliminary tests

A preliminary examination of several different loading conditions was carried out, including: monotonic downward and upward loading, cyclic tests in both directions, and finally a test examining creep displacement of the pipe under constant load. The tests carried out are listed in Table 5-2 below. The focus in this section is on the dry sand tests; the two saturated tests are used as reference for section 5.5.

Table 5-2 Preliminary cyclic tests

ID	Condition	H/D	RD (%)	N	F_{min} (N)	F_{max} (N)	LC (y/n)
P-1a	Dry	3	25	1	-300	Peak	y
P-1b	Dry	3	25	1	-300	Peak	n
P-2	Sat.	3.5	0	1	-100	Peak	y
P-3a,b	Dry	3	25	10,20	-100	0	y
P-4	Dry	3	25	20	0	65	y
P-5	Dry	3	25	-	Creep test		y
P-6	Dry	3	25	-	Monotonic uplift		n
P-7	Dry	4.5	25	-	Monotonic uplift		n
P-8	Dry	3	50	-	Monotonic uplift		n
P-9	Sat.	3.5	0	-	Monotonic uplift		n
Total preliminary cyclic tests = 11							

5.2.1.   Downward stiffness

In the first two tests, the pipe was pushed downward to a net soil force of -300 N after installation, and then pulled up past the peak breakout load. The pipe was installed differently in each test: in the first a load-control routine was used to keep the net force at zero while the sand was placed above the pipe, and in the second no load control routine was used (i.e. the pipe was held at a fixed vertical displacement while the overburden soil was placed). In Figure 5-5, the force-displacement curves for these test are plotted such that the vertical displacement is at the origin when the net soil force on the pipe is 0 N. This shows that the displacement required to load the pipe from 0 to -300 N is the same in both tests, though the shape of the response differs slightly. The uplift section of both curves is also identical and it can be observed that the upward stiffness is much greater than the initial downward stiffness; however, the initial upward stiffness is likely related to the unloading of the soil beneath the pipe, rather than the loading stiffness of the soil above the pipe. From the force-displacement response during installation, it is evident that the origin for bearing beneath the pipe could occur at a load of approximately 90 N on the pipe (a value slightly greater than the predicted weight of the soil block above the pipe). The stiffness of response in pure uplift (at forces

177

greater than 90 N) is then much softer – reaching the peak breakout force at a displacement of several mm.

The next test examines the evolving stiffness and displacement response when the pipe is cycled downwards from 0 N to -100 N. Figure 5-6 shows that in the first cycle, the downward stiffness increases very rapidly, and over a course of cycles it approaches the unloading (upward) stiffness in this region. The incremental change in stiffness decreases after the second cycle. The cyclic displacements continue in the negative (downward) direction, but also become incrementally smaller with each cycle.
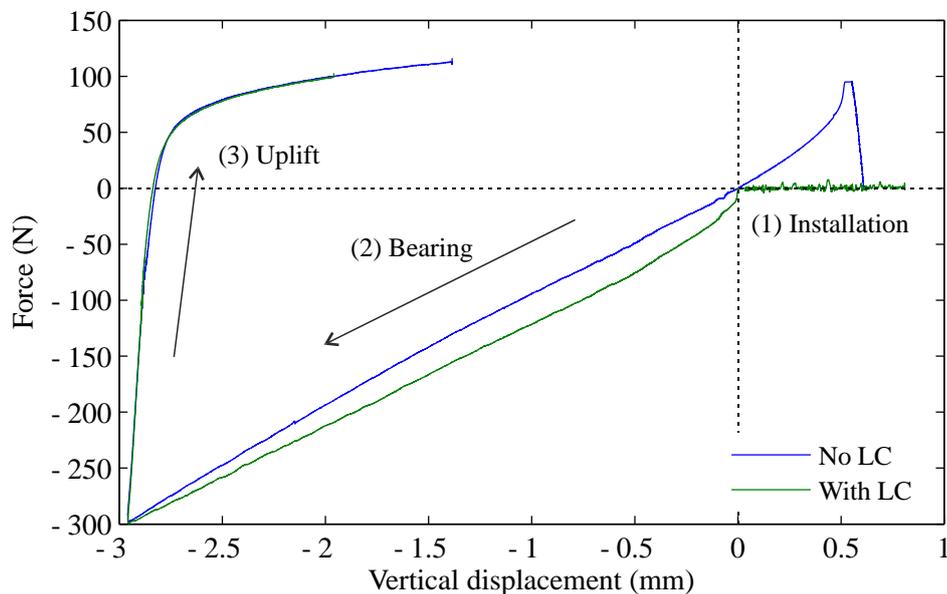

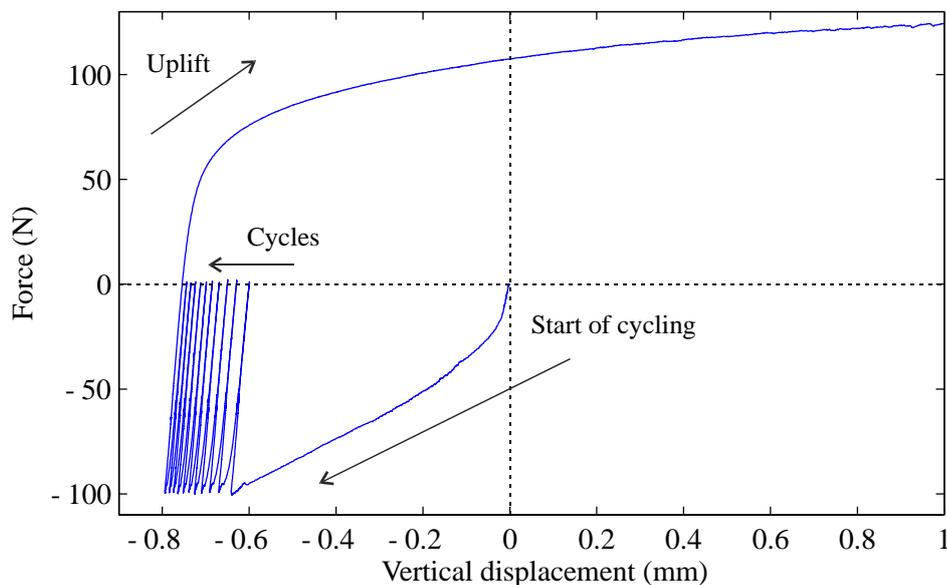*Figure 5-5 Initial downward stiffness (tests: P-1a and P-1b)*

Figure 5-6 Downward cycling 0 to -100 N (test:P-2)

5.2.2. Upward stiffness

As the pipe is cycled in the region below 0 N, it is assumed that the downward response is mainly due to unloading and loading of the soil beneath the pipe, and that there is little contribution from the soil above the pipe, aside from providing some overburden force. In uplift, however, it is slightly more complicated as frictional resistance above the shear planes may start to mobilise even as the soil beneath the pipe unloads. To examine the uplift response in isolation, a monotonic uplift test with no load control during installation is plotted in Figure 5-7.
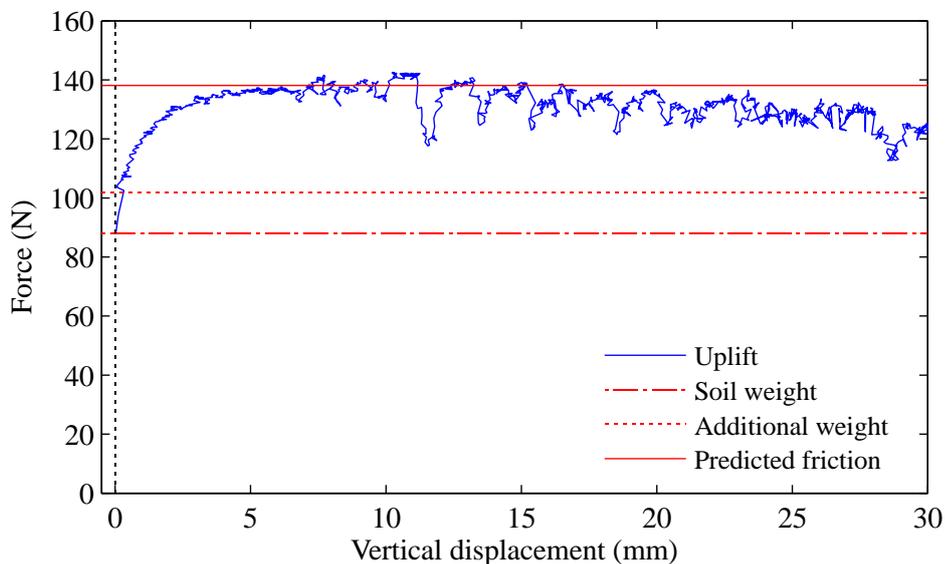

Figure 5-7 Monotonic uplift at H/D = 3 with no initial load control (test:P-6)

Prior to uplift approximately 86 N of soil weight is carried by the pipe section. From this point, an initial small amount of upward displacement causes a stiff linear force increase of a further 16 N; this could be due to a small amount of additional weight being lifted. Beyond this point the remaining force increase is likely caused by friction along the shear planes only, increasing non-linearly up to the peak breakout force. An estimated friction contribution is calculated using the average vertical stress at the embedment depth as follows:

$$F_f = K_0 \tan \phi' \cdot \frac{\gamma' H^2}{2} L \tag{5.3}$$

For *H/D* = 3 and a relative density of approximately 25%, the calculated value of F_f is 36 N. This is added to the total estimated weight (86 plus 16 N), and the resulting force

prediction is shown as a solid red line in Figure 5-7. This line matches well with the peak force mobilised in the test. It should be noted that the contribution of the frictional resistance is less than the value predicted by the adapted vertical slip model (aVSM), resulting in a slightly lower overall peak resistance than predicted. However, as the initial soil weight carried by the pipe (86 N) is close to the predicted value (80 N), the assumption regarding the resistance composition in Figure 5-2 is thought to be adequate for this depth. In the following sections, the possibility of flow-around behaviour occurring (likely in combination with a sliding block mechanism) is dealt with by using the measured monotonic resistance as a reference for each test case.

Figure 5-8 and Figure 5-9 present a cyclic test of 20 cycles starting from 0 N up to a value of 65 N, representing approximately 50% of the peak uplift force at this depth. In Figure 5-8, the net soil force on the pipe and displacements are plotted against time, while Figure 5-9 presents the force-displacement curve. Both show that when the pipe is cycled in the region above 0 N but below the value of the soil weight, the pipe tends to move downwards. It should be noted that these displacements are very small, and degrade incrementally as the soil stiffens in both the upward and downward directions. If a force of 0 N is considered as the origin for cyclic loading, this downward movement of the pipe during cycling is not intuitive. If, however, the soil cover weight is assumed to be the reference point, based on the framework presented in section 5.1.1, downward displacement would be expected anytime the average load during cycling is below this value (due to compression of the downward 'spring'). It is assumed here that this compression is simply due to the unloading and reloading of the soil beneath the pipe, but without measuring the contact forces on the pipe, the exact mechanism cannot be determined. An alternative possibility is that as the pipe moves downwards, an arch above the pipe collapses, attracting a vertical load onto the pipe crown and causing compression of the downward spring (meanwhile, the net soil force remains unchanged).
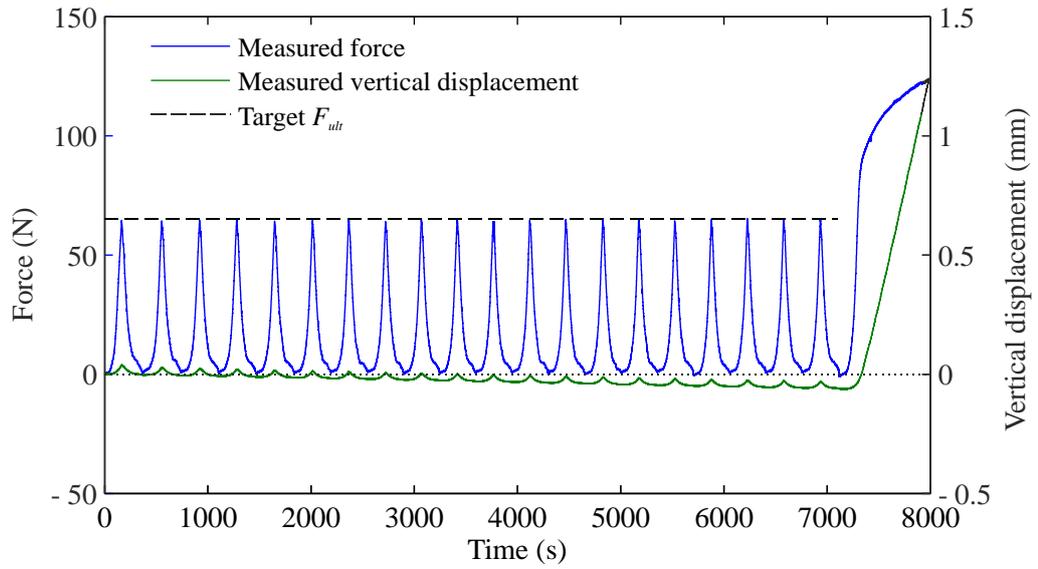
Figure 5-8 Force and displacement vs. time for a cyclic test from 0-65 N (test:P-4)
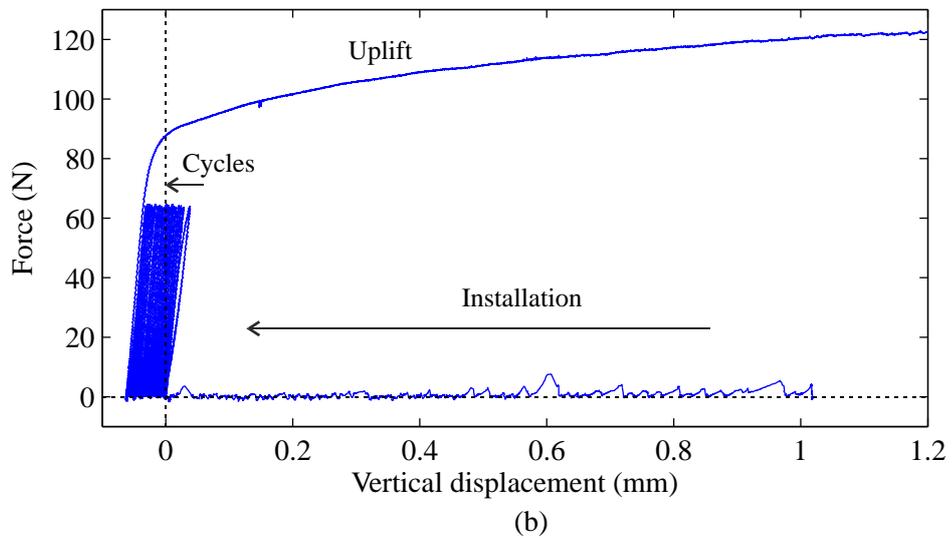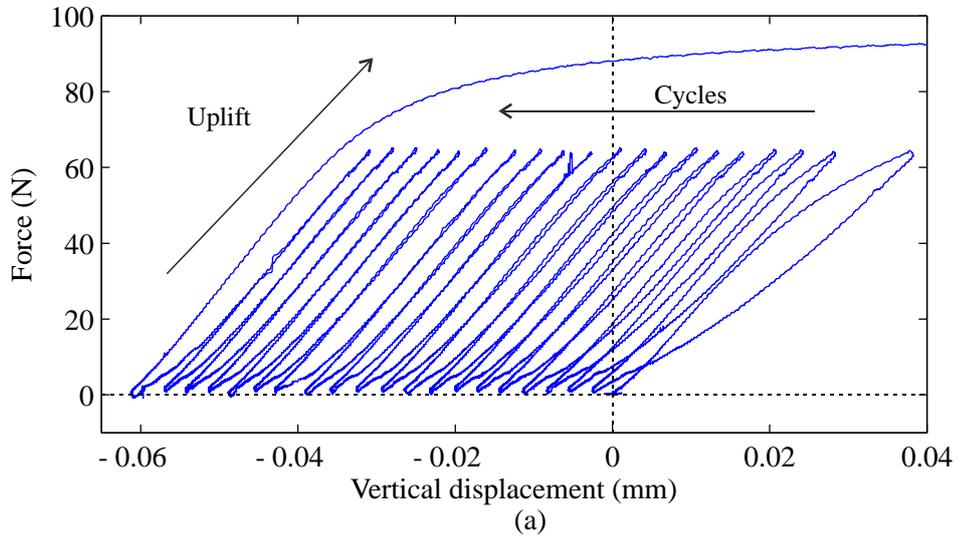

(a)

(b)

Figure 5-9 Force vs. displacement for a cyclic test from 0-65 N (test:P-4): (a) cycles and uplift; (b) including installation.

181

No matter which mechanism governs the downward response, it is likely that if the value of the net soil force increases beyond W_{ref}, the contact forces on the bottom half of the pipe will become negligible, meaning that the response will then be governed by the soil resistance above the pipe. The general theory proposed here is consistent with the response observed in the cyclic test by Wang (2012); the average force in this test is above the calculated soil weight and so, the pipe displaces upward.

5.2.3.   Creep

To examine the displacement of the pipe at various load levels, a creep test was run where the pipe was subjected to constant loads between 0 N and around 95% of the monotonic peak using a load-control routine. The force and displacement are plotted against time for 0-75 N in Figure 5-10, and continued for 100 and 125 N in Figure 5-11. For the load levels below the soil weight in Figure 5-10, the pipe tends to move downwards slightly to maintain a constant force; this is because the pipe must continue to bear down on the soil beneath it to maintain a net soil force below value of the soil weight. As the force approaches the soil weight, the downward displacement reduces. At values exceeding the soil weight (100 and 125 N in Figure 5-11), the pipe mobilises a portion of the shear resistance, but does not appear to displace in either direction. This is interesting, as it means that some frictional resistance developed along the shear planes appears to be maintained without continuing upward movement of the pipe. This has positive implications for upheaval buckling design, as it suggests that the pipe may not creep upwards during operation at locations where a portion of the uplift resistance is mobilised at start-up. It must be noted however, that in the slightly denser sand test reported by Wang (2012), some upward creep does occur when the load is maintained for an unspecified period at the top of each cycle. This suggests that upward movement may be required to maintain the load in tests at deeper embedments or higher densities, when greater frictional forces are mobilised.
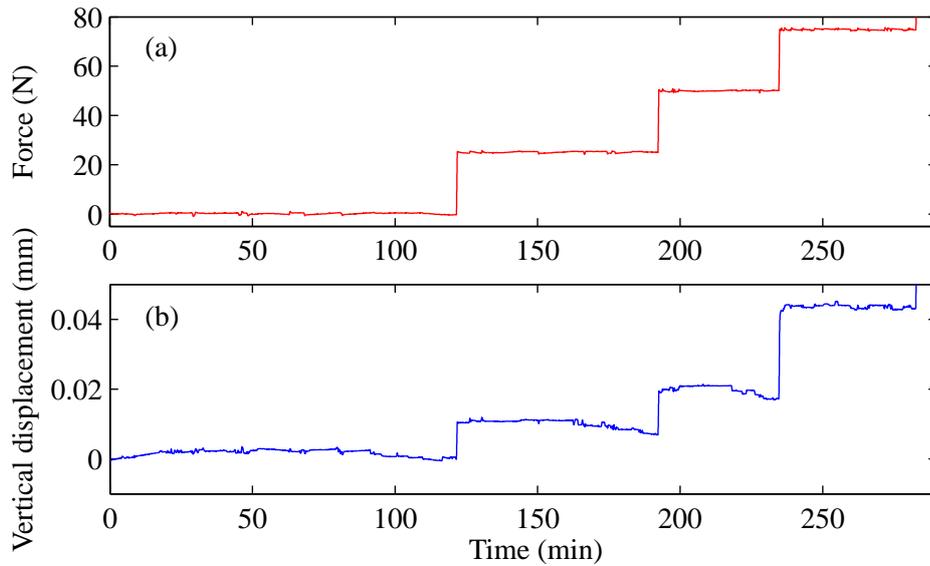
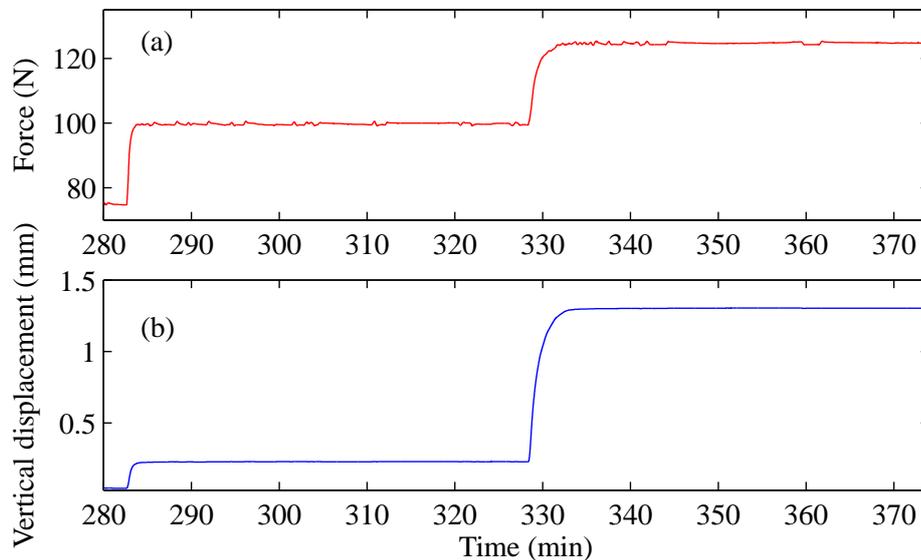*Figure 5-10 Creep test 0-75 N (test:P-5): (a) force; (b) vertical displacement*

Figure 5-11 Creep test (continued) 100-125 N (test:P-5): (a) force; (b) vertical displacement

5.3. Cyclic testing in dry sand

The soil-structure interaction as the pipe transitions from downward to upward movement is very complex; however, the evidence from the preliminary tests supports the hypothesis that the transition between uplift shear resistance and downward bearing capacity occurs at approximately the value of the weight of the soil cover. Although some frictional resistance may be mobilised on any upward movement of the pipe, the unloading of the soil beneath the pipe (and the mobilisation of the soil weight) appears to be the more dominant behaviour

183

when the net soil force is below the value of the soil weight. It therefore makes sense for W_{ref}, used for categorising the direction and magnitude of cycling loading in the following tests (see Table 5-1), to be taken as this value. For consistency with the monotonic dry sand tests, a load control routine maintaining zero net soil force on the pipe was used during installation. Thus, the starting point force for all tests is 0 N, with vertical displacements referenced to this this point.

The following section describes the results of a testing programme examining the general behaviour of a pipe under different cyclic load amplitudes and directions in dry sand, with a focus on the displacement and upward stiffness response across a number of cycles. The primary aim of these tests is to explore the range of behaviours caused by varying loading and backfill conditions. In this section, and throughout the chapter, the cyclic stiffness is taken as the secant stiffness (both unloading and reloading stiffnesses are examined), calculated using the forces and displacements at F_{max} and F_{min}. A base case with $H/D = 3$ and a relative density of approximately 25% was chosen as a starting point for these tests. This embedment was selected as a maximum depth before the flow-around mechanism might be expected to govern over the sliding block mechanism in monotonic uplift. Following several base case tests, the influence of embedment depth and relative density was examined. These tests are summarised in Table 5-3.

Table 5-3 Cyclic tests in dry sand

	Test parameters						Reference values		Load parameters	
ID	H/D	RD (%)	N	F_{min} (N)	F_{max} (N)	LC (y/n)	W_{ref} (N)	$F_{ult\,(ref)}$ (N)	ζ_b	ζ_c
D-1	3	25	100	0	100	y	86	135	0.29	-6.14
D-2a	3	25	100	52	120	n	86	135	0.69	-1
D-2b	3	25	100	52	120	y	86	135	0.69	-1
D-3	3	25	100	86	120	y	86	135	0.69	0
D-4	4.5	25	100	130	210	y	130	250	0.67	0
D-5	4.5	25	50	0	250	y	130	250	1	-1.08
D-6	3	50	100	100	150	y	100	160	0.83	0
Total dry cyclic tests = 7										

The reference values in the table were obtained from the monotonic tests, installed without load control, at the corresponding embedment and relative density (tests P-6 to 8 in section 5.2). The measured force on the pipe after installation and prior to uplift is used for the value of W_{ref} in each case.

5.3.1. Base case

Three tests are described here, corresponding to three different loading scenarios for the base case conditions (tests D-1 to D-3).

5.3.1.1. Cycling below soil weight

The first test, examined in Figure 5-12 and Figure 5-13, is an extension from the test presented in the preliminary section (Figure 5-8 and Figure 5-9). In this test the pipe is subjected to 100 cycles from 0 to 100 N. This is marginally a two-way test in the downward direction, with the average force located well below W_{ref}. The upper limit, F_{max}, was chosen at approximately 74% of the peak force as this occurs just beyond the plastic region in a monotonic test. It can be seen in Figure 5-12 that in the 0th cycle (N_0), the secant upward stiffness is less than the secant downward stiffness and the net displacement is upward. In the next few cycles the uplift stiffness increases rapidly and surpasses the downward stiffness (Figure 5-13 (a)), causing the pipe to move downwards. Figure 5-13 (b), which plots absolute and incremental displacements at F_{max}, shows that the incremental change in both displacements and stiffness decreases with the number of cycles.
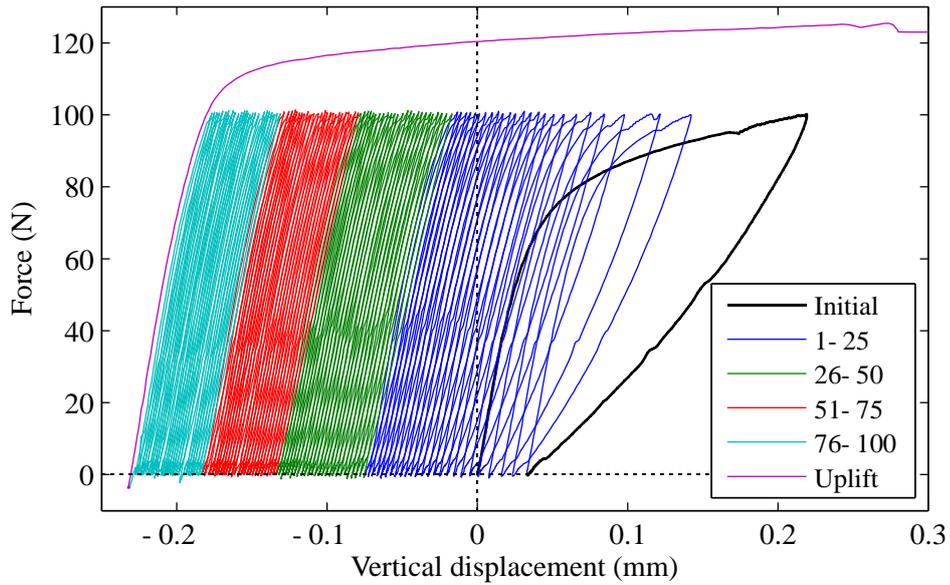
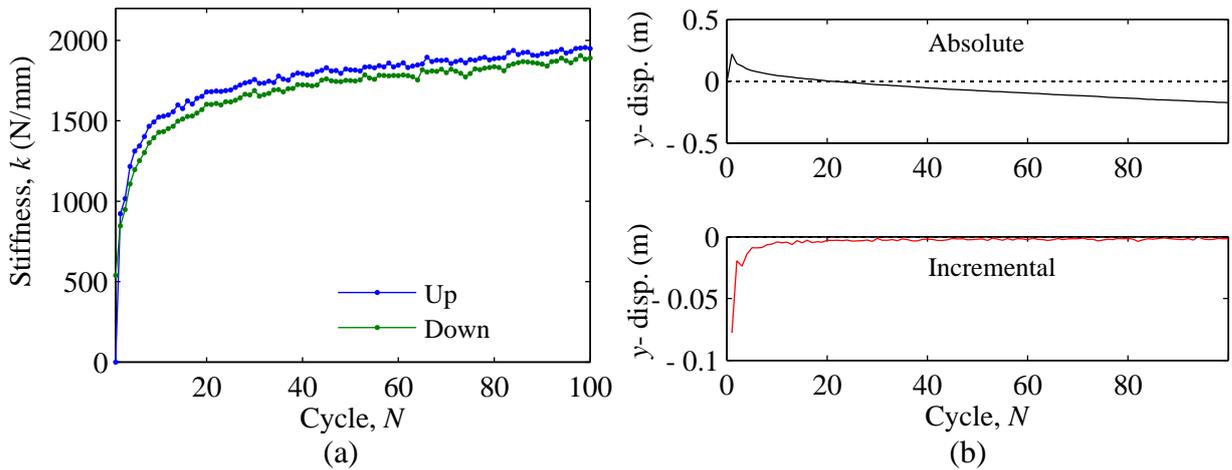*Figure 5-12 Force-displacement response cycling from 0-100 N at H/D = 3 (test: D-1)*

Figure 5-13 Stiffness (a) and displacements (b) cycling from 0-100 N at H/D = 3 (test: D-1)

5.3.1.2. Two-way cycling around soil weight (no LC vs. LC)

Symmetric two-way cyclic tests around the soil weight (average force = W_{ref}) were carried out both with and without the initial load control routine. The cyclic behaviour in these tests is similar (see Figure 5-14), with the 'no LC' test moving very slightly downwards, while the test with LC has no net movement after the first few cycles. This is an expected response for a symmetric two-way test, and Figure 5-15 (a) confirms that the upward and downward stiffnesses are approximately equal after a small number of cycles. Compared to the displacement of the first cycle, the subsequent displacements are extremely small.
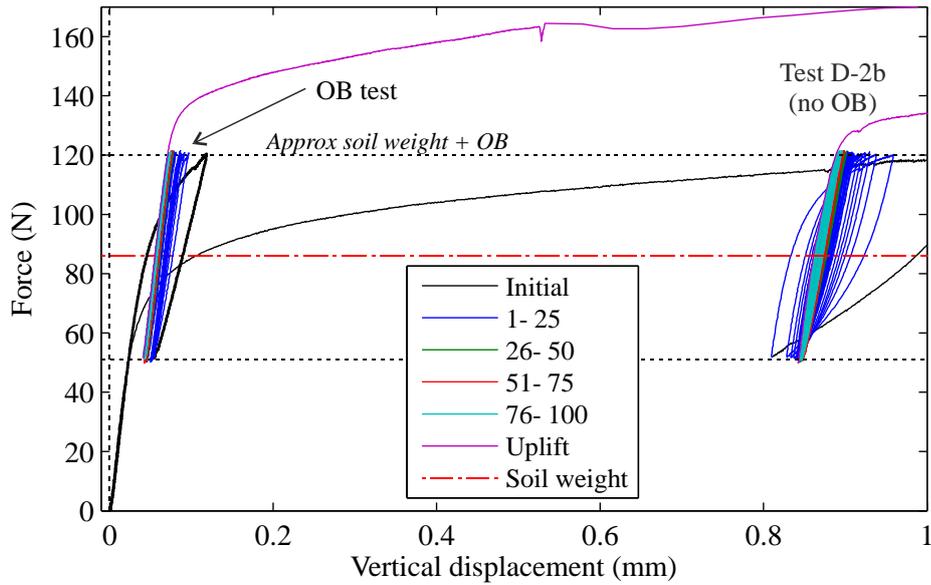
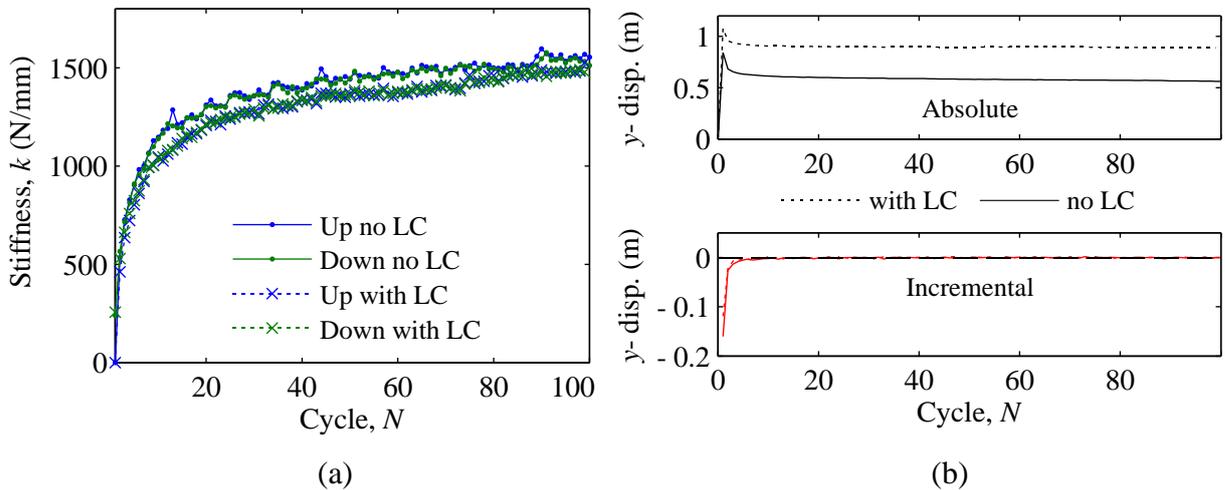*Figure 5-14 Force-displacement response cycling from 52-120 N at H/D = 3 (tests: D-2a and D-2b)*

(a)	(b)

Figure 5-15 Stiffness (a) and displacements (b) cycling from 52-120 N at H/D = 3 (tests: D-2a and D-2b)

5.3.1.3.   One-way cycling above self-weight

The third category of loading examined was one-way loading above the soil weight (Figure 5-16 and Figure 5-17). In this case, the pipe would be expected to move upwards, and beyond the first cycle this is shown to occur. However, there is still an initial downward movement after the 0th cycle. As in the previous two-way case, the displacements from cycle 1 onwards are much smaller than the initial monotonic displacement.
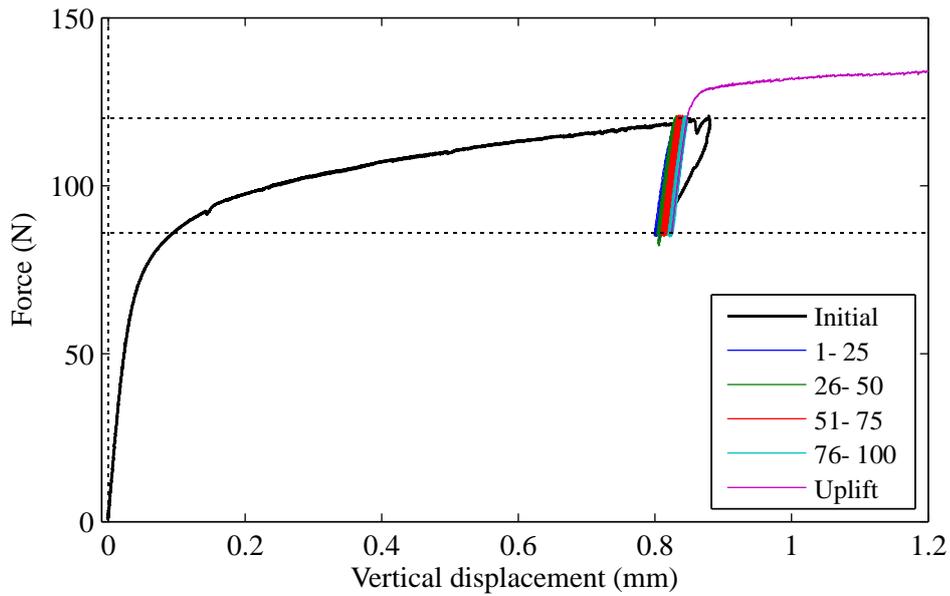
Figure 5-16 Force-displacement response cycling from 86-120 N at H/D = 3 (test: D-3)

(a)	(b)
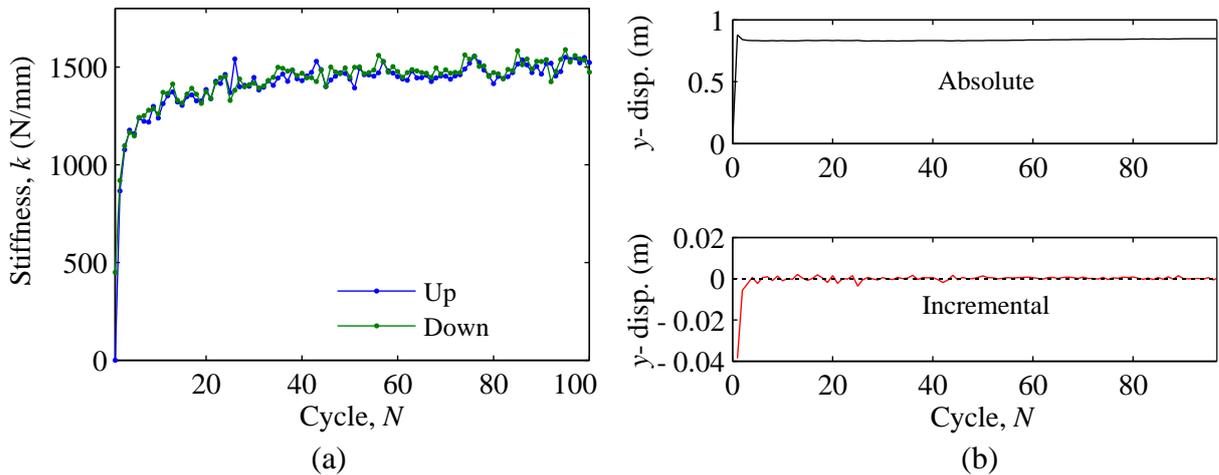
Figure 5-17 Stiffness and displacements cycling from 86-120 N at H/D = 3 (test: D-3)

5.3.1.4.   Comparison between different types of loading

The tests described above show three example types of cyclic loading of a pipe in loose sand. In the last two cases, the pipe is cycled to nearly 90% of the peak load, and so they represent relatively severe loading scenarios. Reducing the magnitude of the load cycles should reduce the net displacement of the pipe. The behaviour shown above appears to be stable, as the incremental stiffnesses in both the upward and downward directions, along with the displacements, decrease with the number of cycles. In Figure 5-18 stiffness values and displacements at F_{max} are presented for each of the three tests. These quantities are normalised

based on the framework presented in Table 5-1. As found by Leblanc et al. (2010), the normalised stiffnesses and displacements can be plotted on a semi-log scale and a log-log scale, respectively. In Figure 5-18 (a), both two-way tests show a linear increase at similar slope, which confirms that a logarithmic relationship exists between the stiffness and cycle number for these downward-moving tests (D-1 and D-2b). The slope for the one-way upward test (D-3) is less than for the previous two. The normalised displacements (Figure 5-18 b) for the two-way tests also show a linear trend (indicating a power relationship), but with different slopes. The slope and intercept values increase (becoming less negative) as the average cyclic force increases (ζ_c becomes less negative). Test D-3 is possibly bilinear, with the change in slope indicating the cycle at which the transition between downward and upward movement occurs.
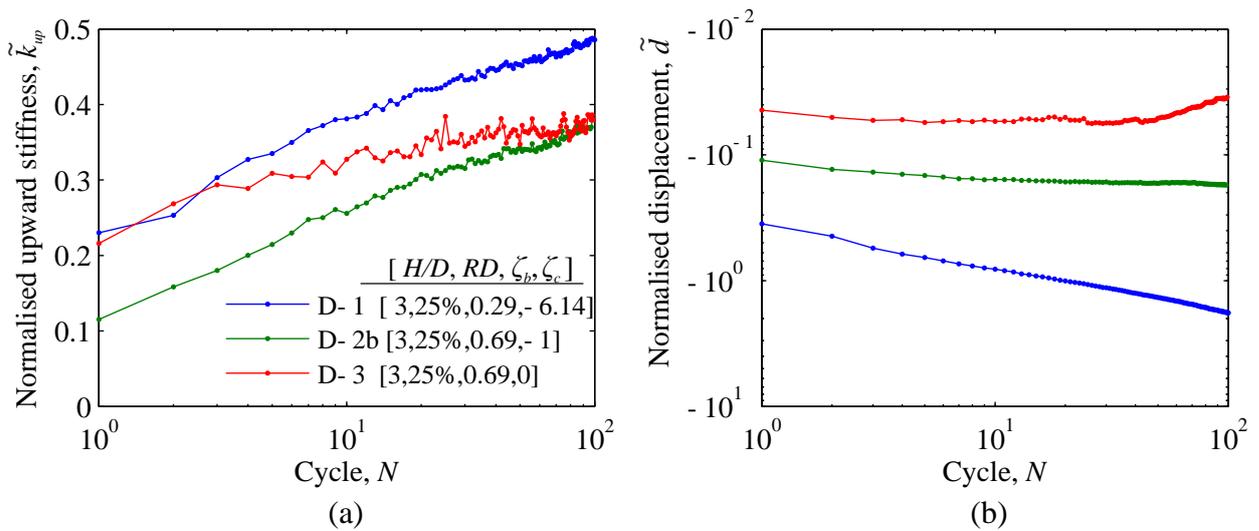
Figure 5-18 Normalised stiffness and displacements for dry base case (tests: D-1 to D-3)

5.3.2. Effect of embedment depth and relative density

In the dry sand tests reported in Chapter 3, differences were observed in the monotonic uplift behaviour related to embedment depth and relative density. These tests found that increasing the embedment depth caused a transition to a possible flow-around failure mechanism, manifesting in a much softer force-displacement response in uplift – particularly

in the portion of the curve above the self-weight. This is illustrated in Figure 5-19 (a), which shows that at $H/D = 4.5$ a higher force is generated by friction (occurring over a larger displacement) as compared to the test at $H/D = 3$. Interestingly, the additional linear response above the initial soil weight is similar in both tests. Figure 5-19 (b) also shows the increase in resistance at $H/D = 3$ when the relative density is increased from 25% to 50%. In this case a greater frictional force is also mobilised, but the force-displacement response becomes more stiff.
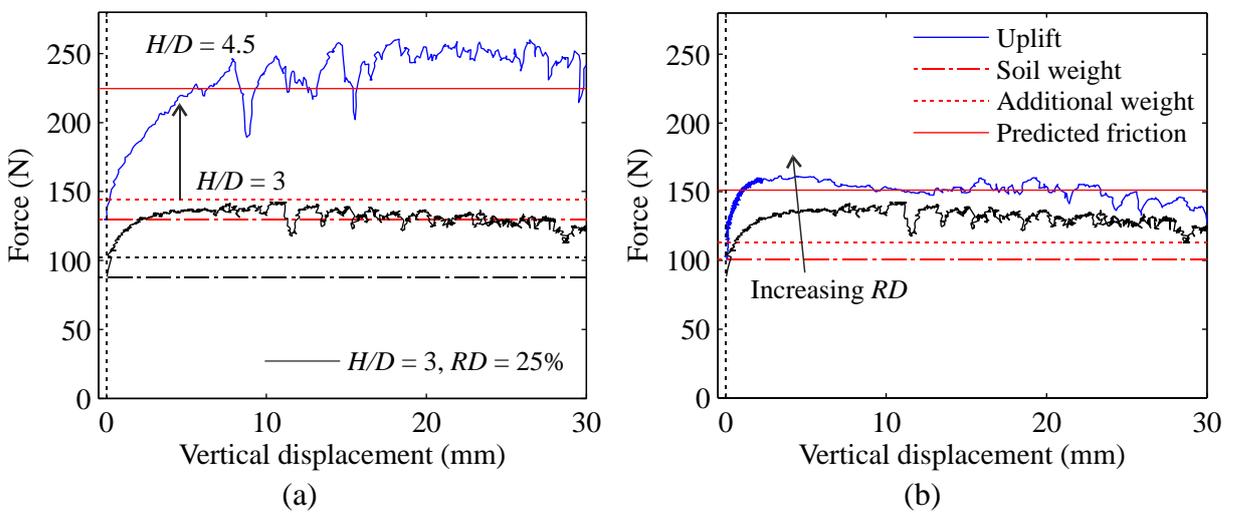
Figure 5-19 Monotonic uplift with no initial load control (tests:P-7 and P-8) for: (a) H/D = 4.5 and H/D = 3, RD = 25%; (b) H/D = 3, RD = 50% and RD = 25%.

5.3.2.1.   *Embedment depth*

Figure 5-20 shows a one-way test at $H/D = 4.5$, cycling from W_{ref} to a value of 85% of the peak breakout force. As the force approaches F_{max} in the initial cycle it begins to fluctuate, which may be an indication of the onset of the flow mechanism. During cycling, the net movement of the pipe is upward and a greater total displacement occurs in this test, compared to the test at $H/D = 3$. This difference could be due to the possible change in failure mechanism at this force level, or the higher value of d_0 in the initial cycle (a greater initial displacement means that possible infilling could occur beneath the pipe). The displacement is still less than the "upper bound" proposed by Wang (2012) for irrecoverable infilling below the pipe, calculated as 11.8 mm using the equation below:

$$d_{UB} = \frac{1}{2}D(\sec \phi_{cs} - 1)$$

A further test at H/D = 4.5 with (symmetric) two-way loading is shown in Figure 5-21. In this test F_{max} is set to the peak monotonic resistance, meaning that an even greater amount of displacement occurs prior to the first cycle (now exceeding 11.8 mm), as well as during cycling. Nevertheless, in both tests the rate of displacement still decreases with the number of cycles.
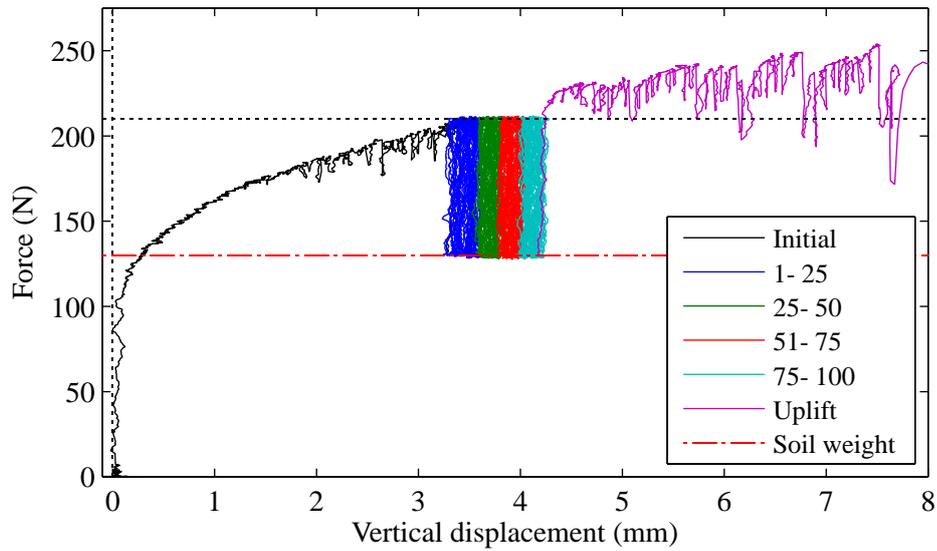

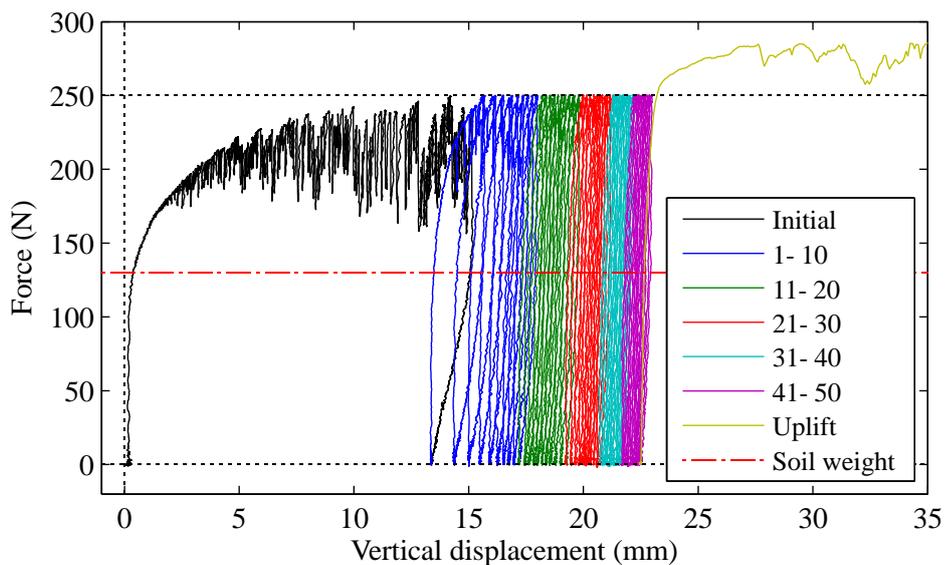Figure 5-20 Force-displacement response cycling from 130-210 N at H/D = 4.5 (test: D-4)

Figure 5-21 Force-displacement response cycling from 0-250 N at H/D = 4.5 (test: D-5)
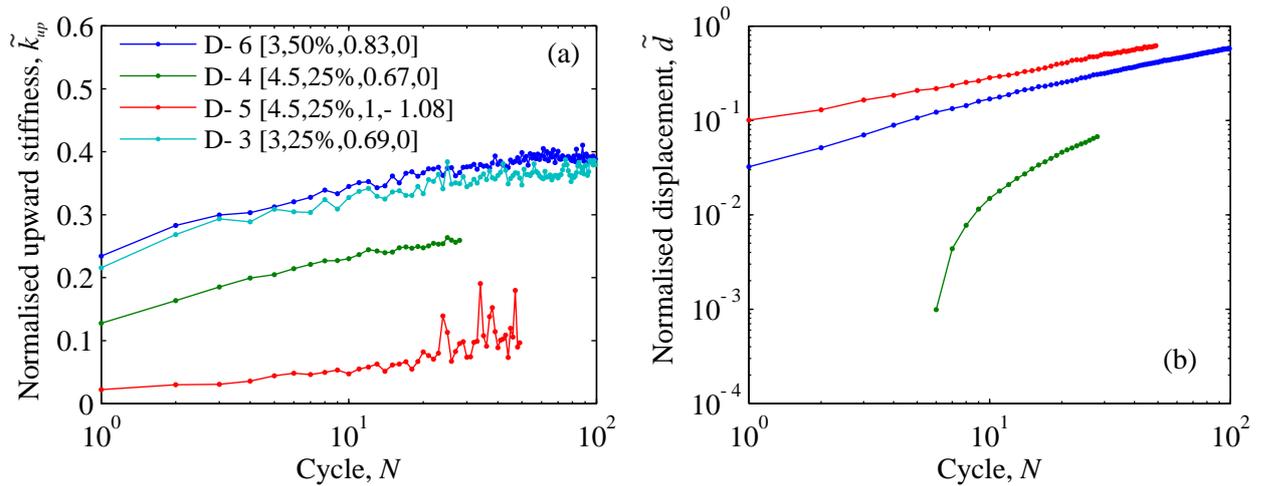
Figure 5-22 Normalised stiffness (a) and displacements (b) for upward moving tests (tests: D-3 to D-6)

Figure 5-22 (a) compares the normalised stiffness values from the tests at $H/D = 4.5$ to the previous one-way test at $H/D = 3$ (D-3). From cycle 10 onwards, the slope of these curves appears to be similar in all three tests. In Figure 5-22 (b) the corresponding displacements are plotted (though only positive values can be shown on a log-log scale and D-3 cannot be included). Although it appears that after a number of cycles the displacement trends are consistent, the response in the first few cycles varies between tests. For example, in test D-5 the initial values are higher, but the incremental displacements reduce more quickly than D-4. This is likely controlled by the initial difference between the upward and downward stiffnesses, and is discussed in a later section.

5.3.2.1.   *Relative density*

One test was conducted at an increased relative density of approximately 50% at $H/D = 3$. The normalised stiffness and displacement values are also shown above in Figure 5-22. In this test the initial upward stiffness is greater than in the looser case; thus, the cycling begins at a smaller upward displacement, d_0 (Figure 5-23). However, the normalised upward stiffness during the cycles is not significantly different to the loose case. As discussed later in this chapter, the difference in the displacement behaviour can be found by examining k_{down}, which starts at a much higher value than k_{up}, causing the pipe to move upwards. As the number of

cycles increases, the values of these two parameters converge and the incremental displacements decrease.
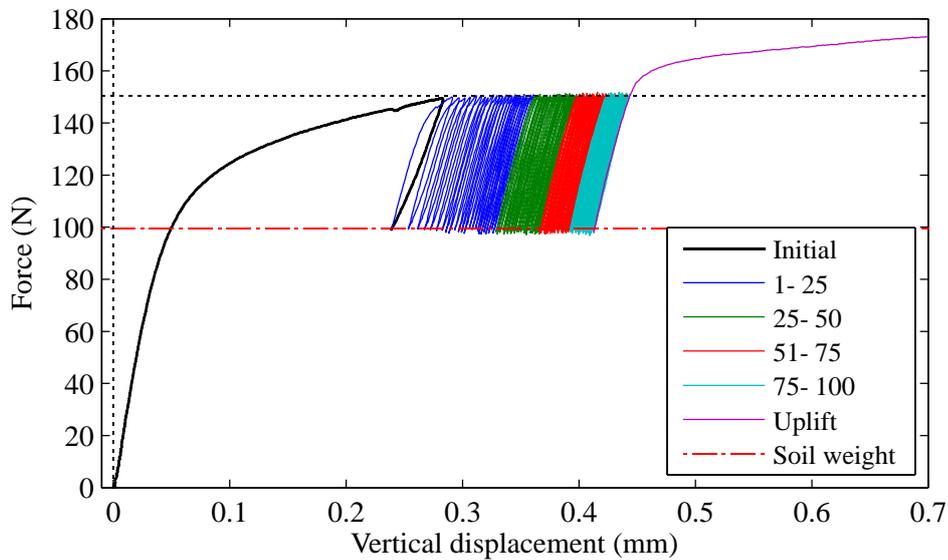
Figure 5-23 Force-displacement response cycling from 100-150 N at H/D = 3 (test: D-6)

5.4. Cyclic loading with overburden pressure (dry sand)

In Chapter 3 it was found that if an overburden (OB) pressure is applied to the soil, the initial force-displacement response during monotonic uplift is similar to tests with no OB at an equivalent embedment ratio (in terms of the weight of the soil cover). For the cyclic tests in this section, an overburden was applied to the soil surface above a pipe buried at $H/D = 3$ in dry sand, to achieve an equivalent embedment $H/D^* = 4.5$. The details of each test are summarised in Table 5-4. In tests OB-1c and OB-2c, the load factors were chosen to enable comparison with cyclic tests at an actual embedment of 4.5. Hence, the W_{ref} and F_{ult} values shown in the table for these two tests relate to this depth, and ζ_b and ζ_c were calculated accordingly. In OB-3c, comparisons are made to cyclic tests at the actual depth, $H/D = 3$, altering the calculated values in Table 5-4.

Table 5-4 Cyclic overburden tests

ID	H/D	H/D*	RD (%)	N	F_{min} (N)	F_{max} (N)	W_{ref}† (N)	$F_{ult,ref}$† (N)	ζ_b†	ζ_c†
OB-1c	3	4.5	25	100	130	210	130	250	0.67	0*
OB-2c	3	4.5	25	50	0	200	130	250	0.58	-1.80*
OB-3c	3	4.5	25	100	52	120	86	135	0.69	-1
Total overburden cyclic tests = 3										

* Denotes the equivalent embedment depth achieved with the surface overburden. † In OB-1c and 2c these fields are calculated using the equivalent *H/D**; OB-3c uses the actual *H/D*.

5.4.1.　Cycling from equivalent *H/D** reference load

The first tests were carried out with the assumption that the cyclic response of a test with *H/D** = 4.5 is similar to a test with no OB at *H/D* = 4.5. Two tests were cycled using W_{ref} from *H/D* = 4.5 as the reference load for cycling: a 'one-way' test from 130-210 N; and a 'two-way' test below the reference weight, from 0-200 N. The force-displacement responses in these tests are plotted in Figure 5-24, along with monotonic test results at *H/D* = 3, and *H/D** = 4.5.
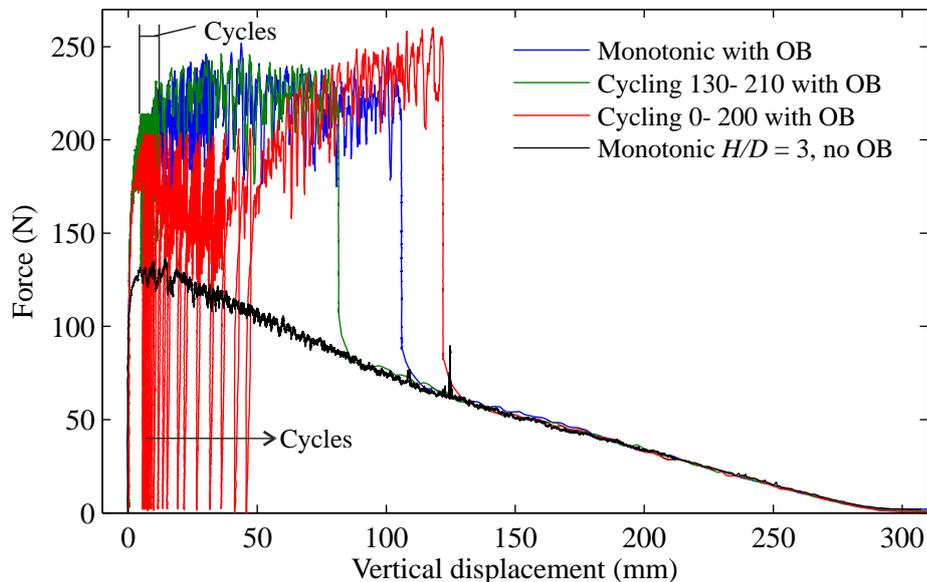
Figure 5-24 Force-displacement response for OB tests at H/D* = 4.5 (tests: OB-1c and 2c)

The figure shows that in each overburden test, when the weights are removed and the test is continued, the force-displacement response is exactly in line with the monotonic tests at the

194

actual embedment of $H/D = 3$. From the long-range displacements it can be seen that while the one-way test from 130-210 N matches reasonably well with the monotonic test at $H/D^* = 4.5$ after 100 cycles, the test from 0-200 N experiences run-away displacements over the first 50 mm (50 cycles).

5.4.1.1. One-way cycling, using equivalent $H/D^* = 4.5$

The force-displacement curve from the one-way test at $H/D^* = 4.5$ (OB-1c), shown above, is plotted against the same cyclic test at an actual depth of 4.5 in Figure 5-25. This figure shows that the total upward displacement is much greater in the test with an OB than without, though the forces eventually converge after cycling. Additionally, the OB test does not appear to experience the same initial increase in resistance after cycling that is seen in the other test. The force-displacement curve from OB-1c is plotted again in Figure 5-26, this time with the cycles indicated. It is now evident that in this test – as in OB-2c – the rate of upward displacement increases with the number of cycles.
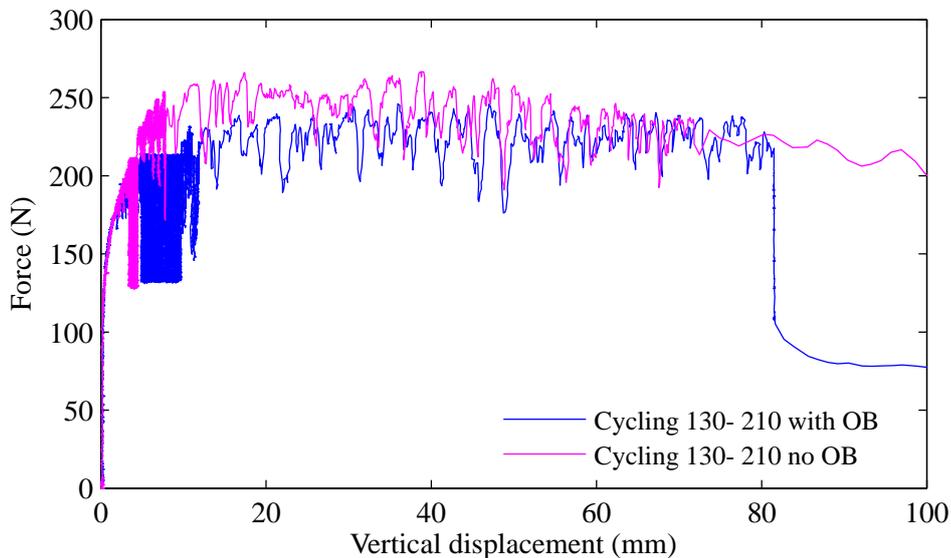
Figure 5-25 Force-displacement response for one-way OB test at H/D* = 4.5 compared to no OB tests (tests: OB-1c and D-4)
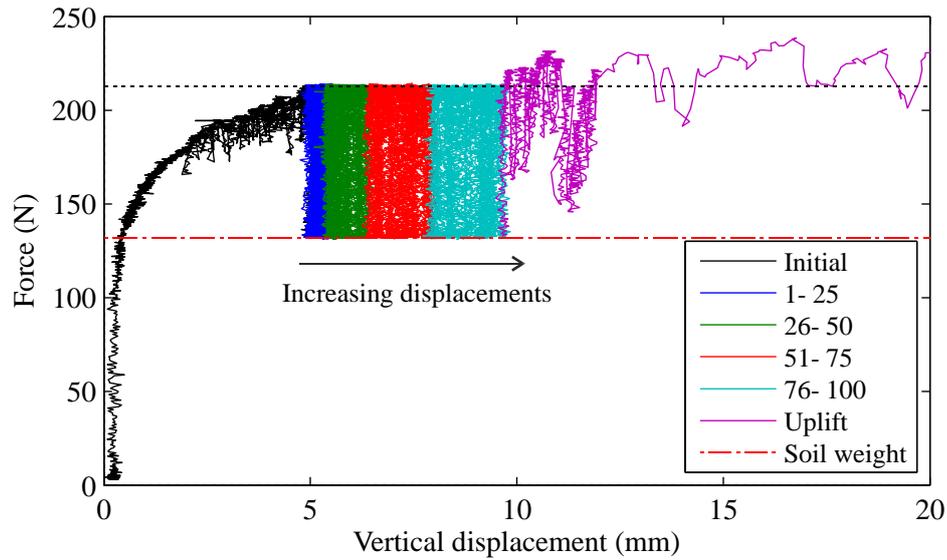
Figure 5-26 Force-displacement response for one-way OB test at H/D* = 4.5

| (a) | (b) |
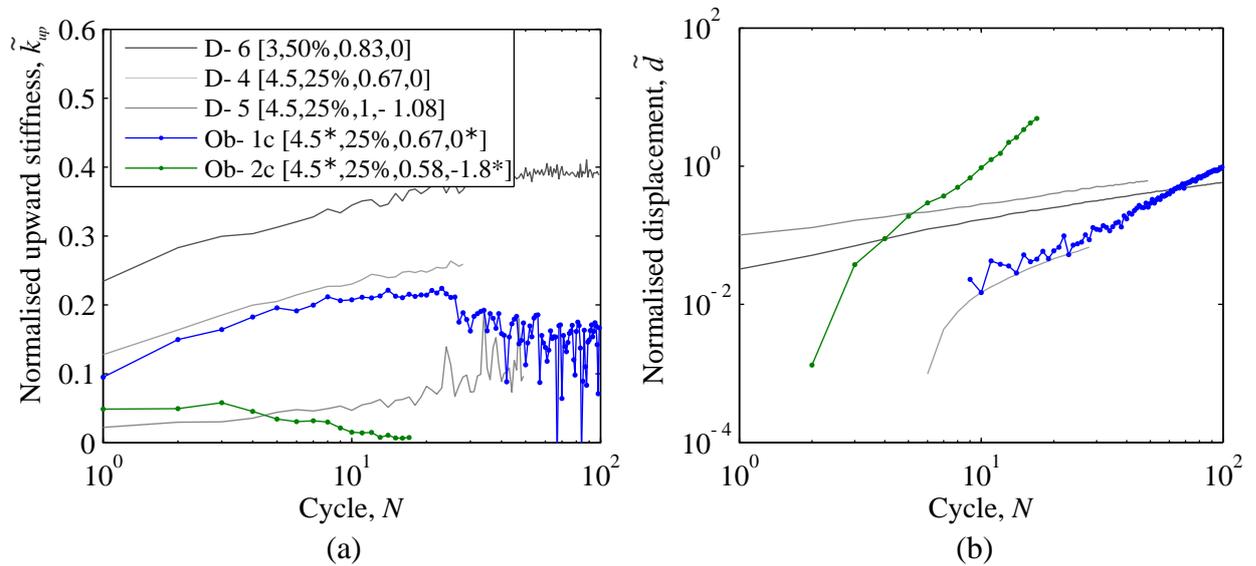
Figure 5-27 Normalised stiffness (a) and displacements (b) for OB tests compared to previous tests (tests: OB-1c and 2c)

Figure 5-27 compares the normalised upward stiffness and displacement values to the previous dry sand tests. Initially, the upward stiffness matches very well to 'equivalent' tests with no OB (i.e. the tests with similar load characteristics). However, after a small number of cycles the upward stiffness begins to decrease rather than increase. This could be because in OB tests, the peak load in each cycle is well above what can be achieved by the soil cover alone, as it is mostly due to the additional overburden contribution. Therefore, the upward stiffness in this force region cannot be expected to increase in the same manner. The

downward stiffness, on the other hand, increases as normal, causing the displacements to run away after a few cycles (Figure 5-27 (b)). This demonstrates that while for monotonic resistance, the application of an overburden pressure can mimic an increase in the embedment depth, the same may not hold true for cyclic loading at these load levels. It should be noted that the response in the cyclic OB tests may depend on how the overburden is applied and how the resultant stresses are carried by the sand (the rigid board may not in fact be representative of a rock berm, which would eventually deform as the pipe moves upwards).

5.4.2.   Cycling from actual *H/D* reference load

One final test was carried out to investigate whether the cyclic response of a test with an overburden can be compared to tests at the actual embedment depth (in this case *H/D* = 3). In this test, the load was varied symmetrically around the actual soil weight, from 52-120 N. This is compared in Figure 5-28 to a cyclic test at *H/D* = 3 with no OB, introduced in section 5.3.1.2 (test D-2b). The figure shows that while the OB test has a much stiffer initial response (similar to *H/D* = 4.5), the cyclic behaviour is consistent in the two tests. The initial displacement downwards is very small, and the incremental displacements decrease with each cycle. Figure 5-29 confirms that the upward stiffness and displacement response are similar in the two tests.
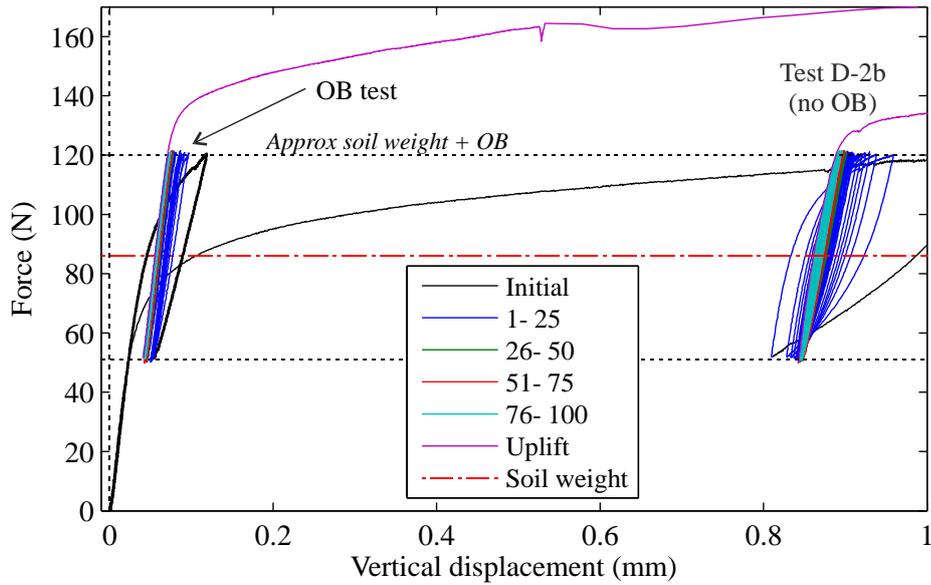
Figure 5-28 Force-displacement response for OB test using W_{ref} based on actual H/D (test: OB-3c)

(a)

(b)
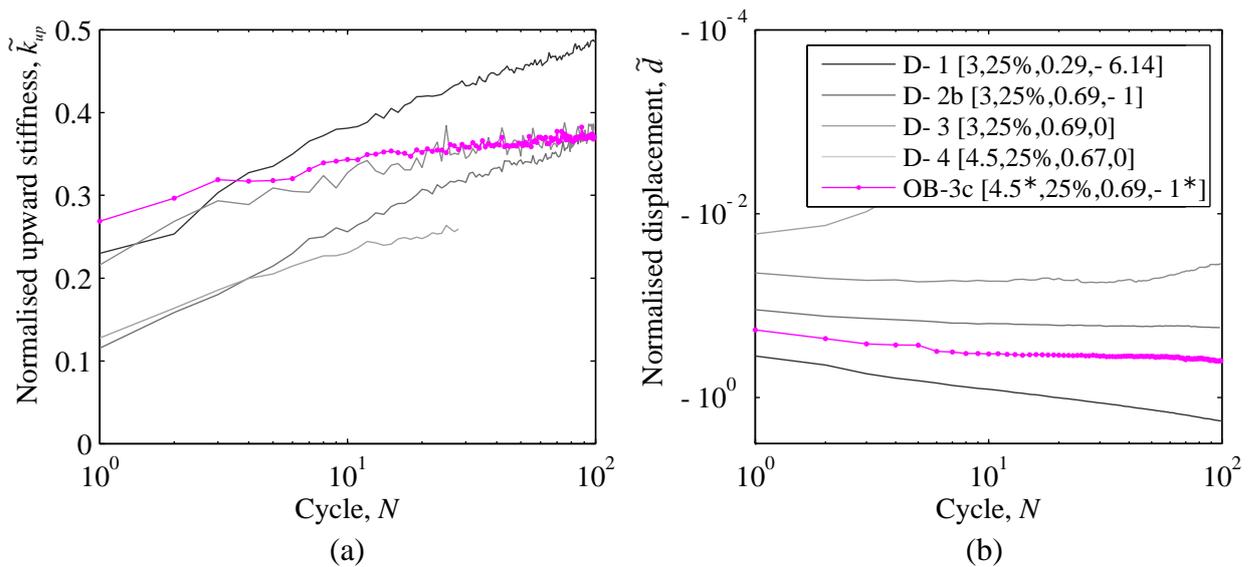
Figure 5-29 Normalised stiffness (a) and displacements (b) for OB tests using W_{ref} based on actual H/D (test: OB-3c)

5.5. Cyclic tests in saturated sand

The dry sand tests demonstrated several scenarios of possible movement that result from variation in loading and backfill parameters. It is clear that the direction of loading with respect to the weight of the soil cover is an important determining factor in the behaviour of the pipe. In general it appears that if the average cyclic load is above the soil weight, the pipe

may move upwards over several cycles, whereas if it is below this value, the pipe will move down. The magnitude of the loading with respect to the uplift resistance (influenced by embedment depth and relative density) also influences the displacement behaviour. Irrespective of the direction of movement, the process appears to be stable; as found by Leblanc et al. (2010) for lateral cycling of piles, the pipe displacements in dry sand degrade over a number of cycles as both the upward and downward stiffnesses increase. An exception to this is in tests with an overburden: if the pipe is cycled within the resistance region provided by the additional weight (i.e. above the peak resistance in a test without an overburden), the process is no longer stable.

The drained monotonic tests presented in Chapter 3 indicated minor differences between the results in dry and saturated conditions. Notably, the normalised peak forces in the loose dry sand tests (RD 20-25%) were more consistent with the loosest saturated tests ($RD = 0\%$) than with the saturated tests at similar densities. Additionally, the lower effective stress levels in the saturated tests result in smaller mobilisation displacements, meaning that the force-displacement response up to peak is generally stiffer. In light of these differences in the monotonic behaviour, a small number of cyclic tests were carried out in very loose saturated Redhill 110 sand ($RD = 0\%$). The objective was to determine whether the cyclic behaviour in saturated conditions is consistent with the dry sand tests (as well as with other saturated tests presented in the literature). A more detailed set of tests was then carried out at $RD = 20\%$ in order to establish trends in the cyclic response related to ζ_b and ζ_c. All saturated tests are summarised in Table 5-5.

Table 5-5 Cyclic tests in saturated sand

ID	H/D	RD (%)	N	F_{min} (N)	F_{max} (N)	W_{ref} (N)	$F_{ult,ref}$ (N)	ζ_b	ζ_c
S-1	3.58	0	13	0	85	54	88	0.91	-1.74
S-2	3.54	0	14	40	85	54	88	0.91	-0.45
S-3	3.6	0	50	55	85	54	88	0.91	0
S-4	3.53	20	27	55	85	55	116	0.49	0
S-5	3.52	20	27	55	105	55	116	0.82	0
S-6	3.5	20	99	55	110	55	116	0.9	0
S-7	3.45	20	50	55	115	55	116	0.98	0
S-8	3.53	20	47	35	115	55	116	0.98	-0.33
S-9	3.51	20	26	20	115	55	116	0.98	-0.58
S-10	3.5	20	206	65	115	55	116	0.98	0.17
Total saturated cyclic tests = 10									

5.5.1.   Initial tests – comparison with dry sand results

These tests were prepared in the same manner as the saturated monotonic tests in Chapter 3, using soil fluidisation and a load control routine (set at -10 N) during installation. A single embedment depth of approximately 3.5 was tested, as this was the 'base case' used in the monotonic tests. The loading rate was again set at 0.002 mm/s to avoid excess pore pressure development, if possible. In all the tests carried out, the pore water pressure around the pipe was monitored. From these measurements, it was observed that the cycling of the pipe at this low speed did not cause any excess pore pressures to develop over time; thus, the tests could be considered drained and compared directly to the dry tests.

Figure 5-30 (a) presents the force-displacement results for several cyclic tests at a soil relative density of 0%, compared with a monotonic pullout test. The calculated soil weight of approximately 54 N is indicated in the figure, along with the apparent weight of the soil found in a test with no initial load control routine. Unlike in the dry sand tests, the weight initially held by the pipe prior to installation is less than what is predicted using $\gamma'HDL$. For these tests the higher calculated soil weight is selected for W_{ref}. The curves shown are a one-way test

above the calculated soil weight (S-2); a two-way test starting from the apparent soil weight (S-3); and a two-way test from zero, with an average force between the apparent and the calculated soil weight (S-1). According to the framework, this means that across the three tests the loading type (ζ_c) is varied, while the magnitude (ζ_b) is kept constant. As indicated in the figure, the pipe in all three tests tends to move down slightly after the initial cycle, although the displacement is progressively less, the closer the test is to one-way (as ζ_c increases). This is generally consistent with the dry sand tests in terms of the effect of the parameter ζ_c. However, in tests S-2 and S-3, the average load is above both the calculated and apparent soil weight. Although at this point the pipe might be expected to move upwards, it still moves down in both cases.
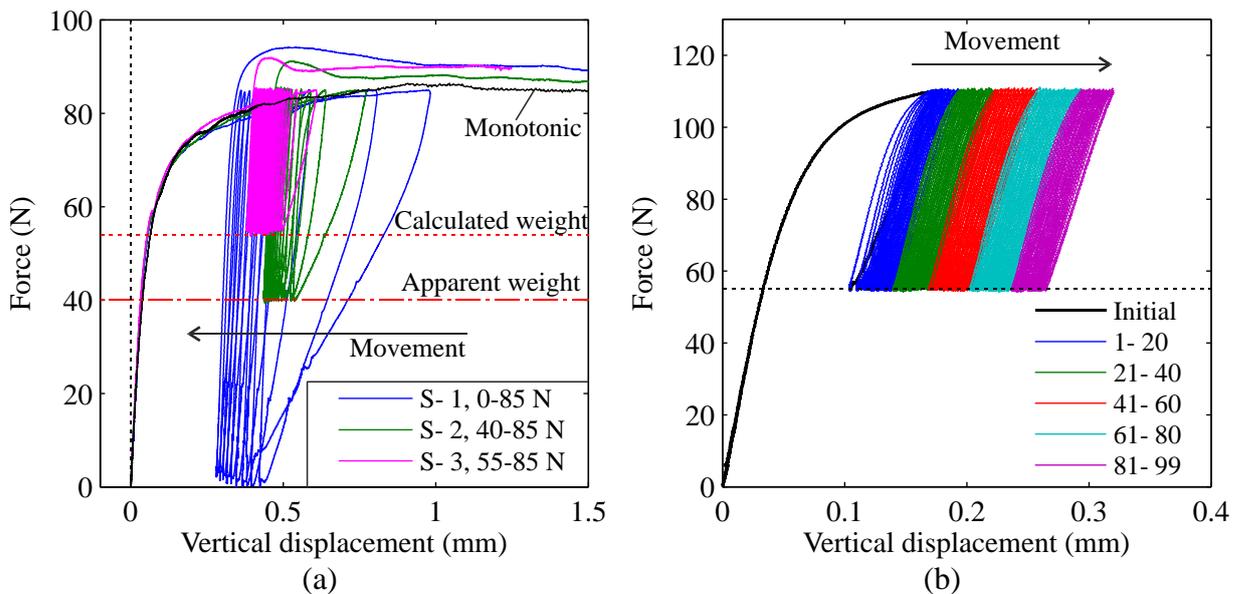
Figure 5-30 Force-disp. response for initial saturated tests: (a) S-1, S-2, S-3, RD = 0%; (b) S-6, RD = 20%

In contrast, Figure 5-30 (b) shows a one-way test (S-6) with a backfill relative density of 20%, where the pipe now moves upwards continuously from the initial cycle. In this test, both the load magnitude and type are the same as in test S-3 – it is only the relative density that has increased, causing the change in the net displacement direction.

An interesting observation from Figure 5-30 (b) is that for the cycles shown, the displacements do not appear to be decreasing with cycle number. This indicates that unlike in

the dry tests, the response does not stabilise. The normalised displacements for the four saturated tests are plotted in Figure 5-31 with the dry test results, to compare the patterns of response. In part (a) – which is plotted on a regular scale to include both upward and downward moving tests – it can be seen that the displacements in the downward saturated tests seem to match the decaying behaviour of the dry tests (moving in both directions). For test S-6, however, the displacements appear to be increasing approximately linearly with cycle number. It must be noted that the actual values of the displacements are much greater for the upward moving dry tests than for S-6: in S-6 the pipe moves upward by around 0.2 mm over 100 cycles, while in D-5, the pipe moves almost 10 mm in half the number of cycles (after an initial displacement of around 13 mm).

Displacements for the downward moving tests are plotted on a log-log scale in Figure 5-31 (b). Here it can be seen that the slope in these tests is similar, and is consistent with the one dry test that moves downwards only (D-1b). If these tests are fitted to a power relationship, as in equation 5.1, the constant value calculated for the exponent is 0.341. This matches well with the value of 0.31 proposed by Leblanc et al. (2010). The fitted parameters for each test, along with the calculated R^2 values, are listed in Table 5-6. The high R^2 values indicate that the response is very well matched by the model.

Normalised upward stiffness values are plotted for the same tests in Figure 5-32, using a regular scale in (a) and a semi-log scale in (b). On the semi-log plot it can be seen that the slope of the stiffness curves is greater for tests experiencing the most negative displacements. This is logical because if the uplift resistance stiffens more rapidly over a number of cycles, it is probably less likely to move upwards. While the shapes of the stiffness curves match quite well for the downward moving tests, test S-6 again does not compare well to the dry test. In fact, in this test the stiffness reaches a peak between 10 and 20 cycles, and then begins to decrease. This implies that the uplift resistance begins to degrade with increasing number of cycles, which explains why the upward displacement does not appear to stabilise.
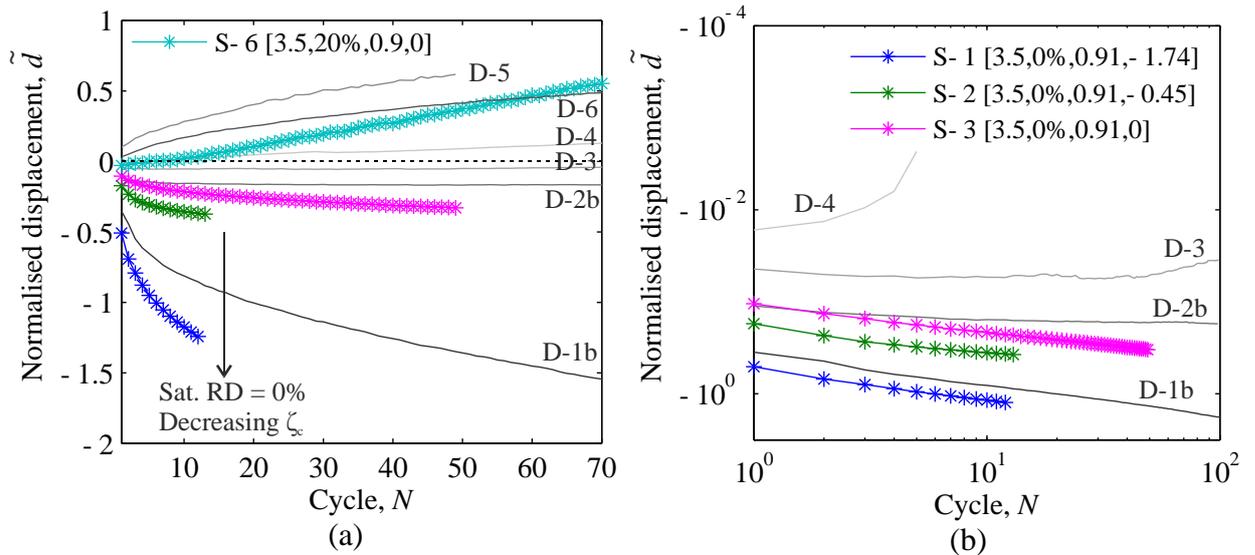
Figure 5-31 Normalised displacements vs. cycle (S-1,2,3,6): (a) plotted on a regular scale; (b) plotted on a log-log scale for downward moving tests only.
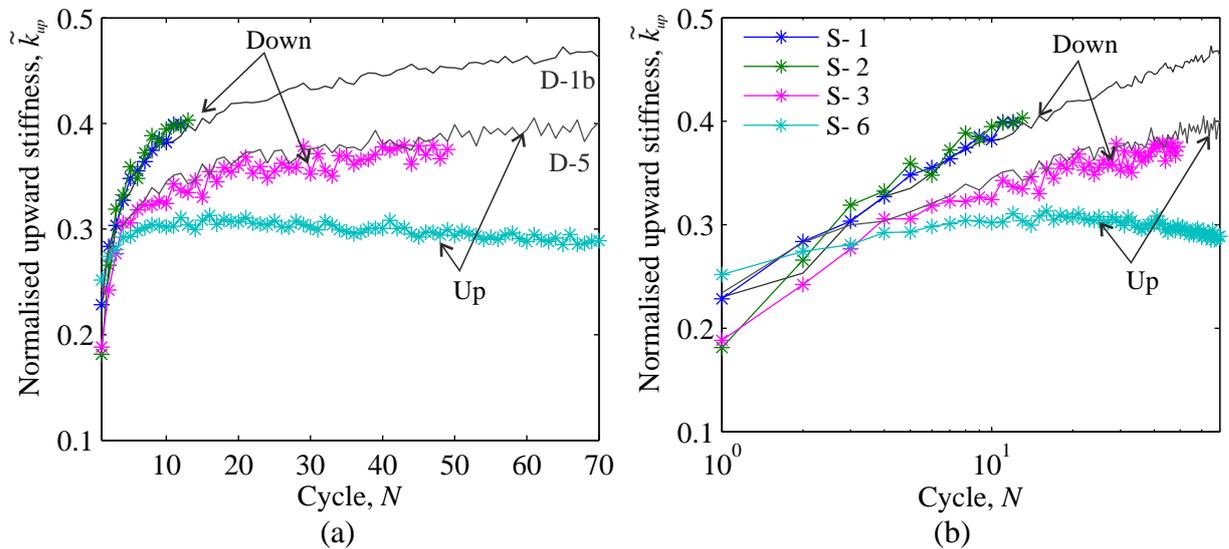
Figure 5-32 Normalised stiffness vs. cycle (S-1,2,3,6): (a) plotted on a regular scale; (b) plotted on a semi-log scale.

From the above comparison between the dry and saturated tests, it can be concluded that the behaviour in the downward-moving tests is similar under both conditions, and that the displacement trends are consistent with the lateral pile case (as shown in Table 5-6). Reducing the load direction parameter (as in S-1 to S-3), has the expected effect of increasing the downward displacements. The upward-moving saturated test (S-6) highlights a critical case where the upward displacements do not appear to decay (beyond around 10-15 cycles), as was observed in in the dry sand tests. This finding does not necessarily contradict the displacement trend in the saturated test by Wang (2012), since only 10 cycles for each loading

203

group were carried out. The cause of the displacement behaviour observed here is explored in the following section, which attempts to isolate the influence of loading parameters in upward-moving saturated tests. The discrepancy between the dry and saturated tests is also addressed in the discussion at the end of this chapter (see section 5.6.1.2).

One final aspect of the response to note is the post-cyclic uplift resistance, shown for the three tests in Figure 5-30 (a). Due to densification of the soil during cycling, the peak resistance is slightly increased from the monotonic value (by up to 10%). This is not significant, as it is less than the 30% improvement caused by increasing the initial soil relative density from 0 to 20% in a monotonic test.

Table 5-6 Displacement curve fits for downward moving tests

	Test parameters				Displacements: $\frac{\Delta\theta(N)}{\theta_s} = C \cdot N^x$		
ID	*H/D*	*RD*	ζ_b	ζ_c	C	*x*	R^2
D-1	3	25	0.29	-6.14	-0.365	0.341	0.997
S1	3.58	0	0.91	-1.74	-0.539	0.341	0.996
S2	3.54	0	0.91	-0.45	-0.164	0.341	0.910
S3	3.6	0	0.91	0	-0.091	0.341	0.975

5.5.2.   Influence of loading parameters in saturated tests

In the context of the pipeline unburial problem, conditions that result in net upward displacements of the pipeline are of the most concern. While it appears from those tests that the pipe is likely to bury itself further during cycling unless the loading magnitude is very high, it is necessary to investigate the influence of different variables further, so this change in response can be predicted. To address this, the remaining cyclic tests in this section examine the effect of varying ζ_b and ζ_c in saturated tests with a relative density of 20%. Two sets of tests were run: first, the load magnitude was varied for tests with $\zeta_c = 0$ (i.e. cycling above the reference weight); and second, ζ_c was varied for very high constant load magnitude. The results are compared, where possible, to the framework of Leblanc et al. (2010).

5.5.2.1. *Varying load magnitude*

Starting from the reference weight, four tests were carried out with varying load magnitudes of 0.49, 0.82, 0.9, 0.98 (for a relative density of 20%). The force, displacement, and stiffness results for these tests are shown in Figure 5-33 to Figure 5-35. It can be seen that cycling in all tests results in upward movement, which is proportional to the load magnitude. In Figure 5-34, the absolute and normalised displacements are plotted against cycle number in (a) and (b), respectively. Both show that the displacement trend is approximately linear with respect to cycle number. Although in all cases the displacement is small, there is no indication that the rate decays within this range of cycles. For the two lowest magnitudes, 0.49 and 0.82, the upward displacement is extremely small, and there is little difference between the two tests, other than in the d_0 value (i.e. the displacement in the 0th cycle). It can also be seen that because d_0 is very small for these cases, the normalised displacement response is slightly amplified. At ζ_b values lower than those tested here, the displacement response might be expected to either exhibit similar behaviour, or to transition to downward movement.

Once the load magnitude is increased above 0.9, the slope of the displacements increases rapidly. From the normalised stiffness values (both downward and upward responses are plotted on a semi-log scale against cycle number in Figure 5-35), it can be seen that in all tests, the initial upward stiffness increases for approximately the first 10 to 15 cycles. At this point the stiffness plateaus or even decreases (as in test S-6). The downward stiffness is higher than the upward stiffness and follows a similar trend, except that the slope has more variability from test to test. In the tests with lower values of ζ_b, the upward and downward stiffnesses tend to converge, reducing net displacements, while at the highest value of ζ_b the upward and downward stiffness seem to remain the same vertical distance apart throughout. The difference between the stiffness values for each test is plotted in Figure 5-35 (b), with a positive value indicating upward movement. It is evident that the greater the load magnitude, the larger the difference between the two stiffnesses, and the less likely they are to converge.

This explains the larger displacements in the test with $\zeta_b = 0.98$, as well as the linear increase with cycle number.

The two-stage stiffness response is likely due to the finite amount of soil cover above the pipe. There is a limit to the additional resistance that can be gained as the pipe displaces upwards. Certainly in the test with a load magnitude of 98% of the peak, the static mobilisation displacement of the pipe-soil interaction is well exceeded after several cycles. The downward stiffness should represent only the unloading response of the soil above the pipe, as the tests are effectively one-way and do not bear on the soil beneath the pipe. In this region, the response is stiffer in unloading than loading – hence, the upward movement.
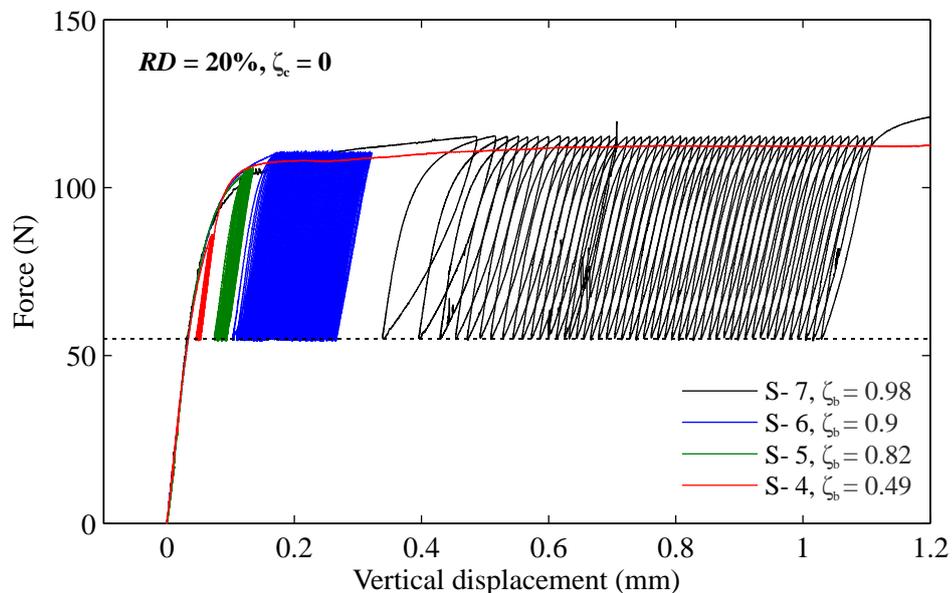

Figure 5-33 Force-displacement response for varying load magnitude (tests: S-4,5,6,7)

Figure 5-34 Displacements vs. N for varying load magnitude: (a) absolute; (b) normalised displacements.

206
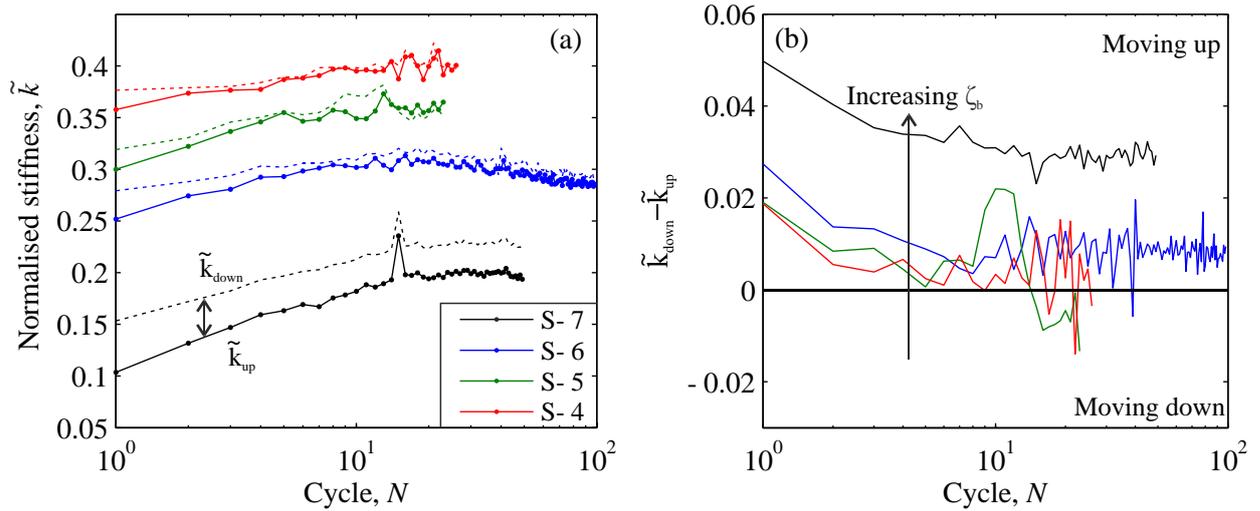
Figure 5-35 Stiffness vs. cycle number for varying load magnitude: (a) normalised up/down; (b) difference.

5.5.2.2.   *Varying load type*

In order to examine a worst-case situation for upward displacements, the highest load magnitude ($\zeta_b = 0.98$) was selected from the above tests to examine the effect of loading type on the cyclic response. Three additional tests were carried out with load-type parameters (ζ_c) of -0.53, -0.33, and 0.17. The results are presented in Figure 5-36 to Figure 5-38. The force-displacement curves in Figure 5-36 show that for the range of load type parameters, the displacements are still generally much higher than for low loading magnitudes (i.e. the variation caused by this parameter is smaller). From this figure (and in Figure 5-37) it can be seen that the worst case in terms of displacements (the greatest slope) appears to be one-way loading from the reference weight ($\zeta_c = 0$). As in the previous tests, the upward displacements exhibit an approximately linear relationship with cycle number. In test S-10, it can be seen that this trend continued for up to 200 cycles.

In Figure 5-38 (a) the range of the normalised stiffnesses is shown to be much smaller than in the previous tests. The curves exhibit similar shapes for different values of ζ_c, although the difference between the upward and downward stiffness varies (Figure 5-38 (b)). As found in Figure 5-35, the test that has the largest difference between the upward and downward stiffness is the test that experiences the most positive displacement. Interestingly, the

difference curve shown in Figure 5-38 (b) levels off in all the tests. This indicates that it is the load magnitude, rather than the load type tested here, which controls whether or not the stiffness values converge and the displacements decay. In other words, the stability of the problem may be governed primarily by the magnitude of the cycling.

The true difference between the tests caused by varying values of ζ_c is perhaps not obvious, since it appears that this factor may be less important than the load magnitude. Also, it must be noted that due to some variation during installation for each test, the initial stiffness response also varies. The variation is small in the initial uplift – below a force of 100 N – but it can be seen in Figure 5-36 that the start of the first cycle is reached at different displacements for each test. The initial downward stiffness also differs as a result of this. Consequently, it may be difficult to isolate the response caused by the installation from the response caused by the load magnitude factor.

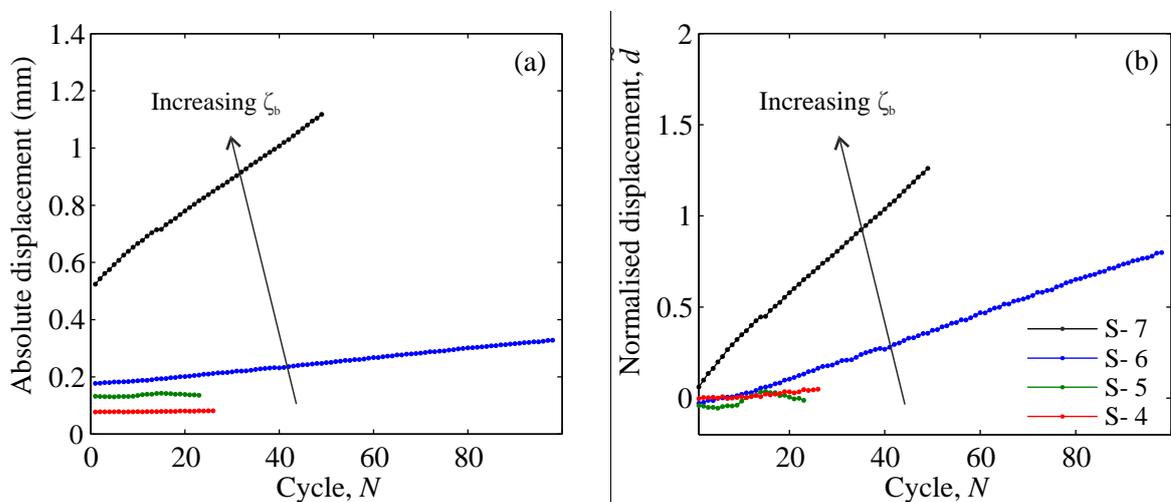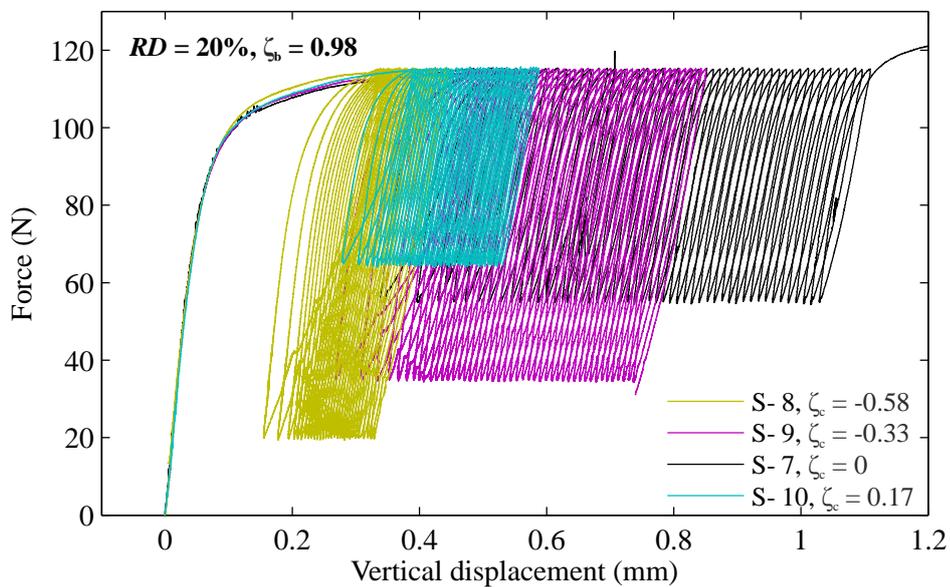*Figure 5-36 Force-displacement response for varying load type(tests: S-7,8,9,10)*
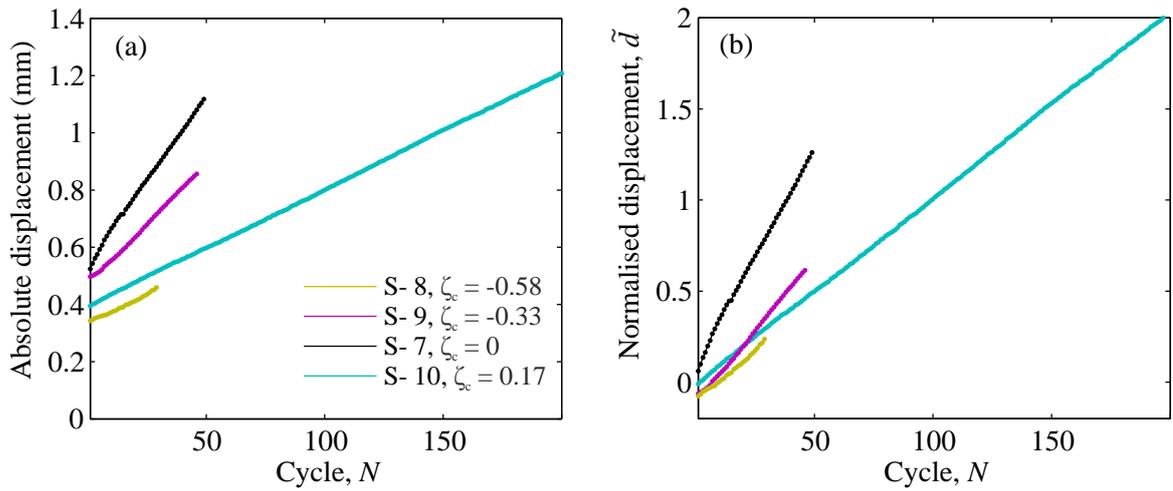
Figure 5-37 Displacements vs. cycle number for varying load type: (a) absolute; (b) normalised displacements.
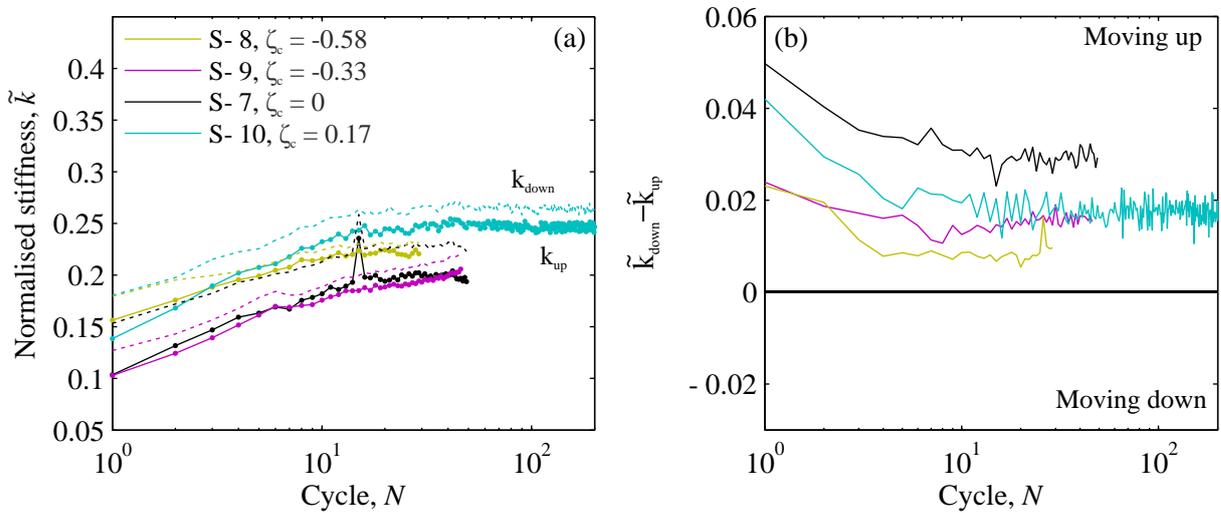
Figure 5-38 Stiffness vs. cycle number for varying load type: (a) normalised up/down; (b) difference.

5.5.3. Parametric curve fit

It is clear that there are several important differences between vertical cycling of pipelines and the lateral cycling of piles, such as the in the loading symmetry (the pipe problem is asymmetric), the effective stress regime, and in the fact that there is limited soil cover above the pipe. The testing conditions in this study also differ from those examined by Leblanc et al. (2010) in terms of the number of cycles (significantly less), and the magnitude of the load (significantly more). As a result, differences in the displacement and stiffness behaviour have been observed − for example, in the linear displacement trends (compared to a power-law decay) and the levelling off of the upward stiffness after a number of cycles. Nevertheless, the

loading parameters, ζ_b and ζ_c, were shown to have a clear influence on the pipe response. This suggests that an adaptation of the framework established for lateral cyclic loading of piles could be useful for this problem. In the following section, the observed trends in displacement and stiffness caused by systematic variation of the load parameters are explored, in an attempt to quantify/predict the response. For context, the established relationships are compared to observations in the pile problem where applicable.

For the normalised upward displacements a linear relationship to cycle number was assumed as follows:

$$\frac{d_N - d_0}{d_0} = A_d \cdot N + b \tag{5.4}$$

where A_d is the product of the factors T_b and T_c, similar to those defined by Leblanc et al. (2010). The factors T_b and T_c are functions of ζ_b and ζ_c, respectively, while relative density (and possibly other factors) may also influence T_b. A least squares regression was carried out to fit the above parameters to the saturated test data (with $RD = 20\%$), constraining b to a constant value. The results are presented in Table 5-7 along with the corresponding R^2 values for each data set. With the exception of test S-4 (shown in italics) and tests with very small displacement magnitudes, the linear fit appears to be a satisfactory approximation. However, since the displacements typically converge over the first ten cycles, the linear approximation is only applicable if a larger number of cycles is considered (for example, $20 < N < 200$).

Curve fits for the normalised stiffness (both upward and downward) are also provided in Table 5-7. As described above, the stiffness response appears to be bilinear when plotted on a semi-log scale, increasing for approximately 15 cycles before either levelling off or decreasing slightly. It is possible that the cycle number at which the stiffness plateaus varies depending on the load magnitude (and/or the displacement relative to the monotonic mobilisation displacement), but for the purpose of this analysis it is assumed that the

transition occurs near the 15th cycle. The initial portion of the upward and downward curves

up to $N = 15$ was fitted to the following relationship:

$$\tilde{k}_N = \tilde{k}_0 + A_k \ln N \qquad (5.5)$$

where:
$$\tilde{k}_0 = K_b(\zeta_b)K_c(\zeta_c)$$

This is identical to the formulation for the pile problem, and appears to provide a good fit

for most of the data, in both loading directions (although again the tests with greater

displacement magnitudes have higher R^2 values for both fits). A constant slope value, A_k, was

fitted separately to the upward and downward data sets. The value of A_k was found to be

slightly higher for the upward stiffness response than for the downward response, while the k_0

values were always higher in the downward direction. This confirms a converging stiffness

response for the first 15 cycles in all tests, which corresponds to decreasing incremental

displacements for these cycles. It can then be hypothesised that once the transition point at 15

cycles is achieved, the upward and downward stiffness curves will remain equidistant for

further cycles, resulting in linear displacement increments. The difference between the two

stiffness values at 15 cycles may therefore determine the rate of displacement.

Table 5-7 Curve fits for displacement and stiffness data (saturated tests)

Test parameters			Displacements $b = -0.037$		Stiffness, $N = 15$ (up) $A_k = 0.0261$		Stiffness, $N = 15$ (down) $A_k = 0.0215$	
ID	ζ_b	ζ_c	A_d	R^2	$\tilde{k}_0$	R^2	$\tilde{k}_0$	R^2
S-4	0.49	0	*0.0036*	*0.295*	*0.339*	*0.273*	*0.353*	*0.116*
S-5	0.82	0	0.0024	0.484	0.299	0.786	0.318	0.802
S-6	0.9	0	0.0084	0.995	0.247	0.762	0.266	0.699
S-7	0.98	0	0.0277	0.964	0.123	0.816	0.164	0.814
S-8	0.98	-0.33	0.0134	0.969	0.115	0.957	0.138	0.936
S-9	0.98	-0.58	0.0077	0.882	0.156	0.979	0.175	0.964
S10	0.98	0.17	0.0104	1.000	0.166	0.892	0.197	0.901

From the above fits, the factors relating to the loading parameters were determined. For the displacements, T_c was set to 1 for $\zeta_c = 0$, such that T_b could be calculated from tests with varying ζ_b. Based on these values, T_c was then calculated for the tests with varying ζ_c. The same assumption was used to calculate the stiffness factors for both loading directions. The calculated coefficients are listed for each test in Table 5-8. Also included in the table are two further calculated quantities, which could provide a good indication of the stability of the problem. The first is $\Delta \tilde{k}_0$, which was calculated by subtracting $\tilde{k}_{0,up}$ from $\tilde{k}_{0,down}$. If this value is positive, the initial cyclic displacement should be upward, since the stiffness in this direction is lower. The second calculation, $\Delta \tilde{k}_{15}$, takes into account both the initial stiffness and the (constant) rate of convergence over the first 15 cycles. As this value approaches zero, the rate of upward displacements would also be expected to do so. These stability indicators could also be described as a function of two factors (not shown in the table) in the same manner as above, for example:

$$\Delta \tilde{k}_0 = C_b(\zeta_b)C_c(\zeta_c)$$

(5.6)

Table 5-8 Calculated factors for displacement and stiffness response (saturated tests)

| Test Parameters			Displacement coefficients		Stiffness coefficients (+)		Stiffness coefficients (-)		Stability indicators	
ID	ζ_b	ζ_c	T_b	T_c	$K_{b,u}$	$K_{c,u}$	$K_{b,d}$	$K_{c,d}$	$\Delta \tilde{k}_0$	$\Delta \tilde{k}_{15}$
S-4	0.49	0	0.0036	1	0.339	1	0.353	1	0.014	0.001
S-5	0.82	0	0.0025	1	0.299	1	0.318	1	0.018	0.006
S-6	0.9	0	0.0084	1	0.247	1	0.266	1	0.019	0.007
S-7	0.98	0	0.0277	1	0.123	1	0.164	1	0.042	0.029
S-8	0.98	-0.33	0.0277	0.485	0.123	0.936	0.164	0.842	0.024	0.011
S-9	0.98	-0.58	0.0277	0.278	0.123	1.274	0.164	1.063	0.018	0.006
S-10	0.98	0.17	0.0277	0.3755	0.123	1.350	0.164	1.196	0.031	0.019
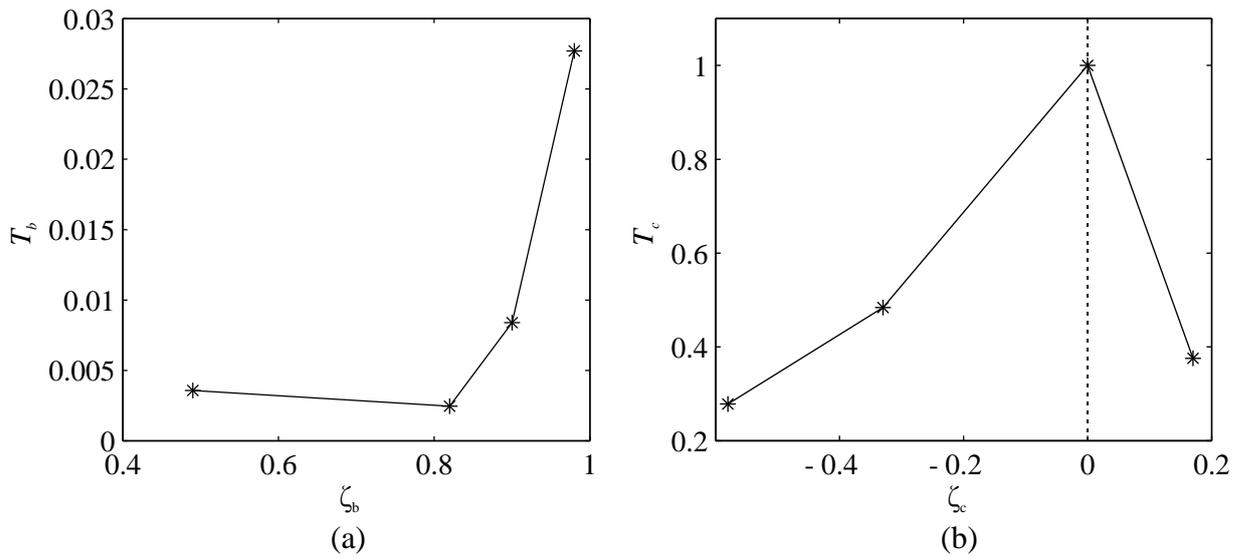
Figure 5-39 Displacement factors w.r.t: (a) load magnitude; (b) load type
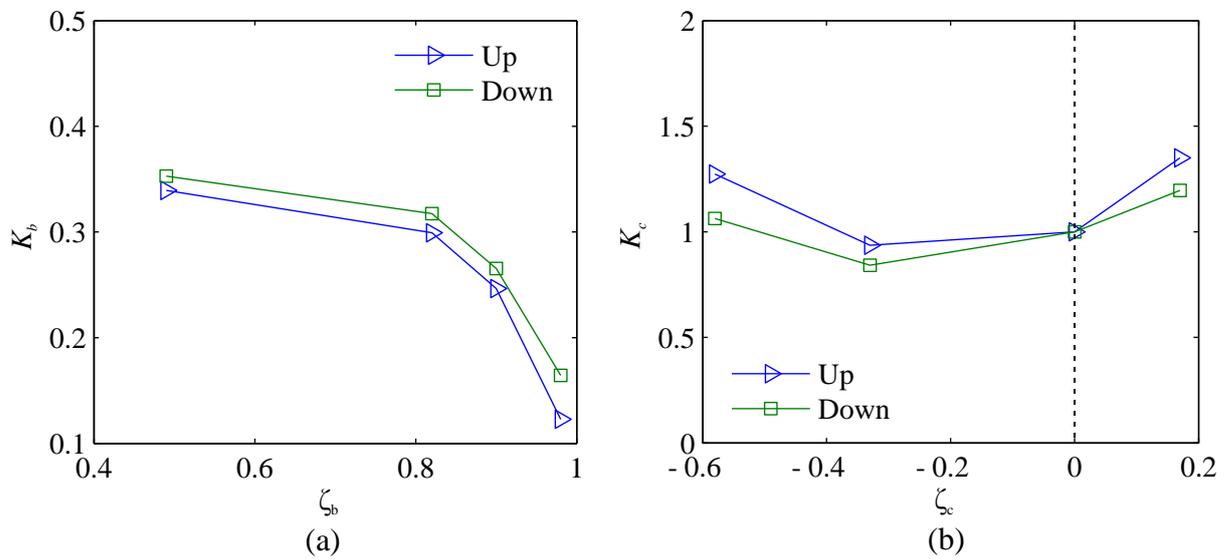

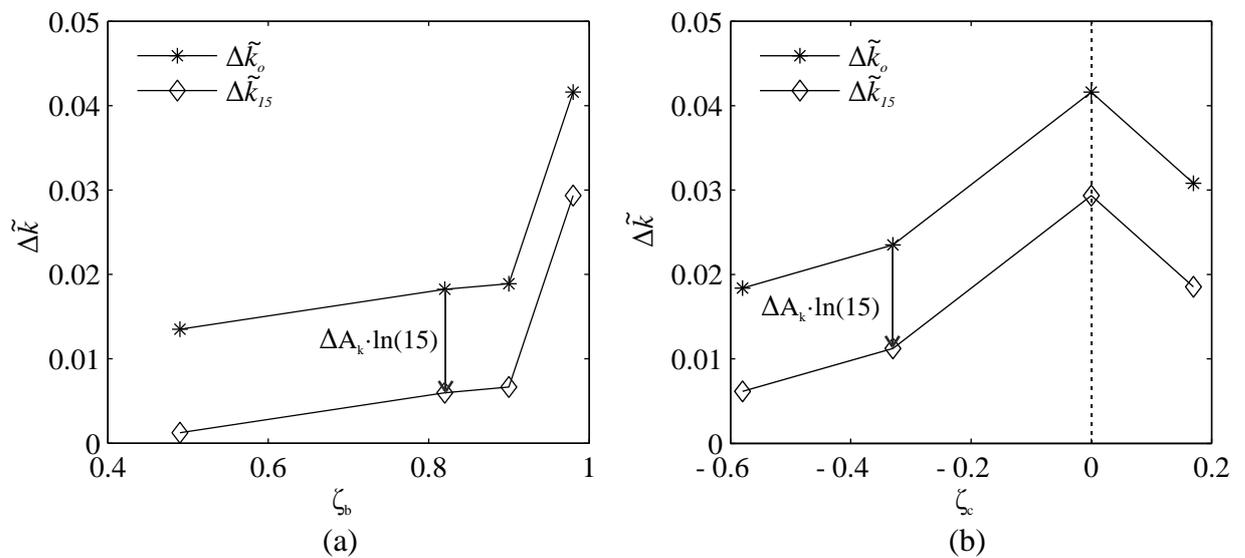*Figure 5-40 Stiffness factors in terms of: (a) load magnitude; (b) load type*

Figure 5-41 Stability factors in terms of: (a) load magnitude; (b) load type.

Trends in the coefficients for displacement, stiffness, and stability are plotted against the corresponding load parameter in Figure 5-39, Figure 5-40, and Figure 5-41, respectively. In Figure 5-39 the displacement factors – which are direct multipliers of the displacement slope – are plotted against the load parameters. Both compare well in a general sense to the trend seen in the pile problem; that is, T_b monotonically increases with the load magnitude while T_c exhibits a peak response at a particular value of the load type parameter. In (a), the function shows a gradual increase of T_b at lower load magnitudes followed by a sharp increase above $\zeta_b = 0.8$. This could be explained by considering the monotonic force-displacement response of saturated Redhill 110, established in Chapter 3. The initial stiffness of response is consistent and high for load levels up to 85 or 90% of the peak force, after which the curve finally begins to soften. The rapid increase in the rate of upward displacement at load levels greater than this range could then be attributed to the corresponding softening of the secant stiffness. This evidence lends itself to the theory that relative density, as well as embedment depth and effective stress level, also affect the rate of displacement since they have a significant effect on the monotonic force-displacement response. Figure 5-39 (b) confirms the observation that for these tests the one-way loading case above the weight of the soil is the most critical load type.

The stiffness coefficients in both loading directions are plotted in Figure 5-40. It should be noted that in (a), the K_b functions are an accurate representation of the difference between the initial upward and downward stiffness, k_0, in terms of ζ_b. The functions in (b), however, are shifted with respect to each other, due to the assignment of $K_c = 1$ for $\zeta_c = 0$ in both cases. The shapes for both the upward and downward stiffness functions are similar. As with the displacements, the trend in the stiffness response can be explained by the force-displacement response of Redhill 110. In fact, the displacement and stiffness functions have similar, but reversed, shapes.

In Figure 5-40 (b) the conclusions drawn with respect to the load type may be less obvious since the initial upward and downward stiffness values may depend more on the installation conditions than the load type parameter. What can be concluded, by comparing the relative values of the factors K_b and K_c, is that the load magnitude is the more critical influence.

Given the complexity of the interaction between the upward and downward resistance, looking at either the upward stiffness or the downward stiffness values on their own may not provide sufficient information to judge the response of the pipe. Instead, it is the difference between the two functions that should perhaps be examined. Figure 5-41 shows the calculated values for $\Delta \tilde{k}_0$ and $\Delta \tilde{k}_{15}$ with respect to the load parameters. In (a) it can be seen that the function matches the trend of T_b very well, while in (b) the match is also good, though with some discrepancy for the $\zeta_c = 0.17$ case. The figures show that the direction of the initial displacements can be determined by $\Delta \tilde{k}_0$ only, but the parameter $\Delta \tilde{k}_{15}$, which takes into account the rate of convergence over the first 15 cycles, may give a useful indication of the severity of the displacements once the limiting resistance is reached.

5.6. Discussion

5.6.1. Prediction of the cyclic behaviour

The dry and saturated tests described in this chapter have demonstrated two broad trends in the vertical cyclic behaviour of a buried pipeline. In general, if the average cyclic load is below the reference load – in this case, the weight of the soil cover – the net movement of the pipe will be in the downward direction (consistent with the average direction of loading). Under these loading conditions, the pipe responds very similarly to piles under cyclic lateral loading, where the soil stiffness increases with cycle number while the rate of displacement decreases.

If, however, the average load is equal to or above the reference force, the pipe may move upwards, depending on a number of factors. This can be considered the more critical case in

the context of upheaval buckling as the soil resistance in the upward direction is limited by the height of the soil cover, which will decrease with increasing upward displacement. In upward-moving saturated tests it was found that the soil stiffness increased for the first 10-15 cycles, before levelling off or even decreasing. This corresponded to a displacement rate that decreased before reaching a constant value; after which, the pipe displaced linearly with time. Using the fitted parameters in Table 5-7, model predictions for this behaviour are plotted against the test results in Figure 5-42. The figure demonstrates that the relationships given in equations 5.4 and 5.5 (for displacement and stiffness, respectively) provide a good representation of the observed behaviour in these tests.
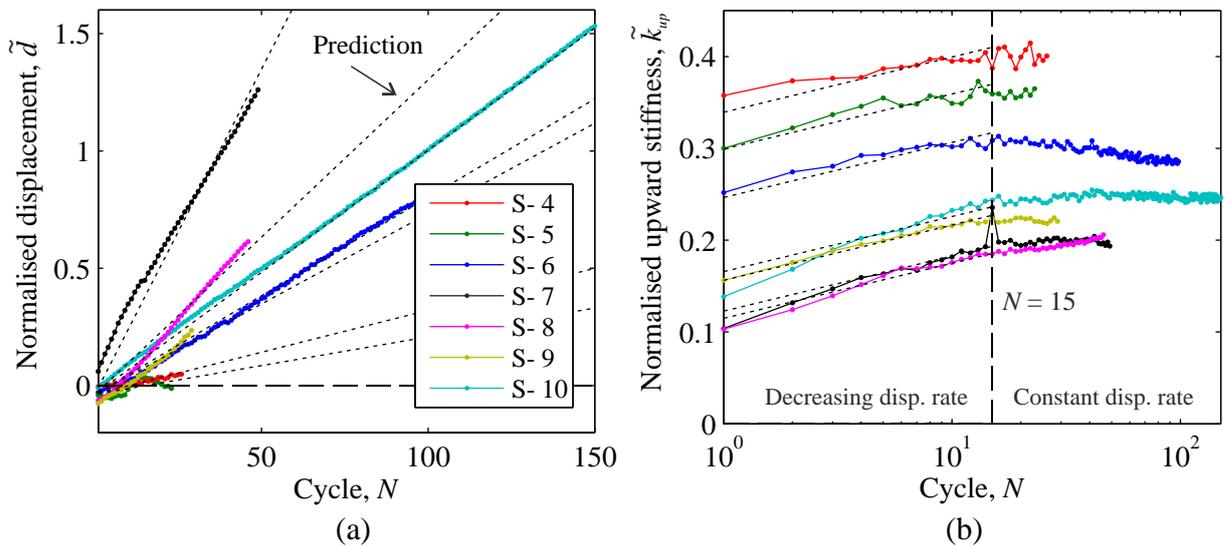
Figure 5-42 Model predictions plotted against saturated sand results for: (a) normalised displacements; (b) normalised upward stiffness

The analysis of the saturated sand tests (section 5.5.3) demonstrated trends in cyclic displacement and stiffness responses based on two loading parameters: one that defines the cyclic load magnitude as a proportion of the peak uplift resistance, and the other that describes the direction of loading with respect to the reference weight. As mentioned above, even if the average direction of loading is upward, the pipe may not necessarily move upward – though it would be conservative to assume that it does. In this final section, the remaining

influences on cyclic behaviour are discussed, with examples from the various tests covered in this chapter.

5.6.1.1.   *Influence of relative density and embedment ratio*

In the saturated parametric study, it was found that the load magnitude has a strong influence on this problem, and that its influence on the pipe behaviour may be related to the monotonic force-displacement response of the soil. It then follows that the effects of relative density and embedment ratio can be explained by their respective influences on the force-displacement response. As shown in Figure 5-19, increasing the relative density or embedment ratio results in a greater frictional contribution to the total resistance. This means that for a given load magnitude – say $\zeta_b = 0.9$ – a greater proportion of this load is comprised of frictional resistance for higher values of *H/D* or *RD*. Consequently, greater irrecoverable plastic deformation of the soil may occur during each cycle, resulting in more critical upward displacements.

In Table 5-9, examples from the previous tests are given to highlight the influence of relative density and embedment ratio on the general displacement and stability trends. The initial saturated tests at *RD* = 0% (S-1 to S-3) provide an example of the influence of relative density and load type, for a given ζ_b. All three of these tests tend to move downwards. This is different to a test at *RD* = 20% (S-6) with the same factors as S-3. The relative magnitude of the displacements is given by the factor $T_b \cdot T_c$ in the table (based on a power fit). It can be seen here that the calculated $\Delta \tilde{k}_0$ predicts the direction of displacement (by its negative value), but does not exactly match the trend in the magnitudes. Interestingly, the values of $\Delta \tilde{k}_{15}$ are almost identical $\Delta \tilde{k}_0$, indicating that the upward and downward stiffnesses are increasing at approximately the same rate. This may explain why the displacements appear to decay following the power relationship (as in the pile problem).

Two dry tests with equal loading factors but different embedments are also shown in the table. Both tests are moving upward (or transitioning to upward movement), and the pipe with

the greater embedment depth experiences higher displacements. Note that the displacement factors for these tests are estimated based on a linear fit, and the stiffness curves were fitted with A_k values of 0.0325 and 0.0312 for the upward and downward directions, respectively. These slope constants are slightly higher than those found in the saturated tests (but are based only on the two tests). Again the stability indicators correctly predict the direction of response. In test D-3, the near-zero value of $\Delta\tilde{k}_0$ is consistent with the observation that the test is transitioning between downward and upward movement.

Table 5-9 Displacement and stability trends for relative density and H/D

	Test parameters				Displacement		Stability indicators	
ID	*H/D*	*RD* (%)	ζ_b	ζ_c	Direction	$T_b \cdot T_c$	$\Delta\tilde{k}_0$	$\Delta\tilde{k}_{15}$
S-1	3.58	0	0.91	-1.74	Down	-0.539	-0.054	-0.054
S-2	3.54	0	0.91	-0.45	Down	-0.164	-0.058	-0.057
S-3	3.6	0	0.91	0	Down	-0.091	-0.036	-0.036
D-3	3	24	0.69	0	Transition-up	0.0002	0.008	0.004
D-4	4.5	24	0.67	0	Up	0.0019	0.049	0.045

5.6.1.2.   Dry vs. saturated sand tests

One issue that has yet to be addressed is the difference between the upward-moving dry and saturated sand tests, most notably in that the stiffness did not appear to level off in the dry tests. As a result, the upward rate of displacement continued to decay in a power relationship to cycle number, for the range of *N* values tested. From the small number of tests carried out it is difficult to ascertain with confidence the reason behind this. One possibility is that this difference is related to the monotonic failure mechanism. In loose dry sand tests at high embedment ratios, the flow-around mechanism is thought to occur. The load magnitude in these tests was selected based on the measured monotonic resistance (with flow-around behaviour occurring); however, at a given embedment depth there is a higher possible resistance that could be achieved with a pure sliding block mechanism. This implies that the

limiting soil resistance for these tests may actually be higher than the monotonic resistance. Therefore, in these tests the increase in stiffness during cycling (due to densification of the soil) may result in a higher eventual pullout resistance. This can be seen in Figure 5-43 for test D-5 (H/D = 4.5; ζ_b = 1; ζ_c = -0.8), in which the final resistance is 15% greater than the monotonic value, despite the significant upward displacements during cycling. For lower load magnitudes, however, the improvement in the final resistance is less significant (usually less than 10%). Although some densification of the soil appears to occur as a result of the cyclic loading, for design purposes it is conservative to assume a limiting stiffness value (as observed in the saturated tests) and no significant increase in pullout resistance.
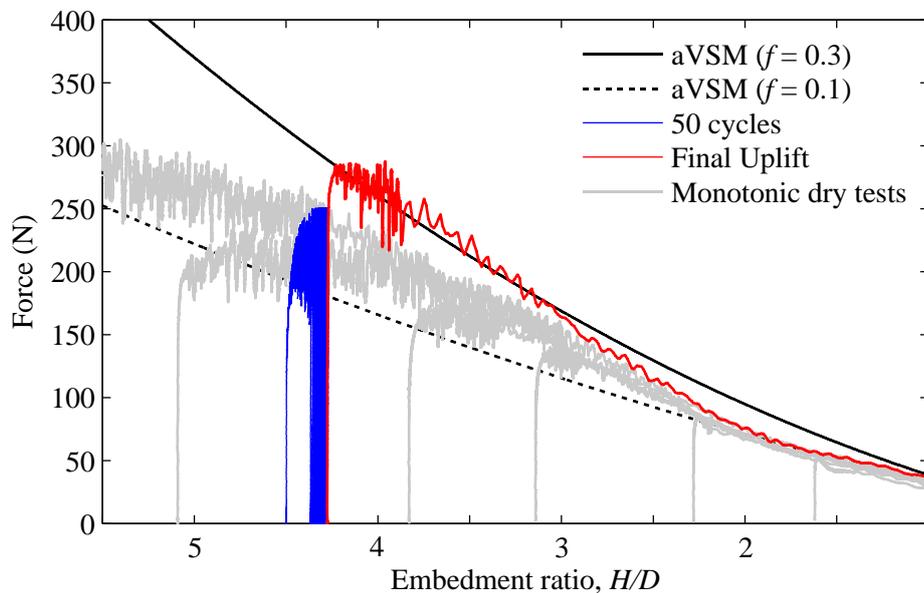
Figure 5-43 Monotonic pull-out resistance after cycling (Test:D-5)

5.6.1.3.   *Influence of overburden pressure and pipe weight*

Selected overburden tests have shown that while the monotonic uplift resistance of a greater embedment depth can be replicated in the laboratory by applying a surface overburden, the cyclic behaviour at this equivalent depth is not matched. If the pipe is cycled up to loads in excess of the resistance provided by the soil cover alone (i.e. in the resistance region provided by the OB), unstable behaviour occurs and the rate of upward displacement increases with

cycle number. This is because the soil stiffness in this region does not increase in the same manner as real soil. If the pipe is cycled only up to the maximum resistance of its actual cover depth, the cyclic behaviour is comparable to a test with no OB at the same depth. In this case, the OB test benefits from a significant increase in stiffness in this region due the additional weight; hence, the overall magnitude of displacements is smaller. This may be similar to the effect of increasing the self-weight of the pipe: the soil resistance above the pipe would remain the same, but the initial uplift response (as the gravity contributions are taken up by the pipe) may be more stiff.

5.6.2.   Implications for design

The work in this chapter has shown that the loading magnitude and direction are the primary factors which control the behaviour of a buried pipe subjected to vertical cycling. Through comparisons with an existing framework for the lateral cyclic loading of stiff piles in sand, trends in the displacement and soil stiffness response due to these variables were established. The influence of the burial conditions was also touched upon. It is clear from the experimental results that the difference between the upward and downward stiffness, which is controlled by the load parameters, determines whether the net movement of the pipe during cycling is up or down. With further experimental work the pile framework could be adapted such that this response could be correctly predicted for known backfill and loading conditions.

It was found that the worst case in terms of upward displacements was for one-way loading above the soil weight, to high load magnitudes nearing the peak uplift resistance. For design purposes, however, the most important finding was that if the average cyclic load is below the weight of the column of soil above the pipe, the pipe will tend to move downward – meaning that 'upheaval creep' would not be an issue. In reality, the loading would be at least partially two-way, given that during a shutdown cycle (when the thermal load is reduced), the pipe will bear on the soil beneath it until the net external force on the pipe becomes zero. Thus, it is unlikely that cyclic loading due to thermal cycles would occur only in the one-way (upward)

region. Also, the very high load magnitudes tested here are unrealistic. If the pipe is loaded such that it displaces in the plastic deformation region near the peak resistance of the cover soil, unstable snap-through buckling on the first cycle is of greater concern.

Based on the findings of this work, some basic design recommendations can be proposed. Assuming that in a typical thermal cycle the minimum load, F_{min}, will reach zero to satisfy equilibrium conditions, it follows that the maximum uplift force mobilised during cycling, F_{max}, should be limited to twice the value of the soil cover weight. This effectively means that the maximum possible value of ζ_c is -1. Furthermore, the value of F_{max} should be less than the peak monotonic resistance by some factor of safety related to the force-displacement response of the soil in uplift. Ideally, restricting the displacements to the elastic region of the uplift response – as recommended by previous researchers (Nielsen et al., 1990b) – would ensure a conservative design. Based on the experimental work in Chapter 3, this could be taken as the location of the slope change in the tri-linear representation of the uplift curve, which was shown to be influenced by the vertical effective stress level at the pipe embedment. This means, for example, that F_{max} could be up to around 80 or 90% of the peak in saturated Redhill 110 (at the H/D ratios tests here), while in dry conditions this may be reduced to 40 or 50% of the peak monotonic load. This is consistent with the cyclic response observed in the dry and saturated tests. As a mitigating measure, increasing the pipe weight or adding some form of surface overburden may reduce the net displacements, but does not increase the allowable cyclic magnitude or direction. Finally, it was observed in all tests that for at least the first 10 to 15 cycles, the rate of displacement decreases. Beyond this, in certain critical cases, a limiting stiffness was reached and displacements became linear. In order to avoid this, the number of cycles a pipeline is subjected to should be limited as much as possible.

5.7. Conclusions

In this chapter, a preliminary investigation of the vertical cyclic loading of buried pipelines in sand has been presented. The work provides a more thorough picture of the behaviour of

the pipe due to this type of loading than has previously been examined in the literature. Comparison of this behaviour to the cyclic lateral loading of stiff piles has demonstrated that a common framework can be used to describe the problem, though some important differences have been highlighted. The primary finding is that upheaval creep or cyclic ratcheting is possible under extreme loading scenarios; however, through reasonable limitations on the magnitude and direction of loading, detrimental cyclic effects can be avoided. Further experimental work could be useful in quantifying the influence of various conditions that have been highlighted here, such that predictions for the pipeline response over a number of cycles can be included in upheaval buckling design.

6   Conclusions

This thesis describes a comprehensive research programme founded on focused and high quality experimental work, which was aimed at addressing key challenges for upheaval buckling design. The research comprised both physical uplift experiments and simplified finite element analysis; together these tools were used to develop a complete picture of the upheaval buckling problem from a soil-structure interaction perspective. A primary focus of this work was to improve the understanding of the influence of backfill soil conditions – particularly loose and liquefiable conditions – on upheaval buckling stability, such that design guidance in this area could be assessed and improved. Key findings from the three main areas of research, along with implications for design, are summarised in the following section. Suggestions for future work following on from this thesis are also presented.

6.1.   Key findings

6.1.1.   Monotonic uplift resistance

- Tests in both dry and drained conditions demonstrated a transition from a sliding block failure mechanism at shallow depths to a probable flow-around failure mechanism at greater embedments, as indicated by a levelling off of peak breakout factors at these depths. This flow mechanism is associated with a lower peak breakout resistance, which is independent of the embedment depth. While current prediction models can accurately predict resistance mobilised through a sliding block mechanism, no such model exists to reliably predict the transition between mechanisms.

- The mobilised failure mechanism was found to be strongly influenced by relative density, as well as grain size (with respect to pipe diameter) and stress level. The most critical case in which possible flow behaviour occurred at shallower embedments was observed in very loose, fine sand. Based on the results, the onset of a flow-around

mechanism could be attributed to contractive behaviour of the sand. The same conditions were also shown to significantly reduce the resistance in partially drained conditions that could arise from fast rates of pipe uplift.

- The influence of these variables was supported by evidence from fast-rate tests which showed that at very low relative density, soil contraction occurs primarily around the pipe, while at higher densities dilation away from the pipe contributes to the resistance. Additionally, the trends in grain size agreed well with previous research findings that in fine soil shear zones are more local to the pipe, whereas in coarse sand a combined heave and flow tends to occur. Finally, overburden tests demonstrated that increasing the stress level of the soil could result in more contractive behaviour, mimicking what occurs at greater embedment depth.

- The initial force-displacement response – including the mobilisation displacement and the initial stiffness – was also shown to be related to the mechanism governing at peak resistance. A flow mechanism is thought to correspond to a much softer overall response and higher mobilisation displacements. It was found that a tri-linear characteristic curve, as specified in the DNV guidelines, can capture the observed force-displacement response if displacements are related to an effective stress ratio instead of embedment ratio. Modifications to the shape-defining parameters given in the guidelines are proposed based on these results.

- Based on the work in Chapter 3, a tentative procedure which allows for the assessment of the governing mechanism, uplift resistance, and force-displacement response, under given installation conditions is proposed. However, it is recommended that for a specified embedment ratio and stress level, a minimum relative density of the backfill soil should be ensured, such that dilation occurs upon shearing of the soil. This in turn means that the flow-around mechanism at peak resistance may be avoided, and the

conservative drained resistance (and force-displacement response) can then be predicted using existing models.

6.1.2. Upheaval buckling modelling

- A finite element model was developed to demonstrate how upheaval buckling behaviour is influenced by the surrounding soil, using a standard non-linear spring representation of the soil resistance. It was observed that the primary role of the axial resistance is in the development of an effective axial force in the pipe; it was shown that the length of pipe displacement required to build-up this force is dependent on the relative axial stiffness of the pipe and spring. Sections of pipe in which the fully-constrained thermal load is reached become effectively anchored. A further influence of the axial resistance is then seen in the amount of feed-in that occurs towards buckles.

- The limiting vertical soil force (i.e. the peak uplift resistance) was found to be a critical influence on the buckling behaviour – if this limit is reached during thermal loading, localised snap-through buckling may occur at the location of an initial imperfection. This is consistent with observations by previous researchers, except that the initial vertical stiffness of the soil prior to peak resistance was shown to significantly influence the buckling load and snap-through stability, similar to the influence of varying imperfection heights.

- A parametric study based on the force-displacement recommendations in the DNV guidelines showed that if a vertical slip model is used to determine the peak soil resistance – the embedment ratio, *H/D*, and the uplift factor, *f*, are the most important parameters in controlling the buckling load. The mobilisation displacement and initial stiffness (within the range specified by the DNV) have relatively less influence. At greater embedment ratios, all parameters – most notably the uplift factor, show a greater range in buckling loads.

- Comparisons using the drained experimental force-displacement results as inputs into the model – accounting only for effects due to relative density and *H/D* – show that the range of buckling temperatures is similar to what is predicted by the DNV guidelines. However, the observed levelling off of the breakout factors is not correctly captured by the guidelines, suggesting that it is not appropriate to use a constant uplift factor for a given relative density, across different embedment ratios.

- Further tests were carried out in which observed stress level effects at higher embedment ratios were also introduced into the model. In this worst-case scenario, the calculated buckling force drops well below the guideline predictions, even reaching a peak at a certain depth. The reduction in stiffness of the soil force-displacement response in these tests was such that snap-through buckling occurred even before the limiting force was reached.

- Finally, preliminary results relating to 'rate effects' or more specifically, to a loss of stiffness caused by pore water effects and liquefaction, show that the pipe may experience lower buckling temperatures in these conditions, compared to a drained scenario. A simple method has been proposed, which uses faster-rate uplift curves as inputs for the structural model, to incorporate possible rate effects in upheaval buckling assessments.

6.1.3. Cyclic loading

- A preliminary investigation into the vertical cyclic loading of buried pipelines was carried out, which provides a more thorough picture of the cyclic behaviour of the pipe than what has previously been examined in the literature. Comparison of this behaviour to the cyclic lateral loading of stiff piles has demonstrated that a common framework can be used to describe this problem, though some key differences were highlighted.

- The hypothesis that the weight of the soil overburden is a key reference point for the cyclic behaviour of buried pipes was confirmed through targeted tests around this load

point. The experiments confirm that the cyclic loading magnitude and direction are the primary factors which control the behaviour of the pipe over a number of cycles. It was found that the worst case in terms of upward displacements was for one-way loading above the soil weight, to high magnitudes nearing the peak monotonic resistance. If, however, the average cyclic load is below the soil weight, the pipe will tend to move downward. The direction of movement is determined by the difference in the upward and downward stiffness at each cycle, which is controlled by the load parameters and other factors.

- Additional variables influencing the cyclic behaviour include the backfill relative density and the embedment depth, due to their respective influences on the force-displacement response. Increasing either variable will increase the rate of displacement for a given load magnitude, due to the increasing proportion of the resistance mobilised through friction. It was also found that as a mitigating measure, increasing the pipe weight or adding some form of surface overburden may reduce the net displacements, but does not increase the allowable cyclic magnitude or direction.

- In all tests it was observed that for at least the first 10 to 20 cycles the rate of displacement decreases, due to increasing (and converging) upward and downward stiffness values. In critical upward-displacing tests, a limiting stiffness was then reached, causing the rate of displacement to become constant. This is due the limited available resistance from the soil cover above the pipe, which cannot increase once the pipe moves closer to the surface. Although this represents an unstable scenario, given the high loading magnitudes necessary for this to occur, snap-through buckling on the first several cycles is probably of greater concern. Nevertheless, the number of cycles a pipeline is subjected to should be restricted as much as possible to avoid reaching this limiting stiffness value.

- The main conclusion of this work is that upheaval creep or cyclic ratcheting – i.e. cumulative upward movement of the pipe – is possible under extreme loading scenarios; however, through reasonable limitations on the magnitude and direction of loading, detrimental cyclic effects can be avoided, for the soil tested. Simple design recommendations were proposed based on the trends observed in both the cyclic and monotonic experiments described in this thesis.

6.2. Future work

- The monotonic uplift tests identified variables that clearly influence the transition from a sliding block to a possible flow-around mechanism at peak. Further work is necessary to develop a model that can be used to predict the minimum uplift resistance that can be mobilised by this flow mechanism, so that the transition depth can be predicted through comparison with sliding block models. A preliminary model has been proposed by Wang (2012), but further experimentation is required for its calibration, such that density, stress level and grain size effects can be incorporated.

- It has been shown above that the flow mechanism may be related to the volumetric behaviour of the backfill soil, and thus any prediction should take into consideration both soil and state parameters. In order to do so, further work is required to develop or extend relationships between soil properties (such as that by Bolton (1986)) to the very low stress levels relevant for this problem.

- In the absence of a reliable prediction model as described above, it is clear that the density of the backfill soil should be monitored to avoid very loose conditions. Additional research is needed to determine field installation backfill densities for pipes installed by jet-trenching and ploughing, as well as more details of the time-dependent densification process after installation.

- Tests for the same sand in both dry and saturated conditions have been used to approximate stress level effects. In a scaled-up buckling model, these effects were shown to have a significant detrimental effect on the peak buckling load. Full-scale uplift experiments (using a pipe diameter of at least twice the size) under the same conditions are required to confirm this trend.

- Several simplifications were made in the upheaval buckling model developed in this thesis, such as in the installation procedure and the pipe material behaviour. Modelling work used for design purposes should include residual stresses in the pipe caused by an initial imperfection, plastic material behaviour of the pipe, as well as the influence of the weight of the pipe and its contents.

- Rate effects were treated in an simplified manner in the buckling model. In reality the rate of pipe movement during buckling is unknown. A progression of the work in this thesis might be to modify the soil-springs based on the rate of displacement. This could help determine whether a sudden loss in resistance at one location in the pipe could lead to 'unzipping' of the pipeline (i.e. a spread of the liquefied zone as faster rates of uplift are induced further along the pipe).

- From the cyclic loading tests it was found that a framework based on the lateral movement of stiff piles could be adapted for the vertical movement of a pipe segment over a number of cycles. Further experimental work is necessary in quantifying the influence of various conditions that have been highlighted in this thesis, such that predictions for the pipeline response over a number of cycles can be included in upheaval buckling design.

- The cyclic load response examined in this thesis considered a uniform material, installed through jet-trenching, located above and below the pipe. Further consideration is needed regarding the effects of a different, or more rigid underlying soil on the net displacements.

- Predictions of the cyclic force-displacement response could also be useful in examining the global response of a pipeline over a number of cycles in an FE buckling model, which would require the soil springs to be updated in each cycle based on the predicted trends. This would be useful in determining the actual cyclic loading magnitudes caused by thermal loading of the pipe, and determining whether this behaviour might lead to eventual upheaval buckling.

References

Abaqus 2010. *Abaqus/CAE 6.10-EF Analysis User's Manual,* Providence, RI, USA, Dassault Systèmes.

ALA. 2001. *Guidelines for the Design of Buried Steel Pipe.* American Lifelines Alliance.

API. 2004. *API 5L: Specification for line pipe.* Washington, D.C.: American Petroleum Institute.

ASTM Standard D4253-00. 2006. *Standard Test Methods for Maximum Index Density and Unit Weight of Soils Using a Vibratory Table.* West Conshohocken, PA: ASTM International.

Ballet, J. P. & Hobbs, R. E. 1992. Asymmetric effects of prop imperfections on the upheaval buckling of pipelines. *Thin-Walled Structures* 13**:** 355-373.

Been, K. & Jefferies, M. 2004. Stress-dilatancy in very loose sand. *Canadian Geotechnical Journal* 41**:** 972-989.

Blakeborough, A. 2012. Personal communication (7th September, 2012).

Boer, S., Hulsbergen, C. H., Richards, D. M., Klok, A. & Biaggi, J. P. 1986. Buckling considerations in the design of the gravel cover for a high-temperature oil line. *Offshore Technology Conference.* Houston, Texas: OTC 5294.

Bolton, M. D. 1986. The strength and dilatancy of sands. *Géotechnique* 36(1)**:** 65-78.

Bonjean, D., Erbrich, C. & Zhang, J. 2008. Pipeline flotation in liquefiable soil. *Offshore Technology Conference.* Houston, Texas: OTC 19668.

Bransby, M. F. & Ireland, J. 2009. Rate effects during pipeline upheaval buckling in sand. *Proceedings of the ICE - Geotechnical Engineering* 162**:** 247-256.

Bransby, M. F., Newson, T. A., Brunning, P. & Davies, M. C. R. 2001. Numerical and centrifuge modelling of the upheaval resistance of buried pipelines. *Proceedings of OMAE '01.* Rio de Janeiro, Brazil: ASME.

Bransby, M. F., Newson, T. A. & Davies, M. C. R. 2002. Physical modelling of the upheaval resistance of buried offshore pipelines. *Proceedings of the 1st International Conference on Physical Modelling in Geotechnics*, St. Johns, Newfoundland. 899-904.

Bruton, D. A. S., White, D. J., Carr, M. & Cheuk, J. C. Y. 2008. Pipe-soil interaction during lateral buckling and pipeline walking - the SAFEBUCK JIP. *Offshore Technology Conference.* Houston, Texas: OTC 19589.

Byrne, B. W., Schupp, J., Martin, C. M., Maconochie, A., Oliphant, J. & Cathie, D. 2013. Uplift of shallowly buried pipe sections in saturated very loose sand. *Géotechnique* 63(5)**:** 382-390.

Byrne, B. W., Schupp, J., Martin, C. M., Oliphant, J., Maconochie, A. & Cathie, D. N. 2008. Experimental modeling of the unburial behaviour of pipelines. *Offshore Technology Conference.* Houston, Texas: OTC 19573.

Cassidy, M. J., Houlsby, G. T., Hoyle, M. & Marcom, M. R. 2002. Determining appropriate stiffness levels for spudcan foundations using jack-up case records. *OMAE'02 - 21st International Conference on Offshore Mechanics and Arctic Engineering.* Oslo, Norway.

Cheuk, C. Y. 2005. *Soil-pipeline interaction at the seabed.* PhD thesis, University of Cambridge.

Cheuk, C. Y., White, D. J. & Bolton, M. D. 2008. Uplift mechanisms of pipes buried in sand. *Journal of Geotechnical and Geoenvironmental Engineering* 134(2)**:** 154-163.

Chin, E. L., Craig, W. H. & Cruickshank, M. 2006. Uplift resistance of pipelines buried in cohesionless soil. *Proceedings of the 6th International Conference on Physical Modelling in Geotechnics*, London. Taylor & Francis Group, 723-728.

Chiou, Y.-J. & Chi, Y., Chi 1993. Limit loads of buried pipelines in inelastic soil medium. *ASCE Journal of Engineering Mechanics* 119(5)**:** 938-954.

Clukey, E. C., Jackson, C. R. & Vermersch, J. A. 1989. Natural densification by wave action of sand surrounding a buried offshore pipeline. *Offshore Technology Conference.* Houston, Texas: OTC 6151.

Cowie, M. & Finch, M. 2001. Backfill improvement techniques - optimising pipeline burial solutions. *Offshore Technology Conference*, Houston, Texas. OTC 13142.

Croll, J. G. A. 1997. A simplified model of upheaval thermal buckling of subsea pipelines. *Thin-Walled Structures* 29(1-4)**:** 59-78.

Damgaard, J. S., Sumer, B. M., Teh, T. C., Palmer, A. C., Foray, P. & Osorio, D. 2006. Guidelines for pipeline on-bottom stability on liquefied noncohesive seabeds. *Journal of Waterway, Port, Coastal, and Ocean Engineering* 132(4)**:** 300-309.

de Groot, M. B., Bolton, M. D., Foray, P., Meijers, P., Palmer, A. C., Sandven, R., Sawicki, A. & Teh, T. C. 2006. Physics of liquefaction phenomena around marine structures. *Journal of Waterway, Port, Coastal, and Ocean Engineering* 132(4)**:** 227-243.

Dean, E. T. R. 2010. *Offshore Geotechnical Engineering: Principles and Practice*, Thomas Telford Limited.

Dickin, E. A. 1994. Uplist resistance of buried pipelines in sand. *Soils and Foundations* 34(2)**:** 41-48.

DNV-RP F110 2007. *Global Buckling of Submarine Pipelines; Structural Design Due to High Temperature/High Pressure.* Norway: Det Norske Veritas.

Dunn, S. L., Vun, P. L., Chan, A. H. C. & Damgaard, J. S. 2006. Numerical modeling of wave-induced liquefaction around pipelines. *Journal of Waterway, Port, Coastal, and Ocean Engineering* 132(4)**:** 276-288.

Ellinas, C. P., Supple, W. J. & Vastenholt, H. 1990. Prevention of upheaval buckling of hot submarine pipelines by means of intermittent rock dumping. *Offshore Technology Conference.* Houston, Texas: OTC 6332.

Finch, M. 1999. Upheaval buckling and floatation of rigid pipelines: the influence of recent geotechnical research on the current state of the art. *Offshore Technology Conference.* Houston, Texas: OTC 10713.

Finch, M., Fisher, R., Palmer, A. & Baumgard, A. 2000. An integrated approach to pipeline burial in the 21st century. *Deep Offshore Technology 2000.*

Finch, M. & Machin, J. B. 2001. Meeting the challenges of deepwater cable and pipeline burial. *Offshore Technology Conference.* Houston, Texas: OTC 13141.

Gao, X.-f., Liu, R. & Yan, S. W. 2011. Model test based soil spring model and application in pipeline thermal buckling analysis. *China Ocean Engineering* 25(3)**:** 507-518.

Gould, N. 2007. *Offshore oil pipeline unburial: Impulse response & uplift resistance.* MEng Thesis, University of Oxford.

Guijt, J. 1990. Upheaval buckling of offshore pipelines: overview and introduction. *Offshore Technology Conference.* Houston, Texas: OTC 6487.

Haigh, S. K., Eadington, J. & Madabhushi, S. P. G. 2012. Permeability and stiffness of sands at very low effective stresses. *Géotechnique* 62(1)**:** 69-75.

Hobbs, R. E. 1981. Pipeline buckling caused by axial loads. *Journal of Constructional Steel Research* 1(2)**:** 2-10.

Hobbs, R. E. 1984. In-service buckling of heated pipelines. *ASCE Journal of Transportation Engineering* 110**:** 175-189.

Houlsby, G. T. 1991. How the dilatancy of soils affects their behaviour. *10th European Conference on Soil Mechanics and Foundation Engineering.* Florence, Italy.

Jefferies, M. & Been, K. 2006. *Soil liquefaction: a critical state approach,* Abingdon, Oxon, UK, Taylor & Francis

Ju, G. T. & Kyriakides, S. 1988. Thermal buckling of offshore pipelines. *Journal of Offshore Mechanics and Arctic Engineering* 110**:** 355-364.

Jung, J. K. 2011. *Soil-pipe interaction under plane strain conditions.* PhD thesis, Cornell University.

Jung, J. K., O' Rourke, T. D. & Olson, N. A. 2013. Uplift soil – pipe interaction in granular soil. *Canadian Geotechnical Journal* 50**:** 744-753.

Kelly, R. B., Byrne, B. W. & Houlsby, G. T. 2006. A comparison of field and laboratory tests of caisson foundations in sand and clay. *Géotechnique* 56(9)**:** 617-626.

Klever, F. J., van Helvoirt, L. C. & Sluyterman, A. C. 1990. A dedicated finite-element model for analyzing upheaval buckling response of submarine pipelines. *Offshore Technology Conference.* Houston, Texas: OTC 6333.

LabVIEW 2009. *Getting Started with LabVIEW,* Austin, Texas, National Instruments.

Leblanc, C., Houlsby, G. T. & Byrne, B. W. 2010. Response of stiff piles in sand to long-term cyclic lateral loading. *Géotechnique* 60(2)**:** 79-90.

Liu, R. & Yan, S. W. 2011. Model test studies on soil restraint to pipelines buried in sand. *Frontiers in Offshore Geotechnics II.* Perth, Australia: Taylor & Francis Group.

Majer, J. 1955. Zur Berechnung von Zugfundamenten. *Osterreichische Bauzeitschrift* 10(5)**:** 85-90.

Maltby, T. C. & Calladine, C. R. 1995a. An investigation into upheaval buckling of buried pipelines I. Experimental apparatus and some observations. *International Journal of Mechanical Sciences* 37(9)**:** 943-963.

Maltby, T. C. & Calladine, C. R. 1995b. An investigation into upheaval buckling of buried pipelines II. Theory and analysis of experimental observations. *International Journal of Mechanical Sciences* 37(9)**:** 965-983.

Marston, A. 1930. The theory of external loads on closed conduits in the light of the latest experiments. *Bulletin 96.* Ames, Iowa: Iowa Engineering Experiment Station.

Matyas, E. L. & Davis, J. B. 1983a. Experimental study of earth loads on rigid pipes. *ASCE Journal of Geotechnical Engineering* 109(2)**:** 202-209.

Matyas, E. L. & Davis, J. B. 1983b. Prediction of vertical earth loads on rigid pipes. *ASCE Journal of Geotechnical Engineering* 109(2)**:** 190-201.

Meyerhof, G. G. & Adams, J. I. 1968. The ultimate uplift capacity of foundations. *Canadian Geotechnical Journal* 5(4)**:** 225-244.

Moradi, M. & Craig, W. H. 1998. Observations of upheaval buckling of buried pipelines. *Centrifuge 98, Kimura, Kusakabe & Takemura (eds)*, Tokyo, Japan. 693-698.

Murray, E. J. & Geddes, J. D. 1987. Uplift of anchor plates in sand. *ASCE Journal of Geotechnical Engineering Division* 113(3)**:** 202-215.

Ng, C. W. W. W. & Springman, S. M. 1994. Uplift resistance of buried pipelines in granular materials. *Centrifuge 94, Leung, Lee & Tan (eds)*, Singapore. 753-758.

Nielsen, N.-J. R., Lyngberg, B. & Pedersen, P. T. 1990a. Upheaval buckling failures of insulated buried pipelines: A case story. *Offshore Technology Conference.* Houston, Texas: OTC 6488.

Nielsen, N. J. R., Pedersen, P. T., Grundy, A. K. & Lyngberg, B. S. 1990b. Design criteria for upheaval creep of buried sub-sea pipelines. *Journal of Offshore Mechanics and Arctic Engineering* 112(4)**:** 290-296.

Palmer, A. C., Ellinas, C. P., Richards, D. M. & Guijt, J. 1990. Design of submarine pipelines against upheaval buckling. *Offshore Technology Conference.* Houston, Texas: OTC 6335.

Palmer, A. C. & King, R. A. 2004. *Subsea pipeline engineering,* Tulsa, OK, PennWell.

Palmer, A. C., White, D. J., Baumgard, A. J., Bolton, M. D., Barefoot, A. J., Finch, M., Powell, T., Faranski, A. S. & Baldry, J. A. S. 2003. Uplift resistance of buried submarine pipelines: comparison between centrifuge modelling and full-scale tests. *Géotechnique* 53(10)**:** 877-883.

Pedersen, P. T. & Jensen, J. J. 1988. Upheaval creep of buried heated pipelines with initial imperfections. *Marine Structures* 1**:** 11-22.

Pedersen, P. T. & Michelson, J. 1988. Large Deflection Upheaval Buckling of Marine Pipelines. *Proceedings of Behaviour of Offshore Structures (BOSS)*, Trondheim, Norway.

Randolph, M. F. & Gourvenec, S. 2011. *Offshore geotechnical engineering*, Spon Press/Taylor & Francis.

Rowe, R. K. & Davis, E. H. 1982. The behaviour of anchor plates in sand. *Géotechnique* 32(1)**:** 25-41.

Sandford, R. J. 2006. *Three dimensional modelling of the upheaval buckling of buried pipelines.* MEng thesis, University of Oxford.

Sandford, R. J. 2012. *Lateral buckling of high pressure/high temperature on-bottom pipelines.* DPhil thesis, University of Oxford.

Schaminee, P. E. L., Zorn, N. F. & Schotman, G. J. M. 1990. Soil response for pipeline upheaval buckling analyses: full-scale laboratory tests and modelling. *Offshore Technology Conference.* Houston, Texas: OTC 6486.

Schupp, J. 2009. *Upheaval buckling and flotation of buried offshore pipelines.* DPhil thesis, University of Oxford.

Schupp, J., Byrne, B. W., Eacott, N., Martin, C. M., Oliphant, J., Maconochie, A. & Cathie, D. 2006. Pipeline unburial behaviour in loose sand. *25th International Conference on Offshore Mechanics and Arctic Engineering.* Hamburg, Germany.

Stone, K. J. L., Newson, T. A. & Bransby, M. F. 2005. Discussion: Uplift resistance of buried submarine pipelines: comparison between centrifuge modelling and full-scale tests. *Géotechnique* 55(4)**:** 338-340.

Sumer, B. M., Hatipoglu, F., Fredsoe, J. & Hansen, N.-E. O. 2006a. Critical flotation density of pipelines in soils liquefied by waves and density of liquefied soils. *Journal of Waterway, Port, Coastal, and Ocean Engineering* 132(4)**:** 252-265.

Sumer, B. M., Truelsen, C. & Fredsoe, J. 2006b. Liquefaction around pipelines under waves. *Journal of Waterway, Port, Coastal, and Ocean Engineering* 132(4)**:** 266-275.

Taylor, N. & Gan, A. B. 1986. Submarine pipeline buckling - imperfection studies. *Thin-Walled Structures* 4(4)**:** 295-323.

Taylor, N. & Tran, V. 1993. Prop-imperfection subsea pipeline buckling. *Marine Structures* 6(4)**:** 325-358.

Taylor, N. & Tran, V. 1996. Experimental and theoretical studies in subsea pipeline buckling. *Marine Structures* 9(2)**:** 211-257.

Thusyanthan, N. I., Mesmar, S., Robert, D. J., Wang, J. & Haigh, S. K. 2011. Upheaval buckling assessment based on pipeline features. *Offshore Pipeline Technology Conference.* Houston, Texas: OTC 21802.

Thusyanthan, N. I., Mesmar, S., Wang, J. & Haigh, S. K. 2010. Uplift resistance of buried pipelines and DNV-RP-F110 guidelines. *Offshore Pipeline Technology Conference.* Amsterdam.

Trautmann, C. H., O'Rourke, T. D. & Kulhawy, F. H. 1985. Uplift force-displacement response of buried pipe. *ASCE Journal of Geotechnical Engineering* 111(9)**:** 1061-1076.

Tvergaard, V. & Needleman, A. 1981. On localized thermal track buckling. *International Journal of Mechanical Sciences* 23(10)**:** 577-587.

Vanden Berghe, J.-F., Cathie, D. & Ballard, J.-C. 2005. Pipeline uplift mechanisms using finite element analysis. *Proceedings of the 16th International Conference on Soil Mechanics and Geotechnical Engineering*, Osaka, Japan. AA Balkema Publishers, 1801-1804.

Vermeer, P. A. & Sutjiadi, W. 1985. The uplift resistance of shallow embedded anchors. *Proceedings of the 11th International Conference on Soil Mechanics and Foundation Engineering*, San Francisco. 1635-1638.

Vesić, A. S. 1972. Breakout resistance of objects embedded in ocean bottom. *ASCE Journal of the Soil Mechanics and Foundations Division* 97(9)**:** 1183-1205.

Villalobos, F. A., Byrne, B. W. & Houlsby, G. T. 2005. Moment loading of caissons installed in saturated sand. *Frontiers in Offshore Geotechnics*, Perth, Australia.

Wang, J. 2012. *Monotonic and cyclic uplift resistance of buried pipelines in cohesionless soils.* PhD thesis, Univeristy of Cambridge.

Wang, J., Ahmed, R., Haigh, S. K., Thusyanthan, N. I. & Mesmar, S. 2010. Uplift resistance of buried pipelines at low cover-diameter ratios. *Offshore Technology Conference*, Houston, Texas. OTC 20912, 11.

Wang, J. & Haigh, S. K. 2011. Mobilization distance in uplift resistance modeling of pipelines. *Frontiers in Offshore Geotechnics II.* Perth, Australia.

Wang, J., Haigh, S. K., Forrest, G. & Thusyanthan, N. 2012. Mobilization distance for upheaval buckling of shallowly buried pipelines. *ASCE Journal of Pipeline Systems Engineering and Practice* 3(4)**:** 106-114.

Wang, W., Liu, R., Yan, S. & Xu, Y. 2011. Vertical upheaval buckling of submarine buried heated pipelines with initial imperfection. *Trans. Tianjin Univ.* 17**:** 138-145.

White, D. J., Barefoot, A. J. & Bolton, M. D. 2001. Centrifuge modelling of upheaval buckling in sand. *International Journal of Physical Modelling in Geotechnics* 1(2)**:** 19-28.

White, D. J., Cheuk, C. Y. & Bolton, M. D. 2008. The uplift resistance of pipes and plate anchors buried in sand. *Géotechnique* 58(10)**:** 771-779.

Williams, E. S., Byrne, B. W. & Blakeborough, A. 2013. Pipe uplift in saturated sand: rate and density effects. *Géotechnique* 63(11)**:** 946-956.

Wroth, C. P. & Houlsby, G. T. 1985. Soil mechanics - property characterisation and analysis procedures. *Proc. 11th Int. Conf. on Soil Mech. and Fndn Engng*, San Fransisco. 1-55.

Xia, G.-p. & Zhang, Z. 2009. A numerical method for critical buckling load for a beam supported on elastic foundation. *Electronic Journal of Geotechnical Engineering*.

Yimsiri, S., Soga, K., Yoshizaki, K., Dasari, G. R. & O' Rourke, T. D. 2004. Lateral and upward soil-pipeline interactions in sand for deep embedment conditions. *ASCE Journal of Geotechnical and Geoenvironmental Engineering* 130(8)**:** 830-842.

Youd, T. L. & Idriss, I. M. 2001. Liquefaction resistance of soils: summary report from the 1996 NCEER and 1998 NCEER/NSF workshops on evaluation of liquefaction resistance of soils. *ASCE Journal of Geotechnical and Geoenvironmental Engineering* 127(4)**:** 817-833.

Yun, H. & Kyriakides, S. 1985. Model for beam-mode buckling of buried pipelines. *ASCE Journal of Engineering Mechanics* 111(2)**:** 235-253.